Alexander C. Monsees

DIAGENETIC CONTROLS ON FLUID FLOW AND MECHANICAL PROPERTIES IN ROTLIEGEND RESERVOIR SANDSTONES

KIT Scientific Publishing

Alexander C. Monsees

Diagenetic controls on fluid flow and mechanical properties in Rotliegend reservoir sandstones

Diagenetic controls on fluid flow and mechanical properties in Rotliegend reservoir sandstones

by
Alexander C. Monsees

KIT Scientific Publishing

Karlsruher Institut für Technologie
Institut für Angewandte Geowissenschaften - Strukturgeologie & Tektonik

Diagenetic controls on fluid flow and mechanical properties in Rotliegend reservoir sandstones

Zur Erlangung des akademischen Grades eines Doktors der Naturwissenschaften von der KIT-Fakultät für Bauingenieur-, Geo- und Umweltwissenschaften des Karlsruher Instituts für Technologie (KIT) genehmigte Dissertation

von Alexander C. Monsees

Tag der mündlichen Prüfung: 24. Februar 2021
Ersten Gutachter: Prof. Dr. Christoph Hilgers
Zweiter Gutachter: Prof. Dr. Harald Stollhofen

Impressum

Karlsruher Institut für Technologie (KIT)
KIT Scientific Publishing
Straße am Forum 2
D-76131 Karlsruhe

KIT Scientific Publishing is a registered trademark
of Karlsruhe Institute of Technology.
Reprint using the book cover is not allowed.

www.ksp.kit.edu

Print on Demand 2021 – Gedruckt auf FSC-zertifiziertem Papier

ISBN 978-3-7315-1107-6
DOI 10.5445/KSP/1000133960

Acknowledgements

My sincerest thanks go to my advisor, Christoph Hilgers, for his guidance, support, and his never-ending suggestions, leading me to new ideas along the way, as well as off track to thematic excursions from time to time. He was also the initiator of the MERID project, which is the nucleus for this doctoral thesis. Numerous long discussions, particularly before submission deadlines, always lead to new and improved insights, showing me a completely new perspective on my work.

Harald Stollhofen is thankfully acknowledged for being the second referee of my doctoral thesis. His vast knowledge about arid sedimentary systems benefitted and improved parts of this work.

Benjamin Busch is sincerely acknowledged for his introduction into diagenesis, as well as for countless hours of discussions about sandstone diagenesis, as well as completely unrelated topics. His positive and supporting attitude continuously provided a pleasant working environment, and his internal reviews of my manuscripts significantly improved their quality.

I want to express my gratitude towards the whole Structural Geology group at KIT – thank you for making this the pleasant experience it was. Ivy Becker, Christina Schmidt and Olajide Adamolekun, you are particularly acknowledged for numerous discussions regarding diagenesis and sedimentology, being my first quality-check for the validity of my ideas. Ivy, thank you for being a supportive senior and office mate during my first year at KIT. Ola, thank you for providing me with a new and incredibly interesting perspective on African politics in our discussions while we shared an office. Tina, we did it together – handing in our thesis shortly after one another and now continuing our careers in new companies!

Stephan Unrein is gratefully acknowledged for thin-section preparation. Without Ulrike Brecht, I oftentimes would have been lost in the maze of German bureaucracy. Additional thanks go out to my colleagues Agnes Kontny, Dennis Quandt and Bruno Mendes for countless discussions about geology and other nice things in life. Alexander Spitzner is acknowledged as HiWi during field work in the UK, making it the pleasant trip it was. I am also proud that my HiWi Felix Allgaier decided to follow in my footsteps as doctoral researcher.

The university collaborators of the MERID project are gratefully acknowledged. I am sincerely grateful to Sven F. Biebricher (RWTH Aachen) for productive fieldwork, his invaluable help with geotechnical standard tests, and pleasant evening discussions. Amol

Subhedar introduced me to the fascinating world of computational fluid dynamics and is sincerely acknowledged for the contribution in form of his numerical models. Further project partners include Martin Feinendegen and Martin Ziegler (both RWTH Aachen), as well as Andreas Reiter and Britta Nestler (both Karlsruhe University of Applied Sciences).

The Federal Ministry of Education and Research (BMBF) is acknowledged for funding (research grant FKZ 03G0868A), while the DGMK e.V. represented by Susanne Kuchling and Dominik Soyk are acknowledged for project coordination between the project partners of the MERID project.

I thankfully acknowledge data provision by Wintershall Dea GmbH, formerly Deutsche Erdöl AG. Hanna-Maria Rumpel and Markus Schleicher are thankfully acknowledged for always promptly answering my requests for additional data, or putting me in touch with people who were able to answer my questions. Nadine Schöner is sincerely thanked for her time and always eager support during the first half of my thesis, including her input on my first paper and insightful discussions about the sedimentology of arid continental systems.

I appreciate and acknowledge scientific discussions about petrophysics and permeability with Alexandra Kushnir, Mike Heap, Alexandra Amann-Hildenbrand, and Frank Schilling, who all shared great insight with me and enhanced my understanding of the topic.

I thankfully acknowledge access and logistical support in the Cornberg quarry provided by the municipality of Cornberg (Hesse, Germany) represented by Helmut Reker and Achim Großkurth, access to the Schwentesius quarry provided by Norddeutsche Naturstein GmbH in Bebertal (Saxony-Anhalt, Germany), and finally access and logistical support provided by Alan of Cumbria Quarry Services Ltd., Penrith (Cumbria, UK). Mitos GmbH is acknowledged for granting an academic discount on x-ray microcomputed tomography scans.

My parents have supported my passion in geology from young age, resulting in the start of my mineral and fossil collection at the age of eight years, ultimately leading me to my degree in Geosciences. I felt their love and unwavering support throughout my whole lifetime, and I am immensely grateful for all they have done for me and all they have given to me.

I look back most fondly to the moments I spent with my friends. I sincerely thank you for all the laughs we shared, and the trips and vacations we have done together. Even more so I appreciate my closest friends who supported me through the most challenging times, and built me up time and time again. You are most important.

Abstract

Reservoir quality of sandstones is mainly derived from their permeability and porosity and their mechanical properties. As a result, porosity-reducing processes need to be understood to evaluate reservoir quality and geotechnical properties in sandstones. This study focusses on a Lower Permian Rotliegend gas reservoir in the Northern German Basin, as well as three Rotliegend outcrop analogs in Germany and the United Kingdom.

In the studied Rotliegend reservoir, the most significant diagenetic factors influencing the development of the intergranular volume (IGV) are quartz cementation and chemical compaction, which are related to the distribution of clay coatings in the grain fabric. This is reflected by the introduced parameters of illitic grain coating coverages on grain-to-IGV (GTI) interfaces on quartz cementation and chemical compaction due to pronounced illitic grain coating coverages on grain-to-grain (GTG) interfaces. Where large proportions of the interface between adjacent grains are coated by illite, stronger chemical compaction (pressure dissolution) was observed to occur. This chemical compaction reduces the IGV, and thus pore space.

Permeability was measured under decreasing confining pressures from 50 to 2 MPa determining the pressure sensitivity of permeability, which ranged from 0.005 to 0.22 MPa^{-1}. The pressure sensitivity of permeability, permeability, and porosity were linked to the petrographic texture, implying three different major rock types: Type A is characterized by an uncemented petrographic texture with high porosity, high permeability, and low pressure sensitivity of permeability. Type B is intensely cement-ed with reduced porosity, reduced permeability, and increased pressure sensitivity of permeability. Type C is characterized by intense chemical compaction leading to the lowest porosity and permeability in concert with the highest pressure-sensitivity of permeability.

The diagenetic impact on reservoir quality was also characterized in three fluvio-eolian Lower Permian Rotliegend analogs. Results show large porosity (10 to 35 %) and permeability (0.01 to 10000 mD) ranges mostly independent of the depositional environment. The major control on reservoir quality in Cornberg Sandstones (eolian dune facies) are dolomite and siderite cementation in conjunction with illitization and illite and kaolinite cementation, leading together with quartz cementation to a mostly cemented IGV and poor reservoir quality. Flechtingen Sandstones (fluvio-eolian facies) are most intensely compacted due to the lack of significant early diagenetic cement phases and continuous illitic grain coatings, which inhibited intense quartz cementation but enhanced chemical compaction at quartz grain contacts, resulting in intermediate reservoir quality. Penrith Sandstones (eolian dune facies) lack significant authigenic phases besides quartz due to carbonate dissolution during uplift and the least number of detrital feldspars and clay minerals, leading to no major reservoir quality reduction by burial diagenetic clay mineral alterations, resulting in good reservoir quality. Additional results highlight smaller permeability anisotropies parallel vs. normal to bedding below the factor 2 in more homogenous, higher permeable sandstones. Although detrital and authigenic sample compositions vary throughout the studied areas, the general effect of grain coatings coverages on syntaxial cement inhibition and chemical compaction can be delineated for each study area.

Initial detrital composition and authigenic alterations during diagenesis of the three aforementioned Rotliegend analogs are related to their mechanical properties. Uniaxial compressive strength (UCS) of sandstones ranges from 3-62 MPa and positively correlates with E (range: 0.3-12.7 GPa) and density (range: 1.75-2.35 g/cm^3). Optical porosity is controlling these parameters and was linked to diagenetic alterations. Diagenetic alterations affecting porosity-reduction are the abundance of clay minerals, the intensity of mechanical and chemical compaction. The latter is controlled by clay mineral coatings on contacts between detrital grains, and the occurrence of authigenic quartz and dolomite. Horizontal contact lengths of grains normalized to their respective particle diameter was defined as effective contact ratio (ECR). The porosity ϕ was identified as a control on the mechanical properties UCS and E, and linked to the grain fabric, which is reflected by the rock strength index $S_R=\phi/ECR$. The results suggest that S_R is able to predict UCS and E based on petrographic information obtained from the studied samples.

X-ray micro-computed tomography (µCT) is able to derive the internal structure of reservoir sandstones for digital fluid flow simulations, while simultaneously assessing mineral distribution in 3D based on mineral densities. The coupling of petrophysical rock characterization and digital rock models demonstrate a closer match of µCT porosity to petrophysical porosity compared to optical porosity. One-phase fluid flow simulations of the gas phase in digital rocks deliver results within 10–20 % of the laboratory measurements. Two-phase flow simulations of gas and water phases in digital rocks enable the assessment of relative permeabilities in rocks with water-sensitive minerals. Due to computational demand of µCT-based fluid flow simulations, a tradeoff between resolution, representative volume, and cost is necessary. Rock composition reconstructed from µCT images can be used as a first-order approximation for sample composition but is unable to confidently identify minerals that occur in minor quantities due to constraints of the chosen resolution.

Kurzfassung

Die Reservoirqualität von Sandsteinen ergibt sich hauptsächlich aus ihrer Permeabilität und Porosität. Daher müssen porositätsreduzierende Prozesse verstanden werden, um die Reservoirqualität und die geotechnischen Eigenschaften von Sandsteinen beurteilen zu können. Diese Studie konzentriert sich auf eine unterpermische Rotliegend-Gaslagerstätte im norddeutschen Becken und vergleicht sie mit Rotliegend-Aufschlüssen in Deutschland und Großbritannien.

In den Rotliegend-Reservoiren wird die Entwicklung des intergranularen Volumens (IGV) von der Quarz-Zementierung gesteuert, die wiederrum von illitischen Kornüberzügen an Korn-IGV Grenzflächen kontrolliert wird. Ein weiterer Faktor ist die chemische Kompaktion aufgrund der ausgeprägten illitischen Kornüberzüge an den Korn-Korn- Grenzflächen. Wo große Anteile der Grenzfläche zwischen benachbarten Körnern mit Illit beschichtet sind, wurde eine stärkere chemische Kompaktion durch Drucklösung beobachtet. Diese chemische Kompaktion reduziert das IGV und damit den Porenraum.

Die Druckempfindlichkeit der Permeabilität, gemessen unter abnehmenden Umschließungsdrücken von 50 bis 2 MPa, reicht von 0,005 bis 0,22 MPa^{-1}. Die Druckempfindlichkeit der Permeabilität, Porosität und Durchlässigkeit wurden mit der petrographischen Textur in Verbindung gebracht, wodurch drei verschiedene Hauptgesteinstypen impliziert werden: Typ A zeichnet sich durch eine unzementierte petrographische Textur mit hoher Porosität, hoher Permeabilität und niedriger Druckempfindlichkeit der Permeabilität aus. Typ B ist intensiv zementiert mit reduzierter Porosität, reduzierter Permeabilität und erhöhter Druckempfindlichkeit der Permeabilität. Typ C ist durch eine intensive chemische Kompaktion gekennzeichnet, die zu der niedrigsten Porosität und Permeabilität in Verbindung mit der höchsten Druckempfindlichkeit der Permeabilität führt.

Der diagenetische Einfluss auf die Reservoirqualität und die Permeabilitätsheterogenität, die parallel und senkrecht zur Schichtung gemessen wurde, wurde auch in drei fluvioäolischen Rotliegend-Analogen unter Verwendung von Point-Counting, Polarisationslichtmikroskopie, Helium-Pyknometrie und Permeabilitätsmessungen charakterisiert.

Die Ergebnisse zeigen breite Porositäts- (10 bis 35 %) und Permeabilitätsbereiche (0,01 bis 10000 mD), die weitgehend unabhängig vom Ablagerungsraum sind. Die wichtigste Kontrolle der Reservoirqualität im Cornberger Sandstein ist die Dolomit- und Siderit-Zementation in Verbindung mit Illitisierung und Illit- und Kaolinit-Zementierung, was zusammen mit der Quarz-Zementierung zu einem größtenteils zementierten IGV und einer schlechten Reservoirqualität führt. Der Flechtinger Sandstein wurde am intensivsten kompaktiert, da es keine signifikanten frühen diagenetischen Zementphasen sowie kontinuierliche illitische Kornüberzüge gab, die eine intensive Quarzzementierung verhinderten, jedoch die chemische Kompaktion an den Quarzkornkontakten erhöhten, resultierend in einer mittleren Reservoirqualität. In den Penrith Sandsteinen sind neben Quarz kaum authigene Phasen erhalten. Dies ist bedingt durch die Karbonatlösung während der Inversion und die geringen Mengen an detritischen Feldspäten und Tonmineralen, was zu keiner größeren Qualitätsminderung der Reservoirqualität durch diagene-tische Tonmineralveränderungen führt, wodurch eine gute Reservoirqualität die Folge ist. Die Permeabilitätsunterschiede zwischen Permeabilitäten parallel und senkrecht zur Schichtung sind größer in weniger permeablen Sandsteinen als in homogeneren, höher permeablen Sandsteinen.

Die detritische Zusammensetzung und authigene Veränderung während der Diagenese der drei oben genannten Rotliegend-Analoge hängt mit ihren mechanischen Eigenschaften zusammen. Die Sandsteine wurden für geotechnische Standardtests (Dichte, einachsige Druckfestigkeit (UCS), Elastizitätsmodul (E), Bruchdehnung (ε)) vorbereitet. Die UCS reicht von 3 bis 62 MPa und korreliert positiv mit der Dichte (1,75 bis 2,35 g/cm³) und E (0,3 bis 12,7 GPa). Die optische Porosität korreliert mit diesen mechanischen Parametern und wurde mit diagenetischen Veränderungen in Verbindung gebracht. Diese sind die Gesamtmenge an Tonmineralien sowie die Intensität der mechanischen und chemischen Kompaktion. Letztere wird durch Tonmineralüberzüge auf den Kontakten zwischen den Detrituskörnern und durch das Vorkommen von authigenem Quarz und Dolomit kontrolliert. Die horizontalen Kontaktlängen der Körner, die auf ihren jeweiligen Partikeldurchmesser (effektive Kontakt-Ratio, ECR) und ihre Porosität normiert sind, werden als eine Kontrolle der mechanischen Eigenschaften UCS und E identifiziert, die sich im Gesteinsfestigkeitsindex S_R widerspiegeln. Die Ergebnisse deuten darauf hin, dass S_R in der Lage ist, UCS und E auf der Grundlage petrographischer Informationen, die aus den untersuchten Proben gewonnen wurden, vorherzusagen.

Die Röntgen-Mikro-Computertomographie (µCT) bietet die Möglichkeit, die innere Struktur von Reservoir-Sandsteinen für digitale Strömungssimulationen abzuleiten und gleichzeitig die Mineralverteilung in 3D auf der Grundlage der Mineraldichten zu bewerten. Die Ergebnisse zeigen eine engere Übereinstimmung der µCT-Porosität mit der petrophysikalischen Porosität im Vergleich zur optischen Porosität und eine akzeptable Übereinstimmung der mineralogischen Hauptbestandteile. Einphasige Fluidströmungssimulationen liefern Ergebnisse innerhalb von 10-20 % der Labormessungen. Zwei-Phasen-Strömungssimulationen ermöglichen die Bestimmung der relativen Permeabilität in Gesteinen mit wasserempfindlichen Mineralen. Aufgrund der Rechenintensivität von µCT-basierten Fluidströmungssimulationen ist ein Kompromiss zwischen Auflösung, repräsentativem Volumen und Kosten erforderlich. Die aus den µCT-Bildern rekonstruierte Gesteinszusammensetzung kann als Annäherung an die Zusammensetzung einer Probe verwendet werden, aufgrund von Beschränkungen der gewählten Auflösung können in geringen Mengen vorkommende Minerale jedoch nicht sicher identifiziert werden.

Contents

Acknowledgements.. i

Abstract.. iii

Kurzfassung..v

Declaration of originality.. xiii

1 Introduction..1

1.1 Motivation..1
1.2 Aims..3
1.3 Overview of the thesis..4
1.3.1 Reservoir rock types (Chapter 2)..4
1.3.2 Reservoir quality analysis in outcrop analogs (Chapter 3)..5
1.3.3 Diagenetic impact on geotechnical parameters (Chapter 4)..6
1.3.4 Digital rock models based on µCT data (Chapter 5)..6
1.4 Parts of this thesis which have been published..7

2 Rock typing of diagenetically induced heterogeneities – A case study from a deeply-buried clastic Rotliegend reservoir of the Northern German Basin..........9

2.1 Abstract..9
2.2 Introduction..10
2.3 Geological setting..11
2.4 Materials & methods..14
2.5 Results..16
2.5.1 Petrography..16
2.5.2 Petrophysical measurements..23
2.6 Discussion..25
2.6.1 Paragenetic sequence..25
2.6.2 Reservoir quality assessment and rock typing..29
2.7 Conclusions..32

3 Compaction control on diagenesis and reservoir quality development in red bed sandstones – a case study of Permian Rotliegend sandstones........................35

3.1 Abstract..35
3.2 Introduction..36
3.3 Geological setting..37
3.3.1 Cornberg Sandstones..37
3.3.2 Flechtingen Sandstones..38
3.3.3 Penrith Sandstones..38
3.4 Material & methods..40

3.5 Results 43
  3.5.1 Petrography 43
  3.5.2 Petrophysics 52
  3.5.3 Influence of petrographic parameters on petrophysical parameters 54
3.6 Discussion 58
  3.6.1 Paragenesis 58
  3.6.2 Vertical permeability heterogeneity 66
  3.6.3 Impact on reservoir quality 67
3.7 Conclusions 73

4 Coupling of diagenetic alterations and mechanical properties of Lower Permian siliciclastic sandstones: a pilot study 75
4.1 Abstract 75
4.2 Introduction 75
4.3 Geological setting 76
4.4 Materials & methods 78
4.5 Results 81
  4.5.1 Rock composition 81
  4.5.2 Rock mechanics 84
  4.5.3 Correlations of petrographic and mechanical properties 89
4.6 Discussion 93
  4.6.1 Petrology and diagenesis 93
  4.6.2 Diagenetic and geomechanical rock properties 94
4.7 Conclusions 99

5 Calibrating micro-computed tomography data to permeability experiments and petrography –insights from Digital Rocks 101
5.1 Abstract 101
5.2 Introduction 101
5.3 Materials & methods 102
  5.3.1 Material and laboratory methods 102
  5.3.2 µCT methods 103
  5.3.3 Simulation methods 104
5.4 Results 107
  5.4.1 Laboratory results 107
  5.4.2 Digital rock results 108
5.5 Discussion 112
  5.5.1 Rock composition 112
  5.5.2 Porosity 113
  5.5.3 Permeability 113
5.6 Conclusions 114

6 Summary **117**
6.1 Heterogeneity in reservoir quality 117
7 Conclusions & Outlook **123**
7.1 Conclusions 123
7.2 Outlook 125
References **127**
Appendix **147**
Alphabetical list of methods 147
Supplementary material I 149
Supplementary material II 157

Declaration of originality

Chapter 2: As first author during his PhD studies, Alexander C. Monsees performed all thin-section analysis, point-counting, and permeability measurements. The provision of thin-sections and decane porosity measurements by co-author Nadine Schöner is highly appreciated. He wrote the entire article with inputs from Benjamin Busch, Nadine Schöner, and Christoph Hilgers. The discussions with all co-authors contributed to this manuscript.

Chapter 3: As first author, Alexander C. Monsees performed all point-counting analysis, data analysis and interpretation, as well as most sample acquisition and petrophysical measurements. Samples and petrophysical measurements provided by co-author Benjamin Busch are highly appreciated. Alexander C. Monsees wrote the entire manuscript with inputs from Benjamin Busch and Christoph Hilgers. The discussions with all co-authors contributed to this manuscript.

Chapter 4: As first author, Alexander C. Monsees performed all petrographic analysis and evaluation of geotechnical data. The conduction of geotechnical tests by co-author Sven F. Biebricher is highly appreciated. Alexander C. Monsees wrote the entire article with inputs from Sven F. Biebricher, Benjamin Busch, Martin Feinendegen, Martin Ziegler, and Christoph Hilgers. The discussions with all co-authors contributed to this manuscript.

Chapter 5: As first author during his PhD studies, Alexander C. Monsees performed petrophysical measurements and petrographic analyses of all rock samples. Computational fluid dynamic modeling was performed by co-author Amol Subhedar. Alexander C. Monsees wrote the entire article with inputs from Amol Subhedar, Benjamin Busch, Britta Nestler, and Christoph Hilgers. The discussions with all co-authors contributed to this manuscript.

1 Introduction

1.1 Motivation

The economic use of sandstone reservoirs has been diversified beyond hydrocarbon extraction in the past two decades, and extended to geothermal energy exploration (Caulk & Tomac, 2017; Heap et al., 2017), energy storage (Henkel et al., 2013; Pfeiffer et al., 2017), as well as CO_2 sequestration (Ambrose et al., 2008; Barnes et al., 2009; Benson & Cole, 2008; Heinemann et al., 2012). Independent of application, two important factors for reservoir quality are the uncemented pore volume (porosity) and the subsequent hydraulic connectivity between the individual pores (permeability). This governs the amount of available volume for fluid or gas storage as well as injection or extraction rates in the subsurface (Ajdukiewicz et al., 2010; Busch et al., 2019; Taylor et al., 2015; Worden et al., 2018).

Sandstone diagenesis and its impact on reservoir quality has been an intensely researched topic in the previous decades (Ajdukiewicz et al., 2010; Becker et al., 2019; Busch et al., 2019; dos Anjos et al., 2000; Ehrenberg, 1990; Gaupp et al., 1993; Gaupp & Okkerman, 2011; Schmidt et al., 2020b; Taylor et al., 2010; Worden et al., 2018). Purely petrophysical assessments of reservoir quality do not consider the effect of different mineral phases and timings on the relationship between porosity and permeability, implying that a combined approach between petrographic and petrophysical methods is required to accurately constrain and quantify reservoir quality controls (Becker et al., 2019; Busch et al., 2020). Special focus during petrographic analysis is put on to the grain-coating clay minerals phases, which are known to inhibit syntaxial quartz and feldspar cementation (Aagaard et al., 2000; Busch et al., 2020; Heald & Larese, 1974; Storvoll et al., 2002), while simultaneously enhancing chemical compaction at quartz grain contacts (Greene et al., 2009; Kristiansen et al., 2011).

Sandstones are naturally heterogeneous, resulting in a wide range of petrophysical parameters ranging from excellent to very poor reservoir quality (Fig. 1.1). Clay mineral coatings were identified to be one of the governing factors affecting petrophysical heterogeneity by reducing quartz cementation but simultaneously decreasing intergranular volume by chemical compaction (Fig. 1.2). Clay mineral coatings may form by clay infiltration in fluvial and sand sheet depositional environments (Ajdukiewicz et al., 2010; Esch et al., 2008), and by redeposition from fluvial environments in dunes (Busch, 2020).

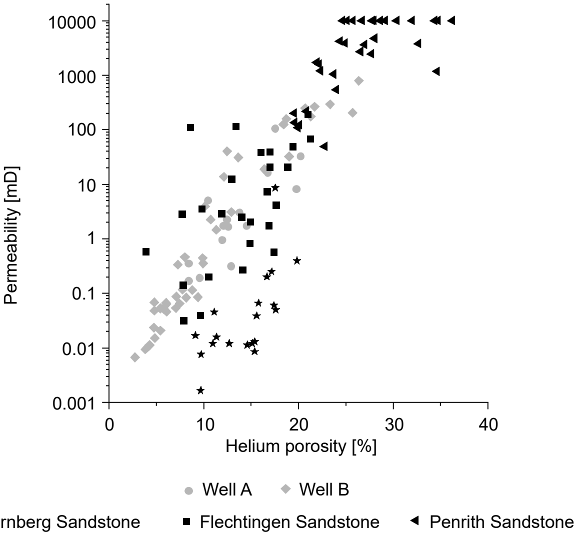

Figure 1.1. Helium porosity (abscissa) and permeability (ordinate) of sandstones deposited in similar in the Lower Permian in subsurface samples and outcrop analogs. Permeability measurements were conducted at a constant confining pressure of 1.2 MPa.

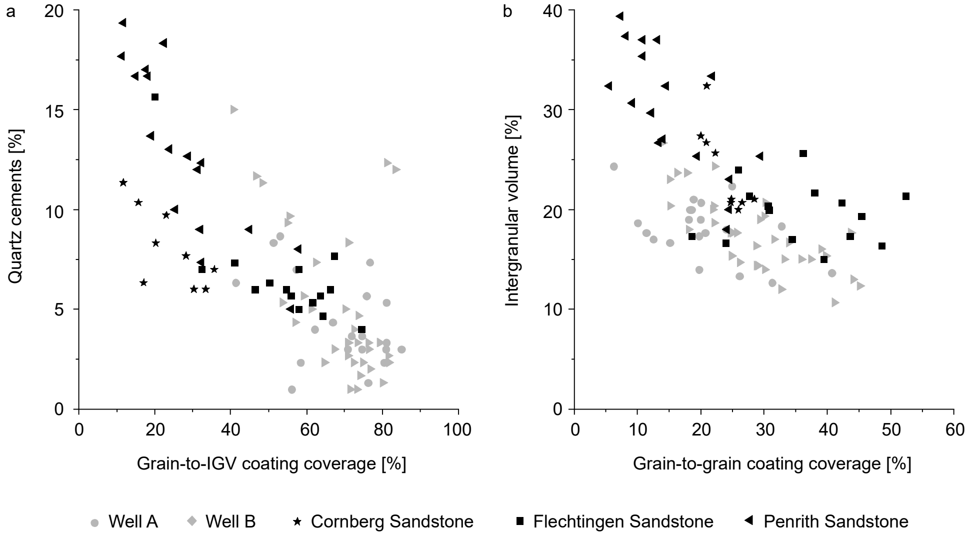

Figure 1.2. Clay mineral illite coatings, showing their inhibiting effect on quartz cementation (a) and their catalyzing effect on chemical compaction (intergranular volume reduction).

Deposition and subsequent burial of sediments induces compaction processes accompanied by authigenic mineral cementation (Paxton et al., 2002). This process called diagenesis generally results in a reduction of open porosity and in consolidation of the sediment to sedimentary rock (Worden & Burkley, 2003). Depending on the type and quantity of authigenic and detrital minerals, diagenetic processes result in a variable intensity of compaction and cementation (Gaupp et al., 1993; Schöner, 2006; Vincent et al., 2018). These processes result in different quantifiable implications for the reservoir quality of sandstones in reservoirs. They also carry implication for the assessment of geomechanical rock properties. Thus, petrophysical and geomechanical properties are linked to rock properties reflected by petrography on the grain composition and fabric. For example, porosity reduction in sandstones controls mechanical parameters and thus reservoir integrity, for instance in response to production-induced pressure changes, and determines during which stress states the reservoir rock will deform and potentially fracture (Hettema et al., 2000; Pijnenburg et al., 2019a; Zoback & Zinke, 2002).

Mechanical parameters like rock strength and deformability have been linked with one another empirically in previous works (Chang et al., 2006; Dyke & Dobereiner, 1991). Rock strength has been correlated with the bulk sandstone composition (Fahy & Guccione, 1979; Ulusay et al., 1994; Zorlu et al., 2008). The effect of grain texture and fabric derived from compressive rock strength is debated in literature: Some authors link it to parameters like grain sizes, quartz percentage, grain sphericity, cements and grain contacts (Fahy & Guccione, 1979), while others argue that the length of the grain contacts in relation to the total grain surface length can be used as a proxy for compressive strength in sandstones (Dyke & Dobereiner, 1991).

In order to generate digitized rock models as close to nature as possible, computer tomography has been utilized at least over the last twenty years to generate 3D rock models, also incorporating rock physics into the digital rock model (Golab et al., 2010; Rassenfoss, 2011; Van Geet et al., 2001). Due to advances in computational power, it has become viable to conduct fluid flow simulations through porous siliciclastic sandstones (Andrä et al., 2013a; Prajapati et al., 2018; Saxena et al., 2017), or to generate mineralogical models based on micro-computed tomography data (Cnudde et al., 2011; Peng et al., 2012).

1.2 Aims

The aim of this study is to better constrain the effect of diagenesis on reservoir quality in Lower Permian Rotliegend sandstones. Furthermore, the impact of grain coating coverage will be linked to rock strength. Samples originating from similar depositional environments, who have undergone different diagenetic pathways, are studied in detail. The petrographic composition and paragenesis derived from transmitted light microscopy (point-counting) and textural observations are integrated with petrophysically determined porosity and permeability, geotechnical standard parameters derived from uniaxial compression tests, and computational fluid dynamic simulations based on x-ray micro-computed tomography data. The focus of this work results in four major aspects:

- The role of pore-lining clay mineral illite cements, inhibiting quartz cementation but potentially driving compaction due to enhanced chemical compaction, and subsequently generating significant porosity-permeability heterogeneities in sandstones with otherwise similar boundary conditions.
- The effect of early diagenetic pore-filling rigid cements stabilizes the grain-framework, preventing compaction, but also enabling intense burial diagenetic pore-filling cementation, resulting in implications for reservoir quality.
- The impact of diagenesis on mechanical parameters of sandstones, as well as the introduction of a petrography-based estimation of rock strength index (S_R) for sandstones.
- The coupling of laboratory derived petrography, permeability, and porosity data with results from X-ray micro-computed tomography used for mineral identification and computational fluid dynamic modelling to determine petrophysical parameters in digital rocks.

1.3 Overview of the thesis

1.3.1 Reservoir rock types (Chapter 2)

Rotliegend reservoir sandstone samples originating from two natural gas wells in the Northern German Basin are studied. Studied samples include polished thin-sections and plug samples, which were used to derive petrographic and petrophysical data. The main constraint on reservoir quality was determined to be the abundance or absence of tangential illite clay mineral coatings, which showed different effects depending on their location. It was distinguished between illite clay mineral coatings on detrital grains in contact with the intergranular volume (GTI coatings) and illite clay mineral coatings on detrital grains in contact with other detrital grains (GTG coatings). GTG coatings were observed to control the intergranular volume due to their enhancing effect on chemical compaction (Kristiansen et al., 2011), while GTI coatings inhibited syntaxial quartz overgrowth.

Higher pressure sensitivities of permeability were observed to coincide with lower permeability and lower porosity, as well as with either less GTI coatings and more pore-filling cements, or more GTG coatings and more compaction identified by smaller intergranular volumes. Rock typing based on these diagenetic and petrographic parameters was performed: Type A is characterized by an uncemented petrographic texture with high porosities (avg. 9.8 %), high permeabilities (avg. 126 mD), and low pressure sensitivities of permeability (avg. 0.019 MPa^{-1}). Type B is intensely cemented with reduced porosities (avg. 4.0 %), reduced permeabilities (avg. 0.59 mD), and increased pressure sensitivities of permeability (avg. 0.073 MPa^{-1}). Type C is characterized by intense chemical compaction leading to the lowest porosities (avg. 1.8%) and permeabilities (avg. 0.037 mD) in concert with the highest pressure sensitivity of permeability (avg. 0.12 MPa^{-1}).

1.3.2 Reservoir quality analysis in outcrop analogs (Chapter 3)

In chapter 3 the reservoir quality development in three fluvio-eolian and eolian deposits, i.e., Cornberg Sandstones (Hesse, Germany), Flechtingen Sandstones (Saxony-Anhalt, Germany) and Penrith Sandstones (Cumbria, UK), is studied, which may be analogs to the subsurface samples investigated in chapter 2. Additionally, to the reconstruction of the paragenetic sequence and a reservoir quality analysis, heterogeneities from permeability measured parallel and normal to bedding were investigated.

Results show large porosity (10 to 35 %) and permeability (0.01 to 10000 mD) ranges mostly independent of the depositional environment. The major control on reservoir quality in Cornberg Sandstones are dolomite and siderite cementation in conjunction with illitization and illite and kaolinite cementation, leading together with quartz cementation to a mostly cemented IGV and poorest reservoir quality (avg. horizontal permeability: 0.96 mD). Flechtingen Sandstones are most intensely compacted due to the lack of significant early diagenetic cement phases and continuous illitic grain coatings, which inhibited intense quartz cementation but enhanced chemical compaction at quartz grain contacts, resulting in intermediate reservoir quality (avg. horizontal permeability: 34.9 mD). Penrith Sandstones lack significant authigenic phases besides quartz due to carbonate dissolution during uplift and the least number of detrital feldspars and clay minerals, leading to no major reservoir quality reduction by burial diagenetic clay mineral alterations, resulting in highest reservoir quality (avg. horizontal permeability: 5900 mD). Additional results highlight smaller horizontal to vertical permeability differences in more homogenous, higher permeable sandstones compared to larger horizontal to vertical permeability differences in more heterogeneous, less permeable sandstones.

1.3.3 Diagenetic impact on geotechnical parameters (Chapter 4)

Detrital composition and authigenic alterations from Cornberg, Flechtingen, and Penrith Sandstones are related to mechanical properties derived from uniaxial compression tests, delivering uniaxial compressive strength (UCS), Young's modulus (E), and strain at failure (ε).

The results show UCS ranges from 3 to 62 MPa, which positively correlate with density (1.75 to 2.35 g/cm^3) and E (0.3 to 12.7 GPa). Optical porosity was determined to be the strongest control on these mechanical parameters, which was linked to diagenetic alterations controlling porosity development. Similar to results presented in chapter 2 and 3, porosity reduction was controlled by the abundance of clay minerals, as well as the intensity of mechanical and chemical compaction, and therefore can be linked to mechanical properties. In order to assess mechanical properties in absence of sufficiently large samples for geotechnical standard tests, a petrographic proxy for rock strength is defined. Horizontal contact lengths of grains including syntaxial overgrowth cements were normalized to their respective particle diameter (including syntaxial overgrowth cements; effective contact ratio, ECR), divided by optical porosity yield the rock strength index (S_R), which shows strong correlation with the uniaxial compressive strength and Young's modulus. The results of this pilot study suggest that S_R is able to predict UCS and E based on petrographic information obtained from the studied samples.

1.3.4 Digital rock models based on µCT data (Chapter 5)

Chapter 5 is an interdisciplinary approach between petrography, petrophysics, and numerical modelling regarding the digitalization of petrographic and petrophysical methods employed in the chapters 2-4. The true 3D structure of an exemplary Penrith Sandstone sample was derived with X-ray micro-computed tomography (µCT). Stacked µCT images were binarized into porosity and solid phases. They were subsequently prepared as 3D structures for fluid flow analyses using Pace 3D employing the lattice Boltzmann method. The same µCT cube was also segmented into grayscales to determine mineralogy based on attenuation contrasts.

The results demonstrate a closer match for µCT porosity to petrophysical porosity compared to optical porosity, and an acceptable first order fit of the main mineralogical constituents. One-phase fluid flow simulations deliver results within 10 to 20 % of the laboratory measurements. Two-phase flow simulations show relative permeabilities. However, µCT-based fluid flow simulations require immense computational power due to the heterogeneity of natural sandstone samples, resulting in a tradeoff between resolution, representative volume, and cost. Rock composition based on µCT images is considered a first-order approximation for the composition of a sample but is unable to confidently identify minerals that occur in minor quantities due to resolution constraints. As a result, µCT analyses is still dependent on the input of experimental results**.**

1.4 Parts of this thesis which have been published

Articles

Monsees, A.C., Busch, B., Schöner, N., and Hilgers, C., 2020. Rock typing of diagenetically induced heterogeneities – A case study from a deeply-buried clastic Rotliegend reservoir of the Northern German Basin, Journal of Marine and Petroleum Geology, Vol. 113, p. 104163.

Monsees, A.C., Subhedar, A., Busch, B., Nestler, B., and Hilgers, C., 2020. Calibrating micro-computed tomography data to permeability experiments and petrography – insights from Digital Rocks, OIL GAS European Magazine, Vol. 70(3), p. 28-33.

Monsees, A.C., Biebricher, S.F., Busch, B., Feinendegen, M., Ziegler, M., and Hilgers, C., 2021. Coupling of diagenetic alterations and mechanical properties of Lower Permian siliciclastic sandstones: a pilot study, Environmental Earth Sciences, Vol. 80, Article number 141 (2021).

Monsees, A.C., Busch, B., and Hilgers, C., 2021. Compaction control on diagenesis and reservoir quality development in red bed sandstones – a case study of Permian Rotliegend sandstones, International Journal of Earth Sciences, Vol. 110, p. 1683-1711.

Conference contributions

Monsees, A.C., Busch, B., and Hilgers, C., 2018. The impact of pore-occluding cementation and chemical compaction on the reservoir quality of deeply buried sandstones. 6th European Geothermal Workshop, Strasbourg.

Monsees, A.C., Busch, B., Subhedar, A., Nestler, B., and Hilgers, C., 2019. Integrating geology and petrophysics into numerical models – A step towards the digitalization of rocks. DGMK/ÖGEW Frühjahrstagung, Celle.

Monsees, A.C., Busch, B., Schöner, N., and Hilgers, C., 2019. Reservoir quality controls in deeply buried Rotliegend sandstones and their outcrop analogs, Annual Conference of the German Geological Society, Münster.

Monsees, A.C., Busch, B., Schöner, N., and Hilgers, C., 2019. Effects of elevated confining pressure and temperature conditions on deeply buried sandstone reservoirs. 7th European Geothermal Workshop, Karlsruhe.

Monsees, A.C., Biebricher, S.F., Busch, B., Feinendegen, M., Ziegler, M., and Hilgers, C., 2020. Coupling mechanical properties in porous siliciclastic rocks with diagenetic alterations – a case study on Rotliegend outcrop analogs, DGMK/ÖGEW Frühjahrstagung, Celle.

Biebricher, S.F., Subhedar, A., Monsees, A.C., Busch, B., Feinendegen, M., Ziegler, M., Nestler, B., and Hilgers, C., 2020. Constructing a reservoir model: Preliminary results of an upscaling approach from a Northern German gas field, DGMK/ÖGEW Frühjahrstagung, Celle.

Monsees, A.C., Subhedar, A., Busch, B., Nestler, B., and Hilgers, C., 2020. The application of digital rock models to petrography and fluid flow simulations in reservoir sandstones, GSSPE Student Technical Congress, Karlsruhe.

2 Rock typing of diagenetically induced heterogeneities – A case study from a deeply-buried clastic Rotliegend reservoir of the Northern German Basin

2.1 Abstract

Reservoir quality of sandstones is mainly derived from their permeability and porosity. As a result, porosity-reducing processes need to be understood in order to evaluate and model reservoir quality in sandstones. This case study from a Rotliegend gas reservoir in the Northern German Basin utilizes petrophysical measurements in conjunction with petrography in order to assess reservoir qualities and define rock types. The most significant diagenetic factors influencing the development of the IGV (intergranular volume) are quartz cementation due to low illitic grain coating coverages on grain to IGV interfaces and chemical compaction due to pronounced illitic grain coating coverages on grain-to-grain interfaces. Where large proportions of the interface between adjacent grains are coated by illite, stronger chemical compaction (pressure dissolution) was observed to occur. This chemical compaction reduces the IGV, and thus open pore space.

Permeabilities measured under decreasing confining pressures from 50 to 2 MPa were used to determine the pressure sensitivities of permeability (David et al., 1994), which ranged from 0.005-0.22 MPa^{-1}. The pressure sensitivity of permeability, porosity and permeability were linked to the petrographic texture, implying three different major rock types: Type A is characterized by an uncemented petrographic texture with high porosities (avg. 9.8 %), high permeabilities (avg. 126 mD), and low pressure sensitivities of permeability (avg. 0.019 MPa^{-1}). Type B is intensely cemented with reduced porosities (avg. 4.0 %), reduced permeabilities (avg. 0.59 mD), and increased pressure sensitivities of permeability (avg. 0.073 MPa^{-1}). Type C is characterized by intense chemical compaction leading to the lowest porosities (avg. 1.8%) and permeabilities (avg. 0.037 mD) in concert with the highest pressure sensitivity of permeability (avg. 0.12 MPa^{-1}). The heterogeneity induced by diagenesis will have an impact on recoverable resources and flow rates in both hydrocarbon and geothermal projects in similar siliciclastic reservoirs.

2.2 Introduction

Clastic reservoir rocks are of significant economic interest as host rocks for natural gas or oil in the hydrocarbon industry, as interim storage medium for natural gas and biogas, as potential long-term storage medium for CO_2 sequestration, and as potential aquifers in geothermal projects (Ambrose et al., 2008; Bachu, 2000; Legarth et al., 2005; Morad et al., 2010; Selley, 1998). Diagenetic processes, for instance authigenic cementation, as well as chemical and mechanical compaction, have a major impact on the quality of clastic reservoirs (Becker et al., 2017; Busch et al., 2017; Paxton et al., 2002; Taylor et al., 2010; Worden et al., 2018; Wüstefeld et al., 2017a). For example, early diagenetic processes, such as grain coatings, may inhibit quartz cementation (Ajdukiewicz & Larese, 2012; Ajdukiewicz et al., 2010; Busch et al., 2020; Busch et al., 2018; Esch et al., 2008; Heald & Larese, 1974; Taylor et al., 2010). Further diagenetic alteration of the sandstones additionally modifies the available pore space by mineral precipitation and dissolution (Worden et al., 2018; Worden & Burkley, 2003) impacting reservoir quality development (Bahlis & De Ros, 2013; Becker et al., 2019; Becker et al., 2017; Busch et al., 2019; Busch et al., 2020; Desbois et al., 2016; Gaupp et al., 1993; Gaupp & Okkerman, 2011; Taylor et al., 2015). Compaction induced modification of the detrital grain framework are also affected by diagenetic alterations, as e.g. cements can preserve the intergranular volume (IGV) (Line et al., 2018; Paxton et al., 2002). Micro-scale sedimentary and structural features may have a profound impact on permeability (Busch et al., 2018; Busch et al., 2015; Gaupp et al., 1993; Morad et al., 2010; Schmidt et al., 2018; Taylor et al., 2010; Taylor et al., 2015), e.g. in eolian dunes, which are characterized by sand bodies with tabular cross-bedding, separated by bounding surfaces (Chandler et al., 1989). As a result, detailed micro-scale studies are necessary in order to understand and assess porous reservoir rock quality, and might prove to be a useful tool during exploration and production of associated industries.

The eolian Rotliegend sandstones are important reservoirs for natural gas in Central Europe (Gast et al., 2010). This study investigates Rotliegend sandstone samples of the Havel subgroup from two wells in Northern Germany. The extent of Rotliegend deposits during the time of deposition and the most important structural features are shown in Figure 2.1.

The aim of this study is to characterize and quantify the impact of diagenetic processes on reservoir properties by linking petrographic with petrophysical information. Based on the combination of petrophysical measurements with petrographic information, rock types with regards to their reservoir quality will be established. The rock-typing does not only consider petrophysical values e.g., porosity, but also the process behind the reservoir quality reduction or preservation during burial and diagenesis.

2.3 Geological setting

The study area is located on the Pompeckj Block (PB) in a North-South orientated graben, part of the fan-shaped graben system (Gast & Gundlach, 2006; Plein & van Adrichem Boogaert, 1995) between Hamburg, Hannover and Bremen (Fig. 2.1) that limits the extent of the studied reservoir with faults on its eastern and western margin. The North German Basin is an element of the Southern Permian Basin (SPB), which also incorporated the Anglo-Dutch Basin and the Polish Trough (Fig. 2.1) (Gast et al., 2010; Ziegler, 1990). The extent of the Northern German Basin is limited by the Variscides in the south, the Anglo-Dutch Basin to the west, the Fennoscandian Shield to the North and the Polish Trough to the East (Fig. 2.1). The SPB was formed between the front of the Variscan orogenic belt and the Mid North Sea High (Katzung, 1988; Ziegler, 1990). West-north-west to west trending faults were initiated by the Variscan collision between Gondwana and Laurussia (Ziegler, 1990). From Stephanian (Upper Carboniferous) onwards, the precursor of the SPB was subsided after a phase of under plating, crustal thinning and uplift (Gast & Gundlach, 2006; Gast et al., 2010; Geluk, 2005). During the Carboniferous, the area of the SPB was drifting northwards from the equator, residing in the desert belt between 10° and 30° on the northern hemisphere during the Permian (Blakey & Wong, 2003; Glennie, 2007; Scotese & Langford, 1995). The base of the Permian is characterized by the Base Permian Unconformity (Ziegler, 1990), which locally leads to a hiatus of up to 60 Myr between Upper Carboniferous and Upper Rotliegend deposits (Geluk, 1999). E-W extension during the Permian induced the formation of N- to NNW-striking faults (Lohr et al., 2007).

The Lower Rotliegend can be found in the subsurface and at outcrops in Northern Germany and primarily comprises of rhyolites, andesites and smaller amounts of basalts (Gast & Gundlach, 2006; Gast et al., 2010; Hoth et al., 1993; Schöner, 2006). The Upper Rotliegend in Germany is divided into Upper Rotliegend I which is restricted to rift basins and grabens, and Upper Rotliegend II, whose deposits can be traced throughout the whole SPB (Schröder et al., 1995) (Fig. 2.2). The Havel and Elbe subgroups of the Upper Rotliegend II (Fig. 2.2) are subdivided into two formations each and have a total sediment thickness of 2500 m (Plein & van Adrichem Boogaert, 1995) deposited over a time span of 5 to 10 Myr in total (Menning, 1995).

Depositional environments in the Upper Rotliegend were influenced by an arid to semi-arid climate and included playas, ergs, and saline lakes (Fryberger et al., 2011; Gast et al., 2010; Gaupp et al., 1993; Kiersnowski, 2013; Kiersnowski et al., 1995). A large saline playa lake was located in the basin center (Fig. 2.1) (Gast et al., 2010). The sedimentary systems developed from alluvial fans close to the Variscan orogen into sandflats and dunes in distal areas (Fryberger et al., 2011; Gast et al., 2010). Playa sediments were deposited around the lake at the center of the basin (Fig. 2.1) (Fryberger et al., 2011). Sediments for the ergs were supplied from the Variscan orogen at the southern margin of the North German Basin (Kiersnowski et al., 1995; McCann, 1998; Rieke, 2001). Deposition was controlled by cyclic climatic forcing controlling the lake-level and the subsequent shift of facies whereas the frequencies of the cycles correspond to the Milankovitch cycles of precession (20 kyr), short eccentricity (100 kyr) and long eccentricity (400 kyr) (Gast, 1993; Sweet, 1999), which may also be identified in purely eolian environments (Kocurek et al., 2001). Each of the four main formations of the Upper Rotliegend II (Fig. 2.2) shows 7 major cycles (Gast, 1993; Sweet, 1999).

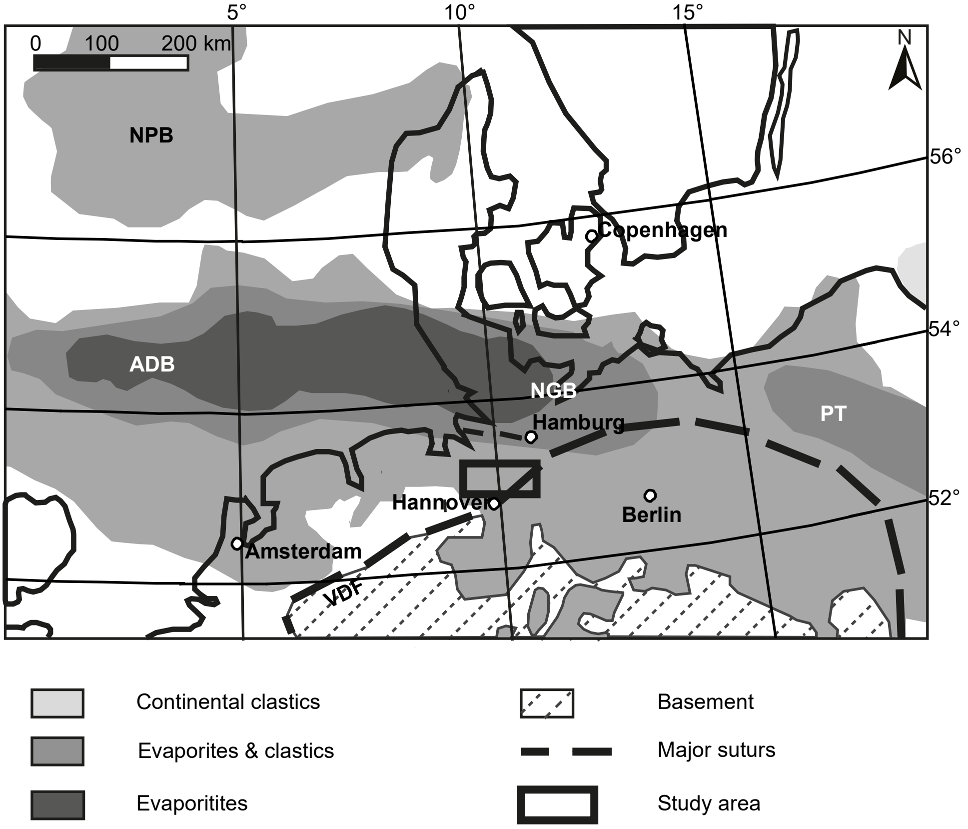

Figure 2.1. Schematic map illustrating the extent of the siliciclastic Rotliegend during the time of deposition in Central Europe. Modified from Moeck et al. (2009), based on Ziegler (1990), Ziegler and Dezes (2005) and Gast and Gundlach (2006). NPB: Northern Permian Basin, CG: Central Graben, ADB: Anglo-Dutch Basin, NGB: North German Basin, PT, Polish Trough, VDF: Variscan Deformation Front.

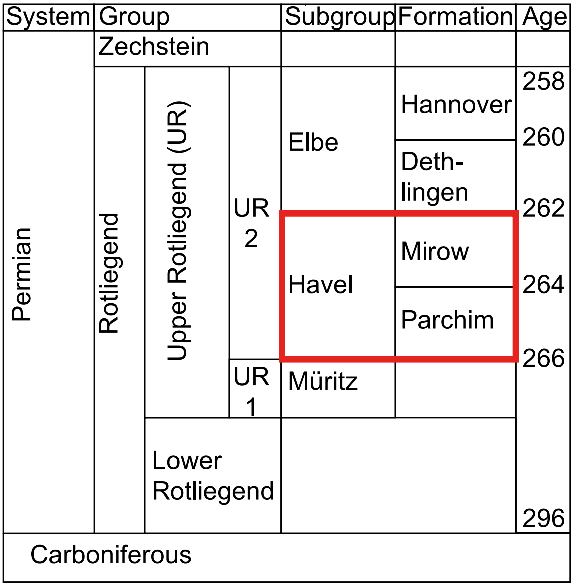

Figure 2.2. Stratigraphic subdivision of the German Rotliegend using ages from Menning (1995), modified from Schöner (2006). The studied sandstones belong to the Havel subgroup (red box).

Throughout the Upper Rotliegend II, a general trend towards higher lake levels in the SPB can be observed from the purely fluvio-eolian Havel Subgroup towards increasingly lacustrine conditions at the top of the Elbe Subgroup (Legler & Schneider, 2008). The depositional setting of the studied area (Fig. 2.1) is an erg and shows dunes and dry sandflats as depositional facies. Rotliegend siliciclastic deposition was terminated by the ingression of the Zechstein sea and the resulting precipitation of evaporites and carbonates during the Upper Permian (Glennie & Buller, 1983; Smith, 1979). Rotliegend sandstones were buried rapidly up to 3000 m depth until the end of the Triassic (Schwarzer & Littke, 2007).

The German Triassic is divided into the fluvio-lacustrine sedimentation of the Buntsandstein, followed by the marine Muschelkalk ingression, which was succeeded by continental brackish to hypersaline deposits of the Keuper (Bachmann et al., 2010). From Keuper to Jurassic, the Northern German Basin experienced an extensional phase in NNE-SSW direction leading to W-to NW-striking faults (Lohr et al., 2007). The onset of the Jurassic lead to the flooding of the epicontinental basin in the area of the SPB by the Tethys Ocean to the south and the Boreal Ocean to the north (Lott et al., 2010). Towards the end of the Jurassic, the study area was uplifted by over 1000 m (Schwarzer & Littke, 2007), forming the Pompeckj Block. The inversion caused the erosion of the majority of Jurassic strata (Binot et al., 1993). Marine epicontinental sedimentation of carbonates and marls, as well as subsequent burial recommenced in the study area during the Late Aptian transgression, which was induced by an eustatic sea level rise in concert with increased subsidence rates (Vejbæk et al., 2010; Ziegler, 1990). The kinematic regime shifted from E-W compression along the existing NW-striking fault system from Santonian to Campanian to N-S compression from Coniacian to Maastrichtian (Lohr et al., 2007), which can be linked to the mechanical coupling of Europe and Africa over Iberia (Kley & Voigt, 2008). Throughout the Tertiary, primarily sands and clays were deposited (Knox et al., 2010). The structural development of the Cenozoic is governed by normal faulting induced by salt diapirism along reactivated fault zones (Lohr et al., 2007) and accelerated subsidence of the Northern German Basin due to collisional processes and subsequent lithosphere folding and faulting associated with the formation of the Pyrenees and the Alps (Kley & Voigt, 2008; Lohr et al., 2007).

2.4 Materials & methods

A total of 55 polished thin-sections orientated across the bedding plane originating from two Northern German gas wells approximately two kilometers apart, were studied. The thin-sections were impregnated with a blue-dyed epoxy resin, prepared to a thickness of 30 µm and stained with Alizarin Red S. Twenty thin-sections from well A representing a total vertical depth (TVD) of 4698 – 4720 m (sampling interval approximately 1 m) and 35 thin-sections from well B, representing a range from a TVD of 4674 – 4706 m (sampling interval approximately 1 m) were studied. The studied samples belong to the Havel subgroup of the Upper Rotliegend. All 55 thin-sections were point-counted (300 counts) on a grid adjusted to the maximum grain size (determined by image analysis) with a semi-automated Pelcon Point Counter installed on a Leitz Aristomet microscope.

The sandstone compositions are classified according to Folk (1980). The intergranular volume (IGV) was classified after Paxton et al. (2002). Compactional and cementational porosity loss as well as compactional indices were calculated after Lundegard (1992). The percentage of clay mineral coatings on grain to IGV (GTI) interfaces was assessed on at least 50 grains per sample (Busch et al., 2017). The length of the grain's illite-coating in contact with the IGV was measured and divided by the length of the total grain circumference in contact with the IGV. Comparator images for different clay-mineral coverages are shown in Figure 2.3. Percentages of illite coatings on grain to grain (GTG) interfaces were evaluated analogously. All microscope images were taken with a Jenoptik ProgRes Gryphax© camera, mounted on a Leica DMLP microscope.

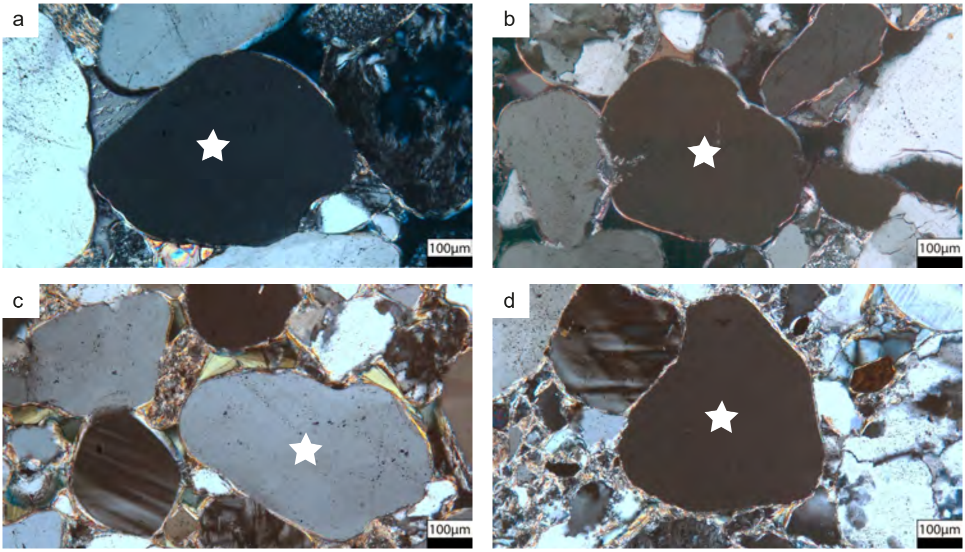

Figure 2.3. Clay-coating coverages on grain to grain (GTG) contacts were quantified by visual image analysis. The grains used for these examples are indicated by a white star. a) Almost no clay coatings on GTG contacts (coverage 10 %, sample A_12). b) Around 30 % illite on GTG contacts (sample B_04). c) 60 % coverage GTG interfaces (sample B_10). d) Complete illite coverages at GTG contacts (>95 %, sample B_15).

Cathodoluminescence (CL) was studied with an optical cathodoluminescence system by Cambridge Image Technology Ltd (CITL) mounted on a Leitz Dialux microscope. The system was operated with a voltage of 15±1 kV for carbonate cements and accessories and 20±1 kV for quartz. Applied currents ranged from 325-350 µA.

Petrophysical measurements were conducted on cylindrical 30 mm plugs. For all samples used in petrophysical analyses a thin-section is available. Decane porosity (φ, n=49) was measured using the Archimedes or flotation/liquid resaturation method with decane as flotation medium. The rock samples were dried at 120° C, weighed, and put in a desiccator. The desiccator was evacuated and afterwards the samples were saturated with decane. Samples were then put in a pressure chamber filled with decane at 9 MPa for one day. Decane saturated samples were weighed in decane and outside decane under normal air pressure. The relative decane porosity was calculated from the determined differences in weight (Kuila et al., 2014). The statistical error of the arithmetic mean was determined by dividing the standard deviation by the square root of the number of samples.

Klinkenberg-corrected permeability (κ, n=49) was measured at a constant confining pressure of 1.2 MPa on 49 plugs with an air permeameter manufactured by Westphal Mechanik using oil-free lab air (80% N_2, 20% O_2). Permeabilities were also measured under decreasing confining pressures (50, 30, 10, 5, 2 MPa) at room temperature (22±1° C) on n=46 samples using helium as a permeate ($\eta = 1.97 * 10^{-5} Pa * s$ at 22° C). All samples were loaded up to 50 MPa confining pressure and permeabilities are measured during the unloading cycle in a DBHS-50-150 pressure cell from GL Test Systems GmbH. The cell is fitted with a hydraulic pump to adjust confining pressures. Apparent permeabilities are measured at varying p_{mean} and corrected for slip flow (Amann-Hildenbrand et al., 2015), using the Klinkenberg correction (Klinkenberg, 1941). The pressure sensitivity coefficients of permeability (γ) were calculated after David et al. (1994).

2.5 Results

2.5.1 Petrography

2.5.1.1 Detrital composition

Subarkoses (well A: 50 %, well B: 68 %) and lithic arkoses (well A: 50 %, well B: 23 %) are the most abundant sandstone types (Fig. 2.4). Sublitharenites (well B: 3 %), feldspathic litharenites (well B: 3 %) and arkoses (well B: 3 %) were not present in samples from well A (Fig. 2.4). The main constituent of the samples is detrital quartz, including mono- and polycrystalline, as well as undulose quartz and metaquartzite varieties (well A: 52-73 %, mean 60 %; well B: 44-71 %, mean 62 %) (Fig. 2.5 a, c, d, supplementary material I). Feldspars (well: A 9-18 %, mean 13 %; well B: 8-21 %, mean 13 %) (Fig. 2.5 a, b, d, supplementary material I) and rock fragments (well A: 3-16 %, mean 8 %; well B: 2-15 %, mean 7 %) are common (Fig. 2.5 d, supplementary material I). Detrital matrix was encountered with a mean of <1 %, although its distribution varies (well A: 0-4 %; well B: 0-10 %) (Fig. 2.5 c). Mica and accessories such as zircon, rutile, tourmaline, or amphibole are very rare (mean <1 %). Chert is very rarely present (mean < 1%). Most of the detrital quartz is monocrystalline (Fig. 2.5 c, d), although every sample contains a varying amount of polycrystalline grains and quartzite as well. The feldspars are dominated by K-feldspars (mean 8 %) showing microcline textures and parquet-twinning (Fig. 2.5 d). Plagioclases (mean <0.3 %) show lamellar twinning. Rock fragments (mean 4 %) consist of volcanic rock fragments, plutonic rock fragments, metamorphic rock, and sedimentary fragments. Volcanic rock fragments (mean 3 %) are of silicic or feldspathic origin (Fig. 2.5 d) and show porphyric, unidirectional textures. Plutonic rock fragments (mean 1 %) are characterized by large, idiomorphic grains of predominately feldspathic or felsic composition (supplementary material). Sedimentary rock fragments (shale, siltstone, and sandstone) contribute around 1 % of the overall composition, while low-grade metamorphic rock fragments like schists and phyllites occur very rarely (mean <1 %) (supplementary material I). The dominating grain size is coarse-skewed medium sand, which shows well to moderately well sorting (supplementary material I).

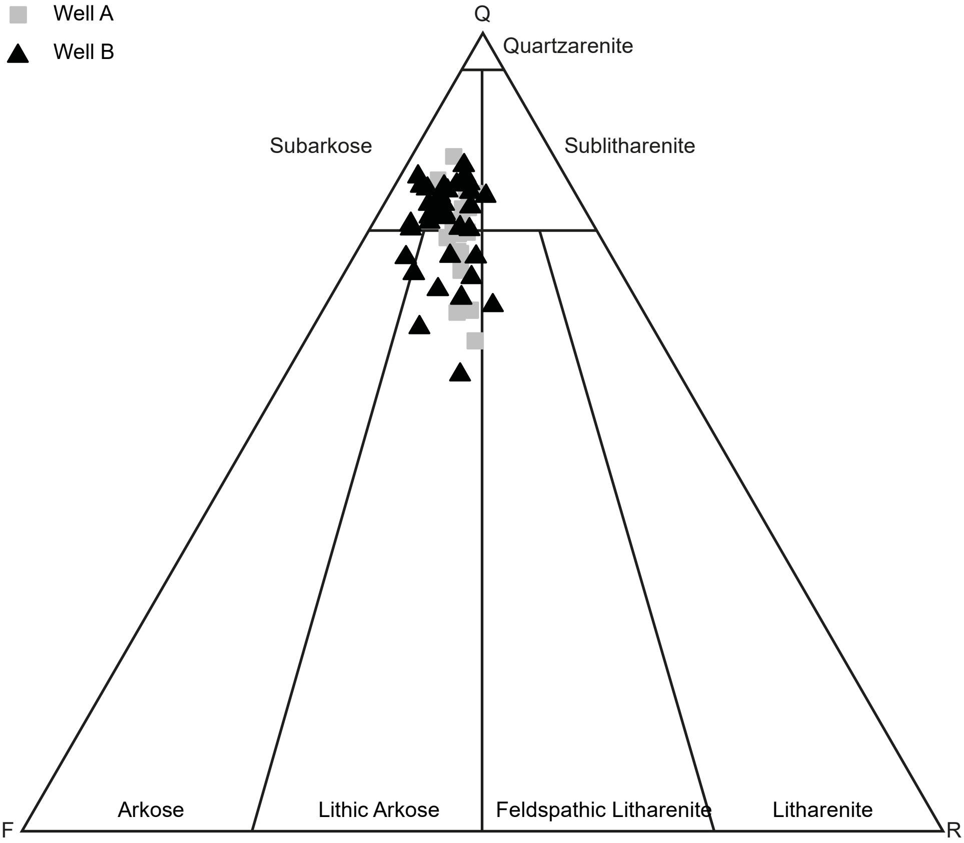

Figure 2.4. Sandstone classification after Folk (1980) based on point-counting results. The studied samples are dominantly subarkoses and lithic arkoses and show no distinct differences between the studied wells.

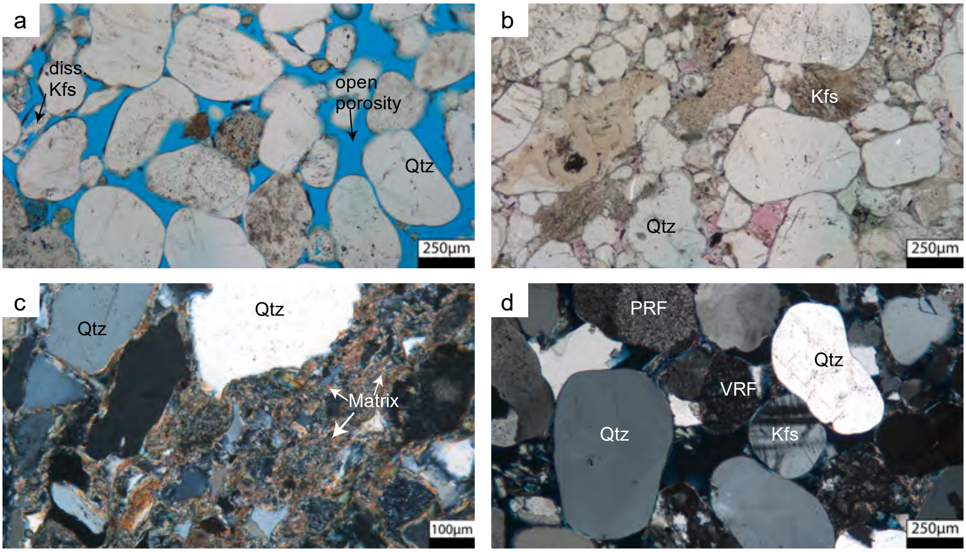

Figure 2.5. Photomicrographs of detrital components in thin-sections under plane-polarized light (ppl) and crossed-polarized light (xpl). a) Porous subarkose of well A, representative for the sections with porosities above 10 % (ppl, sample A_04). b) This lithic arkose is characterized by its very low porosities (ppl, sample B_20). c) Detrital clay matrix, which is abundant in some samples of the lower section of well B (xpl, sample B_16). d) Lithic arkose showing the most common detrital components (xpl, sample A_08). Qtz=quartz, Kfs= potassium feldspar, PRF=plutonic rock fragment, VRF=volcanic rock fragment.

2.5.1.2 Authigenic phases

The most abundant authigenic pore-filling phases are syntaxial quartz cement (well A: 1-9 %, mean 4 %; well B: 1-15 %, mean 3 %) (Fig. 2.6 a) and calcite cement (well A: 0-7 %, mean 2 %, pore-filling; well B: 0-8 %, mean 1 %) (Fig. 2.6 b), which has a poikilotopic texture (Fig. 2.6 e). Quartz cements often occur as euhedral overgrowths (Fig. 2.6 a). Calcite cements appear in two distinct textures. The poikilotopic texture appears to stabilize the grain framework and prevent contacts between detrital grains (Fig. 2.6 e).

The other texture engulfs euhedral syntaxial quartz cements and pore-filling chlorite (Fig. 2.6 g, h). Barite cements (Fig. 2.6 c) and anhydrite cements (Fig. 2.6 d) may contribute up to 5 % in individual samples, but their mean occurrence is below 1 %. Anhydrite occupies open pores, engulfing pore lining illite clay minerals (Fig. 2.7 d) without showing interactions with other pore-filling blocky cements. Barite was encountered only in well A. Barite cements were observed to engulf euhedral quartz cements (Fig. 2.7 e, f). Halite cement, feldspar cement, and gypsum occur in traces in individual samples.

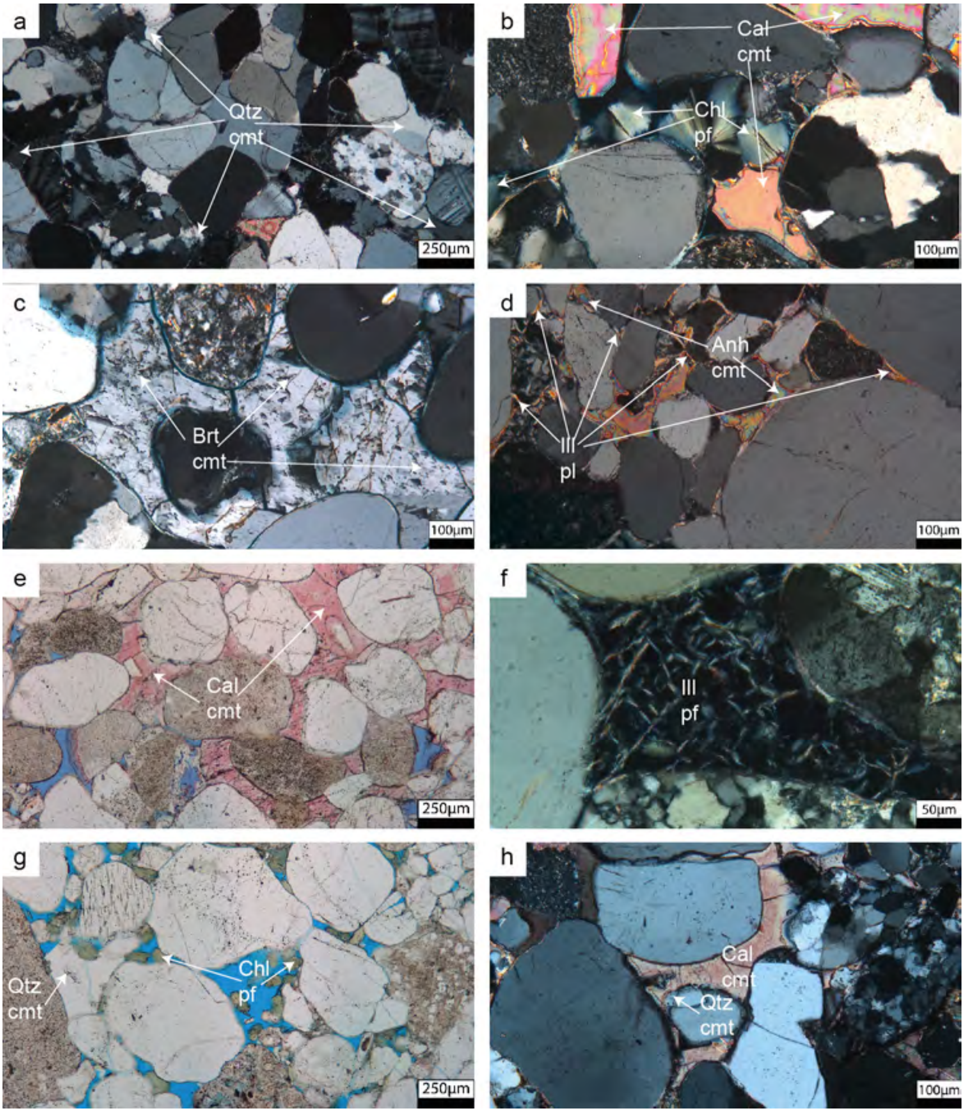

Figure 2.6. Figure caption on the next page.

Figure 2.6. Photomicrographs of authigenic components in thin-sections under crossed-polarized light (xpl) and plane polarized light (ppl). a) Quartz grains overgrown by authigenic quartz due to low clay mineral coverages (here: 40.7%) on GTI interfaces (xpl, sample B_28). b) Calcite cement occupies open pores, and is limited by pore-filling vermicular chlorite (xpl, sample A_02). c) Barite cement occupying pore-space (xpl, sample A_03). d) Smaller patches of pore-occluding anhydrite cement, and illite along the detrital grains (xpl, sample B_23). e) Poikilotopic calcite patches occurred as dominant pore-filling phase (locally up to 10%) in some horizons (ppl, sample B_09). f) Meshwork illite was observed on pore throats and in open pores with an overall occurrence of <1% (xpl, sample B_08). g) Authigenic quartz was observed to overgrow pore-filling vermicular chlorite (ppl, sample A_05). h) Interactions between quartz cement and calcite cement were rarely observed. Small rims of authigenic quartz on their detrital grains were observed to be overgrown by calcite (xpl, sample B_01). GTI: grain to IGV interface, Qtz cmt: authigenic quartz, Chl pf: pore-occluding chlorite, Ill pl: grain-coating tangential illite, Ill pf: pore-filling meshwork illite, Cal cmt: calcite cement, Brt cmt: Barite cement, Anh cmt: Anhydrite cement.

Illite cements (well A: 2-7 %, mean 4 %; well B: 1-13 %, mean 4 %,) occur in every sample as a pore-lining phase (Fig. 2.6 d) on detrital grains and in some samples as a very rare (<1 %) pore-filling phase (Fig. 2.6 f) as well. The pore-lining illite phase shows a tangential texture, encompassing detrital grains with an illite coating (Fig. 2.6 d). Chlorite cements (well A: 0-5 %, mean 2 %, pore-filling; well B: 0-7 %, mean 1 %) (Fig. 2.6 b) occur as pore-filling phase only. Two different forms of pore-filling chlorite can be distinguished: vermicular chlorite (Fig. 2.6 b) occurs in pores that are uncemented besides the vermicular chlorite, and completely pore-occluding occurrences (Fig. 2.5 c) were observed in heavily compacted samples. Replacements of feldspars by illite and volcanic rock fragments by chlorite were consistently observed to be very rare (well A: 0-1 %, mean <1 %; well B: 0-1 %, mean <1 %).

Cathodoluminescence analyses aided the identification of authigenic quartz cements in samples containing prominent dissolution seams where irregular grain shapes and the absence of grain coating material impact the optical assessment (Fig. 2.7). Feldspars showed light blue luminescence, while detrital quartz showed mostly night blue and purple luminescence (Fig. 2.7 b). Authigenic quartz was identified by structural relationships (Fig. 2.7 a) and showed no luminescence (Fig. 2.7 b). Samples with well-developed dissolution seams contain below 3.3 % quartz cement, which is supported by cathodoluminescence images showing mainly luminescing detrital quartz grains (Fig. 2.7 c, d). Non-luminescent barite was observed to engulf non-luminescent euhedral authigenic quartz (Fig. 2.7 e, f).

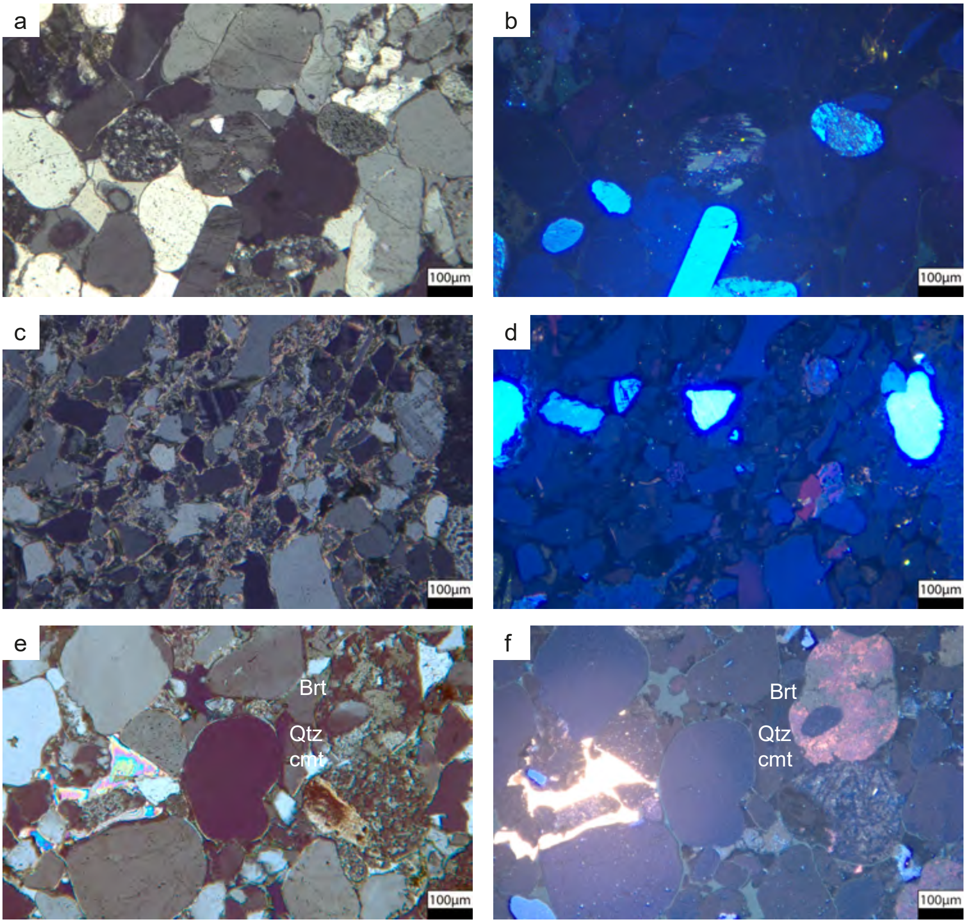

Figure 2.7. Photomicrographs of authigenic and detrital quartz under crossed-polarized light (a, c & e) and cathodoluminescence (b, d & f). a & b) Detrital quartz is characterized by purple and night blue luminescence, while authigenic quartz does not show any luminescence at all (sample B_17). c & d) Photomicrographs of dissolution seam (sample B_16). Cathodoluminescence reveals that the quartz in this chemical compaction seam is detrital, while illite (bright color in xpl) and chlorite appear non-luminescent. K-Feldspar shows bright blue luminescence. e & f) Euhedral authigenic quartz being enclosed by barite cement, while plagioclases show purple luminescence (sample A_03).

2.5.1.3 IGV, Optical Porosity, Compaction and Texture

The IGV shows comparable ranges in both wells (well A 12-24 %, mean: 17 %; well B 11-26 %, mean 17 %). Authigenic minerals are the main contributor to the IGV (well A: 9-19 %, mean 13 %; well B: 7-21 %, mean 14 %) (Fig. 2.8 a). Intergranular optical porosity (stained in blue, compare Fig. 2.5 a) primarily occurs along the bedding plane of less cemented beds, and ranges based on point counting from <1 – 9 % (mean: 4 %) in well A and between 0-11 % (mean: 1 %) in well B. Intragranular optical porosity in feldspar and chert does not contribute to the IGV and is of minor importance for the total optical porosity (well A: mean 1 %; well B: mean <1 %). The porosity-loss in both wells was primarily induced by mechanical compaction based on the assessment of compactional indices (Fig. 2.8 b) after Lundegard (1992). Compactional indices range from 0.63 – 0.88 (well A: avg. 0.79, well B: avg. 0.76, supplementary material I). A relationship between more continuous illite coatings on GTG interfaces and the IGV was observed (Fig. 2.8 c). More continuous illite coatings (>40 % coverage) on GTG interfaces occurred in samples with lowest IGVs (<15 %) (Fig. 2.8 c). Generally, the more surface at GTG contacts is covered by illite, the lower the IGV. Quartz cements primarily occur where pore-lining clay minerals were not continuously covering quartz grains (Fig. 2.6 a). Mostly continuous illite coatings on grain-to-IGV (GTI) interfaces negatively correlate with the amount of authigenic quartz cements (Fig. 2.8 d). Samples with grain coating coverages above 75 % show little to no authigenic quartz (<3 %) (Fig. 2.8 d).

Three main petrographic types were identified based on their texture and clay mineral coverage by petrographic observation, and based on assemblages of blocky pore-filling cements (quartz, carbonates, anhydrite, barite, halite, feldspar, and gypsum) by point-counting. Type A showed open intergranular porosity along the bedding planes (Fig. 2.5 a) with small to intermediate amounts of blocky pore-filling cements (avg. 8.6 %). The sorting along the bedding planes is very good, however there are pronounced differences in grain sizes between different beds. Consequently, porosities are also bound to the bedding, showing generally higher porosities in beds with coarser grain sizes. Clay minerals occur mainly on GTI interfaces (avg. 74.0 %), while clay minerals on GTG interfaces are less common (avg. 20.6 %). Type B is characterized by only locally visible open porosity due to intense cementation (Fig. 2.5 b) by blocky pore-filling cements (avg. 10.2 %). The IGVs are comparable to type A, as well as the good sorting along the bedding planes. There are less GTI coatings (avg. 62.1 %) than in type A, however the amount of GTG coatings is increased (avg. 27.3 %) in comparison. Type C samples (Fig. 2.5 c) show no optical porosity and abundant dissolution seams, visible by serrated contacts between detrital quartz rich grains. Coarse grained beds in type C are primarily composed of rock fragments. Type C shows high clay mineral coverages on both GTI interfaces (avg. 75.8 %) and GTG interfaces (avg. 45.7 %) in concert with less abundant blocky pore-filling cements (avg. 7.5 %).

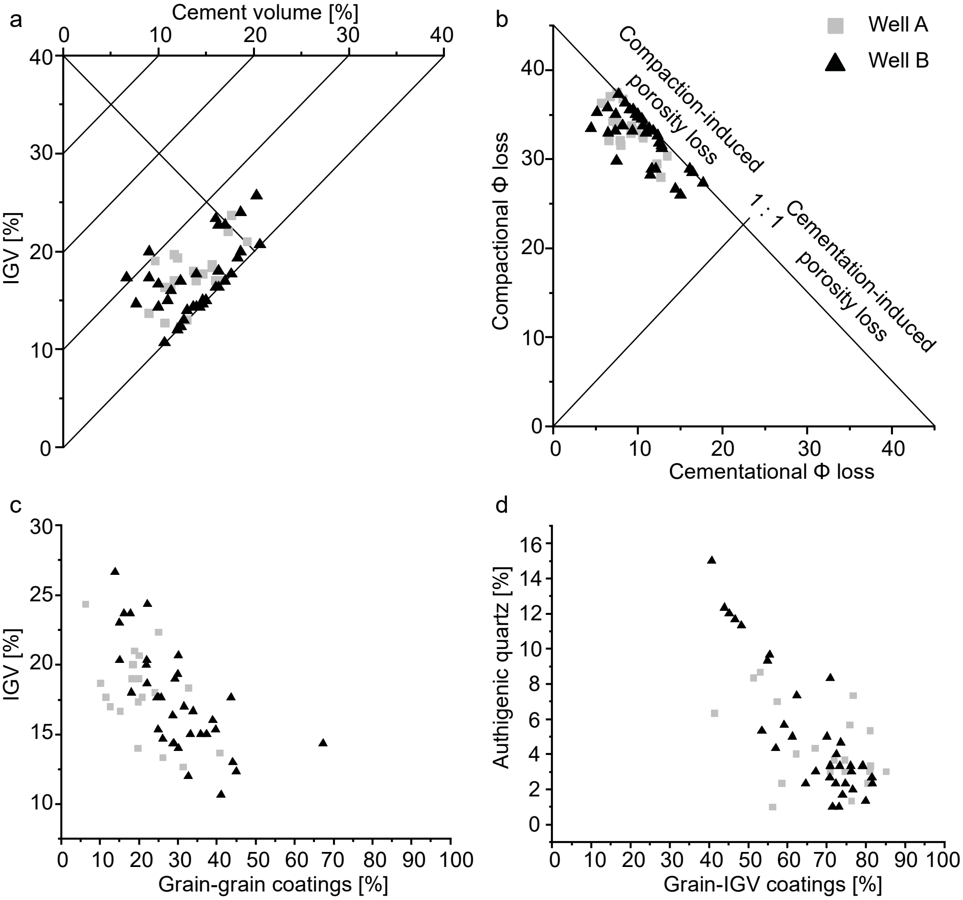

Figure 2.8. a) Houseknecht diagram (Houseknecht, 1987) illustrating the relationship between inter-granular volume (IGV) and cement volume in wells A and B. b) Scatter plot of compactional vs cementational porosity loss (Lundegard, 1992) illustrating the dominance of porosity loss by compaction compared to porosity loss by cementation in both well A and well B. c) Scatter plot of the IGV compared to the coverage of illite coatings on grain to grain interfaces (GTG), showing lower IGVs in case of more continuous GTG coatings. d) Scatter plot of quartz cementation compared to the grain-coat coverage of grains in contact with the IGV, showing the inhibiting effect that grain coatings can have on syntaxial quartz cements.

2.5.2 Petrophysical measurements

Decane porosity ranges from 0.6 % to 14.5 % (Fig. 2.9 a, Tab. 2.1, supplementary material I), with an arithmetic mean of 6.0±0.5 %. Air permeability (1.2 MPa confining pressure) ranges from 0.009 mD to 781 mD (mean 0.96 mD) (Fig. 2.9 a, supplementary material I).

The highest permeabilities were observed in medium to well sorted sandstones with distinct bedding features.

With decreasing confining pressures from 50 to 2 MPa, He-permeabilities are increased (Fig. 2.9 b). At 50 MPa confining pressure, permeabilities range from 0.00002 to 176 mD, whereas at 2 MPa confining pressure, permeabilities range from 0.008 to 287 MPa. Calculated γ coefficients range from 0.005-0.222 MPa^{-1} (supplementary material I) and show higher γ (>0.06 MPa^{-1}) in less porous (<6% decane porosity) (Fig. 2.9 c) and in less permeable samples (<1 mD) (Fig. 2.9 d). Smaller γ (<0.06 MPa^{-1}) values are calculated for samples with higher porosity (>6 % decane porosity) and higher permeability (>1 mD).

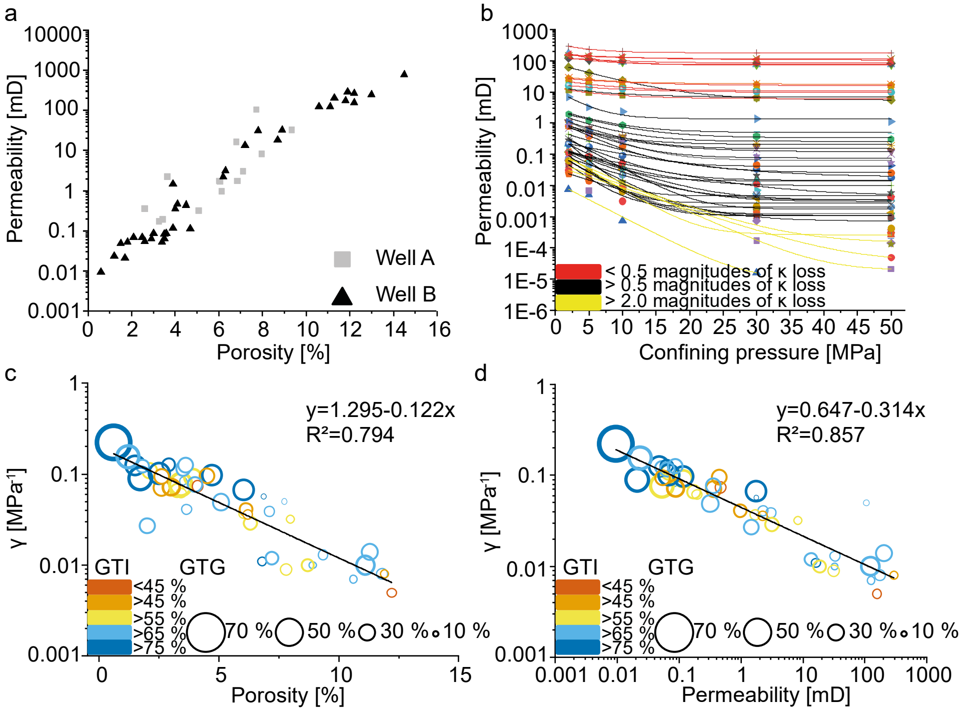

Figure 2.9. a) Decane porosity compared to air permeability (1.2 MPa confining pressure), showing higher permeabilities in more porous horizons. b) He-permeability measured under decreasing confining pressures (50, 30, 10, 5 and 2 MPa) with exponential lines of best fit. c) Scatter plot of the pressure dependent permeability coefficient γ, determined after David et al. (1994), plotted versus decane porosity, with a linear line of best fit. d) Log-log scatter plot of γ versus air permeability (1.2 MPa confining pressure) with an exponential best fit.

Table 2.1. The six major empirical petrophysical and petrographic proxies and their observed values (minimum, maximum and arithmetic mean) used for determining the three rock types. Abbreviations: GTG=grain to grain illite coatings, GTI=grain to IGV illite coating, PF =pore-filling.

	Type A	Type B	Type C
κ	1.7-780.9 mD (Ø=126±40 mD)	0.053–3.13 mD (Ø=0.59±0.2 mD)	0.009–0.068 mD (Ø=0.04±0.01 mD)
φ	6.8–14.5 % (Ø=9.8±0.6 %)	1.8–6.3 % (Ø=4.0±0.3 %)	0.6-2.5 % (Ø=1.8±0.4 %)
γ	0.5-5.7 10-^{2} MPa^{-1} (Ø=1.9±0.33 10-^{2} MPa^{-1})	2.9-12.7 10-^{2} MPa^{-1} (Ø=7.3±0.67 10-^{2} MPa^{-1})	7.7-22.0 10-^{2} MPa^{-1} (Ø=12.9±2.2 10-^{2} MPa^{-1})
GTG coatings	6.3-37.4 % (Ø=20.6±1.7 %)	10.1-44.1 % (Ø=27.3±1.3 %)	32.7-67.4 % (Ø=45.7±4.7 %)
GTI coatings	43.9.7-81.1 % (Ø=74.0±1.4 %)	40.7-85.2 % (Ø=62.1±2.5 %)	70.9-81.6 % (Ø=75.8±3.3 %)
PF cement	3.7-14.0 % (Ø=8.6±0.6 %)	4.0-16.7 % (Ø =10.2±0.7 %)	2.7-11.3 % (Ø=7.5±1.4%)

2.6 Discussion

2.6.1 Paragenetic sequence

2.6.1.1 Early diagenesis

Cementation, dissolution, replacements, and mechanical and chemical compaction were interpreted relative to each other (Fig. 2.10). Mechanical compaction started due to increasing vertical stresses during burial and reduced porosities throughout early diagenesis, until the maximum of mechanical compaction was reached (Paxton et al., 2002). The burial history relating the subsidence and tectonic development with diagenetic alteration is based on basin modeling conducted by Schwarzer and Littke (2007).

Considering the paleo-environment of arid dune to sand flat deposits (e.g. Schöner (2006)), evaporation likely enabled the formation of anhydrite (Fig. 2.6 d) and very local halite during early diagenesis. The occurrence of anhydrite in large pores suggests its formation to pre- or syndate extensive mechanical compaction (Fig. 2.6 d). Due to the presence of rather continuous tangential illitic grain coatings on both GTI- and especially at GTG interfaces in the samples, syn-depositional formation of clay mineral grain coatings is inferred (Molenaar & Felder, 2018; Schöner, 2006). Pore-lining smectite precursors are interpreted to have been present and recrystallized during burial diagenesis (Ajdukiewicz et al., 2010; Gaupp et al., 1993; Liewig & Clauer, 2000; Molenaar & Felder, 2018; Storvoll et al., 2002).

These smectite-precursors likely formed from dust input of the arid environment, leading to clay infiltration during or shortly after deposition and pedogenesis (Molenaar & Felder, 2018). Some of the calcite was interpreted to have formed during early diagenesis, based on the poikilotopic texture supporting the grain framework (Fig. 2.6 e), pre- or syndating extensive mechanical compaction.

2.6.1.2 Burial diagenesis

Due to textural relationships compared to authigenic quartz, vermicular chlorite was likely formed before the onset of quartz cementation, because vermicular chlorite was observed to grow in open pores and was observed to be encompassed by authigenic quartz (Fig. 2.6 g). The vermicular chlorite was often observed close to calcite cement (Fig. 2.6 b), which can be a byproduct of chloritization of kaolinite (Worden & Morad, 2003). However, this would require siderite as a precursor for the calcite phase, which was not observed. Either all siderite was consumed during the formation of chlorite, or it was never present. Alternatively, an external iron source via hydrothermal fluid circulation along the graben fault system could be interpreted to be the main source for reactants (Gaupp et al., 1993; Wüstefeld et al., 2017b).

Based on textural observations (Fig. 2.5 b, 2.6 a-b, g-h, 2.7 a-f), authigenic quartz is interpreted to be the second pore filling cement during burial diagenesis, requiring temperatures above 75° C (Walderhaug, 1994) respectively 80° C (Worden & Morad, 2000) to be pervasive. Considering the modelled geothermal gradient of 37° C/km (Schwarzer & Littke, 2007), the thermal conditions for quartz formation were reached in depths of approximately 2500-3000 m. Relative uplift during the Cretaceous (Fig. 2.10) possibly triggered by erosion due to the Late Albian transgression (Hancock & Kauffman, 1979), did not reduce the burial depth of the sedimentary Rotliegend below 2500 m (Schwarzer & Littke, 2007) (Fig. 2.10). According to Lander and Bonnell (2010), quartz cementation growth rates are significantly higher on non-euhedral surfaces or fractures within quartzes. Continuous clay-mineral grain coatings can inhibit quartz cements from forming on quartz substrates (Ajdukiewicz et al., 2010; Busch et al., 2017; Busch et al., 2018; Heald & Larese, 1974; Storvoll et al., 2002). The correlation of quartz cement volumes in dependence of GTI coating coverages (Fig. 2.8 c) supports this model and is interpreted to be a main control on the variability of authigenic quartz cement amounts in samples of this study. Authigenic quartz cement likely formed throughout the entire burial history since its initialization, as long as sufficient amounts of silica were available. Possible silica sources are autochthonous supply by the illitization of smectite (Worden & Morad, 2003) or from dissolution seams (Walderhaug & Bjørkum, 2003), as well as allochthonous hydrothermal fluids circulating through the Rotliegend strata (Gaupp et al., 1993).

Illite can recrystallize from smectite in the presence of a potassium source (Worden & Morad, 2003). It was differentiated between tangential pore-lining illite and pore-filling meshwork illite (Molenaar & Felder, 2018). Furthermore, illite replacements of potassium feldspars were observed, which likely formed during burial diagenesis (Worden & Morad, 2003). Meshwork illite in open pores was likely sourced by hydrothermal fluids, as there were no potassium feldspars in close proximity to them. Hydrothermal fluids are well documented in Rotliegend sandstones and have been interpreted to strongly influence mineral authigenesis during burial diagenesis (Gaupp et al., 1993; Nadoll et al., 2019; Pudlo et al., 2012; Sullivan et al., 1990; Zwingmann et al., 1998). Hydrothermal fluids were linked to the occurrence of fault systems in Rotliegend and Upper Carboniferous sandstones in the North German Basin (Gaupp et al., 1993). As the fault systems in the studied setting terminate in the overlying Zechstein evaporites (Gast & Gundlach, 2006), fluid flow from overlying stratigraphic units can be excluded due to the integrity of the salt seals (Gast et al., 2010). Consequentially, hot hydrothermal fluids, likely originating from underlying Carboniferous units, must have migrated along the graben faults of the Permo-Carboniferous fault system (Gast & Gundlach, 2006). These fluids transported ions and heat into the system, which enabled the precipitation of late diagenetic alterations such as barite or late calcite (Busch et al., 2019; Gaupp et al., 1993; Nadoll et al., 2019; Zwingmann et al., 1999).

The second carbonate cement phase occurred in minor amounts in samples with intense authigenic quartz (Fig. 2.6 a), and in larger amounts in samples with low to none authigenic quartz (Fig. 2.6 b, h), but continuous tangential illite coatings. It was observed to overgrow both authigenic quartz (occasionally euhedral) (Fig. 2.6 g) and vermicular chlorite (Fig. 2.6 h). Small rims of authigenic quartz overgrown by calcite indicate that the cementation of late calcite began after the onset of quartz cementation, as the cementation of authigenic quartz is dependent on time exposed to sufficient temperatures and silica supply (Busch et al., 2018; Lander & Bonnell, 2010; Lander et al., 2008; Walderhaug, 1994). As a result, the second calcite cement phase was likely formed after the onset of quartz cementation. The second calcite cement phase is interpreted to have formed after the vermicular chlorite based on textural observations, showing that calcite terminates against vermicular chlorite (Fig. 2.6 b).

The pore-occluding chlorite, which was heavily deformed and squeezed between the grains, showed no vermicular texture. It might have been either formed independently from the vermicular chlorite or lost its texture during mechanical and chemical compaction. As this chlorite only occurred in heavily compacted samples, while vermicular chlorite occurred in almost all other samples, the two species of chlorite are interpreted to be of the same origin. The structural differences are therefore just a consequence of the intense mechanical and chemical compaction and not an additional chlorite phase. Authigenic barite occurs as pore-filling cements enclosing euhedral syntaxial quartz cements (Fig. 2.6 c &

2.7 e-f), implying the barite formed during the late burial diagenesis after authigenic quartz reached its euhedral shape (Busch et al., 2019).

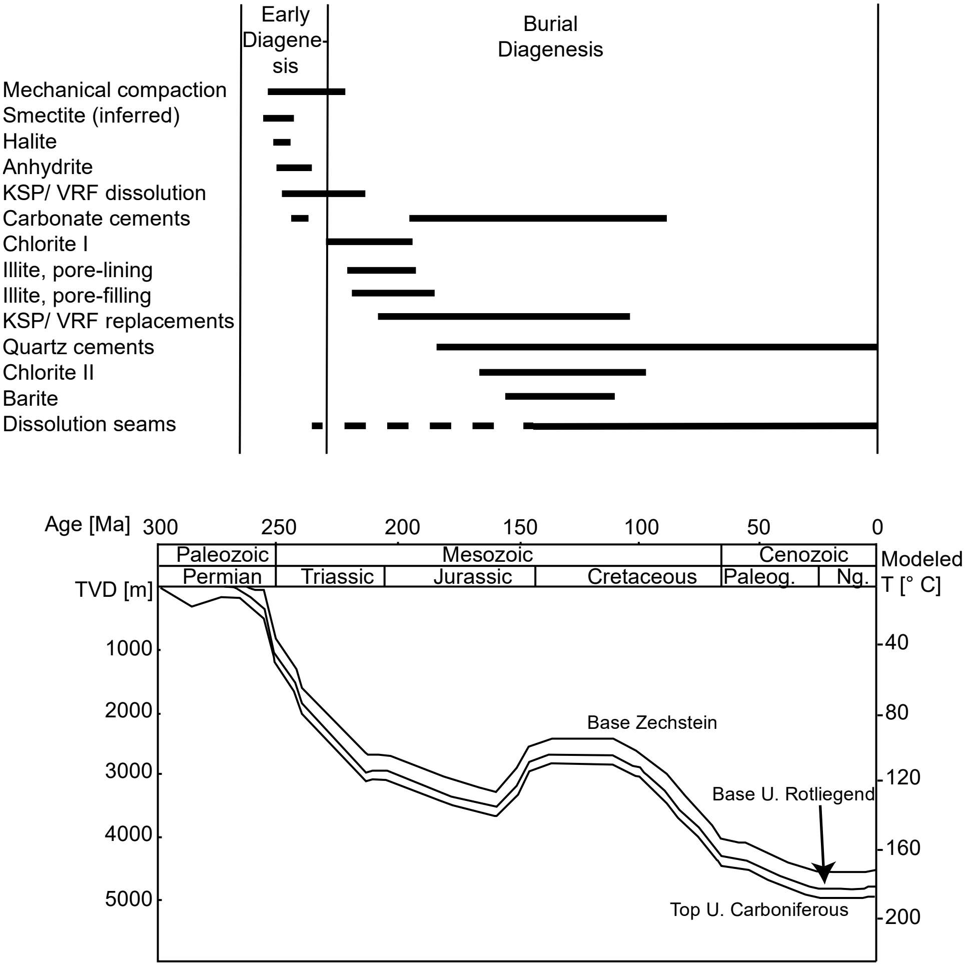

Figure 2.10. Paragenetic sequence in correlation with the burial history for the most abundant cements and alterations. The paragenesis was reconstructed based on textural observations and cathodoluminescence. The burial history and the geothermal gradient (37° C/km) were taken from Schwarzer and Littke (2007) and correlated to the paragenesis.

Cathodoluminescence was used to assess the quartz cement content of samples containing serrated quartz grains (night blue luminescence) in samples with pervasive chemical compaction, as the interpretation of detrital and authigenic quartz was difficult due to the absence of grain coating phases (Fig. 2.6 a-b). Authigenic quartz consistently did not show luminescence (Fig. 2.6 c-d), as a result the consistently luminescent quartz in dissolution seams is interpreted to be of a detrital origin. Chemical compaction in return is discussed to be favored by the occurrence of grain-coating illite around detrital quartz (Greene et al., 2009; Kristiansen et al., 2011). The maximum encountered IGV was 25.7 %, which matches the empirically determined maximum IGV of 26 % purely by mechanical compaction (Paxton et al., 2002). However, observed IGVs as low as 11 % cannot be attributed to mechanical compaction alone in an idealized sphere packing without major detrital ductile grains according to Paxton et al. (2002). The studied sandstones are interpreted as such due to their well sorting (moderately well to extremely well, supplementary material) and their low detrital clay content (avg. 0.9 %, supplementary material I). As a result, chemical compaction reduced the IGV in these low IGV samples. Larger amounts of grain-to-grain illitic grain coatings were observed to correlate with a decrease in the IGV (Fig. 2.7 c). Therefore, chemical compaction may be quantitatively assessed using the illite coverage on GTG interfaces compared to the IGV. As a result, illite coverage on GTG interfaces was interpreted to be the main controlling factor for the intensity of chemical compaction in different samples.

2.6.2 Reservoir quality assessment and rock typing

Rock typing attempts have been made to assess the reservoir quality and behavior under elevated pressure conditions. Based on petrophysical and petrographic criteria, three types were distinguished (Fig. 2.11). These types were based on permeability, decane porosity, authigenic phases, clay mineral coatings, γ coefficients, petrographic observations, detrital composition, and the reconstructed paragenetic sequence. Although possibly relevant for the pressure sensitivity of permeability for individual samples, consistent trends for the influence of blocky cements, ductile rock fragments and sorting could not be established.

As permeability measurements under decreasing confining pressures showed varying intensity in permeability enhancement (Fig. 2.9 b), exponential lines of best fit analog to David et al. (1994) were used to quantify the exponential relationship between permeability and pressure sensitivity of permeability from 50 MPa to 2 MPa confining pressure. High decane porosity samples experienced permeability enhancement of less than one order of magnitude under decreasing confining pressures, while low decane porosity samples were reduced by several orders of magnitude (Fig. 2.9 b). Similar observations have been made in a study on Rotliegend sandstones from a tight gas reservoir in northern Germany (Albrecht, 2015). Due to the good empirical correlation between decane porosity and permeability (Fig. 2.9 a), between decane porosity and the pressure sensitivity of permeability (Fig. 2.9 c), as well as between permeability and the pressure sensitivity of permeability (Fig. 2.9 d), the petrophysical data allows a straight-forward approach for reservoir quality assessment and will be used synonymously for reservoir quality. The rock typing was conducted under consideration of the petrophysical data in combination with the main petrographic texture and resulting diagenetic alteration attributed to the reduction or preservation of open porosity, thus linking certain diagenetic features and processes to petrophysical properties (Fig. 2.11). As a result, three rock types were identified (Fig. 2.11).

Type A shows intermediate to high decane porosities (6.8-14.5 %, avg.: 9.8 %) and permeabilities at 1.2 MPa confining pressure >1 mD (1.7 to 780.9 mD, avg.: 126.7 mD) (Fig. 2.8). Permeability was enhanced within the same order of magnitude under elevated confining pressures from 50 to 2 MPa (Fig. 2.9 b), which is in agreement with observations in previous studies (Albrecht, 2015; David et al., 1994). Calculated γ coefficients between 0.005-0.057 MPa^{-1} (Table 2.1, Figure 2.11) are mostly in agreement with values for sandstones (0.0014-0.02 MPa^{-1}) stated by literature (David et al., 1994; Yale, 1984). Clay mineral grain coating coverages are mostly large (avg.: 74 %, Table 2.1) on grain to IGV interfaces (Fig. 8 c, Fig. 2.11), which are known to inhibit quartz cement (avg.: 4.9 %, supplementary material I) (Ajdukiewicz et al., 2010; Busch et al., 2017; Molenaar & Felder, 2018). Clay mineral coatings on grain-to-grain interfaces may occur (avg.: 21 %), but they are not frequent enough to lead to intense chemical compaction. As a result, the pore space and pore throats of type A are relatively uncemented and open represented by a moderate amount of intergranular cements (avg.: 8.6 %). In summary, rock type A enabled to retain decane porosities >6.5 % as low to medium GTG coatings reduced the porosity loss by chemical compaction, while medium to high GTI coatings minimized the amount of authigenic quartz.

Type B is defined by intermediate to poor reservoir qualities with permeabilities at 1.2 MPa confining pressure generally below <1 mD (0.053–3.13 mD, mean: 0.59 mD) and decane porosities <6.5 % (1.8–6.3 %, mean: 4.0 %). The permeability enhancement in type B ranges from 1-2 orders of magnitude, thus showing the similar permeability enhancements as Albrecht (2015) demonstrated for samples with comparable permeabilities. The γ coefficients (avg.: 0.073 MPa^{-1}, Fig. 2.11) are in agreement with ranges for tight sandstones (>0.038 MPa^{-1}) (David et al., 1994; Yale, 1984). Less continuous (avg.: 62 %) illite coverages on grains in contact with the IGV were observed (Fig. 2.11, Table 2.1). Consequently, pore-occluding cements, especially quartz, occur in larger quantities than in type A (avg.: 10.2 %, Fig. 2.11). This leads to a reduction in available open pore space and smaller pore throats, reducing porosity and permeability (Fig. 2.11). It needs to be considered that micro porosities in the pore-filling chlorite/illite might have a positive effects on reservoir quality (Aagaard et al., 2000). Thus, the main process controlling the reduction in reservoir quality in type B are the low GTI coatings facilitating intense quartz cementation.

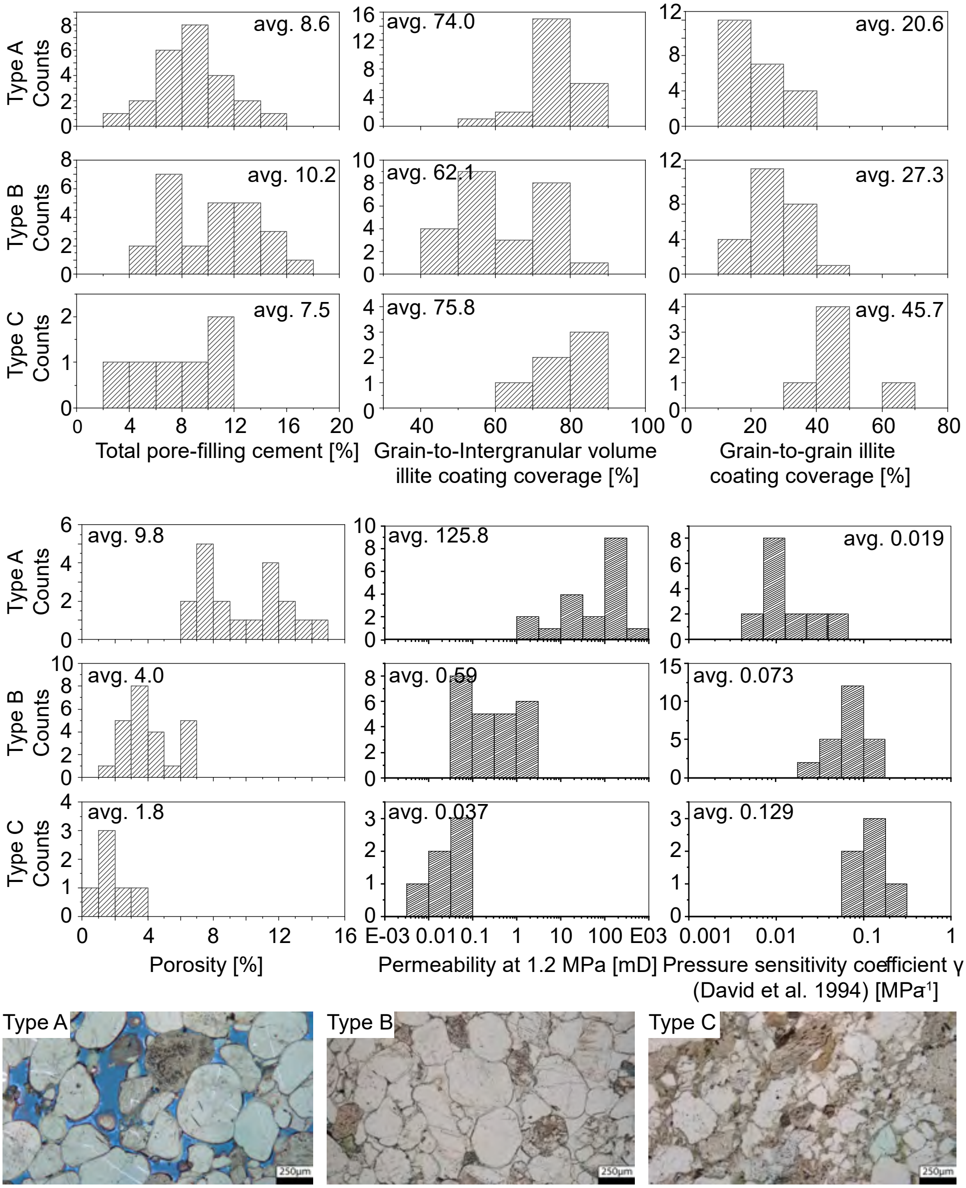

Figure 2.11. Histograms of the statistical distribution of the petrographic (upper) and petrophysical (lower) data used to determine the rock type. Error bars and threshold values for these proxies are shown in Table 2.1. Typical examples of the textures of the three rock types are shown as photomicrographs.

The open pore volume of type C is almost completely occluded, resulting in low decane porosities (cutoff here: <3 %, 0.6-2.5 %) and permeabilities at 1.2 MPa confining pressure (cutoff here: <0.1 mD, 0.009-0.068 mD), and thus poor reservoir qualities (Fig. 2.11). Type C is characterized by permeability enhancements of >2 orders of magnitude from 50-2 MPa confining pressure (Fig. 2.9 b, 2.11). γ coefficients (avg. 0.129 MPa^{-1}, Table 2.1) are the highest in this study, and do exceed values reported for tight sandstones (>0.038 MPa^{-1}) (David et al., 1994; Yale, 1984).

The most extensive clay mineral coatings on GTG interfaces encountered in this study were observed in type C (33-67 %, avg.: 46 %, Fig. 2.11, Tab. 2.1). These intense GTG coatings are interpreted to have enhanced chemical compaction (Greene et al., 2009; Kristiansen et al., 2011) due to the electrochemical potential difference between illite/muscovite and quartz (Kristiansen et al., 2011). Another characteristic are high amounts of illite coatings (avg.: 76 %, Fig. 2.11, Tab. 2.1) on GTI interfaces as well as the lowest amount of pore-filling cements of the three rock types (avg.: 7.5 %). Consequentially, reservoir quality in type C was primarily reduced by intense chemical compaction due to the high GTG coatings and the absence of pore filling syntaxial cements stabilizing the grain framework due to relatively large GTI grain coating coverages.

2.7 Conclusions

Reservoir quality in the studied wells is mainly controlled by compactional porosity-loss due to mechanical compaction, authigenic quartz overgrowth cements, and chemical compaction. Three rock types based on their different linked compactional and diagenetic alterations were defined based on the amount and location of illite coatings, as well as their decane porosity and their permeability under elevated confining pressures.

Type A is characterized by mostly continuous illite coatings (avg.: 74 %) on grain-to-IGV (GTI) interfaces, which inhibited quartz cementation and preserved reservoir quality. Porosities (avg.: 9.8 %) and permeabilities (avg.: 126 mD) are the highest among the studied rocks. The pressure sensitivity of permeability (avg. 0.019 MPa^{-1}) is lowest, indicating a smaller reduction of permeability under elevated confining pressures.

Type B shows the most discontinuous illite coatings on GTI interfaces (avg.: 62 %), as well as the highest amount of pore-filling authigenic cements (avg.: 10.3 %), especially quartz and calcite, occluded pore spaces and pore throats in Type B. As a result, decane porosity and permeability were reduced to an average of 4.0 % and 0.59 mD. The pressure sensitivity (avg.: 0.073 MPa^{-1}) is larger than for type A.

Type C is characterized by the highest coverage of illite coatings on grain-to-grain (GTG) interfaces (avg.: 46 %). In contrast to Type B, the illite coverages on GTI interfaces are high (avg.: 76 %) while the amount of pore-filling cements are the lowest (avg.: 7.5 %).

Intense chemical compaction was enabled due to the presence of illite coatings at the contacts of detrital quartz grains, thus reducing the IGV and preserved porosities (avg.: 1.8 %). Consequently, permeability is also very low (avg.: 0.037 mD), and the pressure sensitivity of permeability is about a magnitude higher (avg.: 0.129 MPa^{-1}) compared to Type A and B.

3 Compaction control on diagenesis and reservoir quality development in red bed sandstones – a case study of Permian Rotliegend sandstones

3.1 Abstract

Authigenic minerals formed during diagenesis in conjunction with compaction by burial have long been known to lead to porosity-loss of sandstones, and a subsequent deterioration in reservoir quality. The diagenetic impact on reservoir quality and permeability heterogeneity measured horizontal and vertical to bedding was characterized in three fluvio-eolian Lower Permian Rotliegend outcrops from the Flechtingen High, the northern Hesse Basin (both Germany) and the Vale of Eden (UK) using point-counting, polarized light-microscopy, helium pycnometry and permeability measurements.

Results show significant porosity (10 to 35 %) and permeability (0.01 to 10000 mD) ranges largely independent of depositional environment. The major control on reservoir quality in Cornberg Sandstones are dolomite and siderite cementation in conjunction with illitization and illite and kaolinite cementation, leading together with quartz cementation to a mostly cemented IGV and poorest reservoir quality (avg. horizontal permeability: 0.96 mD). Flechtingen Sandstones are most intensely compacted due to the lack of significant early diagenetic cement phases and continuous illitic grain-to-grain coatings, which inhibited intense quartz cementation but enhanced chemical compaction at quartz grain contacts, resulting in intermediate reservoir quality (avg. horizontal permeability: 34.9 mD). Penrith Sandstones lack significant authigenic phases besides quartz due to carbonate dissolution during uplift. They show the least amount of detrital feldspars and clay minerals, leading to no major reservoir quality reduction by burial diagenetic clay mineral alterations, resulting in highest reservoir quality (avg. horizontal permeability: 5900 mD).

Additional results highlight higher horizontal to vertical permeability ratios k_h/k_v in less homogeneous sandstones of <10 mD of 10, and in more homogenous, higher permeable sandstones >1000 mD of 1.

Although detrital and authigenic sample compositions vary throughout the studied areas, the general effect of grain coatings coverages on syntaxial cement inhibition and chemical compaction can be delineated.

This study increases the understanding of porosity reduction in sandstones, as it confirms the necessity to differentiate between the illitic grain-to-grain coatings and illitic grain-to-IGV coatings. As a result, the enhancing effect of illite on chemical compaction on quartz grain-grain boundaries can be better constrained, as well as the effect of grain coatings on quartz cementation. This is relevant for reservoir quality and risk assessment in hydrocarbon and geothermal plays as well as in storage.

3.2 Introduction

Siliciclastic sandstone reservoirs are hosting about 60 % of the world's hydrocarbons (Bjørlykke & Jahren, 2010) and are thus of significant economic interest. The utilization of such reservoirs have been extended beyond hydrocarbon extraction in the past two decades, being used for geothermal energy exploration (Caulk & Tomac, 2017; Heap et al., 2017), hydrogen storage (Henkel et al., 2013; Pfeiffer et al., 2017), or CO_2 sequestration (Ambrose et al., 2008; Barnes et al., 2009; Benson & Cole, 2008; Heinemann et al., 2012). After deposition as sand, mechanical and chemical compaction induce the consolidation process to sandstone during diagenesis over geological timescales (Greene et al., 2009; Houseknecht, 1987; Kristiansen et al., 2011; Lundegard, 1992). Diagenesis affects the rock's porosity and permeability, and its viability as a reservoir (Morad et al., 2010; Taylor et al., 2010; Wadsworth et al., 2016). Sandstones experience diagenetic alterations during burial; these are related to the initial detrital composition and grain coating minerals (Aagaard et al., 2000; Busch et al., 2020; Monsees et al., 2020a), fluid type, -chemistry and -pressure (Bjørlykke & Høeg, 1997; Gaupp et al., 1993), thermal exposure over time (Becker et al., 2019; Busch et al., 2018; Lander et al., 2008), and faults controlling temperature-overprint by hydrothermal fluid circulation (Farrell & Healy, 2017; Farrell et al., 2014; Wüstefeld et al., 2017b).

Monsees et al. (2020a) proposed grain-coatings to be a controlling factor on cementational and compactional behavior of Lower Permian Rotliegend sandstones natural gas reservoir in the North German Basin. The aim of this study is to test if the observed controls on chemical compaction by grain-to-grain coatings and on chemical compaction and by grain-to-intergranular volume coatings on quartz cementation can also be delineated in similar settings with variable source areas and burial paths. Therefore, study areas have been constrained to depositional parameters (terrestrial, fluvio-eolian sandstones) and ages (Rotliegend, Lower Permian) similar to the boundary conditions presented by Monsees et al. (2020a). Samples were collected from the Cornberg Formation in Cornberg, Hesse, Germany, the Mirow and Parchim Formations in Bebertal, Saxony-Anhalt, Germany, and the Penrith Sandstone Formation near Penrith, Cumbria, UK. Results may highlight, that in addition to vertical effective stresses during burial, the presence of a) mechanical, and b) chemical compaction enhancing illite controls the compactive behavior of reservoir sandstones. This case study is highlighting the heterogeneous effect of diagenetic overprint on the petrophysical parameters porosity and permeability of three exhumed Permian sandstone lithologies located in Germany and the UK, which were deposited in similar fluvio-eolian depositional environments, while source areas and depositional ages vary. The complex relationship between cementation and compaction will be assessed and its impact on reservoir quality will be determined. Heterogeneities from permeability measurements conducted parallel to bedding compared to permeability normal to bedding will be quantitatively constrained. Insights gained from this study will help to assess the variability of diagenetic alterations in sandstones of similar depositional settings, and might improve quantitative constraints applicable in subsurface reservoir quality assessment for hydrocarbon exploration, geothermal energy, hydrogen storage, and CO_2 sequestration.

3.3 Geological setting

3.3.1 Cornberg Sandstones

Cornberg sandstones (CS) belong to the uppermost Rotliegend (Lower Permian) lithostratigraphic unit (Kowalczyk et al., 2012), which is also referred to as the Weißliegend (Paul, 2012). The Cornberg Formation crops out in Cornberg quarry (Quarry A) in the Nentershäuser Basin, which is a sub-basin of the Hesse Basin in central Germany (Kulick et al., 1984) (Fig. 3.1). The Nentershäuser Basin has been interpreted as a pull-apart basin due to its thickness increase of Rotliegend deposits from tens to hundreds of meter over lateral distances <10 km (Kowalczyk et al., 2012; Kulick et al., 1984). Based on meter-scale cross-bedded strata, the depositional system of the sandstones has been controversially discussed (Gast, 1994; Pryor, 1971; Schumacher, 1985). Recent studies interpret them to be of eolian origin due to the distinct cross-bedding and tetrapod tracks (Gast, 1994; Haubold et al., 1995; Kowalczyk et al., 2012). The thickness of the formation in the outcrop is up to 20 m (Kowalczyk et al., 2012), being conformably overlain by the Kupferschiefer claystone marking the onset of the Zechstein transgression (Kowalczyk et al., 2012), and underlain by gray, sandy conglomerates and red conglomeratic sandstones and pelites (Aehnelt & Katzung, 2007). Therefore, Cornberg Sandstones represent the uppermost Rotliegend below the Zechstein base (Fig. 3.2), which is defined by the Kupferschiefer claystone (Menning et al., 2011; Paul, 2012). A published burial model for Cornberg Sandstones is not available, however Rotliegend burial models 170 km further north show burial to more than 4-5 km maximum burial depth (Fig. 1 d, burial curve i) until the Upper Cretaceous inversion (Schwarzer & Littke, 2007). Inversion likely took place from Late Cretaceous onwards, as described for other Permian exposures in Central Germany (Kley & Voigt, 2008).

3.3.2 Flechtingen Sandstones

Upper Rotliegend fluvio-eolian Flechtingen Sandstones (FS) are exposed in the Schwentesius quarry (Quarry B) 1 km north of Bebertal, Saxony-Anhalt, Germany, and in a decommissioned quarry 1 km southwest of Bebertal, (Quarry C, Fig. 3.1), located on the margins of the Flechtingen High (Gaitzsch et al., 2004). The Flechtingen High is a NW-SE striking structural high uplifted during the Upper Cretaceous inversion (Kley & Voigt, 2008; Otto, 2003). The extent of the Flechtingen High is limited by the Haldensleben thrust fault to the NE and the Aller lineament to the SW, which belongs to the Elbe-Fault zone. Rotliegend sedimentary rocks exposed around Bebertal are commonly used as analogs for the North German Rotliegend hosted hydrocarbon reservoirs (Gast et al., 2010; Schröder et al., 1995). The Rotliegend sandstones exposed near Bebertal are equivalent to the Mirow Formation and Parchim Formation of the Havel Subgroup based on regional stratigraphic correlations (Gaitzsch et al., 2004; Schneider & Gebhardt, 1993). Therefore, their absolute sedimentation age is 266 to 262 Ma (Menning, 1995). The total thickness of the Havel subgroup equivalent exposed on the Flechtingen High amounts to roughly 160 m (Gaitzsch et al., 1995). The Havel subgroup is unconformably underlain by the Müritz subgroup and the Altmark subgroup, and unconformably overlain by dominantly fluvio-eolian sandstones of the Elbe subgroup (Gaitzsch et al., 2004) (Fig. 3.2). For Flechtingen Sandstones, a burial model based on thermal data proposed by Fischer et al. (2012) shows a rapid burial reaching over 200° C in early Triassic. Their resulting burial depth of approximately 6 km assumes a normal geothermal gradient of 35° C/km (Fig. 3.1 d, burial curve ii). Inversion was initiated in the late Cretaceous (Fischer et al., 2012). The burial model proposed by Kohlhepp (2012) (well Peckensen 7 80 km NNE of Bebertal) agrees with rapid initial subsidence during the Upper Permian, with maximum burial depth for Upper Rotliegend proposed to be at 3 km for Rotliegend deposits at the basin margin (Fig. 3.1 d, burial curve iii) or 5 km at the basin center (Fig. 3.1 d, burial curve iv) before the Upper Cretaceous inversion (Kohlhepp, 2012).

3.3.3 Penrith Sandstones

Permian Penrith Sandstones (PS) crop out in the Vale of Eden half graben, Cumbria, UK (Fig. 3.1), covering an area of approximately 48 × 6 km (Busch et al., 2017; Macchi, 1981; Turner et al., 1995). Penrith Sandstones were studied in Bowscar quarry (Quarry D) 3 km north of Penrith, in the Salter Hill outcrop (Quarry E) 5 km southeast of Penrith, and in

Penrith Beacon outcrop (Quarry F) 1 km northeast of Penrith (Fig. 3.1). The extent of the Vale of Eden is limited by the Pennine Mountains to the east, the Dent fault system to the south, and the Lake District complex to the west (Fig. 3.1). The Appleby Group consists of the eolian Penrith Formation and basal alluvial deposits locally referred to as the Brockram facies (Macchi, 1981), and is time—equivalent to the Central European Rotliegend (Jackson et al., 1997) (Fig. 3.2). The total thickness of the Penrith Sandstone is discussed to reach between 100 m (BGS, 2020) and up to 1 km in the subsurface towards the East Irish Sea (Turner et al., 1995). Upper Carboniferous siliciclastic rocks in the northern Vale of Eden and Lower Carboniferous limestones in the south are unconformably overlain by the Appleby Group (Arthurton & Wadge, 1981; Macchi, 1981; Turner et al., 1995). The Appleby Group is conformably overlain by shales, evaporites and dolomite of the Zechstein, which are combined in the Eden Shales Formation (Arthurton & Wadge, 1981). Penrith Sandstones were buried during the late Paleozoic, reaching a thermal maximum of 120° C in the early Cretaceous at approximately 3-4 km burial depth (Fig. 3.1 d, burial curve v), before Upper Cretaceous inversion took place (Turner et al., 1995).

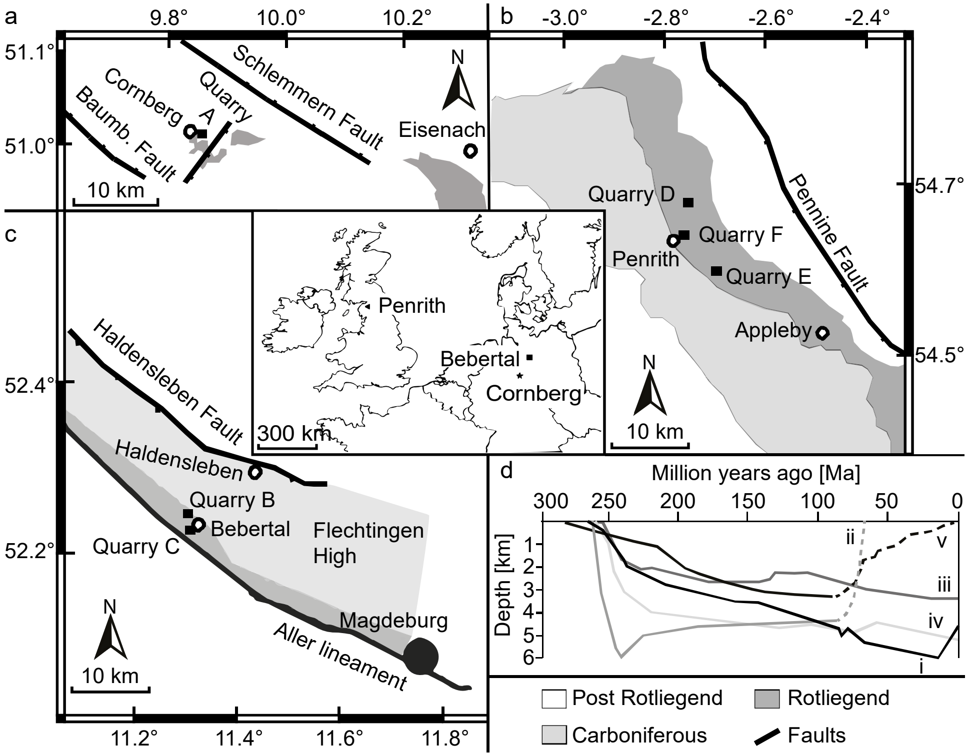

Figure 3.1. Figure caption on the next page.

Figure 3.1. Schematic geological maps of the vicinity of the studied quarries. a) Extent of Rotliegend deposits in the northern Hesse Basin, redrawn from Kowalczyk et al. (2012). Fault orientation and kinematics based on Motzka-Nöring et al. (1987). b) Present-day geology of the Vale of Eden highlighting the extent of Rotliegend deposits, redrawn from Turner et al. (1995) and modified with fault kinematics and orientations taken from Underhill et al. (1988) and Woodcock et al. (2008). c) Geology of the Flechtingen High, showing the location of fluvio-eolian Rotliegend marginal deposits. Surface geology redrawn from Fischer et al. (2012) and modified with fault orientation and kinematics adapted from Kley and Voigt (2008), Otto (2003) and Scheck et al. (2002). The Aller Lineament is not indicated as normal fault, as it consists of several graben faults with strike-slip component (Lohr et al., 2007). d) Burial models for the respective study areas, compiled from published research. i: Northern German Basin (Schwarzer & Littke, 2007), ii: Flechtingen High (Fischer et al., 2012), iii: Altmark basin margin (Kohlhepp, 2012), iv: Altmark basin center (Kohlhepp, 2012), v: Penrith Formation (Turner et al., 1995).

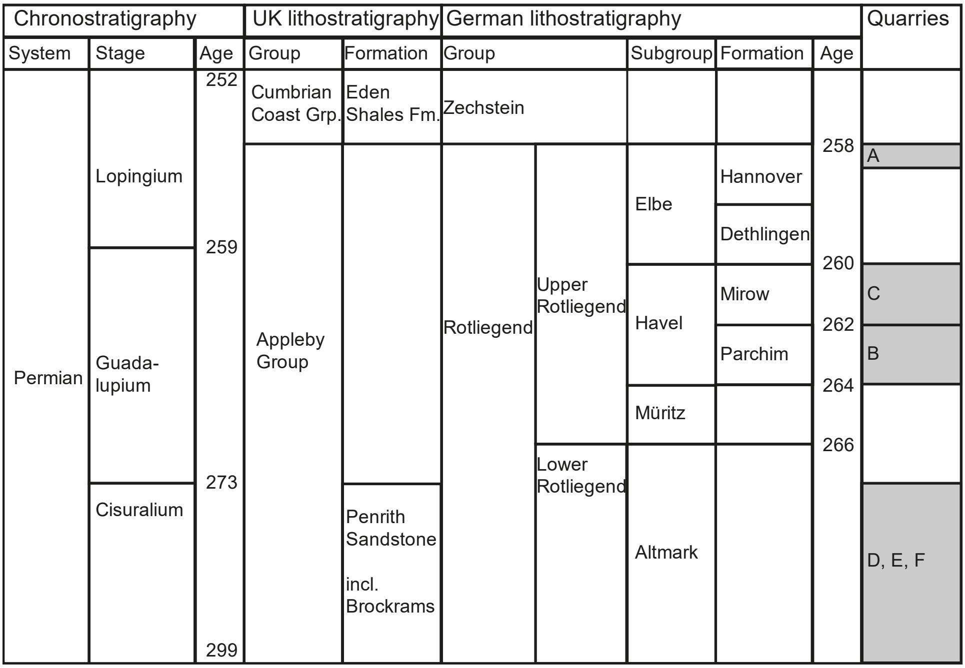

Figure 3.2. Stratigraphic overview of the studied sandstones. Subgroups and formations compiled from BGS (2020), Gaitzsch et al. (1995), Kowalczyk et al. (2012) and Paul (2012). Ages in million years ago. The chronostratigraphic ages and subdivision were taken from Cohen et al. (2013), while ages for regional lithostratigraphic groups are based on Menning (1995).

3.4 Material & methods

Rock samples were taken from quarries and plugs were drilled parallel to bedding for petrographic analysis, as well as normal and parallel to bedding for petrophysical analysis. A total of 41 thin-sections originating from each of the three main studied sandstones

Cornberg Sandstone (n=9, 1 outcrop, Fig. 3.1, Tab. 3.1), Flechtingen Sandstone (n=15, 2 outcrops, Fig. 3.1, Tab. 3.1), and Penrith Sandstone (n=17, 3 outcrops, Fig. 3.1, Tab. 3.1) were analyzed. The thin-sections were impregnated with a blue-dyed epoxy resin to highlight porosity. Thin-sections are prepared to a thickness of 30 µm and in some cases stained with a combined Alizarin Red S and potassium ferricyanate solution in 0.5% HCl to aid the identification of carbonate minerals.

Grain sizes were determined on 100 grains with image analysis using ImageJ (Becker et al., 2017). Skewness and sorting was determined based on grain size measurements after Trask (1930). Point-counting (300 counts) was performed on a grid adjusted to the maximum grain size with a semi-automated Pelcon Point Counter installed on a Leitz Aristomet microscope. The statistical error of point-counting data was determined population-based by dividing the standard deviation by the square root of the number of samples (Becker et al., 2017). Average occurrence rates below 0.3 % were referred to as in traces. Sandstone compositions were classified after Folk (1980). The intergranular volume (IGV) was classified according to Paxton et al. (2002) as the sum of the intergranular pore space, intergranular cement, and detrital matrix. Compactional porosity loss, cementational porosity loss, and compactional indices were calculated after Lundegard (1992). The value for the compactional index ranges between zero (porosity lost exclusively to cementation) and one (porosity lost exclusively to compaction). The percentage of clay mineral coatings on grain-to-IGV (GTI) interfaces was assessed on at least 50 grains per sample (Busch et al., 2020). Percentages of illite coatings on grain-to-grain (GTG) detrital quartz interfaces were evaluated after Monsees et al. (2020a) by microscopy-aided image analysis. Microporosity in clays was estimated based on quantitative electron microscopy data on different clay mineral data sets (Hurst & Nadeau, 1995). The abundance of clay minerals was multiplied with the amount of microporosity as determined by Hurst and Nadeau (1995) for illite (63±10 %), kaolinite (43±11 %) and clay clasts (10±3 %).

Petrophysical measurements were performed on cylindrical plugs (2.54 cm diameter, 4 cm length), and therefore are within the guidelines for petrophysical measurements on sandstones recommended by Heap (2019). In total, 75 plugs were prepared: 19 plugs for the Cornberg Sandstone, 25 plugs for the Flechtingen Sandstone, and 31 plugs for the Penrith Sandstone (Tab. 3.1). In total 30 horizontal plugs directly correspond to thin-sections (Tab. 3.1). Samples were dried in a vacuum oven at 40° C and 0.1 bar for at least 72 hours prior to the petrophysical measurements. Helium porosity (φ) was measured with an AccuPyc II 1340 pycnometer, measuring the connected porosity (Becker et al., 2017). The porosity values given here are the average of ten measurement cycles per sample. Permeability (κ) was measured on 75 plugs with an air permeameter (measurement range 0.001 to 10,000 mD, $1\ \text{mD} \triangleq 9.869 * 10^{-16}\ \text{m}^2 \approx 10^{-15}\ \text{m}^2$) manufactured by Westphal Mechanik using oil-free lab air as the permeant (80 % N_2, 20 % O_2). Laminar-flow conditions are determined during the measurement by the software used to operate the permeability cell, ensuring that all measurements were taken under laminar-flow conditions and thus do not require a Forchheimer correction (Whitaker, 1996). A constant confining pressure of 1.2 MPa was applied to the samples throughout the measurement, which was applied two minutes before the measurement was conducted at ambient laboratory temperature (T=22 °C) and until steady-state flow conditions were achieved. Permeability values are Klinkenberg-corrected (Klinkenberg, 1941).

Table 3.1. Sample overview, listing quarry or outcrop names, their abbreviations used in the text, latitude and longitude, their study area, and the respective sample quantity and sample type. Values in brackets in row "n horizontal plugs" represent the amount of available horizontal plugs directly corresponding to these individual thin-sections.

Quarry/ outcrop name	Quarry	Quarry location [°]	Study area	n thin-sections	n total plugs	n horizontal plugs	n vertical plugs
Cornberg quarry	A	51.042386 9.865660	Cornberg	9 (8)	19	10	9
Schwentesius quarry	B	52.254338 11.337711	Flechtingen	8 (2)	3	2	1
Decommissioned quarry	C	52.231433 11.319722	Flechtingen	7 (6)	22	11	11
Bowscar quarry	D	54.701049 -2.746095	Penrith	13 (12)	22	13	9
Salter Hill outcrop	E	54.630138 -2.647602	Penrith	2 (1)	7	4	3
Penrith Beacon outcrop	F	54.675278 -2.735556	Penrith	2 (1)	2	1	1
Total	-	-	-	41 (30)	75	41	34

3.5 Results

3.5.1 Petrography

3.5.1.1 Texture

Eolian Cornberg Sandstones are deposited as decimeter thick, cross bedded dunes (Fig. 3.3 a), partly showing Liesegang rings in outcrops. On the plug scale, they show bed-size dependent grain-size variations from fine to medium sand (Fig. 3.3 b) (avg.: 0.32±0.2 mm, range: 0.24-0.48 mm) with well rounded and moderately well to very well sorting (Fig. 3.3 c, supplementary material II).

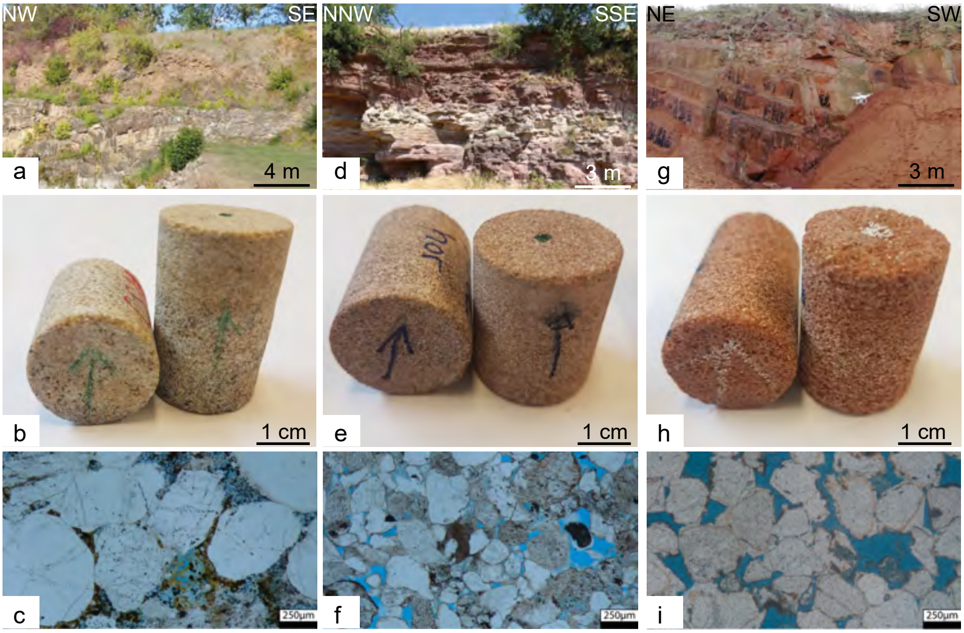

Figure 3.3. Overview over the studied sandstones by study location from meter scale (a, d, g) over cm scale (b, e, h) to µm scale (c, f, i), sorted in rows by location. Here, Cornberg Sandstone is shown in quarry A (images a-c, sample A_01 shown in c), Flechtingen Sandstone is shown in quarry C (images d-f, sample C_07 shown in f), and Penrith Sandstone is shown in quarry D (images g-I, sample D_01 shown in i).

Fluvio-eolian Flechtingen Sandstones are deposited as stacked fluvial channels, and eolian dunes intercalating with sheet sands (Fig. 3.3 d). Their bedding planes on the plug scale are not very clearly pronounced (Fig. 3.3 e), showing subrounded to rounded grains (Fig. 3.3 f). Their median grain size ranges from fine to medium sand, averaged to fine medium sand (avg.: 0.29±0.02 mm, range: 0.17-0.43 mm), and their sorting is moderately well to very well (supplementary material II).

Eolian Penrith Sandstones are very homogenous dune deposits, characterized by cross-bedded red sandstones on outcrop scale (Fig. 3.3 g) and pronounced cm-thick beds with seemingly repeating grain-size variations. On the plug scale, the bedding planes are barely recognizable due to homogeneity within one of the grain size classes (Fig. 3.3 h). The grain size ranges from fine medium sand to fine coarse sand, and averages to medium sand (avg.: 0.42±0.02 mm, range: 0.28-0.55 mm) (supplementary material II). The grains are subrounded (Fig. 3.3 i), and the sorting of the detrital grains is well to extremely well in quarries D and E, and moderately well in quarry F (supplementary material II).

3.5.1.2 Detrital composition

The sandstone classification results in three groups based on the three study areas (Fig. 3.4). Cornberg Sandstones are classified as quartzarenites to sublitharenites, Flechtingen Sandstones show a less mature composition of lithic arkoses, feldspathic litharenites and subarkoses, while Penrith Sandstones are similarly mature as Cornberg Sandstones, however showing a larger quantity of feldspars compared to rock fragments, resulting in the classification as quartzarenites to subarkoses (Fig. 3.4). There are no differences in compositions for samples originating from the same study area, but different quarries (Fig. 3.4).

The most abundant detrital mineral in all samples and study areas is detrital quartz (Fig. 3.5 a). The sum of monocrystalline (Fig. 3.5 a), polycrystalline (Fig. 3.5 b, d) and undulose detrital quartz ranges from 54.0 to 67.0 % in Cornberg Sandstones (avg.: 62.8±1.4 %), from 42.0 to 60.7 % in Flechtingen Sandstones (avg.: 51.7±1.3 %) and from 53.0 to 74.3 % in Penrith Sandstones (avg.: 62.0±1.4 %). Rock fragments (RF) were classified as metamorphic RF (Fig. 3.5 c, d) sedimentary RF (Fig. 3.5 e), volcanic RF (Fig. 3.5 f), plutonic RF, undifferentiated RF, and chert (Fig. 3.5 b). Rock fragments are the second most abundant detrital constituent in Cornberg Sandstones ranging from 4.7 to 8.7 % (avg.: 6.4±0.2 %), while rock fragments are the third most abundant detrital constituent in Flechtingen Sandstones ranging from 15.3 to 31.7 % (avg.: 20.3±1.1 %) and in Penrith Sandstones ranging from 1.0 to 4.3 % (avg.: 2.5±0.2 %) (supplementary material II). Potassium feldspars (Fig. 3.5 a) and plagioclases (Fig. 3.5 b) are the third most abundant detrital constituent in Cornberg Sandstones with a range of 2.0 to 4.7 % (avg.: 3.1±0.2 %), while feldspars are the second most abundant detrital constituent in Flechtingen Sandstones ranging from 15.7 to 27.0 % (avg.: 20.9±0.7 %) and Penrith Sandstones with a range of 4.0 to 12.0 % (avg.: 8.6±0.7 %). The fourth group of detrital constituents are the accessory minerals and matrix, including mica, zircon, and hornblende. Accessories were encountered consistently in Cornberg Sandstones (avg.: 1.1±0.1 %), while they are very rare in Flechtingen Sandstones (avg.: 0.5±0.2 %), and only found in traces in some Penrith Sandstone samples (avg.: 0.1±0.0 %).

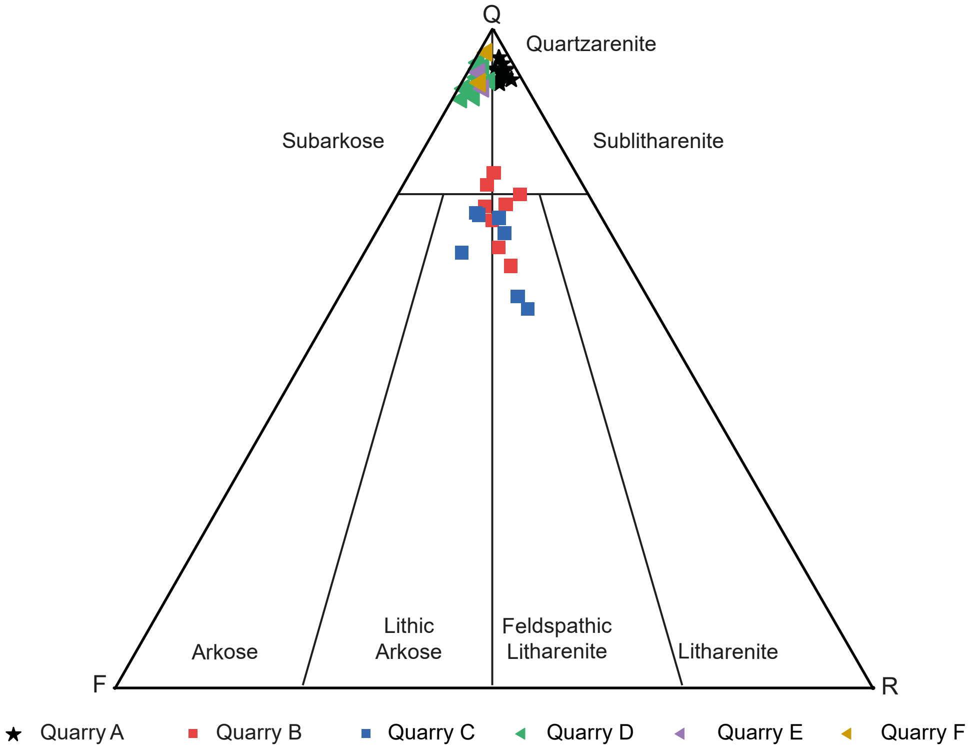

Figure 3.4. Ternary sandstone classification after Folk (1980). F: feldspar, Q: quartz, R: rock fragments. Quarries: A – Cornberg, B & C – Flechtingen, D to F – Penrith.

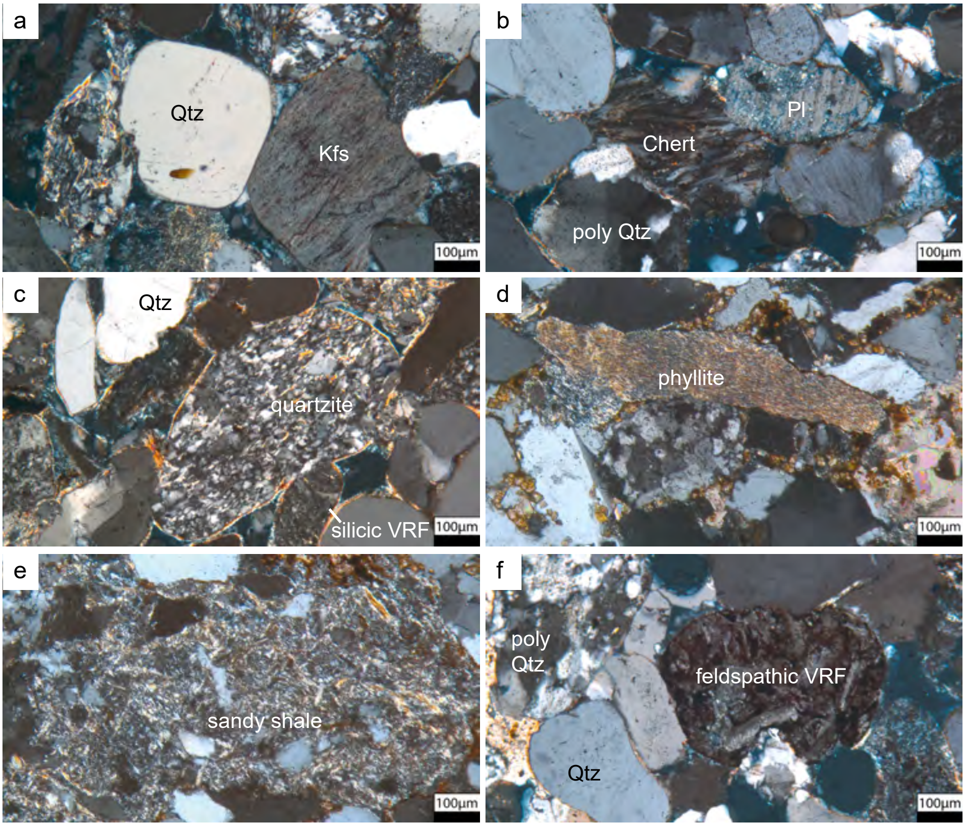

Figure 3.5. Thin-section images in cross-polarized light of detrital components encountered in the studied samples. Abbreviations: qtz – quartz, Kfs – potassium feldspar, Pl – Plagioclase, poly qtz – polycrystalline quartz, VRF – volcanic rock fragment. Samples shown here: C_07 (a, b), C_03 (c), A_03 (d, e), C_01 (f).

3.5.1.3 Authigenic composition

Cornberg Sandstones

The most abundant authigenic mineral in Cornberg Sandstones are quartz cements (avg.: 8.1±0.6 %) ranging from 6.0 to 11.3 %. The second most abundant authigenic minerals are carbonates, comprised of dolomite and siderite (avg. 5.8±1.4 %), showing a high sample variability in occurrence from 0.7 to 15.0 %. The third most common authigenic component is pore-filling illite (avg.: 5.7±1.1 %), ranging from 2.3 to 12.3 %. Additional authigenic phases include illite replacements of potassium feldspars (avg.: 2.6±0.4 %), iron hydroxides and oxides (avg.: 1.8±0.3 %), pore-filling kaolinite (avg.: 1.4±0.4 %), authigenic rutile (avg.: 1.3±0.3 %), dolomite replacements of potassium feldspar (avg.: 1.0±0.2 %), kaolinite replacements of potassium feldspar (avg.: 0.9±0.3 %), pore-lining illite (avg.:

0.7±0.2 %), and pore-lining iron oxides (avg.: 0.3±0.1 %). Illite replacements of potassium feldspar were encountered in traces (supplementary material II).

In Cornberg Sandstones, detrital grains are occasionally covered by tangential illitic grain coatings (Fig. 3.6 a). The detrital grains, which are predominately quartz, are commonly overgrown by syntaxial quartz cements (Fig. 3.6 a), and in contact with siderite, pore-filling illite (Fig. 3.6 a), and dolomite. Detrital grains show long to concavo-convex grain contacts (Fig. 3.5 d-e). Rhombohedral siderite was observed to overgrow quartz cements (Fig. 3.6 a), while dolomite encompassed several detrital grains directly in a patchy, poikilotopic texture maintaining floating to point contacts (Fig. 3.6 b). Pore-filling illite was observed to overgrow dolomite, siderite, and quartz cements (Fig. 3.6 a), also encompassing authigenic rutile (Fig. 3.6 c). Kaolinite was observed to overgrow quartz cements (Fig. 3.6 c). Amorphous iron hydroxides were observed in relatively large patches, overgrowing quartz and dolomite cements and clay mineral cements (Fig. 3.6 c). The majority of detrital feldspar was observed to have been replaced by illite (Fig. 3.6 d).

Flechtingen Sandstones

In Flechtingen Sandstones, quartz cements (avg.: 6.6±0.7 %) ranging from 4.0 to 15.7 % are the most common authigenic mineral. The second most abundant authigenic mineral is pore-lining-illite (avg. 5.0±0.5 %), showing sample variability in occurrence from 2.0 to 11.3 %. The third most common authigenic component are illite replacements of potassium feldspar (avg.: 1.5±0.2 %), ranging from 0.0 to 4.0 %. Additional authigenic phases include feldspar cements (avg.: 1.4±0.2 %), sample-specific occurring calcite (avg.: 1.2±0.5 %), pore-lining iron oxides (avg.: 0.8±0.1 %), iron hydroxides and oxides (avg.: 0.9±0.2 %) and pore-filling illite (avg.: 0.4±0.1 %). Calcite replacements of feldspars, pore-filling kaolinite, kaolinite replacements of feldspars, radial illite, barite and authigenic rutile were encountered in traces (supplementary material II).

Detrital grains in Flechtingen Sandstones are encased by illitic grain coatings, occasionally stained red by hematite (Fig. 3.6 e), mostly showing concavo-convex to sutured grain contacts (Fig. 3.5 b-c, f). Rarely, pigmented pore-lining iron oxide grain coatings occur instead of pore-lining illitic grain coatings. Iron oxide coatings show the same textural relationships as illite coatings with the exception of being directly overgrown by quartz cements. In absence of illite or iron oxide grain coatings or at sites with an incomplete grain coating coverage, detrital quartz grains are overgrown by euhedral quartz cements (Fig. 3.6 e). Calcite cements occur only in some samples as patchy poikilotopic phase, encompassing detrital grains independent of their composition maintaining floating to point contacts (Fig. 3.6 f). Detrital feldspars, if not encompassed by illite coatings, are overgrown by syntaxial feldspar cements (Fig. 3.6 g). Two feldspar cement phases can be identified based on textural relations; phase I encompasses the detrital feldspar, while phase II encompasses phase I feldspar cements (Fig. 3.6 g). A second calcite phase overgrowing quartz and feldspar overgrowth cements rarely occurs in individual samples (Fig. 3.6 h).

Penrith Sandstones

The most abundant authigenic mineral in Penrith Sandstones are quartz cements (avg.: 12.8±1.0 %) ranging from 5.0 to 19.3 %. The second most abundant authigenic mineral is pore-lining illite (avg. 1.7±0.2 %), ranging from 0.7 to 3.7 %. The third most common authigenic component are pore-lining iron oxides (avg.: 0.7±0.1 %), ranging from 0.0 to 2.0 %. Additional authigenic phases include illite replacements of potassium feldspars (avg.: 0.5±0.1 %), pore-filling iron hydroxides and oxides (avg.: 0.4±0.1 %), pore-filling illite (avg.: 0.3±0.2 %), and authigenic rutile (avg.: 0.3±0.1 %). Kaolinite replacements of feldspar, pore-filling kaolinite, feldspar cements, and illite replacements of kaolinite were encountered in traces (supplementary material II).

The detrital grains of Penrith Sandstones are mostly encompassed by iron oxide grain coatings (Fig. 3.6 i) or pore-lining illitic grain coatings (Fig. 3.6 j). Grain contacts range from floating to point contacts (Fig. 3.3 i) to point to long contacts (Fig. 3.5 i). Similar to the Flechtingen Sandstones, detrital quartz coated in pigmented iron oxides are overgrown by quartz cements, which have reached or are approaching euhedral form (Fig. 3.6 i, j), while continuous illitic grain coatings inhibited quartz cementation (Fig. 3.6 j). Rhombohedral husks in quartz cements can be encountered occasionally (Fig. 3.6 i), which hint the occurrence of a cement phase, that has been dissolved and now occurs as porosity.

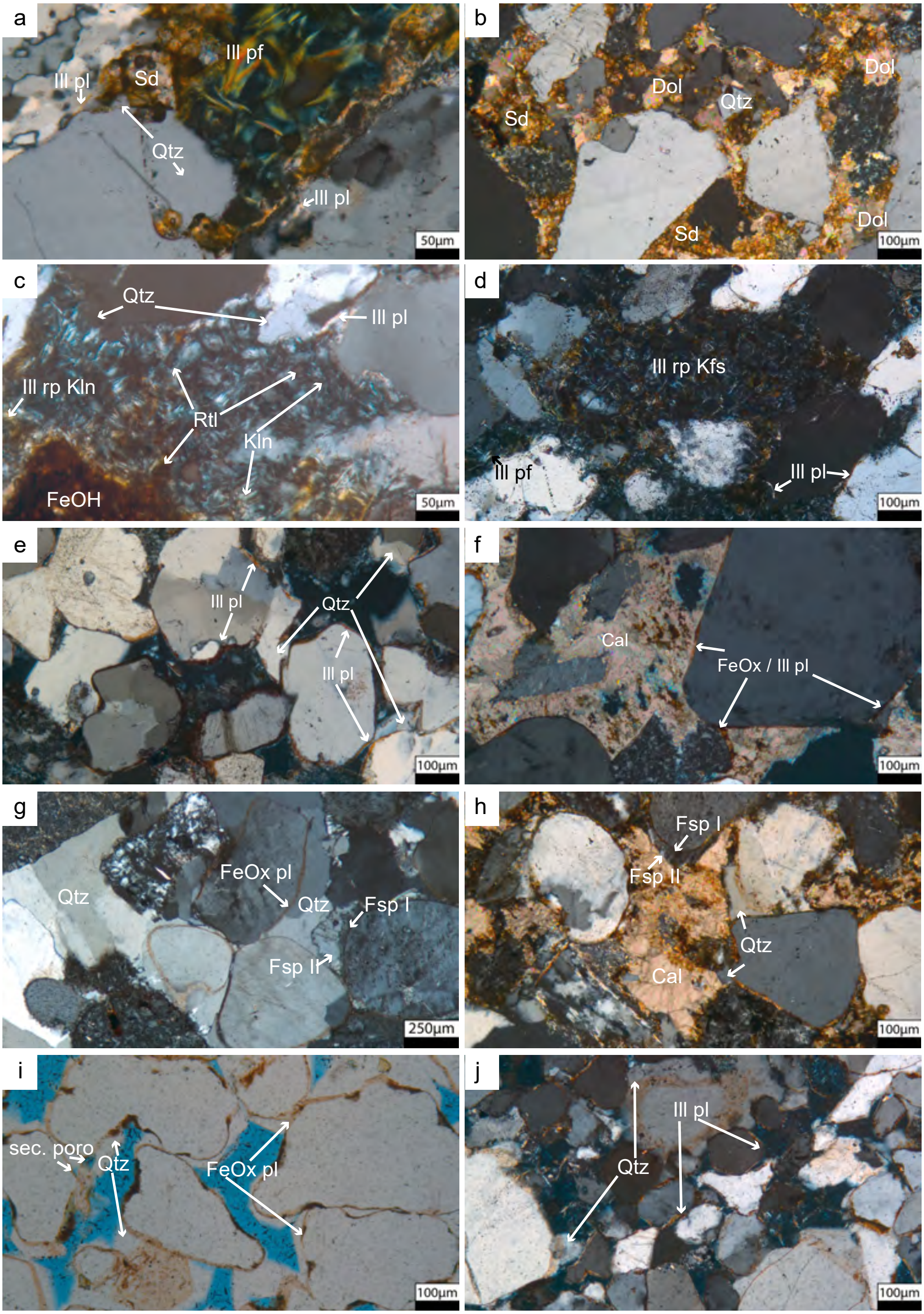

Figure 3.6. Figure caption on the next page.

Figure 3.6. Thin-section images under cross-polarized light (xpl, images a-h, j) and plain-polarized light (ppl, image i) of authigenic minerals encountered in the study areas. Porosity is colored in blue in ppl images and very dark blue in xpl images. a-d: Cornberg Sandstones, e-h: Flechtingen Sandstones, i-j: Penrith Sandstones. Abbreviations: pl – pore-lining, pf – pore filing, Sd - siderite Qtz – quartz, Dol – dolomite, FeOH – iron hydroxides, Rtl – rutile, Kln – kaolinite, Cal – calcite, Fsp – feldspar, FeOx – iron oxides, Dol por – secondary porosity due to dolomite dissolution. Samples shown here: A_01 (a), A_03 (b), A_02 (c, d), C_01 (e, f), C_07 (g), C_10 (h), D_01 (i), F_01 (j).

Optical porosity

Optical porosities are generally lowest in Cornberg Sandstones (Fig. 3.3 c, avg.: 1.5 %), and highest in Penrith Sandstones (Fig. 3.3 i, avg.: 15.1 %), while Flechtingen Sandstones show lower to intermediate optical porosities (Fig. 3.3 f, avg.: 4.8 %). Intergranular porosity is the largest contributor to optical porosity in all study areas, however with different relative fractions; roughly 90 % of optical porosities in Penrith Sandstones are due to intergranular porosities (supplementary material II). In Cornberg Sandstones, intergranular porosities account for roughly 75 % of all optical porosity, while intergranular porosity in Flechtingen Sandstones contributes only about 60 % to optical porosity (supplementary material II). The remainder of optical porosity is due to isolated intragranular or intracrystalline porosity (Fig. 3.5 b, Fig. 3.6 i) in altered feldspars, rock fragments or dissolved cement phases.

Compaction

Cornberg Sandstones experienced a nearly complete loss of their initial porosity due to intense pore-filling cementation, and compaction, with compaction being the slightly more important factor (Fig. 3.7 a). Flechtingen Sandstones show a compaction induced porosity loss leading to a porosity reduction of about 5 % (Fig. 3.7 a), with quarries B and C showing a comparable range of values. Porosity loss in Penrith Sandstone was least severe and was slightly dominated by compactional porosity loss (Fig. 3.7 a). Quarry F seems to be an exception for Penrith Sandstones, showing higher compaction and less porosity (Fig. 3.7 a). These results are also reflected in the Houseknecht diagram, showing almost all of the IGV in Cornberg Sandstones being occupied by cement, generally smaller IGVs in Flechtingen Sandstones with lower cement volumes and higher porosities than in Cornberg Sandstones, and highest IGVs and porosities in Penrith Sandstones (Fig. 3.7 b).

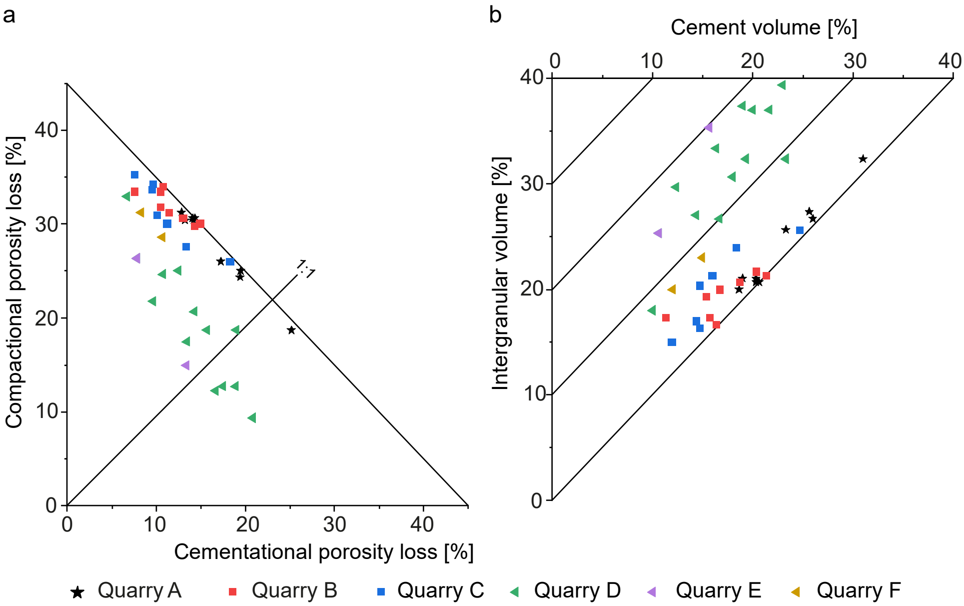

Figure 3.7. a) Porosity loss diagram after Lundegard (1992), illustrating the relative amount of relative porosity caused by cementation (abscissa) and compaction (ordinate). The data shows no clear distinction for the porosity loss process by study area. Almost no porosity was preserved in Cornberg Sandstones, intermediate amounts of porosity was preserved in Flechtingen Sandstones, and highest amounts of porosity were preserved in Penrith Sandstones. b) Houseknecht diagram (Houseknecht, 1987), plotting the cement volume on the abscissa versus the intergranular volume (IGV, as defined by Paxton et al. (2002)) on the ordinate. Cornberg Sandstones show high IGV and high cements, and low porosity, Flechtingen Sandstones show less IGV, less cements and slightly higher porosity, and Penrith Sandstones show highest IGVs and intermediate cement volumes with highest porosities. Quarries: A – Cornberg, B & C – Flechtingen, D to F – Penrith.

Grain coatings

The dominant grain-coating phase in the studied sandstones is illite (Fig. 3.6 a, f, j, supplementary material II). Generally, Cornberg Sandstones show the lowest grain-to-IGV (GTI) coating coverage of illite (avg.: 24.0±2.6 %), followed by Penrith Sandstones, (avg.: 28.3±3.3 %) while Flechtingen Sandstones show largest average GTI coating coverage (avg.: 54.3±3.6 %) (Fig. 3.8 a, supplementary material II). Samples with higher GTI coating coverages show less authigenic quartz, while samples with less GTI coating coverage show larger amounts of quartz cements (Fig. 3.8 a). This negative correlation (R^2=0.55) seems to be more clearly demonstrated in Penrith and Flechtingen Sandstones than in Cornberg Sandstones (Fig. 3.8 a). Quarry F shows higher GTI coating coverages than the other Penrith Sandstone samples (Fig. 3.8 a). The grain-to-grain (GTG) coating coverage is highest in Flechtingen Sandstones (avg.: 35.9±2.4 %) and lowest in Penrith Sandstones (avg.:

15.5±1.7 %) (Fig. 3.8 b). Higher amounts of GTG coatings coincide with generally lower intergranular volumes (R²=0.56, Fig. 3.8 b).

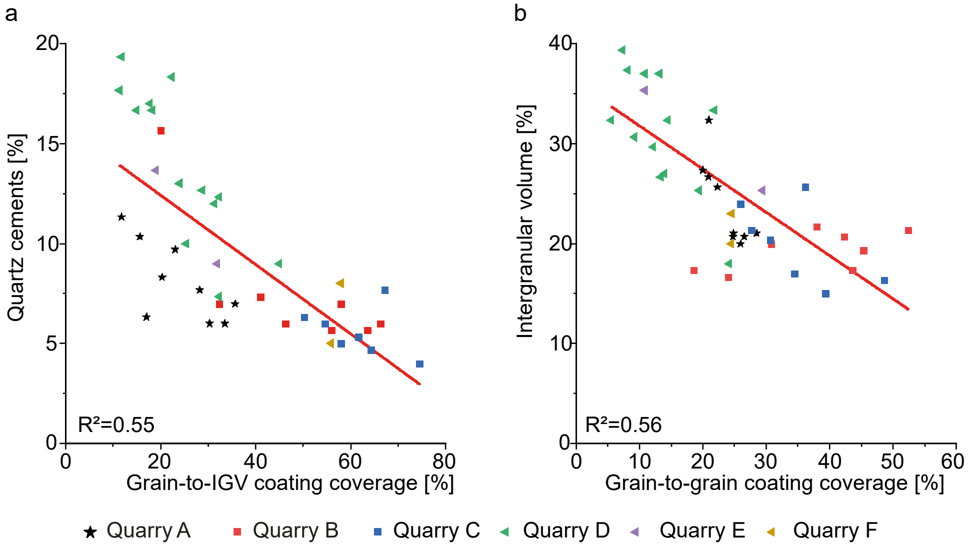

Figure 3.8. Grain-to-IGV (GTI) coating coverage on the abscissa versus quartz cements on the ordinate. Flechtingen Sandstones show highest GTI coating coverage and lowest quartz cements, while Penrith Sandstones show lowest GTI coating coverage, but the highest amount of quartz cements. Cornberg Sandstones show intermediate quartz cements and GTI coating coverage. b) Grain-to-grain (GTG) coating coverage on the abscissa versus intergranular volume (IGV). Flechtingen Sandstones show highest GTG coatings and lowest IGVs, Cornberg Sandstones show intermediate GTG coatings and IGVs, and Penrith Sandstones show lowest GTG coatings but highest IGVs. Quarries: A – Cornberg, B & C – Flechtingen, D to F – Penrith.

3.5.2 Petrophysics

Helium porosity ranges from 3.9 to 36.2 % (avg.: 19.3 %) for all samples, while permeability of all samples ranges from 0.002 to >10000 mD (avg.: 2155 mD) (Fig. 3.9, supplementary material II). Separated by study area, Cornberg and Flechtingen Sandstones show comparable average porosities of 14.4 % (range: 9.1 to 19.9 %), respectively 14.3 % (range: 7.7 to 21.3 %), while Penrith Sandstones show highest average porosities of 26.4 % (range: 19.6 to 36.2 %) (Fig. 3.9). Permeabilities of Cornberg Sandstones are lowest (avg.: 0.52 mD, range: 0.002 to 8.6 mD), Flechtingen Sandstones have intermediate permeabilities (avg.: 27.9 mD, range: 0.03 to 190 mD), and Penrith Sandstones have very high permeabilities (avg.: 5192 mD, range: 48 to >10000 mD) (Fig. 3.9 a). Generally, higher helium porosity correlates with higher permeability (Fig. 3.9 a). Outliers from this correlation are Cornberg Sandstones and samples with permeabilities above 10000 mD (Fig. 3.9 a).

Grouped by studied quarry, an apparently different porosity-permeability relationship from quarry B to quarry C in Flechtingen Sandstones is identified (Fig. 3.9 a). Sandstones in quarry B show comparable permeabilities to sandstones in quarry C, although their porosities are 6 to 8 % lower (Fig. 3.9 a). The porosity-permeability relationship in quarries D-F follows the same gradient, however quarry E represents only the higher range of observed values and quarry F only the lower range, while quarry D shows the whole range of measured porosity and permeability data in Penrith Sandstones (Fig. 3.9 a). The depositional system does not exhibit a consistent control on porosity and permeability of the studied sandstones (Fig. 3.9 b). Both the highest and lowest porosities and permeabilities were measured in dune sandstones, with permeabilities ranging from 0.002 to >10000 mD and helium porosities ranging from 9 to 39 % (Fig. 3.9 b). Fluvial sandstones, encountered only in quarry C, range from 0.03 to 100 mD in permeability and 8 to 22 % in porosity (Fig. 3.9 b). Sheet sands show the narrowest permeability range and porosity range from 0.05 to 4 mD and 7 to 12 %, however they were also the least abundant depositional system (n=5, Fig. 3.9 b).

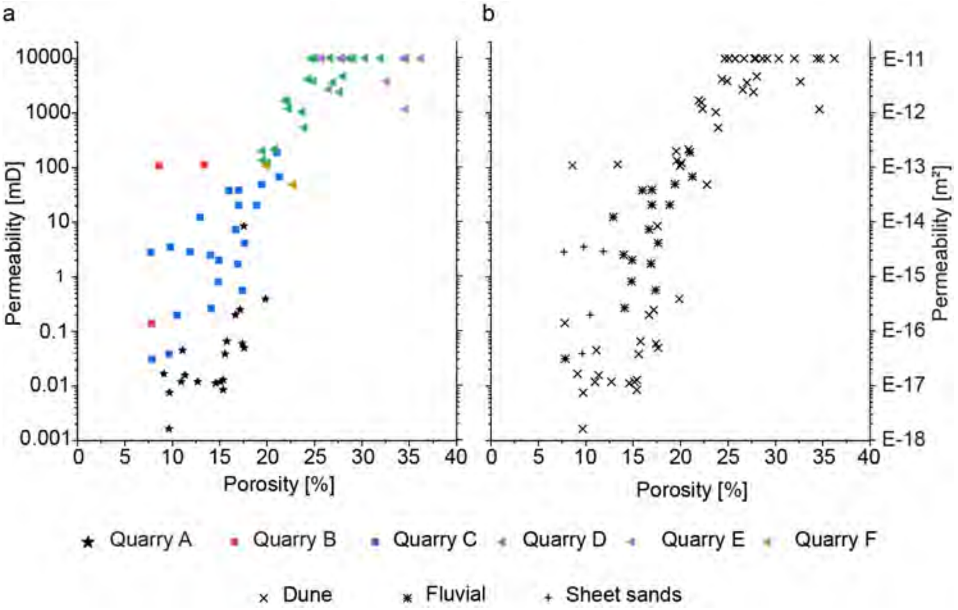

Figure 3.9. Porosity determined by helium pycnometry (abscissa) versus Klinkenberg-corrected air permeability at 1.2 MPa confining pressure (ordinate) plotted on logarithmic scaling. The upper measurement limit of the permeability cell is 10000 mD (=9.869e^{-12} m²). Cornberg Sandstones show lowest porosities and permeabilities, Flechtingen Sandstones show intermediate porosities and permeabilities, and Penrith Sandstones show highest porosities and permeabilities. Helium porosity (abscissa) and permeability (ordinate) categorized by quarry (a) and by depositional system (b).

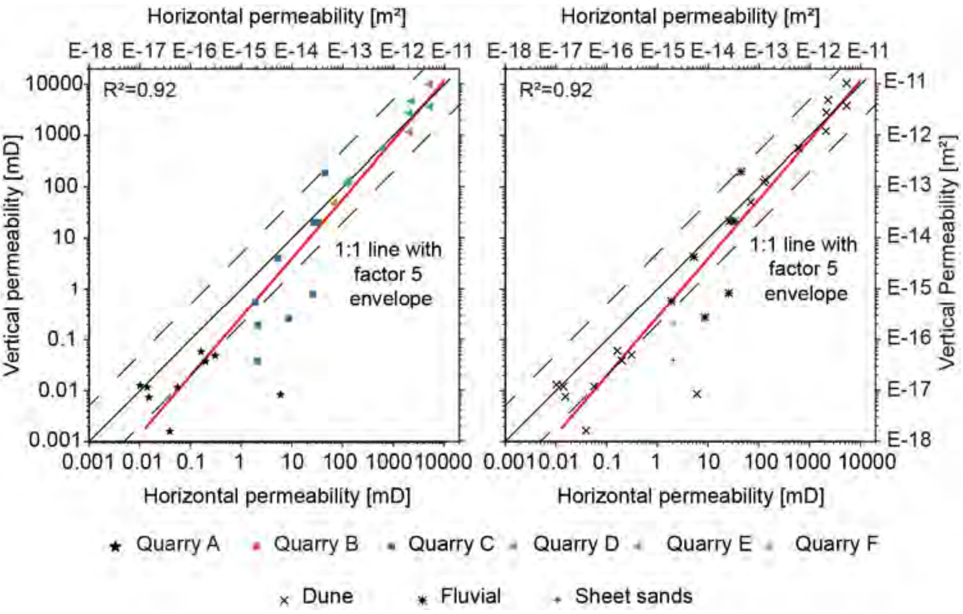

Figure 3.10. Klinkenberg-corrected permeability measured on plugs drilled parallel to bedding (abscissa) versus the corresponding plugs drilled normal to bedding (ordinate). Both axes are plotted in logarithmic scale. The red line shows a logarithmic correlation (R²=0.92). The black line is a 1:1 line encompassed by a dotted factor 5 and divisor 5 envelope of the 1:1 line, demonstrating larger permeability differences from horizontal to vertical measurements in less permeable samples. Quarries: A – Cornberg, B & C – Flechtingen, D to F – Penrith.

Permeabilities of plugs drilled parallel to bedding are almost exclusively higher than vertical permeabilities (Fig. 3.10). The offset between the permeability difference is smaller for higher permeabilities. Plugs with horizontal permeabilities above 100 mD consistently show a reduction in vertical permeability of less than a factor of 5 (Fig. 3.10). If horizontal permeabilities are below 100 mD, vertical permeabilities are reduced by a factor of 5 or larger (Fig. 3.10).

3.5.3 Influence of petrographic parameters on petrophysical parameters

Grain size and sorting

The effect of detrital grain size on permeability and helium porosity is indistinct when considering all data points, with grain sizes around 0.3 to 0.4 mm showing permeabilities ranging from 0.01 to over 1000 mD and helium porosities ranging from below 10 to 25 % (Fig. 3.11 a). Considering the study areas individually, Cornberg Sandstones show larger grain sizes of 0.3 to 0.4 mm in less porous (<15 % He porosity) and less permeable

(<0.1 mD) samples, while grain sizes of 0.2 to 0.3 mm coincide with helium porosities above 15 % and permeabilities above 0.1 mD (Fig. 3.11 a). Flechtingen Sandstones show no correlation between grain size and porosity or permeability (Fig. 3.11 a). Larger grain sizes in Penrith Sandstones above 0.5 mm coincide with permeabilities above 10000 mD and porosities around 30 %, however smaller grain sizes also feature comparably permeable samples up to 10000 mD (Fig. 3.11 a). The permeability and porosity range in Penrith Sandstones around or below 1000 mD and 25 % is exclusively showing grain sizes below 0.4 mm (Fig. 3.11 a).

Better sorted sandstones seem to show a tendency towards higher porosities and permeabilities (Fig. 3.11 b). This relationship is clearest in Penrith Sandstones, where better sorting of 1.3 or below results in permeabilities of at least 1000 mD, while all samples below 1000 mD show sorting around 1.4 or higher (Fig. 3.11 b). The effect of sorting in Cornberg Sandstones on permeability and porosity is indistinct, as there is only one data point with slightly worse than average sorting in the lower permeability ranges (Fig. 3.11 b). Flechtingen Sandstones show no consistent correlation between sorting and permeability or porosity (Fig. 3.11 b).

Optical porosity, IGV and compaction

Optical porosity shows a positive correlation with permeability and helium porosity (Fig. 3.11 c). In all samples, optical porosity is much lower than helium porosity. This contrast is particularly obvious in Cornberg Sandstones with optical porosities as low as 10 % of their corresponding helium porosity, while optical porosities in Flechtingen Sandstones amount to approximately 30 % of helium porosity, whereas optical porosities in Penrith Sandstones are approximately 50 % of helium porosity (Fig. 3.11 c). Flechtingen Sandstones and Cornberg Sandstones show similar helium porosity, but Flechtingen Sandstones show higher optical porosity, also showing a consistent trend with the less porous samples of Penrith Sandstones, which have the highest optical porosity (Fig. 3.11 c).

Intergranular volume (IGV) shows no correlation with neither permeability nor helium porosity (Fig. 3.11 d). IGV has no distinct relation to helium porosity or permeability in Cornberg and Flechtingen Sandstones. Most of the lowest IGVs in Penrith Sandstones occur in the least porous and least permeable samples, however there are also samples with permeabilities around 10000 mD with similarly low IGVs for Penrith Sandstones (Fig. 3.11 d). The compactional index shows no consistent correlation regarding porosity or permeability, neither for all samples nor study area-based (Fig. 3.11 e).

Clay mineral coatings

Illitic grain-to-IGV (GTI) coatings show no correlation to helium porosity or permeability (Fig. 3.11 f). There are no clear correlations visible within the Cornberg and Flechtingen Sandstones either, however GTI coatings coverage seems to be generally higher in less permeable and less porous samples of Penrith Sandstones, barring one outlier (Fig. 3.11 f). Illitic grain-to-grain (GTG) coatings are the least abundant in highly permeable and porous samples (Fig. 3.11 g). Cornberg Sandstones show a slight increase in the abundance of GTG coatings towards less permeable and less porous specimen (Fig. 3.11 g). This trend cannot be observed in Flechtingen Sandstones, where no correlation between GTG coatings and permeability or porosity is apparent (Fig. 3.11 g). Penrith Sandstones show no correlation either, however lowest GTG coatings are often coinciding with higher permeabilities and porosity specimen (Fig. 3.11 g).

Cements and clay microporosity

Considering all data points, samples with higher abundances in quartz cement show higher permeability and helium porosity (Fig. 3.11 h). In Cornberg Sandstones, this trend cannot be observed. Instead, the specimen with the highest amount of quartz cement show among the lowest permeabilities and porosities (Fig. 3.11 h). Flechtingen Sandstones show no correlation between quartz cements and permeability or porosity (Fig. 3.11 h), while the highly porous and permeable specimen in Penrith Sandstones show a tendency towards higher quartz cements abundance (Fig. 3.11 h).

Carbonate cements only occur in a limited number of samples, mostly within Cornberg Sandstones and some Flechtingen Sandstones, which show lower permeabilities and porosities than the samples with less or no carbonate cements (Fig. 3.11 i).

The abundance of all clay minerals (sum of all authigenic clay minerals, clay mineral replacements, detrital matrix, and shale rock fragments) shows a negative correlation with permeability and helium porosity over the whole population (Fig. 3.11 j), being lowest in the most permeable/porous specimen. Study-area based however, there is no distinguishable trend (Fig. 3.11 j). The impact on permeability and porosity is clearer when clays and carbonate cements are considered together (Fig. 3.11 k).

Microporosity was calculated based on the point-counted amount of all clay minerals. As these are of predominately illitic composition (supplementary material II), a microporosity of illite of 60 % (Hurst & Nadeau, 1995) was used to quantify the total amount of microporosity in clays and their impact on permeability and helium porosity (Fig. 3.11 l). Microporosities are lower in higher permeable and more porous samples (Fig. 3.11 l), and vice-versa. There are no clear correlations within the individual populations of Cornberg, Flechtingen or Penrith Sandstones (Fig. 3.11 l).

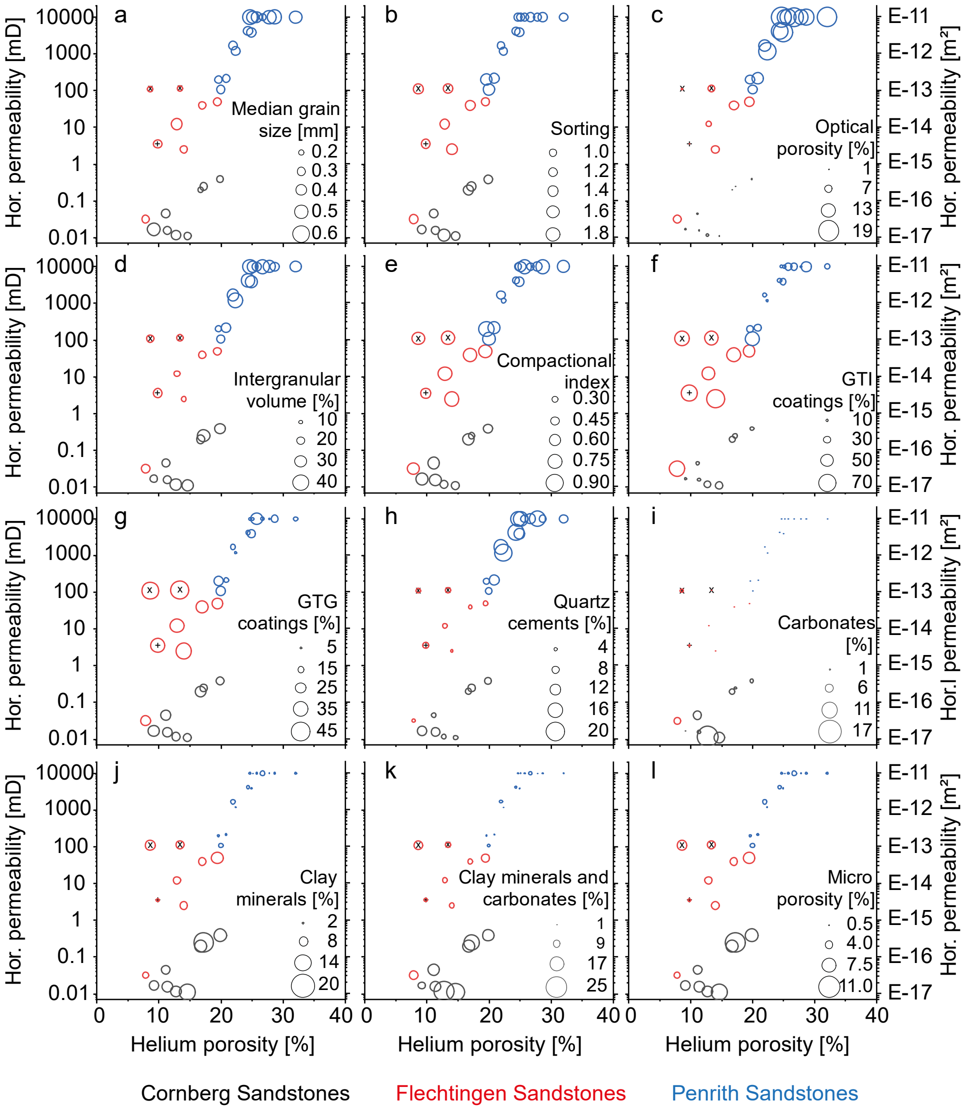

Figure 3.11. Matrix-scatter plotter with helium porosity on the abscissa and horizontal permeability on the ordinate in log-scale. Each diagram is labeled a) to l) in its upper left corner. Bubble sizes indicate a variable specific to the respective diagram in relation to the porosity and permeability. The variable is given with scale bar in the lower right of the respective diagram. Color coding refers to the three study areas. Three specific Flechtingen Sandstone specimen were indicated with an x (dune) or + (sheet sands), while fluvial Flechtingen Sandstones have not been marked. Abbreviations: GTG – grain-to-grain, GTI – grain-to-IGV, IGV – intergranular volume.

3.6 Discussion

3.6.1 Paragenesis

3.6.1.1 Early diagenesis

Mechanical compaction

Mechanical compaction commenced after initial deposition due to burial. Due to ongoing consolidation, both by compaction and cementation, the effect on porosity reduction by mechanical compaction in clean sandstones typically begins to approach equilibrium at burial depths exceeding 2 km (Paxton et al., 2002).

Clay mineral and iron oxide grain coatings

Tangential clay mineral or iron oxide grain coatings have been encountered in all three study areas (Fig. 3.6 a, f, i, j), encompassing detrital grains and present at grain contacts, thus predating any other authigenic mineral. Pigmented and continuous iron oxides coatings (Fig. 3.6 i) are interpreted to be formed by sediment reddening, sourced by weathering of iron-bearing minerals e.g. biotite and hornblende (Walker & Honea, 1969). Grain coatings are a well described occurrence in arid fluvio-eolian depositional environments (Esch et al., 2008; van Houten, 1973), and have been previously related to be formed by clay infiltration (Matlack et al., 1989; Molenaar & Felder, 2018), as well as surface and soil formation processes (Walker & Honea, 1969). Grain coatings are apparently not linked to the depositional environment in arid continental systems (Busch, 2020; Busch et al., 2020), while the distribution of grain coatings can be correlated to depositional environments in modern estuarine sediments (Woolridge et al., 2017). Grain coatings are shown as inferred smectite coatings in Fig. 3.12, which serve as precursors for tangential illite coatings in arid Rotliegend sandstone systems (Molenaar & Felder, 2018). The varying distribution of clay mineral grain coatings in Penrith Sandstones could be caused by clay abrasion caused by grain migration (Ajdukiewicz et al., 2010), where only the smaller grains were able to retain their clay coats, which would be in agreement with our observation, showing preserved clay coatings primarily on smaller grains (Fig. 3.6 j). A further potential control on grain coatings might be the climate due to an increasing/decreasing amounts of humidity (Mader & Yardley, 1985).

Feldspar dissolution

As feldspars are not stable under pH conditions encountered in meteoric waters (Lanson et al., 2002; Yuan et al., 2015), dissolution processes leading to the formation of secondary feldspar porosity (Fig. 3.5 b) may have started pre-deposition already, and likely commenced throughout early diagenesis until the influence of meteoric waters seized during burial diagenesis.

Kaolinite

As kaolinite was illitized in some samples from Cornberg and Penrith Sandstones (Fig. 3.6 c) it must have formed prior to illitization in these samples, likely during early diagenesis as described also by Becker et al. (2017). Early diagenetic processes include the dissolution of feldspar and subsequent formation of kaolinite (Ketzer et al., 2003; Lanson et al., 2002) in the presence of undersaturated meteoric waters (Lanson et al., 2002). Kaolinite formed during early diagenesis is replaced during subsequent burial by kaolinite/dickite assemblages, and can form illite in geochemically open system if a K^+ source is available (Berger et al., 1997; Lanson et al., 2002).

Carbonate cements

Calcite cements in Flechtingen Sandstones are showing poikilotopic textures encasing grains with floating to point grain contacts (Fig. 3.6 f), indicating early diagenetic cementation prior to significant mechanical compaction (Morad, 1998; Walderhaug, 1990), likely formed during an evaporative stage typical for arid fluvio-eolian systems (Morad, 1998). Similar poikilotopic textures of dolomite with floating to point grain contacts can be observed in Cornberg Sandstones (Fig. 3.6 b) and may be related to marine ingressions (Morad, 1998; Vincent et al., 2018), for instance the Zechstein Sea ingression in the late Permian (Legler & Schneider, 2008; Stollhofen et al., 2008).

3.6.1.2 Burial diagenesis

Illitization of clays and feldspars, and feldspar replacements

As illitic grain coatings are present at grain contacts, they, or a precursor mineral phase, must have been present prior to mechanical compaction. The recrystallization of tangential illite was also inferred from K/Ar dating of illite in other Rotliegend deposits (Liewig & Clauer, 2000) supporting the burial diagenetic recrystallization or replacement of a precursor clay mineral grain coating. For other Rotliegend deposits in northern Germany, Busch et al. (2020) derived a smectitic-chloritic clay mineral grain coating phase, interpreted to form via the recrystallization of a smectitic precursor phase. However, illitic and illite/smectite mixed layer clays as grain coatings have also been reported as a detrital to eodiagenetic component in active eolian depositional systems (Busch, 2020).

Two phases of feldspar cements were observed in Flechtingen Sandstones: a potassium feldspar cement (Fsp I) encompassing detrital feldspar grains, and an albite cement (Fsp II) encompassing Fsp I (Fig. 3.6 g). Albite was also observed to partially replace detrital feldspars (Fig. 3.6 g) in Flechtingen Sandstones. Additionally, feldspars were replaced by illite, which was encountered in all study areas (Fig. 3.6 d). The two feldspar overgrowth generations are in agreement with results of Fischer et al. (2012). Also considering feldspar cement ages in Flechtingen Sandstones determined by earlier studies (Fischer et al., 2012) as well as textural relations (Fig. 3.6 g), we interpret feldspar cementation to be related to burial diagenetic processes pre to syn-dating quartz cementation.

Illite was observed to replace early diagenetic kaolinite in minor quantities (Fig. 3.6 c) in Cornberg Sandstones. Partial illitization of kaolinite has been reported in previous studies on samples origination from below the Kupferschiefer and elsewhere (Becker et al., 2017; Ehrenberg & Nadeau, 1989; Lanson et al., 2002). A limited source of K^+ driving the reaction to form illite from kaolinite constrained by reaction kinetics and the K^+/H ratio was identified as control on illitization in previous studies (Huang et al., 1993). Based on the kinetic constraints illustrated by Lander and Bonnell (2010), we interpret the partial illitization of early diagenetic kaolinite to be due to a very limited K^+ supply. Previous studies on the timing of illite replacements and cements in the Northern German Basin suggest a wide time-range from 210 to 140 Ma (Liewig & Clauer, 2000; Ziegler, 2006; Zwingmann et al., 1998), however they all relate feldspar overgrowths and illitization to burial diagenetic processes (Ziegler, 2006). A paragenetic interpretation of feldspar cements based on textural relations only is not straight-forward due to small volumes of feldspar cements. Based on textural evidence, Fsp II must have formed after Fsp I, and also in temperature settings likely exceeding 145° C based on dissolution kinetics of feldspars compared to albite growth rates (Aagaard et al., 1990). Illite in parts of the Northern German Basin was interpreted to be associated with Carboniferous fluids, driving feldspar dissolution and subsequent illitization (Gaupp et al., 1993). Two major phases of illite were reported in the Northern German Basin and Dutch Basin dated to 200-180 Ma and around 90 Ma (Gaupp et al., 1993; Gaupp & Okkerman, 2011), which coincide with the opening of the Atlantic ocean and the Late Cretaceous basin inversion (Kley & Voigt, 2008; Ziegler, 1990). The tectonic activity was interpreted to have enabled the reactivation of old Permo-Carboniferous fault systems, on which acidic fluids were able to circulate (Gaupp et al., 1993). We interpret feldspar cementation and replacements as well as illitization of kaolinite to be possible throughout the entire burial diagenesis, however likely prevalent in an early phase (Fsp I) and a later phase (Fsp II) (Fig. 3.12), which could be linked to increased fluid migration during Early Jurassic Atlantic opening.

Quartz cements

The formation of quartz cements generally requires temperature exceeding 75-80° C (Walderhaug, 1994). Assuming a geothermal gradient of 35° C/km, this would result in minimum burial depths of 2 km. Possible early diagenetic silica cement may have formed in an arid depositional system (Folk & Pittman, 1971) and has been interpreted to be present as poikilotopic textures in Flechtingen Sandstone samples by Fischer et al. (2012). However, these poikilotopic quartz cements are frequently observed to encase both phases of feldspar cement (Fig. 3.6 g), which in turn are related to burial diagenesis. Thus, a burial diagenetic origin of quartz cements based on textural relations is favored. Although it contradicts other interpretations in the same study area (Fischer et al., 2012; Heidsiek et al., 2020), it is in accordance with observed petrographic textures from different outcrops (Fig. 3.1c, 3.6g).

Early diagenetic chalcedony cementation was proposed by (Waugh, 1970b). In their model, siliceous dust was remobilized by highly alkaline evaporitic groundwaters, and finally recrystallized to quartz during burial diagenesis. However, cathodoluminescence studies show at least two discrete growth events and no petrographic evidence for recrystallization, implying the primary origin of the quartz cements (Turner et al., 1995). Furthermore, fluid-inclusion data suggest a precipitation temperature of at least 95° C for quartz cements in Penrith Sandstones (Turner et al., 1995). Quartz cementation is dependent on silica availability, which can be sourced by the autochthonous illitization of smectite (Lanson et al., 2002), from dissolution seams (Walderhaug & Bjørkum, 2003) or allochthonous hydrothermal fluid circulation (Gaupp et al., 1993) during burial. Silica in Cornberg Sandstones is interpreted to be mainly sourced by the autochthonous illitization of smectite (Lanson et al., 2002) due to large amount of illite and feldspars replacements (Fig. 3.6 a, c-d). The silica origin of the Northern German Basin Rotliegend and potentially also Flechtingen Sandstones might be related to hydrothermal fluid circulation (Gaupp et al., 1993) in addition to autochthonous processes.

Due to the small abundance of feldspars in Penrith Sandstones, an allochthonous source for silica for the abundant quartz cements is implied. Turner et al. (1995) discussed the underlying Carboniferous shales to be a minor contributor via pressure dissolution of silt-sized quartz in mudstones (Milliken, 1992). Quartz cementation is more easily facilitated on a quartz grain or rock fragment containing quartz, as a result reduced substrate areas by clay coatings result in reduced abundance of quartz cements (Ajdukiewicz & Larese, 2012; Busch et al., 2017; Monsees et al., 2020a; Pittman et al., 1992). Grain sizes and mono- or polycrystallinity of quartz substrates also affect overgrowth cement volumes (Lander et al., 2008; Waugh, 1970a). Smaller volumes of syntaxial overgrowth cements are formed on smaller grains as opposed to coarser grains, when subject to the same conditions during diagenesis (Lander et al., 2008; Prajapati et al., 2018). Monocrystalline grains form larger volumes of syntaxial quartz cement as opposed to polycrystalline grains of the same size when subject to the same conditions during burial (Lander et al., 2008). Growth rates of quartz cements are also increasing with grain size (Lander et al., 2008; Prajapati et al., 2020; Walderhaug et al., 2000), and are significantly higher prior to reaching euhedral shape, and significantly lower after the euhedral shape was reached (Lander et al., 2008; Prajapati et al., 2020). This is reflected by Penrith Sandstone samples showing the largest volumes of quartz cements and lowest GTI coating coverages, while Cornberg and Flechtingen Sandstones show smaller quartz cement volumes (Fig. 3.8 b). However, illite GTI coatings in Cornberg Sandstones are almost as low as in Penrith Sandstones.

Additionally, the occurrence and preservation of early diagenetic carbonates in Cornberg Sandstones is interpreted to have reduced the reactive surface area of quartz grains, resulting in smaller substrate area. The smaller grain sizes in Flechtingen and Cornberg Sandstones therefore are interpreted to be an additional controlling factor resulting in smaller quartz cement abundances. As a result, silica provided by the illitization of feldspar, smectite and kaolinite (McKinley et al., 1999), potentially enhanced by hydrothermal fluids enriched in silica (Gaupp et al., 1993) in conjunction with silica mobilized by quartz dissolution during chemical compaction (Kristiansen et al., 2011), are interpreted to be responsible for in-situ formation of quartz cements throughout burial diagenesis (Fig. 3.12).

Carbonate cements

As siderites in Cornberg Sandstones are partly overgrowing quartz cements (Fig. 3.6 a, b), they are interpreted to be syn- to postdating quartz precipitation (Fig. 3.12). Similarly, the rare second calcite phase in Flechtingen Sandstones was observed to overgrow both quartz and feldspar cements (Fig. 3.6 h), and is therefore interpreted to postdate quartz and feldspar cementation (Fig. 3.12). Quartz solubility increases under alkaline conditions (Knauss & Wolery, 1988), while carbonate solubility generally increases under acidic conditions (Morad, 1998). The contemporaneous formation of quartz and siderite would be geochemically plausible under relatively neutral pH systems. Burial diagenetic siderite in the Dutch part of the Southern Permian Basin has been discussed to be linked to a shift in fluid chemistry to a predominately alkaline pH during Jurassic-Cretaceous uplift (Gaupp & Okkerman, 2011).

Pore-filling illite

Due to the overgrowth of pore-filling illite on siderite and all previously discussed cement phases in Cornberg Sandstones, they are interpreted to have formed after the burial diagenetic siderites in Cornberg Sandstones, respectively quartz cements in Flechtingen and Penrith Sandstones (Fig. 3.12). The formation of illite is generally favored in acidic pH conditions (Gaupp et al., 1993; Gaupp & Okkerman, 2011), and dependent on the process of formation, temperatures ranging from 70 to 140° C (Worden & Morad, 2003). Pore-filing illite in Cornberg Sandstones being more abundant than in the other study areas is interpreted due to the close proximity to fault zones (Motzka-Nöring et al., 1987), which has been identified to be the main driver of pore-filling meshwork illite cementation in the Northern German Basin (Gaupp & Okkerman, 2011). Based on the textural relationships in combination with the timing of pore-filling meshwork illite in the Northern German and Dutch Basin (Gaupp et al., 1993; Gaupp & Okkerman, 2011), pore-filling illite is interpreted to have formed during burial diagenesis postdating the onset of quartz cementation but predating the late Cretaceous inversion. Previous studies determined illite ages in Rotliegend sandstones with K-Ar dating, demonstrating that illite formed between 180 to 210 Ma in the German part of the Southern Permian Basin (Clauer et al., 2012; Liewig & Clauer, 2000; Zwingmann et al., 1998). Illite ages become younger towards the Dutch and

UK sector with ages ranges from 100 to 190 Ma (Clauer et al., 2012). Textural observations suggest that diagenetic rutiles postdate pore-filling illites and kaolinites in Cornberg Sandstone (Fig. 3.6 c), supporting the episodic growth of illite during burial diagenesis (Fig. 3.12). Therefore, we interpret illite growth to be episodic in the early Jurassic as proposed in previous studies, likely related to a hyperthermal plate tectonic event, e. g. the opening of the Atlantic ocean (Liewig & Clauer, 2000; Zwingmann et al., 1999).

Chemical compaction

Long grain contacts between quartz grains encasing illitic grain coatings form quartz-illite-quartz interfaces, which enhance chemical compaction by electrochemical potential differences (Greene et al., 2009; Kristiansen et al., 2011). Therefore, intense chemical compaction should require mostly continuous illite GTG coatings, as well as an absence of major pore-filling early diagenetic cements, which would inhibit s the development of long, concavo-convex, or sutured grain-to-grain contacts. Chemical compaction appears to correlate with GTG coatings, where higher grain coating coverages coincide with smaller IGVs in this study (Fig 3.8 b), which is in agreement with Monsees et al. (2020a). Previously the amount of pressure dissolution was related to the total amount of clay in the sandstones (Tada & Siever, 1989), but these results in conjunction with previous results from Monsees et al. (2020a) highlight that the local abundance of illitic clay minerals at grain contacts may aid in extending such a model. Flechtingen Sandstones lacking major pore-filling cements, showing the most continuous illite coatings, and lowest IGVs therefore are interpreted to have experienced the highest degree of chemical compaction. Mechanical compaction in clean sands like Cornberg and Penrith Sandstones did not reduce IGVs below the theoretical minimum of 26 % (Paxton et al., 2002), however IGVs in Flechtingen Sandstones are reduced down to 15 %. Considering burial histories for study areas where they are available (Kohlhepp, 2012; Turner et al., 1995), burial depths are interpreted to be sufficient to lead to a maximum mechanical compaction under the boundary conditions proposed by Paxton et al. (2002). Chemical compaction has been discussed to be mainly controlled by thermal boundary conditions in burial depths exceeding 2 to 3 km, and only to a lesser extent by effective stresses (Bjørlykke, 2006). Large IGV reductions therefore might not require extreme burial, but can also be observed in the same well, only several meters apart (Monsees et al., 2020a). This is interpreted to be due to a combination of chemical compaction as shown by partly sutured grain contacts (Fig. 3.5 b-c), and the poorest average sorting (supplementary material II). The presented correlation of illitic GTG grain coating coverages and IGV (Fig. 3.8 b) also implies that the variability of burial scenarios, i.e., variability in effective vertical stresses, does not appear to be the main control on the process of chemical compaction. Consequently, intense early diagenetic dolomite cementation in Cornberg Sandstones, and intense quartz cementation in Penrith Sandstones not inhibited by intense clay coatings are interpreted to mitigate major effects of chemical compaction in these study areas.

3.6.1.3 Uplift diagenesis

Kaolinite and feldspar dissolution

Kaolinite was observed to overgrow quartz cements in Cornberg Sandstones (Fig. 3.6 c), thus postdating quartz cements formed during burial diagenesis. Kaolinite however is typically formed during early diagenesis, favoring lower temperatures and meteoric waters compared to its burial diagenetic products dickite, illite and chlorite (Lanson et al., 2002; Worden & Morad, 2003). However, textural evidence suggests only minor amounts of early diagenetic kaolinite, possibly due to very acidic fluids (Lanson et al., 2002). Possible K^+ sources during diagenesis are dissolving K-feldspars (Ehrenberg & Nadeau, 1989). Early diagenetic kaolinite was subsequently partly illitized during burial diagenesis (Lanson et al., 2002). Early diagenetic carbonates are preserved (Fig. 3.6 b), suggesting a limited exposure to very acidic fluids. Therefore, kaolinite in Cornberg Sandstones is interpreted to have formed during early diagenesis and uplift diagenesis (Fig. 3.11) under the influence of meteoric waters and below earliest illitization temperatures of 60° C (Lanson et al., 2002; Worden & Morad, 2003). A later phase of feldspar dissolution is interpreted to have occurred during uplift and exposure at the surface due to interactions with meteoric waters.

Iron hydroxides

Textural relations imply a formation of iron hydroxides in Cornberg Sandstones syn- to postdating uplift related kaolinite cement (Fig. 3.6 c), as well as postdating quartz cement formation in Flechtingen and Penrith Sandstones. Detrital or early diagenetic goethite would have been altered to hematite under burial diagenetic conditions (Berner, 1969), therefore it is more plausible for iron hydroxides to have been transported under oxic conditions along fractures, also explaining observed Liesegang rings on outcrop scale (Chan et al., 2000). Due to textural relations of iron hydroxides with burial diagenetic minerals in all studied samples, iron hydroxides are interpreted to have formed during the latest stages of uplift diagenesis (Fig. 3.12) under the influence of humid conditions in the UK and Germany.

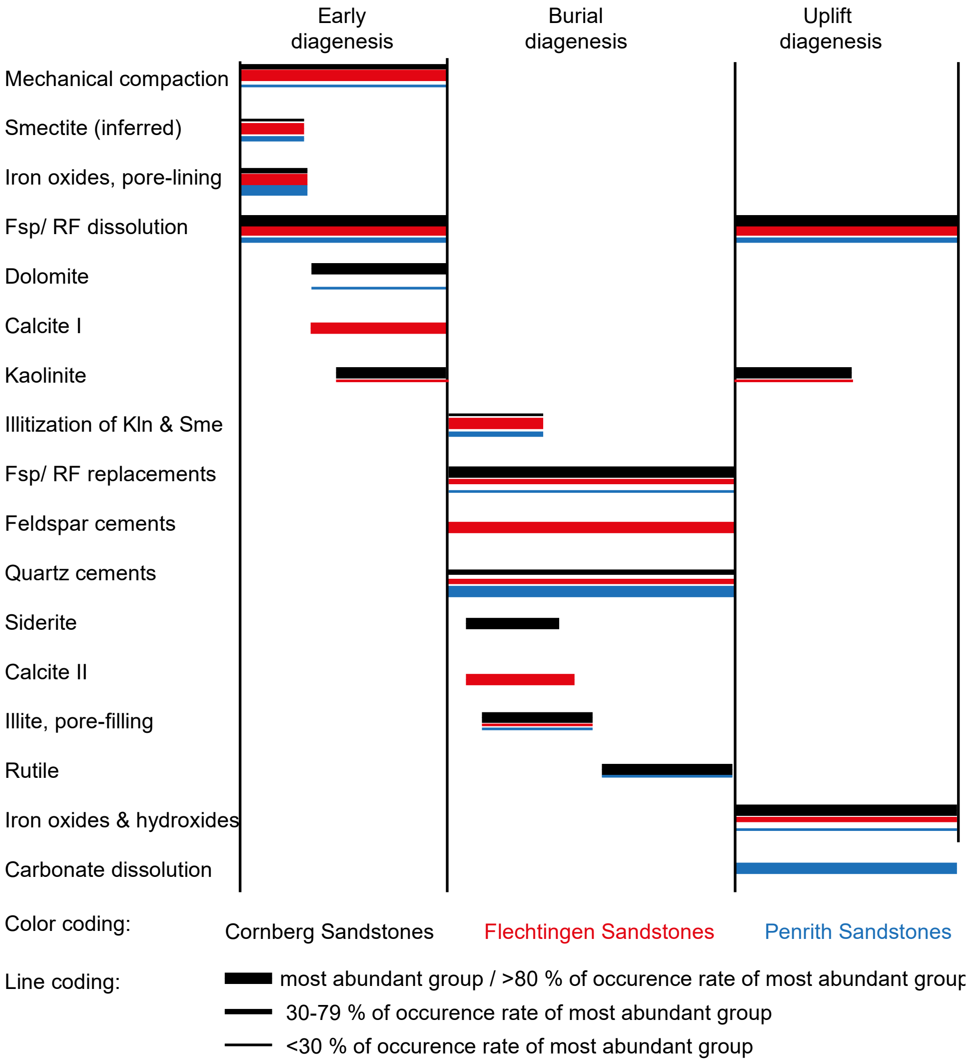

Figure 3.12. Paragenetic sequence determined from textural and spatial relations of authigenic. minerals. The left line is giving the respective diagenetic alteration sorted by relative first occurrence. Diagenetic alterations are subsequently interpreted to have been formed during early, burial, and/or uplift diagenesis. Color coding relates to the three study areas. Line thickness coding relates to the abundance of the respective diagenetic alterations based on the average petrographic parameter for the study area (data in supplementary material II). Abbreviations: Fsp – Feldspar, RF – rock fragment, Kln – kaolinite, Sme - smectite.

Carbonate dissolution

Carbonate dissolution in Penrith Sandstones is apparent by the rhombohedral secondary porosity engulfed by quartz cements (Fig. 3.6 i), implying the dissolution process took place after quartz cementation. The occurrence of dolomite cements in Penrith Sandstone samples from the subsurface (Turner et al., 1995), in combination with the solubility of carbonate minerals by meteoric waters (Morad, 1998) support the theory of dolomite dissolution during uplift diagenesis (Fig. 3.12). The significantly higher permeabilities in Penrith Sandstones are interpreted to have catalyzed carbonate dissolution additionally, while low permeability Cornberg Sandstones were able to retain significant carbonate cement volumes up to 15 %.

3.6.2 Vertical permeability heterogeneity

Results demonstrate a larger offset between horizontal (k_H) and vertical permeability (k_V) in less permeable sandstones (Fig. 3.10), which carries implication for permeability related modelling approaches in sandstones. Industry practice assumes vertical (normal to bedding) permeabilities to be 10 % of horizontal (parallel to bedding) permeabilities (Cannon, 2018; Gibbons et al., 1993). Recent outcrop analog studies also demonstrated heterogeneity in lateral permeability in Triassic Buntsandstein of up to two orders of magnitude in a single bed several meters apart (Schmidt et al., 2020b). Upper Carboniferous sandstones also show lateral permeability variations by two orders of magnitude over 150 m lateral distance in a 3 m bed (Becker et al., 2019; Becker et al., 2017). However, it is commonly assumed to not vary significantly in lateral direction in reservoir modelling approaches (Cannon, 2018; Gibbons et al., 1993). Minimal reduction from k_H to k_V for sandstones exceeding permeabilities of 100 mD is interpreted to be an effect of sample homogeneity, having no significantly less permeable laminae normal to bedding. This in agreement with previous experimental studies on homogenous sandstones over 100 mD (Iheanacho et al., 2012; Meyer, 2002). Micro-computer tomography based permeability simulations of Penrith Sandstones also show insignificant variations from horizontal to vertical permeability from 1500 to 800 mD (Monsees et al., 2020b). Sandstones with permeabilities below 10 mD show larger permeability reduction from k_H to k_V (this study, Iheanacho et al. 2012), which are interpreted as a heterogeneity imposed by depositional environment, grain size and diagenetic alteration. There seems to be no direct control of the depositional environment on permeability in this data set (Fig. 3.10), rather the vertical permeability seems to be linked to horizontal permeability, which is mostly controlled by diagenetic alterations (this study, Becker et al. 2017, Busch et al. 2020). The depositional environment and grain size should be of larger importance in shallow and thus not heavily diagenetically overprinted settings, while diagenetically induced permeability reduction in sandstones will increase with burial depth (Paxton et al., 2002) and temperature exposure (Busch et al., 2018; Lander et al., 2008; Walderhaug et al., 2000). In summary, low permeability samples are either heavily compacted (Flechtingen Sandstones) or heavily cemented (Cornberg Sandstones, also forming planar dissolution seams due to chemical compaction), which may impede fluid flow and thus permeability (Fossen et al., 2011).

3.6.3 Impact on reservoir quality

Depositional parameters

The detrital composition is interpreted to have no effect on reservoir quality, as both Cornberg Sandstones and Penrith Sandstones show a predominantly mature, quartz-dominated detrital composition (Fig. 3.4), but significant permeability and porosity contrasts (Fig. 3.9 a). The impact of depositional environments is not straightforward, as both the best and worst reservoir qualities were observed in eolian dunes, and intermediate reservoir qualities in fluvial sandstones (Fig. 3.9 b). Depositional systems are discussed to be one of the main or main controlling factors on reservoir quality in literature (dos Anjos et al., 2000; Griffiths et al., 2019; Morad et al., 2010). It is further developed towards an integrated approach of depositional systems overprinted by diagenesis during burial (Becker et al., 2019; Busch et al., 2020; Ehrenberg, 1990; Gaupp & Okkerman, 2011; Taylor et al., 2010). This study comprises of fluvio-eolian sandstones only, consequently a population bias against a strong control depositional control due to the lack of depositional system variety is introduced into the data set. As opposed to Heidsiek et al. (2020) a facies dependent reservoir control on plug-scale reservoir quality analyses cannot be delineated in Flechtingen Sandstones, as is also supported by previous studies in similar arid or semi-arid fluvio-eolian deposits (Busch et al., 2019; Busch et al., 2020; Kunkel et al., 2018; Monsees et al., 2020a). The effect of grain size on permeability is also interpreted to be partly caused by a population bias, which is also discussed by Wadsworth et al. (2016). Larger grain size generally results in higher permeability (Shepherd, 1989), which is also evident in Penrith Sandstones, however no such distinctions can be made for Flechtingen and Cornberg Sandstones (Fig. 3.11 a). Better sorting is discussed to have a positive effect on reservoir quality due to larger packing induced porosities (McKinley et al., 2011), however no such effect can be observed in this data set (Fig. 3.11 b). The lack of clear correlations of depositional parameters with reservoir quality is interpreted as significant diagenetic overprint superimposed on reservoir quality controlling parameters during deposition, particularly in Cornberg and Flechtingen Sandstones. Consequently, reservoir quality assessment should always include the analysis of diagenetic alteration.

Mechanical compaction and early diagenetic blocky cements

Mechanical compaction generally is considered the most significant factor in porosity loss of clean sandstones during early and burial diagenesis due to the reduction of potential porosity (IGV) from approximately 45 % to 26 % (Lundegard, 1992; Paxton et al., 2002). However, mechanical stresses alone do not explain observed IGVs of up to 40 % in Penrith Sandstones, which have been buried to approximately 3 km depth (Turner et al., 1995), resulting in an expected IGV below 30 % (Paxton et al., 2002). Furthermore, high porosities and IGVs in hydrocarbon reservoir also make a purely stress-dependent porosity reduction unlikely (Salem et al., 2000; Taylor et al., 2010). Outcrop analog studies on Lower

Triassic Buntsandstein sandstones demonstrated differences in the porosity reduction process from mainly compactional to mainly cementational control over a lateral distances of only several meters (Schmidt et al., 2020a; Schmidt et al., 2020b). This IGV loss might be counteracted by grain-stabilizing early diagenetic cementation of carbonate minerals, anhydrite or halite (Ajdukiewicz et al., 2010; Mahmic et al., 2018), which are discussed to positively contribute to reservoir quality due to the possible dissolution and formation of secondary intergranular porosity during burial (Taylor et al., 2010; Worden et al., 2018). High IGVs and dissolved dolomite rhombs in Penrith Sandstones are interpreted to indicate an early diagenetic cement phase, however the total amount of dissolved carbonates or other phases is unclear. The identified amounts of carbonate dissolution porosity in Penrith Sandstones encased in quartz overgrowths are too small to be of significant impact on overall permeability.

Grain coatings and chemical compaction

Grain coatings, quantified as the grain coating coverage, generally can inhibit quartz cementation (Fig. 3.8 a) (Ajdukiewicz & Larese, 2012; Esch et al., 2008), showing similar trends reported in previous works (Busch et al., 2017; Monsees et al., 2020a). Cornberg Sandstones show a different trend than Flechtingen and Penrith Sandstones due to early diagenetic carbonate precipitation, which is independent of grain coating coverage in siliciclastic sandstones (Ajdukiewicz et al., 2010; Esch et al., 2008). Early diagenetic carbonate cementation in Cornberg Sandstones is interpreted to have reduced the effective surface area of detrital quartz grains, leading to comparable amounts of quartz cement as Flechtingen Sandstones, although the grain coating coverage in Flechtingen Sandstones is much higher (Fig. 3.8 a). The direct impact of GTI grain coatings on reservoir quality however remains indistinct (Fig. 3.11 f).

Grain-to-grain (GTG) coatings deliver the same trend as originally described by Monsees et al. (2020a), showing smaller IGVs weakly correlating with larger GTG coatings due to catalyzed chemical compaction by electrochemical potential differences on quartz-illite-quartz interfaces (Greene et al., 2009; Kristiansen et al., 2011). The ambivalent effect of illite clay coatings of potentially inhibiting quartz cementation but driving chemical compaction has led some authors to the conclusion, that contrary to chlorite coatings, illite coatings mostly have a deteriorating effect on reservoir quality (Gaupp & Okkerman, 2011; Storvoll et al., 2002). Thus, a differentiation between GTI and GTG coatings is necessary to fully address the variable effect of illitic grain coatings on reservoir quality based on our results and recent studies (Busch et al., 2020; Monsees et al., 2020a). The effect of GTG coatings on chemical compaction is interpreted to be reduced by the early diagenetic blocky cements in Cornberg Sandstones, but shows a trend in systems without early diagenetic blocky cements towards better reservoir quality with less GTG coverage (Fig. 3.11 g).

Clay minerals and microporosity

An increased amount of clay minerals has been observed to coincide with a reduction in reservoir quality (Fig. 3.11 j), which is the expected result (Ajdukiewicz et al., 2010; Worden et al., 2018). As microporosity was derived from the abundance of clay minerals, it consequently also shows a negative correlation with reservoir quality (Fig. 3.11 l). Permeability is driven by the interconnectivity of the larger pores (Klinkenberg, 1941), therefore the increased amount of porosity due to microporosity should have a minor impact on overall permeability. If petrographically derived microporosities after Hurst and Nadeau (1995) are subtracted from the helium porosity, a better fit with permeability is generated (Fig. 3.13). This effective helium porosity (ϕ_E) is interpreted as a closer representation of the well-connected pore volume, as the better fit suggests that microporosity in clays contributes only to a minor degree to overall permeability in the studied sample set. Effective helium porosity shows a positive correlation of $R^2=0.93$ with helium porosity, which is closer to a 1:1 fit in more porous samples (Fig. 3.13 a). This is interpreted as the higher offset between ϕ and ϕ_E due to the increased abundance of clay minerals in the less porous samples. The derived scatter plot between permeability and ϕ_E (Fig. 3.13 b) shows an improved correlation coefficient of $R^2=0.78$ compared to regular helium porosity (Fig. 3.9 a). Excluding the dune facies from Flechtingen Sandstones, which clearly show a different porosity-permeability relationship seemingly independent of porosity variation from all other data points (Fig. 3.13 b) would result in an even better correlation coefficient of $R=0.91$. Overall, clay minerals are interpreted to be one of the main controls on a deterioration of reservoir quality, as they might retain porosity in form of microporosity but contribute to a loss of effective porosity, resulting in reduced permeabilities, which is in line with results of previous studies (Becker et al., 2019; Ehrenberg, 1990; Gaupp & Okkerman, 2011).

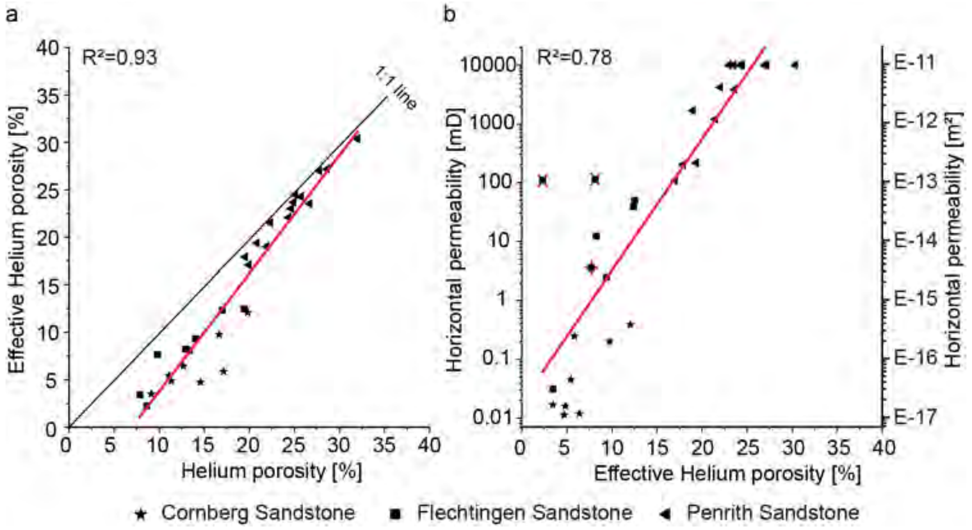

Figure 3.13. a) Scatter plot of Helium porosity (abscissa) against effective Helium porosity (ordinate) with linear line of best fit (red) and 1:1 line (black). b) Effective Helium porosity (abscissa) against horizontal permeability (ordinate) with linear line of best fit (red). Facies outliers in Flechtingen Sandstones are indicated by red x (dunes) and + (sheet sands) symbols.

Burial diagenetic blocky and clay mineral cementation

Quartz cement volumes shows a positive correlation with permeability (Fig. 3.11 h), although in fact the opposite would be expected (Ajdukiewicz et al., 2010; Becker et al., 2019; Busch et al., 2018; Ehrenberg, 1990; Gaupp & Okkerman, 2011). Because quartz cements are most abundant in Penrith Sandstones, other preserved cements are lacking (Fig. 3.6 i-j), and have been compacted the least amount (Fig. 3.7). The large quartz cement volumes and IGVs imply a stabilization effect on the grain framework commonly observed for early diagenetic carbonates (Paxton et al., 2002). As a result, quartz cementation in Penrith Sandstones is interpreted to have a positive effect on reservoir quality by framework stabilization and inhibiting further compaction.

An increased amount of carbonate and clay minerals was also observed to be an important factor in reservoir quality deterioration in Cornberg and Flechtingen Sandstones (Fig. 3.11 i-j). Considered individually, the effect on reservoir quality does not result in a good correlation (Fig. 3.11 i-j), however previous studies in Triassic red bed sandstones reported a combined control of carbonates and clay minerals on reservoir quality (Schmid et al., 2004), which can also be observed here (Fig. 3.11 k). Pore-filling burial diagenetic illite cementation has been discussed as a reservoir quality deterioration factor in Northern German and Dutch Rotliegend reservoir rocks, showing a significant reduction in permeability (Gaupp et al., 1993; Gaupp & Okkerman, 2011) while retaining porosity (Hurst &

Nadeau, 1995). Pore-filling illites are interpreted to be a significant factor in reservoir quality deterioration based on their highest abundance in barely permeable Cornberg Sandstones.

Uplift diagenesis

Diagenetic alterations attributed to uplift diagenesis are interpreted to be of minor importance to reservoir quality due to the small volumetric abundance of iron hydroxides and kaolinites, which is largest in Cornberg Sandstones with around 3 %, and much lower in in Flechtingen and Penrith Sandstones. Secondary porosity caused by carbonate dissolution in Penrith Sandstones (avg.: 0.1 %) is also negligible compared to their total porosity (avg. ϕ: 25.9 %). The uplift diagenetic dissolution of other pore-filling mineral phases can only be speculated since characteristic dissolution molds as in Penrith Sandstones are absent. Meanwhile, the uplift diagenetic dissolution of feldspars and rock fragments contributing to up to 40 % of the total optical porosity in Flechtingen Sandstones and up to 25 % in Cornberg Sandstones represent a major part of optical porosity. Feldspars are chemically unstable under meteoric waters (Aagaard et al., 1990; Yuan et al., 2015). While microporosity in feldspar is considered a negligible contribution to permeability (Walker et al., 1995), intense formation of secondary porosity has been discussed to decrease overall reservoir quality if coinciding with pore-filling clay mineral cementation (Ehrenberg, 1990). Mahmic et al. (2018) interpret feldspar dissolution to contribute positively to reservoir quality if the dissolved grains are connected to intergranular porosity, thus contributing to the effective porosity. This is in agreement with Flechtingen Sandstones showing higher permeability than Cornberg Sandstones, but comparable porosity. Feldspar dissolution coinciding with intense pore-filling clay mineral cementation (Fig. 3.6 c) in Cornberg Sandstones is interpreted to represent a case as described by Ehrenberg (1990), resulting in a negative impact on reservoir quality. In contrast, secondary porosity in Flechtingen Sandstones is commonly connected to the intergranular porosity (Fig. 3.5 b). In combination with overall higher intergranular porosity in Flechtingen Sandstones, feldspar dissolution is interpreted to positively contribute to reservoir quality in Flechtingen Sandstones.

Reservoir quality controls

The reservoir quality controls so far have been compiled to a schematic diagram illustrating reservoir quality development during diagenesis (Fig. 3.14). The studied sandstones were deposited as unconsolidated sands with different compositions, which affects their compactive behavior and diagenesis. Early diagenetic carbonate cementation in Cornberg Sandstones reduced compaction and is interpreted to have partly inhibited quartz cementation by encompassing detrital quartz grains (Fig. 3.14).

During burial diagenesis, intense illitic grain coatings in conjunction with the largest amounts of ductile rock fragments led to highest compaction in Flechtingen Sandstones, while their absence led to lowest compaction in Penrith Sandstones (Fig. 3.14). Reservoir quality was reduced by pore-filling quartz, illite and siderite cements (Fig. 3.14). Due to the large intergranular volumes in Penrith Sandstones, intense quartz cementation is interpreted to have improved reservoir quality due to the prevention of further compaction. Reservoir quality in Flechtingen Sandstones was primarily reduced by chemical compaction, while reservoir quality in Cornberg was reduced by intense cementation of illite, quartz and carbonates during early and burial diagenesis (Fig. 3.14). Published burial scenarios show peak subsidence of 3.4 km (Penrith, (Turner et al., 1995)), and varies between modeled 5-6 km (Flechtingen, Bebertal outcrop (Fischer et al., 2012)) and 2.5 km (well Peckensen 7 80 km NNE of Bebertal outcrop (Kohlhepp, 2012)). As chemical compaction is mostly dependent on temperature and only to a lesser extent on effective stresses (Bjørlykke, 2006), lower maximum temperatures are interpreted to have favored a preservation of porosity in Penrith Sandstones. This is also reflected by lowest IGVs in Flechtingen Sandstones at Bebertal and highest IGVs in Penrith Sandstones (Fig. 3.11 d). While no thermal data for Cornberg Sandstones is available, the intermediate IGVs in Cornberg Sandstones still match with modeled peak subsidence of 5 km further north (Schwarzer & Littke, 2007) due to the preserved early diagenetic cementation inhibiting further mechanical compaction.

Uplift is interpreted to have had only minor improving impact on reservoir quality as the volume of dissolved dolomite rhombs is negligible compared to the intergranular porosity in Penrith Sandstones (Fig. 3.14). Uplift-related feldspar dissolution is interpreted to positively contribute to reservoir quality due to the lack of pore-filling clay minerals in Flechtingen Sandstones, but negatively contribute to reservoir quality in Cornberg Sandstones because of additional kaolinite precipitation (Fig. 3.14). No clear indicators for carbonate dissolution in Cornberg Sandstones were identified, and reservoir quality was deteriorated even more by the formation of pore-filling iron hydroxides (Fig. 3.14). These diagenetic controls are interpreted to have resulted in poor reservoir quality in Cornberg Sandstones with intermediate porosity and low permeability, intermediate reservoir quality with intermediate porosity and permeability in Flechtingen Sandstones, and large porosity and permeability in Penrith Sandstones (Fig. 3.14). Nevertheless, plug-based reservoir quality analyses do not consider fracture networks, which are necessary for upscaling of reservoir properties (Busch et al., 2019; Kushnir et al., 2018).

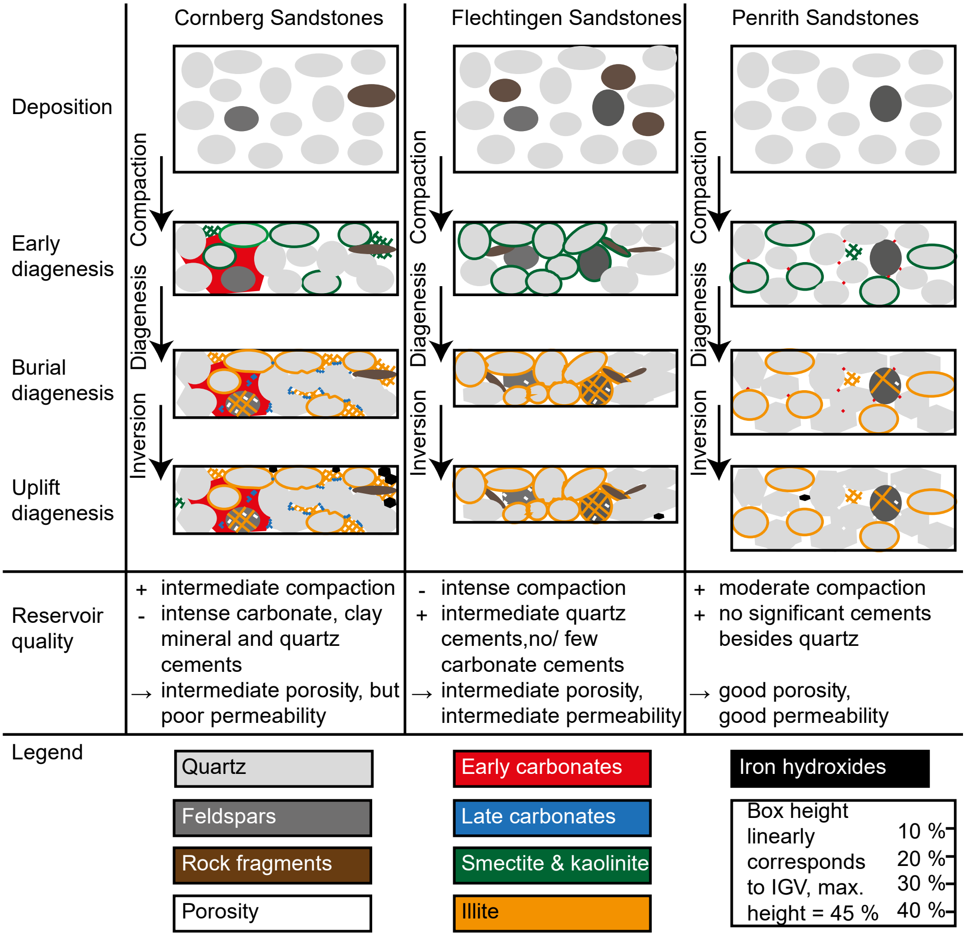

Figure 3.14. Schematic illustration showing the process of reservoir quality reduction for Cornberg Sandstones, Flechtingen Sandstones and Penrith Sandstones during deposition, early diagenesis, burial diagenesis, and uplift diagenesis. Depositional compositions, IGVs, authigenic mineral volumes and porosity correspond to typical samples. Abbreviations: IGV – intergranular volume.

3.7 Conclusions

Compaction is mechanical during early diagenesis, and includes chemical compaction during burial diagenesis being highest in Flechtingen Sandstones. Several phases of pore-filling cementation were identified: Quartz, feldspar, dolomite, calcite, siderite, illite, kaolinite and iron hydroxides. While early carbonate cementation is most intense in Cornberg Sandstones, cements in highly compacted Flechtingen Sandstone was mostly formed during burial diagenesis. Inversion resulted only in minor amounts of cementation and secondary porosity development by dissolution.

Grain-to-grain (GTG) clay mineral grain coatings show an enhancing effect on chemical compaction in all studied settings. Differences in the degree of compaction can be related to the relative timing of framework stabilization by early blocky cementation, and by the continuity of GTG-coating processes, highlighting the necessity for detailed diagenetic studies in reservoir quality assessments.

Depositional parameters such as initial composition, depositional environments, grain size and sorting are shown not to be the main governing factors for reservoir quality in the studied fluvio-eolian Permian Rotliegend sandstones. Reservoir quality is interpreted to mainly depend on a combination of initial composition, early diagenetic framework stabilizing cementation, illitic GTI grain coatings which prevent quartz cementation, illitic GTG coatings which enhance chemical compaction, and burial diagenetic porosity-reducing cementation.

Poorest reservoir quality (avg. horizontal permeability: 0.96 mD) was encountered in Cornberg Sandstones linked to intense cementation (avg. cement volume: 24.9 %) and intermediate compaction (avg. intergranular volume: 26.4 %). Intermediate reservoir quality (avg. horizontal permeability: 34.9 mD) in Flechtingen Sandstones is controlled by intense mechanical and chemical compaction (avg. intergranular volume: 19.6 %) in conjunction with intermediate cementation (avg. cement volume: 16.7 %). Penrith Sandstones showed best reservoir quality (avg. horizontal permeability: 5906 mD) due to lowest compaction (avg. intergranular volume: 30.0 %) supported by framework-stabilizing quartz cements (avg. cement volume: 16.4 %), resulting in a large and well-connected pore system with high permeability. These contrasts in reservoir quality are interpreted to be the result of diagenesis, which is controlled by the combined effect of depositional composition, fluid flow, burial history, and thermal exposure.

The ratio between vertical (normal to bedding) and horizontal (parallel to bedding) permeability is close to 1 in higher permeable samples (> 1000 mD), and lower in low permeable samples. Samples over 100 mD show ratios above 0.2, while only samples below 10 mD showed ratios of 0.1 or below, which is the standard industry assumption for permeability modelling in the subsurface. Additional research on a larger data set may aid in better statistical constraining horizontal and vertical permeability in fluvio-eolian sandstones.

4 Coupling of diagenetic alterations and mechanical properties of Lower Permian siliciclastic sandstones: a pilot study

4.1 Abstract

Initial detrital composition and authigenic alterations during diagenesis of three sandstone types are related to their mechanical properties. Sandstones were prepared for geotechnical standard tests (density, uniaxial compressive strength (UCS), Young's modulus (E), strain at failure (ε)) and thin-sections for petrographic analyses (point counting). UCS ranges from 3-62 MPa and positively correlates with density (1.75-2.35 g/cm³) and E (0.3-12.7 GPa). Optical porosity is controlling these mechanical parameters and was linked to diagenetic alterations. Diagenetic alterations affecting porosity-reduction are the abundance of clay minerals, the intensity of mechanical and chemical compaction. The latter is controlled by clay mineral coatings on contacts between detrital grains, and the occurrence of authigenic quartz and dolomite. Horizontal contact lengths of grains normalized to their respective particle diameter (effective contact ratio, ECR) and porosity are identified as a control on the mechanical properties UCS and E, reflected by the rock strength index S_R. The results of this pilot study suggest that S_R is able to predict UCS and E based on petrographic information obtained from the studied samples. These results enhance the understanding of the coupling between mineralogy and geomechanics and highlight the impact of diagenesis on geomechanical behavior.

4.2 Introduction

Deeply buried Lower Permian Rotliegend sandstones are the most important reservoir rocks for natural gas in Central Europe (Gast et al., 2010). These reservoirs are of increasing interest for applications other than hydrocarbon extraction, such as geothermal energy exploration, gas and hydrogen storage, or CO_2 sequestration (Ambrose et al., 2008; Bachu, 2000; Legarth et al., 2005; Moeck et al., 2009; Regenspurg et al., 2015). The pore pressure and effective stress of these porous reservoir rocks will decrease during production in hydrocarbon or geothermal reservoirs, which may result in compaction and / or rock failure over reservoir timescales (e.g., Hettema et al. (2000); Talwani and Acree (1985); Zoback and Zinke (2002)).

Therefore, studies assessing geomechanical properties are well established methods in reservoir studies (Ghassemi, 2012; Sayers & Schutjens, 2007). Reservoir sandstones also compact mechanically and chemically over geological timescales affecting petrophysical and mechanical properties (Houseknecht, 1987; Lundegard, 1992). Their reservoir properties change during subsidence, their diagenesis related to initial composition and grain coating (Aagaard et al., 2000; Busch et al., 2020; Monsees et al., 2020a), fluid type, -chemistry and -pressure (Bjørlykke & Høeg, 1997; Gaupp et al., 1993), thermal exposure over time at depth intervals (Becker et al., 2019; Busch et al., 2018; Lander et al., 2008), and faults controlling temperature-overprint by hydrothermal fluid circulation (Wüstefeld et al., 2017b). It is thus of crucial importance for assessing the rock's porosity and permeability, and its viability as a reservoir (Morad et al., 2010; Worden et al., 2018).

Empirical relations between parameters like rock strength and deformability are well established (Chang et al., 2006; Dyke & Dobereiner, 1991) and have been correlated with the bulk sandstone composition (Fahy & Guccione, 1979; Ulusay et al., 1994; Zorlu et al., 2008). Fahy and Guccione (1979) demonstrated the dependence of compressive rock strength on grain sizes, quartz percentage, sphericity, cements and grain contacts. Dyke and Dobereiner (1991) showed that the length of the grain contacts in relation to the total grain surface length can be used as a proxy for compressive strength in sandstones. Zorlu et al. (2008) performed multiple regression analysis on a large sandstone data set (n=138), evaluating and quantifying the effects of quartz content, cement volumes, grain size, grain contacts and packing density on compressive strength. They concluded that packing density, grain contacts and quartz content are the most important parameters.

The objective of this study is to investigate and quantify relationships between diagenetic and geomechanical properties of porous sandstones. In this context, petrographic data is gathered from optical microscopy, point-counting, grain-coating analyses, and effective contact ratios (ECR). The petrographic data will be compared with geomechanical data, using uniaxial compression tests, delivering data on Young's modulus (E), uniaxial compressive strength (UCS), density and strain at failure (ε). The influence of petrographic parameters and diagenesis on geotechnical parameters will be evaluated and quantified and discussed with respect to reservoir- and geological timescales.

4.3 Geological setting

The sandstones of the Cornberg quarry (CS) belong to the uppermost Rotliegend (Lower Permian) lithostratigraphic unit (Kowalczyk et al., 2012), also referenced to as the Weißliegend (Paul, 2012). The Cornberg Formation crops out in the Nentershäuser Basin, which is a sub basin of the Hesse Basin in central Germany (Kulick et al., 1984) (Fig. 4.1).

The Nentershäuser Basin has been interpreted as a pull-apart basin due to its thickness increase of Rotliegend deposits from tens to hundreds of meter over lateral distances <10 km (Kowalczyk et al., 2012; Kulick et al., 1984). Based on meter-scale cross-bedded strata, the depositional system of the sandstones has been controversially discussed (Gast, 1994; Pryor, 1971; Schumacher, 1985). Recent studies interpret them to be of eolian origin (Gast, 1994; Kowalczyk et al., 2012). The thickness of the formation is up to 20 m (Kowalczyk et al., 2012), being conformably overlain by the Kupferschiefer claystone marking the onset of the Zechstein transgression (Kowalczyk et al., 2012), and underlain by gray, sandy conglomerates and red conglomeratic sandstones and pelites (Aehnelt & Katzung, 2007). Maximum burial depth and precise inversion timing is unclear (Kowalczyk et al., 2012).

Upper Rotliegend fluvio-eolian Flechtingen Sandstones (FS) are exposed in a decommissioned quarry 1 km southwest of Bebertal, Saxony-Anhalt, Germany (Fig. 4.1), located on the margins of the Flechtingen High (Gaitzsch et al., 2004). Rocks of the Bebertal quarry are commonly used as analogs for the North German Rotliegend hosted reservoirs (Fischer et al., 2012; Gast et al., 2010; Schröder et al., 1995). According to the regional stratigraphic correlation conducted by Schneider and Gebhardt (1993) and field studies by Gaitzsch et al. (2004), the Rotliegend sandstones exposed near Bebertal belong to the Mirow Formation of the Havel Subgroup, resulting in a sedimentation age between 264-262 Ma (Menning, 1995). The series has a thickness of 10-16 m (Gaitzsch et al., 2004) and is conformably underlain by conglomerates (the *Oberes Konglomerat* series), and unconformably overlain by dominantly fluvial sandstones (the *Oberer Rundkörniger Sandstein* series) (Gaitzsch et al., 2004). Flechtingen Sandstones were rapidly buried reaching a thermal maximum of 200-250° C in early Triassic (Fischer et al., 2012), and subsequently uplifted by the inversion of the Flechtingen High initiated by the Late Aptian transgression (Otto, 2003).

Permian Penrith Sandstones (PS) crop out in the Vale of Eden half graben, Cumbria, UK (Fig. 4.1), covering an area of approximately 48 × 6 km (Busch et al., 2017; Macchi, 1981; Turner et al., 1995). The Appleby Group consists of the eolian Penrith Formation and basal alluvial deposits locally referred to as the Brockram facies (Macchi, 1981), and is time—equivalent to the Central European Rotliegend (Jackson et al., 1997). The total thickness of the Penrith Sandstone is discussed to reach up to 1 km (Turner et al., 1995). Upper Carboniferous siliciclastic rocks in the northern Vale of Eden and Lower Carboniferous limestones in the south are unconformably overlain by the Appleby Group (Arthurton & Wadge, 1981; Macchi, 1981; Turner et al., 1995). The Appleby Group is conformably overlain by shales, evaporites and dolomite of the Zechstein, which are combined in the Eden Shales Formation (Arthurton & Wadge, 1981). The Penrith Sandstones were buried to maximum burial depth up to 3500 m (120° C) in the Cretaceous, and were inverted in the Late Cretaceous/ Early Tertiary (Turner et al., 1995).

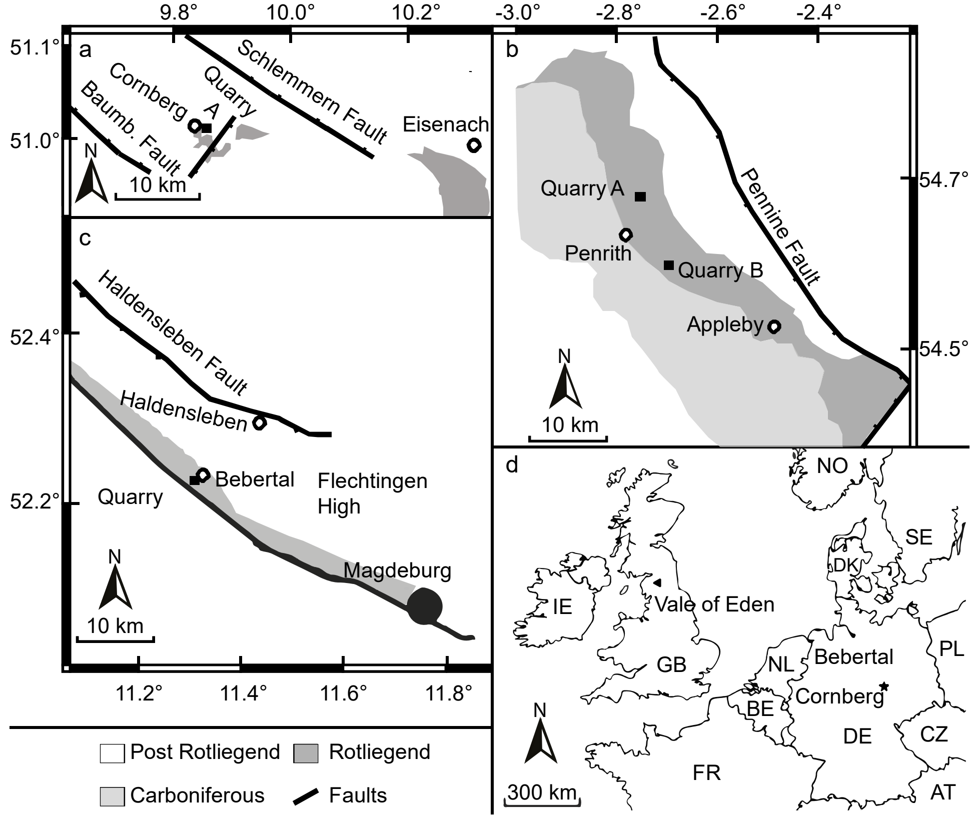

Figure 4.1. Schematic geological maps of the vicinity of the studied quarries. a: Extent of Rotliegend deposits in the northern Hesse Basin, redrawn from Kowalczyk et al. (2012). b: Present-day geology of the Vale of Eden highlighting the extent of Rotliegend deposits, redrawn from Turner et al. (1995). c: Geology of the Flechtingen High, showing the location of fluvio-eolian Rotliegend marginal deposits, modified from Fischer et al. (2012). d: Overview map of western Central Europe, showing the study areas in Germany and the UK.

4.4 Materials & methods

Large rock samples were taken from quarries and drilled normal to bedding for mechanical data, and parallel to bedding for petrographic analysis. A total of seven polished thin-sections originating from each of the seven rock samples used to prepare the cylinders (CS (n=2), FS (n=2) and PS (n=3)) were analyzed. The thin-sections were impregnated with a blue-dyed epoxy resin to highlight porosity. Thin-sections are prepared to a thickness of 30 µm and stained with a combined Alizarin Red S and potassium ferricyanate solution to aid the identification of carbonate minerals. Sample PS1 and PS2 originate from quarry A, while sample PS3 originates from quarry B (Fig. 4.1 b).

Grain sizes were measured along their long-axis on 100 grains with digital image analysis using ImageJ (Becker et al., 2017). Median grain sizes determined by digital image analysis have been demonstrated to reach accuracies of >96% compared to conventional methods like sieving (Barnard et al., 2007). Sorting was determined according to Trask (1930). Point-counting (300 counts) was performed on a grid adjusted to the maximum grain size with a semi-automated Pelcon Point Counter installed on a Leitz Aristomet microscope. This leads to a point-counted area of 350 to 500 mm² considering step size and grain size. Point-counted optical porosity was used as a benchmark for the representative elementary area (volume) of the thin-sections, compared to increasing areal dimensions covered on comparator images. Consistent porosities were obtained from comparator images of Cornberg sandstones with an area larger 100 mm², from Flechtingen sandstones for an area larger than 150 mm², and for Penrith sandstones for an area larger than 30 mm². The minimum point-counted area controlled by grain-size and step-size is larger than 300 mm², therefore exceeding delivering porosities in agreement with the representative elementary volume concept. The statistical error of the arithmetic mean of point-counting data was determined by dividing the standard deviation by the square root of the number of samples.

The sandstone compositions were classified after Folk (1980). The intergranular volume (IGV) was classified according to Paxton et al. (2002). The IGV is the sum of the intergranular pore space, the intergranular cement and detrital matrix. Compactional porosity loss versus cementational porosity loss and compactional indices were calculated after Lundegard (1992), and used to determine the compactional index (Lundegard, 1992). The compactional index is the fractional ratio of compaction porosity loss and the sum of compaction porosity loss plus the cementation porosity loss, assuming an initial porosity of 45 %. The value ranges between zero (porosity loss only by cementation) and one (porosity loss only by compaction). The percentage of clay mineral coatings on grain-to-IGV (GTI) interfaces was assessed on at least 50 grains per sample (Busch et al., 2020). Both the part of a grain's circumference in contact with the IGV and the length of the GTI interface covered with clay minerals were manually measured using image analysis software. The grain's aspect ratio was normalized as a percentage and averaged over at least 50 measurements per sample. Percentages of illite coatings on grain-to-grain (GTG) detrital quartz interfaces were evaluated after Monsees et al. (2020a) by microscopy-aided image analysis. GTG coatings determine the clay coat coverage on grain-grain contacts in contrast to the total length of the grain's circumference in contact with other grains.

The effective contact length (ECL) is introduced as a new approach to quantify the length of physical quartz-quartz, quartz-feldspar, and feldspar-feldspar particle contacts (grain plus syntaxial cement) orientated subparallel (max. ±20°) to the bedding axis (Fig. 4.2 a). Possible syntaxial cementation of grains is included in the contact length (Fig. 4.2 a). It quantifies what otherwise is noted as point-, long-, convex-concave- and sutured contact (Schmidt et al., 2020a; Taylor, 1950). The effective contact length was determined by digital image analysis with ImageJ on randomly selected grain contacts using oriented thin-sections. A total of at least n=50 grain contacts are measured per sample. Median grain size is used as a quality check for the representability of the sample's population (Fig. 4.2 b). The effective contact length was normalized by the grain diameter of the smaller of the two touching grains (D_g), measured by image analysis along its long axis and resulting in the effective contact ratio (ECR). An averaged diameter of both touching grains is avoided since the diameter of the smaller grain limits the effective contact length (ECL). The effective contact ratio is a grain-size independent parameter quantifying the relative contact area of strong mineral contact in porous siliciclastic rocks. A rock strength index S_R was determined by dividing the optical porosity (ϕ) with the effective contact ratio (ECR) (Eq. 4.1).

$$S_R = \frac{\phi}{\mathrm{ECR}} \qquad \text{with} \quad ECR = \frac{ECL}{D_g} \qquad (4.1)$$

The uniaxial compression test according to DIN18136 (2003) and Mutschler (2004) determines the uniaxial compressive strength (UCS) as well as Young's modulus (E). The cylindrical specimens are cored from rock samples normal to bedding with a diameter of 38.1 to 92.5 mm, the height of the specimens ranges from 68.6 mm to 203.6 mm. For the study, 19 cylinders were drilled out of seven rock samples: Cornberg Sandstone (n=5), Flechtingen Sandstone (n=2) and Penrith Sandstone (n=12). The test results and sample dimensions are shown in Tab. 4.1. The cylinders are loaded in axial direction at a constant deformation rate with unconstrained lateral expansion. The test speed is approx. 0.5 to 1 % of the initial height of the specimen per minute. The test is considered to be completed when the specimen has fractured (i.e., the measured axial force does not increase any further) or the strain has reached a value of 20 %. For the evaluation, the uniaxial compressive strength UCS, the associated strain during fracturing ε_v and the Young's modulus E is determined from the stress-strain-diagram. Results of geotechnical tests are displayed as averages with their measured ranges.

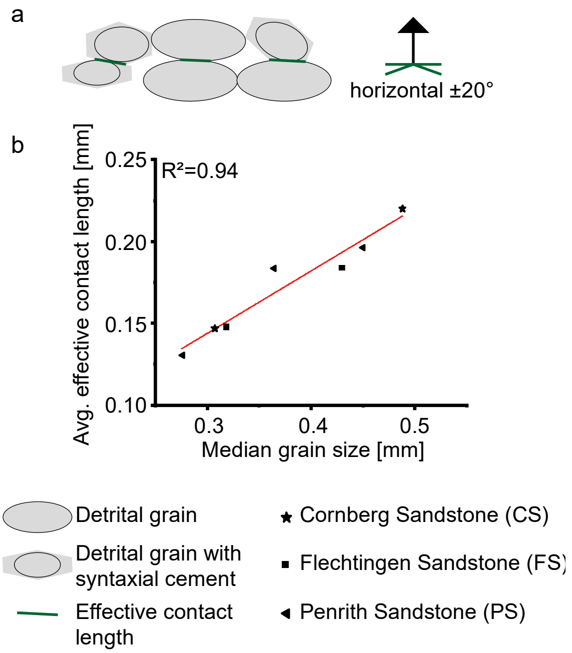

Figure 4.2. a) Effective contact lengths were determined on physical contacts between detrital grains with and without syntaxial cements. Only contacts within ±20° to the true horizontal were measured. Stress direction is normal to the horizontal. b) Median grain size used as quality control on average effective contact length.

4.5 Results

4.5.1 Rock composition

4.5.1.1 Detrital composition

Texture

Measured grain sizes range from 0.275 mm to 0.488 mm (Tab. 4.3). Cornberg Sandstones show a uniform, homogenous texture with barely visible bedding (Fig. 4.3) and are very well sorted (Tab. 4.3). Flechtingen Sandstones show distinct bedding, as well as bedding-bound heterogeneities (Fig. 4.3 b) and are very well sorted (Tab. 4.3). Penrith Sandstones generally are very homogenous (Fig. 4.3 c) with very well to extremely well sorting (Tab. 4.3).

Composition

Quartz (incl. metaquartzite, Fig. 4.3 a-f) consistently is the most abundant detrital constituent in all studied samples (CS avg.: 64.0±1.7 %, FS avg.: 48.5±1.1 %, PS avg.: 61.9±3.1 %) (Tab. 4.2). All samples contain minor amounts of feldspars (avg. PS: 3.1±0.4 %) and rock fragments (avg. CS: 2.8±0.1 %, avg. FS: 14.3±3.7 %), which are the second to third most abundant detrital constituents, depending on sample location (Fig. 4.3 b) (Tab. 4.2). Rock fragments in samples from FS are mainly volcanic rock fragments (VRF: 10.0±3.1 %, plutonic RF: 2.2±0.5 %, sedimentary RF: 1.0±0.0 %, metamorphic RF: 0.8±0.1 %, undifferentiated RF: 0.3±0.0 %). Rock fragments in PS are mainly volcanic and undifferentiated (VRF: 0.7±0.1 %, undifferentiated RF: 0.4±0.2 %, sedimentary RF: 0.4±0.2 %, plutonic RF: 0.1±0.1 %). The most common rock fragments in Cornberg Sandstones are undifferentiated rock fragments (undifferentiated RF: 1.5±0.3 %, sedimentary RF: 1.0±0.1 %, metamorphic RF: 0.3±0.2 %). Detrital clay mineral matrix and mica are very rare (avg. < 1.0 %) throughout all studied locations (CS avg.: 0.0 ±0.1 %, FS avg.: 0.8±0.3 %, PS avg.: 0.3±0.2 %), while zircon appears only in traces (avg. < 0.3 %) (Tab. 4.2). The studied rock samples show a distinct clustering in sandstone types after Folk (1980). Cornberg Sandstones are sublitharenites to quartzarenites, Flechtingen Sandstones lithic arkoses to feldspathic arkoses, while Penrith Sandstones are classified as subarkoses (Fig. 4.3 h).

4.5.1.2 Authigenic minerals

Composition

The most abundant authigenic minerals are quartz and illite. Quartz cement ranges between 6.0 and 14.3 % (CS avg.: 7.2±0.7 %, FS avg.: 5.7±0.4 %, PS avg.: 13.1±0.5 %) (Fig. 4.3 c, Tab. 4.2). Pore-filling illite ranges between 0.3 and 9.0 % (CS avg.: 8.8±0.1 %, FS avg.: 1.2±0.5 %, PS avg.: 0.3±0.2 %, Fig. 4.3 d), while pore-lining illite ranges from 0.7 to 4.7 % (CS avg.: 1.0±0.2 % FS avg.: 4.8±0.1 %, PS avg.: 2.2±0.5 %) (Fig. 4.3 e, f). Dolomite cements (avg.: 5.7±1.4 %) and pore-filling kaolinite (avg.: 1.3±0.2 %) are only present in the Cornberg Sandstones (Fig. 4.3 d). The Flechtingen Sandstone shows feldspar cements (avg.: 1.2±0.1 %), pore-lining FeOx (avg.: 0.8±0.1 %) and pore-filling FeOx (avg.: 0.7±0.1 %). Authigenic minerals are less frequent in the Penrith Sandstones. They include authigenic anatase (avg.: 1.1±0.2 %), pore-lining FeOx (avg.: 0.8±0.1 %) (Fig. 4.3 c, f), pore-filling FeOx (avg.: 0.6±0.3 %), and pore-filling illite (avg.: 0.3±0.2 %), while feldspar cements occur only in traces (avg. >0.3 %). Cornberg sandstone samples also contain pore-filling FeOx cements (avg.: 1.7±0.6 %) (Fig. 4.3 d), authigenic anatase (avg.: 1.2±0.1 %) (Fig. 4.3 a), and barite in traces (avg. <0.3 %) (Tab. 4.2).

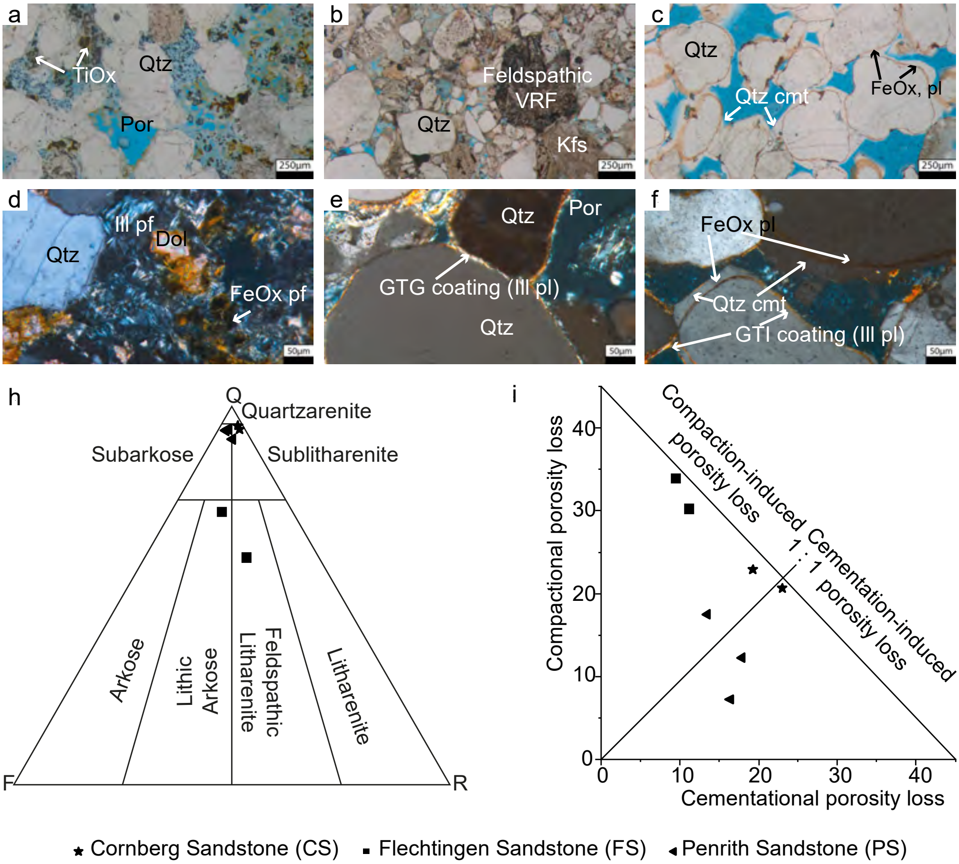

Figure 4.3. Results of petrographic analyses. a: Overview photomicrograph of Cornberg Sandstone (sample CS 1, ppl) containing quartz as the dominant detrital mineral. Authigenic TiOx occurs in open pores. b: Overview photomicrograph of Flechtingen Sandstone (sample FS 2, ppl), containing K-feldspar and VRF besides quartz grains and open porosity. c: Overview photomicrograph of Penrith Sandstone (sample PS 1, ppl), containing detrital quartz encompassed by pore-lining FeOx, overgrown by authigenic quartz. d: Photomicrograph of CS (sample CS 2, xpl). Pore-filling illite, dolomite rhombs, pore-filling FeOx. e: Photomicrograph of FS (sample FS 1, xpl). Tangential pore-lining illitic grain coatings encompassing quartz grains, as well as grain-to-grain illite coatings (GTG coating). f: Photomicrograph of PS (sample PS 3, xpl). Tangential pore-lining illitic grain coatings, as well as pigmented FeOx rims. FeOx rims were observed to be overgrown by authigenic quartz, while continuous illite coatings were observed to inhibit quartz overgrowth. h: Ternary sandstone diagram after Folk (1980), showing sandstone types for the different study areas. Cornberg Sandstones were classified as subarkoses, FS were classified as lithic arkoses to feldsphatic litharenites, and PS were categorized as sublitharenites to quartzarenites. i: Porosity-loss diagram after Lundegard (1992). FS samples are mostly compaction dominated, while CS and PS plot in slightly compaction to slight cementation dominated area, with PS being able to retain significantly more open porosity. Por: open porosity, Qtz: quartz, TiOx: titanium oxide, ppl: plane polarized light, xpl: cross-polarized light, Kfs: K-feldspar, VRF: volcanic rock fragment, FeOx: iron oxides, cmt: cement, Ill: illite, pl: pore-lining, pf: pore-filling dol: dolomite, GTG: grain-to-grain, GTI: grain-to-intergranular-volume.

Grain coating phases

Grain-to-grain clay coating coverages range from 20-21 % in Cornberg Sandstones, from 28-35 % in Flechtingen Sandstones, and from 11-18 % in Penrith Sandstones (Tab. 4.3). Grain-to-IGV clay coatings range from 20-34 % in Cornberg Sandstones, from 50-55 % in Flechtingen Sandstones, and from 15-22 % in Penrith Sandstones (Tab. 4.3).

Optical porosity

Intergranular porosities of Cornberg Sandstone samples are on average at 2.7±0.6 %, with low intragranular porosities (avg.: 0.3±0.2 %), resulting in optical porosities of up to 3.7 % (Tab. 4.3). Intergranular porosities in Flechtingen Sandstone samples are on average 4.0±0.8 %, while intragranular porosity contributes on average 4.0±0.4 % to the optical porosity, totaling at an average of 8.0 %. Penrith Sandstones show intergranular porosities on average at 18.9±1.5 %, intragranular porosity of 1.3±0.2 % and total optical porosities of 20.2±1.4 %. Sample PS3 is an outlier compared to PS1 and PS3 showing highest measured optical porosities at 23.7 %.

Compaction

The Cornberg Sandstones experienced a balanced porosity reduction between compactional and cementational porosity loss (avg. compaction index: 0.51, Fig. 4.3 i) with IGVs ranging from 28.7 to 30.7 % (avg.: 29.7 %). Porosity in Flechtingen Sandstones was dominantly reduced by compaction (avg. compaction index: 0.75, Fig. 4.3 i), leading to IGVs from 17.0 to 21.3 % (avg.: 19.2 %). Penrith Sandstones are slightly dominated by porosity loss by cementation (avg. compaction index: 0.43, Fig. 4.3 i). Their IGVs are ranging from 33.3 to 40.7 % (avg.: 37.0±1.0 %). Sample PS3 records the highest IGV at 40.7 % and the lowest compactional index of 0.30 (Tab. 4.3).

Effective contact lengths and effective contact ratio

Effective contact lengths range from 0.15-0.22 mm for Cornberg Sandstones, from 0.15-0.18 mm for Flechtingen sandstones, and from 0.13-0.20 mm for Penrith Sandstones (Tab. 4.3). The normalized effective contact ratio ranges from 67.2-67.2 % for Cornberg Sandstones, from 64.7-68.6 % for Flechtingen Sandstones, and from 56.4-62.2 % for Penrith Sandstones (Tab. 4.3).

4.5.2 Rock mechanics

Results of geotechnical tests are displayed as averages with their measured ranges (Fig. 4.4). The unconfined compressive strength (UCS) ranges from 3.2 to 61.7 MPa (Tab. 4.1). Cornberg Sandstones show highest average strength (UCS 57.6 MPa), Flechtingen Sandstones shows comparable strength (avg. UCS 53.9 MPa), and Penrith Sandstones show the lowest average compressive strength (avg. UCS 16.4 MPa) (Tab. 4.1,

Fig. 4.4). Rock failure was observed at fracture angles between 65 and 85°. Strain at failure ε ranges from 0.46 to 1.05 % (Tab. 4.1), with strain at failure averages of 0.58 % (CS), 0.70 % (FS) and 0.64 % (PS) for the respective sample locations. Young's modulus ranges from 0.324 to 12.679 GPa. Cornberg Sandstones show highest Young 's moduli (avg.: 11.597 GPa, range: 9.921 to 12.679 GPa), followed by Flechtingen Sandstones (avg.: 9.988 GPa, range: 8.997 to 10.979 GPa), while Penrith Sandstones are lowest (avg.: 4.865 GPa, range: 0.319 to 7.422 GPa). Bulk densities range from 1.71 g/cm³ to 2.35 g/cm³, with Flechtingen Sandstones showing the highest densities (avg.: 2.31 g/cm³, range: 2.27 to 2.35 g/cm³), closely followed by Cornberg Sandstones with very similar densities (avg.: 2.28 g/cm³, range: 2.25 to 2.30 g/cm³). The densities in Penrith Sandstones samples are lower (avg.: 1.99 g/cm³, range: 1.71 to 2.11 g/cm³) (Tab. 4.1).

Table 4.1. Geomechanical results. UCS – unconfined compressive strength, E - Young's modulus, e – strain.

Sample	UCS [MPa]	Density [g/cm³]	E [GPa]	ε [%]	Length [mm]	Diameter [mm]
CS 1 a	61.7	2.245	12.68	0.57	203.6	92.5
CS 1 b	52.7	2.248	11.70	0.58	203.5	92.5
CS 2 a	56.9	2.303	11.32	0.56	201.0	92.1
CS 2 b	54.8	2.293	9.92	0.61	201.5	92.1
CS 2 c	61.7	2.292	12.37	0.56	201.5	92.5
FS 1	46.4	2.268	9.00	0.63	124.0	50.0
FS 2	61.5	2.353	10.98	0.77	125.0	50.0
PS 1 a	20.9	2.051	6.31	0.57	81.5	38.1
PS 1 b	19.1	2.06	5.87	0.51	82.0	38.1
PS 1 c	22.0	2.084	7.42	0.46	80.9	38.1
PS 1 d	23.0	2.114	6.80	0.61	81.5	38.1
PS 1 e	20.6	2.069	6.14	0.54	81.5	38.1
PS 2 a	22.2	2.078	6.19	0.58	81.1	38.1
PS 2 b	19.5	2.055	5.50	0.58	82.5	38.1
PS 2 c	20.4	2.059	6.40	0.53	81.3	38.1
PS 2 d	19.4	2.094	6.34	0.49	80.9	38.1
PS 3 a	3.6	1.793	0.62	0.86	81.1	38.1
PS 3 b	3.2	1.708	0.32	1.05	80.5	38.1
PS 3 c	3.2	1.747	0.47	0.86	68.6	38.1

Table 4.2. Point-counting results (300 counts per sample). All values are in %. RF: rock fragment, VRF: volcanic RF, PRF: plutonic RF, MRF: metamorphic RF, rp: replaces, undiff.: undifferentiated.

	CS 1	CS2	FS 1	FS 2	PS 1	PS 2	PS 3
Detrital components							
Quartz	65.3	60.3	47.3	48.0	60.7	55.3	53.7
K-feldspar	1.0	1.0	13.7	10.0	2.0	2.7	2.3
Plagioclase	0.0	0.0	0.0	0.0	0.7	0.0	0.0
Matrix undiff.	0.0	0.0	0.0	0.0	0.0	0.3	0.0
Shale RF	0.7	1.0	0.7	0.7	0.0	0.0	0.0
Sandstone RF	0.3	0.0	0.7	0.3	0.0	0.3	0.7
Silicic VRF	0.0	0.0	1.7	1.3	0.3	0.3	0.3
Feldspathic VRF	0.0	0.0	2.0	1.3	0.3	0.3	0.0
VRF undiff.	0.0	0.0	2.3	2.0	0.0	0.0	0.0
Felsic PRF	0.0	0.0	0.3	0.0	0.0	0.0	0.0
Granitic PRF	0.0	0.0	1.7	1.3	0.0	0.0	0.3
Quartzite	1.7	0.7	1.7	2.3	0.7	0.3	0.7
Phyllite	0.0	0.0	1.0	0.3	0.0	0.0	0.0
MRF undiff.	0.7	0.0	0.0	0.3	0.0	0.0	0.0
RF undiff.	1.0	2.0	0.0	0.0	0.0	0.0	0.0
Chert	0.0	0.0	0.7	0.3	0.3	1.0	0.0
Mica	0.0	0.0	0.3	1.3	0.0	0.3	0.0
Zircon	0.0	0.0	0.0	0.0	0.0	0.0	0.0
Authigenic minerals							
Quartz	8.3	6.0	5.0	6.3	12.7	12.3	14.3
Dolomite	3.3	8.0	0.0	0.0	0.0	0.0	0.0
K-feldspar	0.0	0.0	2.3	1.3	0.0	0.3	0.3
Illite, pore-filling	9.0	8.7	0.3	2.0	0.0	0.7	0.3
Illite, pore-lining	0.7	1.3	5.0	4.7	2.0	3.3	1.3
Kaolinite, pore-filling	1.7	1.0	0.0	0.0	0.0	0.0	0.0
FeOx, pore-filling	0.7	2.7	0.7	0.7	0.3	1.3	0.0
FeOx, pore-lining	0.0	0.0	1.3	1.0	0.7	0.7	1.0
TiOx	1.3	1.0	0.0	0.0	0.7	1.3	0.7
Barite	0.0	0.3	0.0	0.0	0.0	0.0	0.0

Table 4.2 (cont.). Point-counting results (300 counts per sample). All values are in %. RF: rock fragment, VRF: volcanic RF, PRF: plutonic RF, MRF: metamorphic RF, rp: replaces, undiff.: undifferentiated.

	CS 1	CS2	FS 1	FS 2	PS 1	PS 2	PS 3
Replacements							
Carbonate rp K-feldspar	0.3	0.0	0.0	0.0	0.0	0.0	0.0
Illite rp K-feldspar	0.0	3.3	2.0	4.0	0.0	0.7	0.3
Illite rp kaolinite	0.3	0.0	0.0	0.0	0.0	0.0	0.0
Kaolinite rp K-feldspar	0.0	0.3	0.0	0.3	0.0	0.0	0.0
Optical porosity							
Intergranular porosity	3.7	1.7	5.7	5.3	17.0	17.0	22.7
Secondary porosity K-feldspar	0.0	0 .0	3.7	3.7	1.3	0.7	1.0
Secondary porosity undiff. RF	0.0	0.7	0.0	1.0	0.3	0.7	0.0

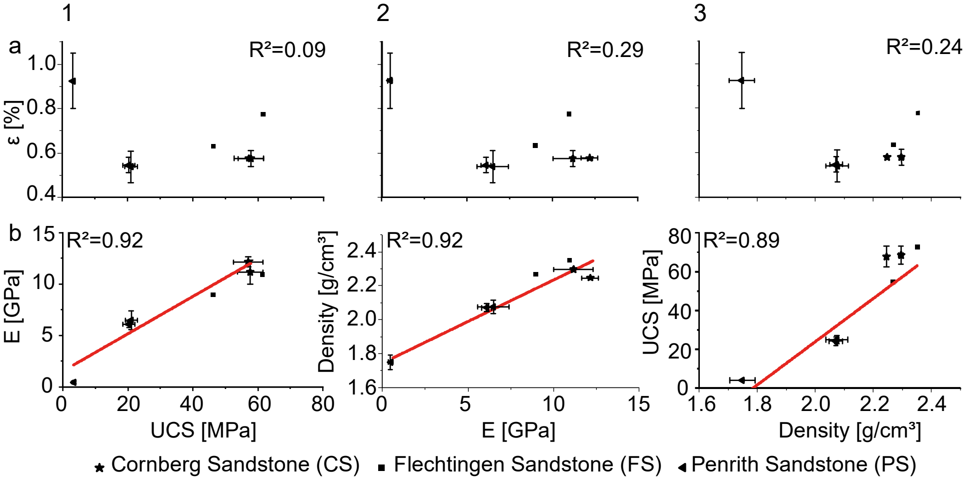

Figure 4.4. Cross plots of geotechnical tests, with all tested parameters plotted against each other. Symbols indicate average values of tested samples; error bars represent the measured range of values. Linear lines of best fit indicate correlations and the corresponding R². The outlier sample PS3 in a) negatively affects an otherwise good correlation. UCS: Uniaxial compressive strength, E: Young's modulus, ε: strain at failure.

Table 4.3. Petrographic data for sandstone classification, porosity reduction mechanism, and mechanical behavior. Quartz, feldspar and rock fragment pole were classified after Folk (1980). All values, if not specified, are in %. vws: very well sorted, ews: extremely well sorted, IGV: intergranular volume.

	CS 1	CS2	FS 1	FS 2	PS 1	PS 2	PS 3
Sandstone classification							
Median grainsize [mm]	0.49	0.31	0.32	0.43	0.36	0.28	0.45
Sorting (Trask 1930)	vws	vws	vws	vws	vws	vws	ews
Quartz pole	94.8	93.8	73.7	60.1	94.4	92.3	93.7
Feldspar pole	1.4	1.5	16.6	17.2	4.1	4.4	4.6
Rock fragment pole	3.8	4.6	9.8	22.7	1.5	3.3	1.7
Porosity reduction							
Optical porosity	3.7	2.3	10.0	6.0	18.7	18.3	23.7
Cement volume	25.0	28.3	16.0	14.3	16.3	20.0	18.0
Intergranular volume	28.7	30.7	21.3	17.0	33.3	37.0	40.7
Compactional porosity loss	22.9	20.7	30.1	33.7	17.5	12.7	16.7
Cementational porosity loss	19.3	23.0	11.2	9.5	13.5	17.5	7.3
Compactional indices	0.54	0.47	0.73	0.78	0.56	0.42	0.30
Grain-to-grain clay coating coverage	20.0	20.9	27.7	34.5	18.1	15.9	11.1
Grain-to-IGV clay coating coverage	20.3	33.5	50.2	54.6	20.3	22.4	14.7
Effective contact length [mm]	0.22	0.15	0.15	0.18	0.18	0.13	0.20
Effective contact ratio	67.2	67.3	64.7	68.6	59.4	62.2	56.4
Mechanical behavior							
Total clay	13.7	15.7	9.3	13.3	2.0	5.3	2.0
Rock strength index	0.055	0.035	0.155	0.087	0.314	0.295	0.420

4.5.3 Correlations of petrographic and mechanical properties

Petrographic correlations

Optical porosity shows a negative correlation the effective contact ratio (ECR, R^2=0.91) (Fig. 4.5 f1). The intergranular volume shows a positive correlation with quartz cements (R^2=0.73) (Fig. 4.5 a2) and a positive correlation with the compactional index (R^2=0.92) (Fig. 4.5 c2). It seems to be negatively correlated with ECR (R^2=0.61) (Fig. 4.5 f2) but does not clearly correlate with the median grain size (R^2=0.47) (Fig. 4.5 d2). Grain-to-grain and grain-to-IGV clay coatings shows a negative correlation with quartz cements (R^2=0.69, R^2=0.66) (Fig. 4.5 a3, a4) and a negative correlation with the intergranular volume (R^2=0.97) (Fig. 4.5 b3, b4). It also positively correlates with the compactional index (R^2=0.90, R^2=0.84) (Fig. 4.5 c3, c4), while a correlation with optical porosity and ECR remain indistinct (Fig. 4.5 d3, d4).

Samples with higher porosities show higher quantities of quartz cements (Fig. 4.5 a1). Samples from northern England (PS) show the highest amount of quartz cements while simultaneously having the lowest grain-to-IGV coatings (Fig. 4.5 a4). Sandstones from the Flechtingen High (FS) show the smallest amounts of quartz cements while having the highest grain-to-IGV coating coverage in this data set. Outlying Cornberg Sandstones (CS) samples show dolomite cementation (Fig. 4.3 d). Optical porosity and grain-to-IGV coatings show no clear correlation (Fig. 4.5 d4) due to the increased abundance of pore-filling dolomite and illite in Cornberg Sandstone samples (Tab. 4.2). Penrith Sandstone samples show highest porosities (Tab. 4.3), lowest grain-to-IGV coating coverage (Tab. 4.3) and highest amount of quartz cements (Tab. 4.2).

Density shows a negative correlation with optical porosity (R^2=0.80, Fig. 4.6 b2) and with IGV (R^2=0.71, Fig. 4.6 a2). It has a positive correlation with the compactional index (R^2=0.62, Fig. 4.6 c2), the total clay fraction (R^2=0.71, Fig. 4.6 d2) grain-to-grain coatings (R^2=0.69, Fig. 4.6 e2), and with grain-to-IGV coatings (R^2=0.54, Fig. 4.6 f2), and the ECR (R^2=0.89, Fig. 4.6 g2). Amounts of total clays in both Flechtingen- and Cornberg Sandstones are similar (Tab 4.2, 4.3), while IGV is ~ 50 % larger for Cornberg samples (Tab. 4.3). This results in a correlation coefficient below 0.5 between IGV and total clay (Fig. 4.5 b2).

Mechanical correlations

Young's modulus correlates well with UCS (R^2=0.92, Fig. 4.4 b1) and density (R^2=0.92, Fig. 4.4 b2). Similarly, rock density correlates with compressive strength (R^2=0.89, Fig. 4.4 b3). Strain does not correlate with compressive strength (Fig. 4.4 a1), E (Fig. 4.3 a2) or bulk density (Fig. 4.4 a3).

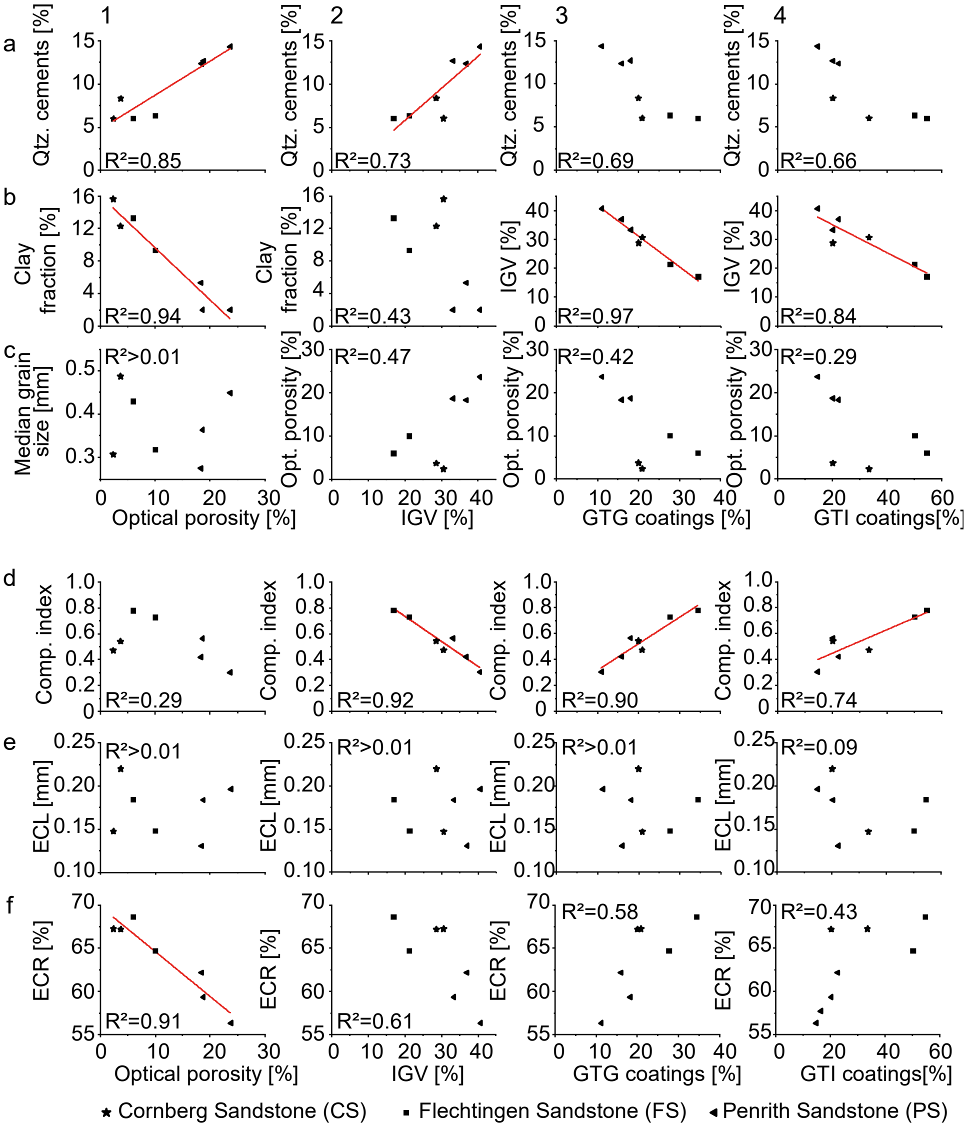

Figure 4.5. Cross plots of petrographic parameters, with selected parameters plotted against optical porosity, IGV, grain-to-grain coatings and grain-to-IGV coatings. Linear lines of best fit indicate correlations and the corresponding R². Correlations on porosity, quartz cement and ECR would improve if the Cornberg Sandstones preserving early carbonate cements would not be considered. ECR: Effective contact ratio, IGV: Intergranular volume, GTG: grain-to-grain, GTI: grain-to-IGV.

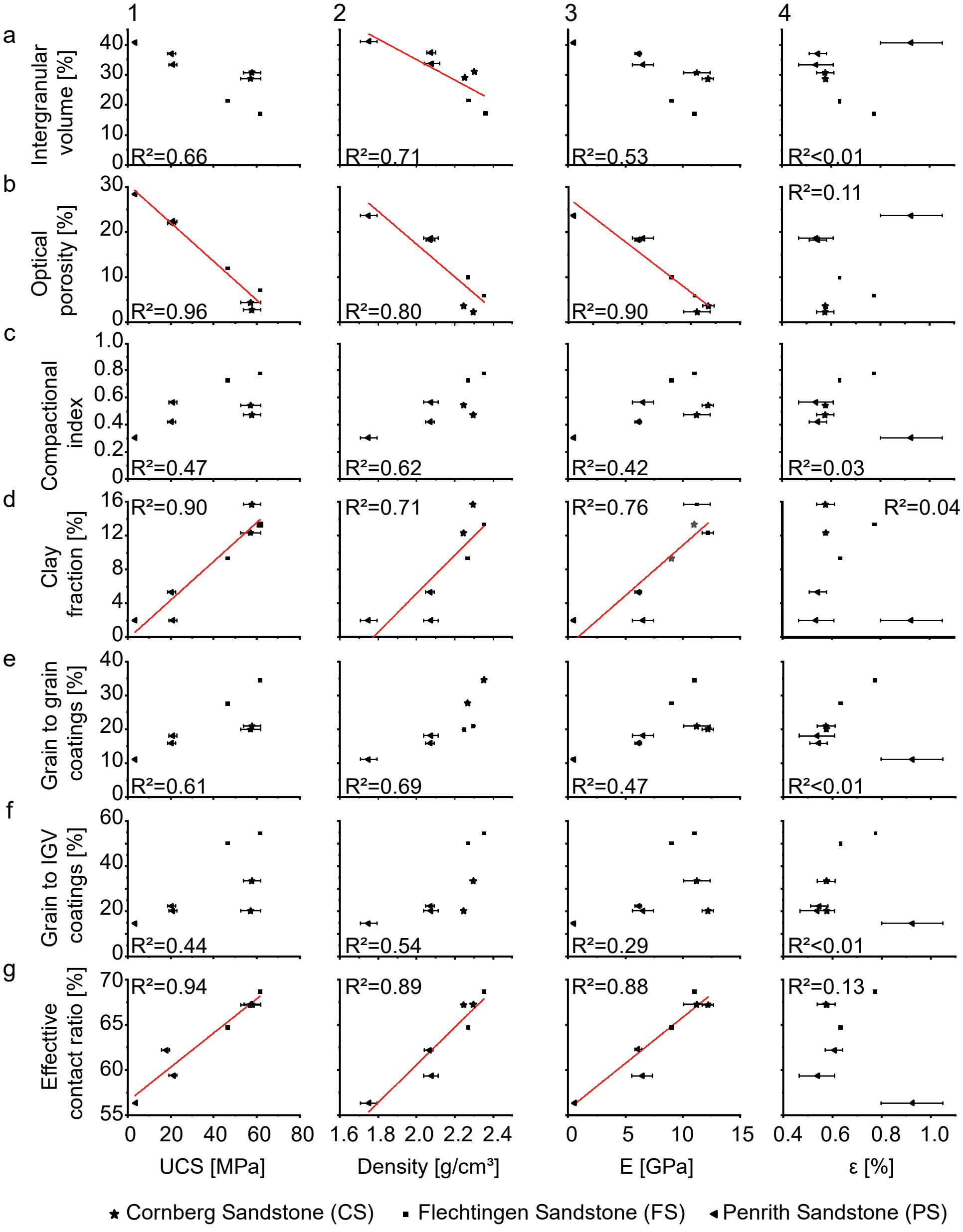

Figure 4.6. Cross plots of all geotechnical parameters on the x-axis compared to selected petrographic parameters on the y-axis. Linear lines of best fit indicate correlations with $R^2 \leq 0.7$ and the corresponding R^2. Correlations on IGV and coatings with mechanical parameters would improve if the diagenetic difference of preserved early carbonate cements of Cornberg sample would be considered outliers. UCS: Uniaxial compressive strength, E: Young's modulus, ε: strain at failure.

Correlations between petrographic and mechanical parameters

The rock strength shows a negative correlation with the intergranular volume (R^2=0.66, Fig. 4.6 a1) and a negative correlation with optical porosity (R^2=0.96, Fig. 4.6 b1). The rock strength relates positively to the total clay fraction (R^2=0.90, Fig. 4.6 d1) and the distribution of authigenic clay coats on detrital quartz grains. The amount of illite coats along the grain-to-grain contacts show a reasonable correlation (R^2=0.61, Fig. 4.6 e1), while the illite coats along the grain-to-IGV do not correlate (R^2=0.44, Fig. 4.6 f1). The effective contact ratio shows a positive correlation with rock strength (R^2=0.94, Fig. 4.6 g1).

The Young's modulus shows a positive correlation with the total clay fraction (R^2=0.76, Fig. 6 d3) and a negative correlation with the IGV (R^2=0.53, Fig. 6 a3). It correlates negatively with optical porosity (R^2=0.90, Fig. 4.6 b3). A correlation with the compactional index (R^2=0.42, Fig. 4.6 c3) and grain-to-grain coatings is indistinct (R^2=0.47, Fig. 4.6 e3). The effective contact ratio shows a positive correlation with Young's modulus (R^2=0.88, Fig. 4.6 g3). Strain shows no correlation with any of shown petrographic parameters (Fig. 4.6 a4-g4), which is further explored in the discussion.

The rock strength index ranges from 0.035 to 0.420 (Tab. 4.3) and shows positive correlations with the uniaxial compressive strength (R^2=0.97), Young's modulus (R^2=0.94) and density (R^2=0.85) (Fig. 4.7).

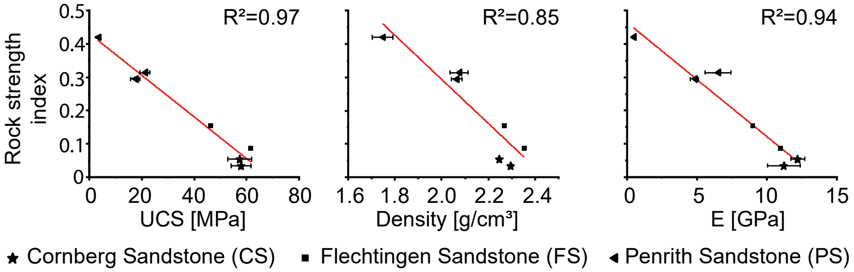

Figure 4.7. Rock strength index versus uniaxial compressive strength (UCS), Density and Young's modulus (E).

4.6 Discussion

4.6.1 Petrology and diagenesis

The assessment of detrital and authigenic phases, as well as mechanical and chemical compaction and their documented impact on the modification of the pore space, over geologic time scales, is the basis for the evaluation of the mechanical properties relevant at reservoir timescales. Here, the variations and implications of different rock types, as a function of different provenances, and cementation and compaction, as a function of different burial histories are discussed for the presented samples.

Impact of petrology

A positive correlation exists between the IGV and porosity (Fig. 4.5 d2), if Cornberg samples are not considered (R^2=0.97). Similarly, the compactional index based on Lundegard (1992) correlates well with the optical porosity (R^2=0.91) when Cornberg Sandstones are excluded (Fig. 4.5 c1). The preservation of early carbonate cementation limited to Cornberg Sandstones, preventing mechanical compaction (Fig. 4.3), is interpreted to be responsible for these outliers.

Impact of chemical compaction

Higher coverages of illitic grain-to-grain coatings at quartz-quartz interfaces are a major control of chemical compaction due to electrochemical potential differences on quartz-illite/muscovite-quartz interfaces (Greene et al., 2009; Kristiansen et al., 2011; Monsees et al., 2020a). This is supported by the negative correlation between the compactional index and IGV (Fig. 4.5 c2). The negative correlation between grain-to-grain coatings and quartz cement (Fig. 4.5 c3) is interpreted as side-effect of the reduction of IGV by compaction (Fig. 4.5 c2), leading to less potential cement volume, which is also supported the positive correlation between IGV and quartz cements (Fig. 4.5 d2).

Impact of cementation

Smaller grain-to-IGV coating coverages are interpreted to control the IGV (Fig. 4.5 b4) by enhancing syntaxial quartz cementation (e.g. Busch et al. (2017)). This results in a stabilization of the grain fabric and subsequently less mechanical compaction. The link between mechanical compaction and the reduction of pore-filling cementation is also demonstrated by the correlation between the compactional index after Lundegard (1992) and grain-to-IGV coatings (Fig. 4.5 c4).

The unique diagenetic feature of Cornberg Sandstone compared to the other samples of this study is the abundant preservation of early carbonate cements, which are still present in subsurface equivalents of Flechtingen Sandstone (Mumm & Wolfgramm, 2002) and

Penrith Sandstone (Turner et al., 1995). Minor amounts of mouldic pores in authigenic quartz cement (Fig. 4.3 c) were attributed to dolomite cement dissolution and occasionally occur in Penrith Sandstone (Busch et al., 2017), however they were not encountered during point-counting. Similarly, authigenic calcite in Flechtingen Sandstone samples as reported by Fischer et al. (2012) were not encountered during point-counting in the studied samples.

Impact on porosity

The apparent contradiction between highest amounts of quartz cements and highest porosities highlights its dependence of the IGV on several parameters. Therefore, the degree of compaction represented by compactional indices ranging from 0.2 to 0.8 and IGVs ranging from 17.0 to 40.7 % are identified as one of the main controls on the porosity evolution. Porosity is generally reduced with reducing IGV (Paxton et al., 2002). IGVs in quartz sandstones are exponentially reduced during burial up to 26 % by mechanical loading due to ideal packing of spherical grains, assuming well sorting and no major detrital clay (<5 %) as boundary conditions (Paxton et al., 2002). The sandstone composition in this study matches these criteria (Tab. 4.2, 4.3). IGVs as low as 17 % indicate that chemical compaction on long grain contacts took place, which is reflected by the increase in ECR for samples with lowest IGV (Fig. 4.5 f2) and highest grain-to-grain illite coatings (Fig. 4.5 f3) (Monsees et al., 2020a). Studies from natural sandstones show an influence of median grain size on porosity ranging from very significant to completely insignificant (Baud et al., 2014; Bell, 1978; David et al., 1998; Fahy & Guccione, 1979; Taylor et al., 2010). This has been explained by the influence of porosity, detrital and authigenic components and various amounts of compaction (McKinley et al., 2011; Morad et al., 2010). The control on optical porosity in this study is the sum of detrital and authigenic clay based on linear regression analysis (Fig. 4.5 b1), showing the expected negative correlation with optical porosity due to the ductile properties of clay. Median grain size is not a controlling factor on porosity in this study (Fig. 4.5 d1). Detrital composition also does not have a clear impact on the porosity evolution in this data set, because Cornberg- and Penrith Sandstones with very similar detrital composition (Fig. 4.3 h) show large porosity differences (Fig. 4.5 a-f1).

4.6.2 Diagenetic and geomechanical rock properties

Since diagenesis, as a function of provenance, mechanical and geochemical alteration modifies the pore structure and particle contacts over geological timescales, the diagenetic contribution to present-day measured geomechanical properties, relevant for production timescales, should be derivable. Positive correlations between UCS, Young's modulus and rock density (Fig. 4.3) are well established elsewhere (Dobereiner, 1986; Shakoor & Bonelli, 1991). UCS, Young's modulus and bulk density consistently show similar trends when plotted against the petrographic proxies IGV, optical porosity, compactional index, clay, GTG and GTI coatings, and effective contact ratio (Fig. 4.6), however correlation coefficients vary.

Impact of chemical compaction

Grain size in artificial pure sandstones (quartz arenite) without chemical compaction correlates well with UCS (Atapour & Mortazavi, 2018). Chemical compaction is driven by (i) the amount of overburden, temperature, and fluid pressure i.e. the effective stress and the amount and size of quartz grains, and is reflected by the type of quartz grain-contacts (Bjørlykke & Høeg, 1997; Renard et al., 1997), and (ii) the extent of clay coating on rigid quartz along quartz-quartz contacts driving pressure solution (Greene et al., 2009; Kristiansen et al., 2011; Monsees et al., 2020a).

Impact of porosity

Optical porosity seems to control UCS (Fig. 4.6 b1) and density (Fig. 4.6 b2) due to lower strength and densities (Atapour & Mortazavi, 2018; Baud et al., 2014; Hsieh et al., 2008; Weng et al., 2005). Thus, the reduction of porosity and the increase of the effective contact ratio (ECR) during diagenesis needs to be constrained in order to assess rock strength in context of diagenetic alterations.

Impact of cementation

Cross-plots between geotechnical parameters and individual authigenic minerals such as quartz cements yielded no conclusive results. However, using the intergranular volume as the sum of intergranular porosity and cements, samples with less IGV, thus more heavily compacted, show higher UCS (Fig. 4.6 a1), Young's modulus (Fig. 4.6 a2) and densities (Fig. 4.6 a2). This is interpreted to be due to the fraction of intergranular porosity, which leads to lower rock strength and density, and due to authigenic minerals, also contributing to the IGV. The observed negative correlation between UCS and clay content (Fig. 4.6 d1) seems counter-intuitive, implying a higher clay content in sandstones would result in higher strength. Similar negative correlations have been reported in weak sandstones with UCS < 20 MPa (Chen & Hu, 2003), however they were limited to the same rock type. The negative correlation in this study is due to CS and FS samples being either significantly more cemented (CS) with higher clay contents, or more compacted and cemented (FS), while PS samples show higher IGVs, higher optical porosities, and lower UCS (Fig. 4.6 a1, b1, e1).

Impact of clay coatings

Clay coatings seem to exhibit a small to intermediate control on geomechanical properties. Illitic grain coatings can inhibit syntaxial quartz cementation but may drive chemical compaction (Busch et al., 2020; Monsees et al., 2020a). Consequently, the absence of illitic grain coatings favors early syntaxial cementation, thus reducing the effect of mechanical compaction. These processes are reflected by the GTG and GTI coating analyses (Monsees et al., 2020a) and the compactional index (Lundegard, 1992), respectively.

Grain-to-grain coating clay increases the density (Fig. 4.6 e2) due to their inferred control on chemical compaction (Fig. 4.5 c3) (Monsees et al., 2020a), subsequently also enhancing the UCS (Fig. 4.6 e1) and E (Fig. 4.6 e3). The correlation of grain-to-IGV coatings with density is barely meaningful (Fig. 4.6 f2) and implies that more quartz cementation results in lower density, as GTI coatings were observed to exhibit a control on quartz cementation (Fig. 4.5 a4). The IGVs are higher in the sample group with the highest amounts of quartz cements (PS, see Fig. 4.5 d2), as a result the counter-intuitive positive correlation between GTI coatings and density is due to less compaction, and thus less reduction of potential porosity (e.g. Paxton et al. (2002)). Correlations of GTI coatings with UCS (Fig. 4.6 f1) and E (Fig. 4.6 f3) show the same positive trend due to the good correlation between UCS, E and density (Fig. 4.3 b1-3), however their correlation coefficients consistently are around or below R^2=0.5.

Implications for deformation

No linear correlation of strain at failure (ε) with any of the petrographic proxies could be established (Fig. 4.6). However, there seems to be a logarithmic relationship between ε and the ratio of IGV/compactional index (Fig. 4.6 a4, c4) if the outlier in the upper right (sample PS3 from quarry B, see section 4.5) would be removed. Similar observations were made for the plots comparing ε and grain-to-grain coatings (Fig. 4.6 e4, f4), if sample PS3 would be excluded. The resulting correlation coefficients would be around R^2=0.7 for Fig. 4.6 a4, c4, f4 and around R^2=0.85 for Fig. 4.6 e4. This would result in inelastic deformation represented by ε being controlled by grain-to-grain coatings (Fig. 4.6 f4), which would be in agreement with recent research on inelastic deformation of reservoir sandstones (Pijnenburg et al., 2019b), resulting in implications for induced seismicity (Pijnenburg et al., 2019a).

The higher porosity and resulting lower rock strength of sample PS3 due to being less compacted result in stronger displacement, explaining the higher ε compared to the possible strain-petrography relationship discussed here. Consequently, this would infer that this proposed relationship between strain at failure (ε) and the ratio of IGV/compaction index is only valid for sandstones that have undergone a certain amount of compaction and porosity reduction. UCS and E were determined in the same experiment as ε and showed consistent results.

Implications for the rock strength index

The rock strength in sandstones increases with the amount of porosity reduction (Fig. 4.6 b1) and increases with higher effective contact ratios between grains and cements (Fig. 4.6 g1). Both mechanical and chemical compaction reduce porosity and increase rock strength (Bjørlykke & Høeg, 1997). As both porosity (Fig. 4.6 b1) and effective contact ratios between particles (Fig. 4.6 g1) were shown to correlate with mechanical properties, we propose to calculate a rock strength index S_R for the samples in this study (Fig. 4.7).

The rock strength index shows a linear relationship for the tested UCS range from 3-60 MPa in the presented data set (Fig. 4.7), and enables a first order UCS, density and Young's modulus estimation based on petrographic data.

Implications for reservoir timescale

All interactions between parameters described so far can be categorized on the geologic and the reservoir timescale. The geologic timescale features processes of porosity reduction and compaction increasing rock strength, reflected by the effective contact ratio of grain contacts (Fig 4.6 g1), and decrease in porosity (Fig. 4.6 b1). On the reservoir timescale, the mechanical rock properties are related to cementation and chemical compaction, which are reflected by the effective contact ratio and rock strength index S_r (Fig. 4.8). Larger cement volumes and enhanced chemical compaction both enhance the effective contact ratio, thus reflecting the impact of diagenesis. The importance of clay mineral coatings in sandstones on reservoir timescales has been well established from geomechanical experiments (Pijnenburg et al., 2019b), while the quantification of this effect in heterogeneous sandstones may not universally applicable as presented in this study.

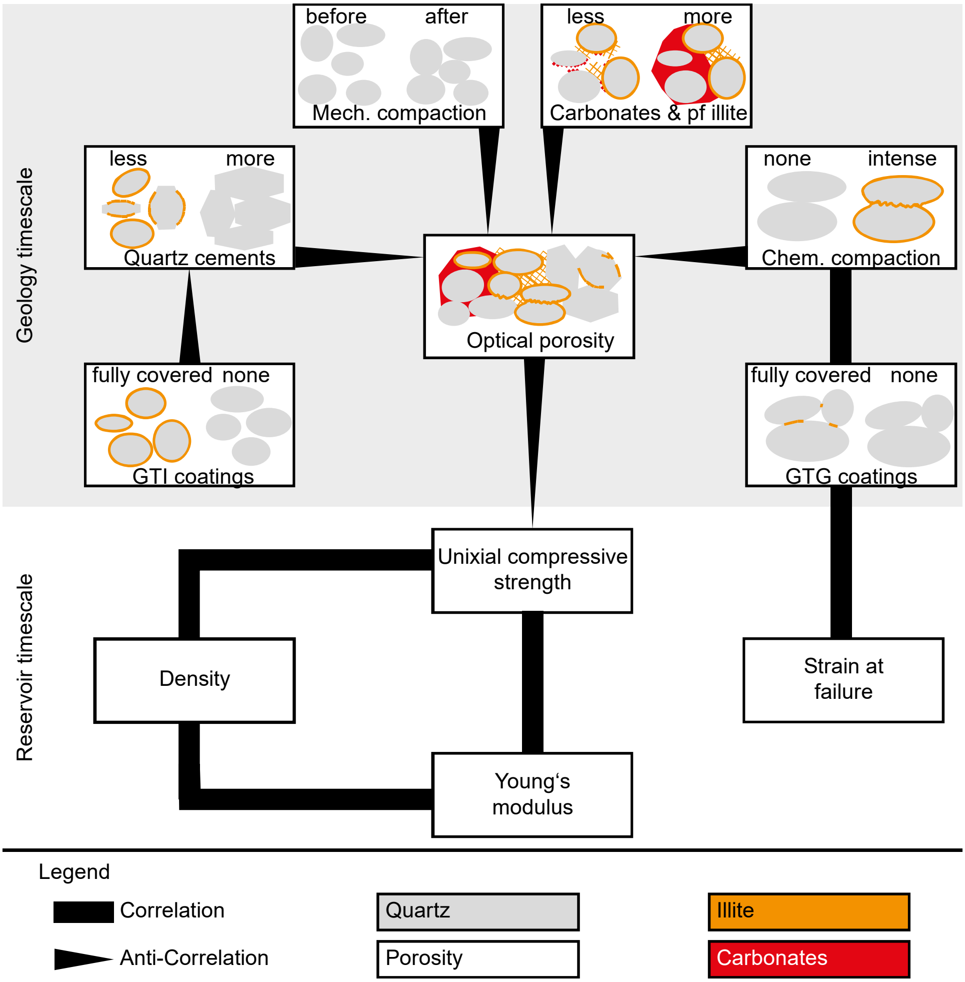

Figure 4.8. Schematic overview of the effect of diagenetic alterations on optical porosity and geomechanical properties. The geologic setting controls the initial parameters such as composition and depositional environment, as well as boundary conditions like temperature, pressure, ion availability etc. Each correlation line symbolizes a positive correlation e. g. if the uniaxial strength is high, Young’s modulus is also high. Each anti-correlation line symbolizes a negative correlation, e. g. if optical porosity is high, then uniaxial compressive strength is low. Effective contact lengths (Fig. 4.2) are increased by all compaction and cementation processes. GTI: Grain-to-IGV, GTG: grain-to-grain, pf: pore-filling.

4.7 Conclusions

The studied Rotliegend sandstones represent fluvio-eolian depositional environments mostly comprised of detrital quartz with close to no detrital clay component. Due to different diagenetic histories, their corresponding diagenetic alterations and porosity is different. Authigenic quartz is major diagenetic phase in all samples. Cornberg Sandstones show intermediate compaction and high cementation, Flechtingen Sandstones experienced a high amount of compaction and intermediate cementation, while Penrith Sandstones show low compaction and intermediate cementation.

Mechanical compaction was observed to be dependent on the abundance of pore-filling rigid authigenic minerals like carbonates and quartz stabilizing the grain-framework. Chemical compaction was assessed based on the illite coverages on grain-to-grain interfaces. Generally, higher compaction induced a porosity reduction depending on the different sample groups and diagenetic pathways. The presence of preserved early carbonate cementation in Cornberg samples was identified as a reason for outliers when assessing the petrographic properties in comparison to mechanical properties. Such different diagenetic evolution of similar sandstones might explain generally well working correlations in artificial (pure) sandstones compared to contradicting studies featuring natural, heterogeneous specimens.

Optical porosity was identified as the main control on UCS, Young's modulus and density with a pronounced negative correlation ($R^2>0.80$). Optical porosity is controlled by diagenetic alterations in this study, namely authigenic quartz, dolomite, and clay minerals together with mechanical and chemical compaction. Chemical compaction is dependent on the spatial relationships and abundance of grain-coating clay minerals and detrital and authigenic quartz.

The length of horizontal grain contacts normalized to the individual grain size relates grain fabric to mechanical properties. Effective contact ratios show positive correlations with UCS ($R^2=0.97$), Young's modulus ($R^2=0.94$) and density ($R^2=0.85$). Such petrography-based rock strength index based on porosity and effective contact ratio may be tested for other study areas.

The results of this study help to understand and quantify the relation between diagenetic parameters and geomechanical properties utilizing the rock strength index representing the sum of diagenetic influence on porosity reduction and grain connectivity orientated to the stress conditions. Consequently, they may be applied as first-order estimate of mechanical properties for sandstones with similar boundary conditions, if sufficiently large specimen for geotechnical standard tests are not obtainable.

5 Calibrating micro-computed tomography data to permeability experiments and petrography – insights from Digital Rocks

5.1 Abstract

Petrophysical measurements on core plugs integrated with petrographic information from thin-sections are established methods in reservoir quality assessment. X-ray micro-computed tomography (µCT) presents an opportunity to derive the internal structure of reservoir sandstones for digital fluid flow simulations, while simultaneously assessing mineral distribution in 3D based on mineral densities. We compare the single-phase permeabilities obtained with fluid flow simulations and experiments and discuss the anisotropic nature of the permeability tensor in both single- and two-phase flow. The results demonstrate a closer match for µCT porosity to petrophysical porosity compared to optical porosity, and an acceptable first order fit of the main mineralogical constituents. One-phase fluid flow simulations deliver results within 10–20 % of the laboratory measurements. Two-phase flow simulations enable the assessment of relative permeabilities in rocks with water-sensitive minerals. However, µCT-based fluid flow simulations are computationally very demanding and time consuming due to the heterogeneous nature of natural sandstone samples, and require a tradeoff between resolution, representative volume, and cost. Rock composition reconstructed from µCT images can be used as a first-order approximation for the composition of a sample, but is unable to confidently identify minerals that occur in minor quantities due to constraints of the chosen resolution. Thus, sandstone analyses by µCT cannot completely replace established methods. Calibrating µCT data to permeability experiments and petrography in Digital Rocks

5.2 Introduction

Petrographic analyses using thin-sections and petrophysical analyses utilizing core plugs are well established methods for reservoir characterization (Busch et al., 2020; Monsees et al., 2020a). “Digital Rocks” has become an established term, generally describing the digitization of structure and rock composition (Rassenfoss, 2011). Computer tomography has been utilized at least over the last twenty years as an upscaling approach from 2D thin-sections to 3D petrography models, incorporating rock physics (Golab et al., 2010;

Rassenfoss, 2011; Van Geet et al., 2001). Advances in computational power over the last decade combined with the ongoing process of digitization present new opportunities regarding fluid flow simulations through porous siliciclastic sandstones (Andrä et al., 2013a; Prajapati et al., 2018; Saxena et al., 2017).

We present digital rock volumes and numerical one- and two-phase fluid flow simulations based on x-ray micro-computed tomography (µCT) images. µCT is calibrated by petrophysical and petrographical laboratory analysis that determines porosity, permeability, and mineral distribution, highlighting the opportunities and challenges of digital rocks for petrophysical and mineralogical analysis (Fig. 5.1).

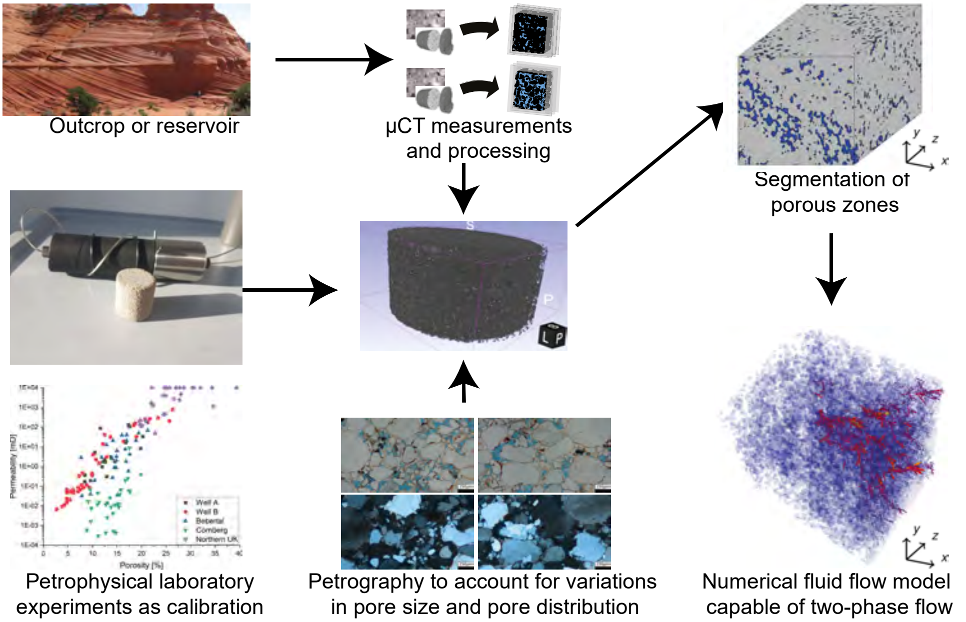

Figure 5.1. Schematic overview of the workflow used to simulate two-phase flow in siliciclastic reservoir rocks.

5.3 Materials & methods

5.3.1 Material and laboratory methods

A sample originating from the Upper Rotliegend siliciclastic Penrith Formation from the Vale of Eden half-graben (Cumbria, UK) is studied to highlight the approach. The particular sample was described in a petrographic study (sample BQ_1 in Busch et al. (2017)).

All petrophysical measurements are performed on a cylindrical sandstone plug (diameter: 25.4 mm, length: 40.0 mm) drilled parallel to bedding. The thin-section taken from the plug cap compares to the x-z plane of the computed model detailed further below and outlines the rock composition on a grain scale. The normal to bedding is reflected by the y-direction.

Petrophysical measurements include porosity and ambient permeability. Porosity was determined using helium pycnometry. Klinkenberg-corrected ambient permeability was measured at a constant confining pressure of 1.2 MPa with an air permeameter (Becker et al., 2017). Permeability is the connected porosity and describes how easy a fluid can flow through porous media. It is commonly measured in millidarcy (mD).

The petrographic data is derived from a transparent thin-section prepared from the plug cap. The plug cap was impregnated with a blue-dyed epoxy resin to highlight porosity and prepared to a thickness of 30 µm. Point-counting (300 counts) was performed on a grid adjusted to the maximum grain size with a semi-automated Pelcon Point Counter installed on a Leitz Aristomet microscope. The error of point-counting is dependent on the amount of counts and the counts per category, and was statistically quantified within confidence levels of 95 % (Howarth, 1998).

The plug for micro-computed tomography (µCT) is drilled normal to the petrophysical plug axis after petrophysical measurements are completed. The µCT plug has a diameter of 6.5 mm and a length of 13.0 mm.

5.3.2 µCT methods

Micro-computed tomography (µCT) scans were performed by MITOS GmbH with an image resolution of 2048*2048 px. This results in a horizontal µCT resolution of 3.3 µm/px. Petrography and porosity measurements serve as calibration for the segmentation of pore-space in the µCT image batch. The permeability measurement on rock plugs is used as the benchmark for the results of single-phase fluid in digital rock flow simulations. Images from µCT were stacked and segmented with ImageJ, using helium porosity from rock plugs as a control factor on the segmented porosity (Fig. 5.2). Two image sequences are generated for µCT analysis: One for density-based mineralogy assessment, and one for fluid flow simulations. The mineralogy data set is exported as a gray-scale data set, while the simulation image sequence is exported as a binary color set, segmented for porosity and solids. Contrast enhancements are necessary in order to enable a more precise segmentation for porosity or mineralogy.

The Beer-Lambert law describes the interaction between an x-ray beam and the material (Van Geet et al., 2001). The grayscale intensities are related to differences in x-ray attenuation of the respective minerals, which is parameter-specific and depends on atomic mass and density. It is incorporated in the Beer-Lambert law as attenuation coefficient (Curry et al., 1990). For the mineral assessment, µCT images are imported in the CT processing program Slicer to render a high-resolution 3D petrographic model. The segmentation was conducted with the segmentation tool in Slicer, which is able to separate a 3D model into its constituents based on grayscale intensities. The grayscale color intensities are dependent on the attenuation of the respective minerals. Under consideration of the rock composition given by point-counting, grayscales in the stacked µCT images can be segmented for mineralogy based on grayscale thresholds. The total and relative volume of segmented classes can be checked or exported at any time, and are used as a quality check.

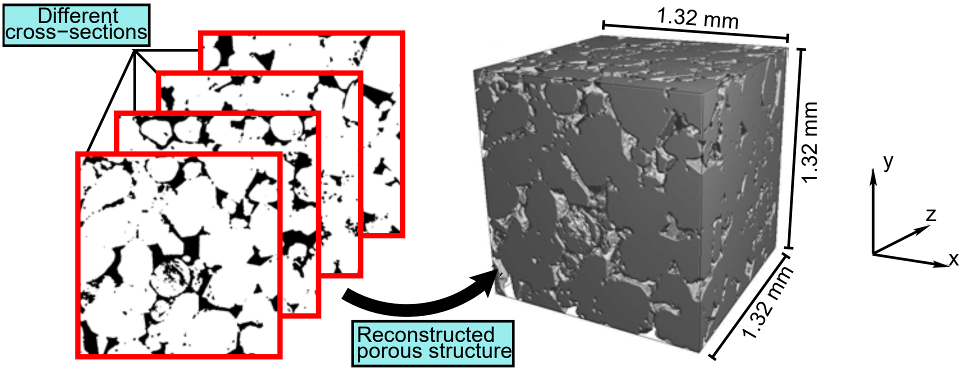

Figure 5.2. Digitized 3D structure using the µCT images. This example demonstrates a 400-pixel block, with a resolution of 3.3 µm/px. Cross-sections on the left reflect the texture of the x-y plane at different positions in z direction.

5.3.3 Simulation methods

For the purpose of solving fluid dynamical equations at the pore-scale, the color-gradient based lattice Boltzmann method is used in the present study. This method can deal with the wetting boundary condition and a range of fluid dynamic viscosity ratios. The numerical model's ability to capture these physical phenomena is tested with various benchmark tests. One of the main challenges of two-phase flow simulations lies in driving the flow through the narrow pores of digital rock structures. The numerical model utilizes a diffuse interface that can be as large as some of the pore throats, thus potentially unable to capture the capillary effects. As a compromise between the computational cost and reliability of simulations, numerical interface width is kept at six grid spacing. The simulation domain is a cube with dimensions of 1.32 mm (400*3.3 µm) in each direction (Fig. 5.2). The numerical interface width is then 6 times the grid spacing or roughly 19 micrometers. The cross-section images are in x and y direction for the fluid simulations (Fig. 5.2). These images are then stacked along z direction (Fig. 5.2).

For the evaluation of macroscopic properties (such as permeability) of generated digital structures, it is important to ensure that a sufficiently large domain is used. To choose such a volume, first, a series of single-phase permeability tests is carried out at increasingly large simulation domains. Once the permeability values obtained at two successive simulation domains are close to each other, this volume is chosen as the representative volume of the given sample. In this case, such a representative model is achieved with a cube of 400*400*400 pixel. This representative volume is then further utilized in the fluid flow simulations (Fig. 5.2).

5.3.3.1 One-phase flow

In the first step, single-phase intrinsic permeabilities of the sample are computed. For this purpose, a single-phase fluid is filled inside the simulation domain and is driven via gravity. The single-phase Darcy's law is

$$\overline{U} = \frac{\boldsymbol{K}.(-\nabla p + \rho\, \boldsymbol{g})}{\mu} \tag{5.1}$$

where $\overline{U}$ is the average fluid velocity, μ is dynamic viscosity, p is hydrodynamic pressure, g is the acceleration due to gravity, p is density and K is the intrinsic permeability tensor. The average fluid velocity is found as,

$$\overline{U} = \frac{1}{V} \sum U \tag{5.2}$$

where summation is carried out over entire volume V of the simulation domain and U is the local fluid velocity. The local fluid velocity U, in turn, is found from the solution of fluid dynamical equations via the lattice Boltzmann method. The density ρ=1000 kg/m^3 and dynamic viscosity μ = 3∗Pa.s (water) is chosen for the single/-phase fluid in the simulations. The single-phase permeability of any porous medium depends upon its pore-geometry and –size alone and is independent of the physical properties of the fluid used in the simulation. Thus, the simulated permeabilities can be compared directly with the experimental ones. To find the principal component of the permeability tensor K_{jj} (for brevity K_j is used hereafter), the component of the gravity vector g_j in the direction j is switched on. Direction j is a dummy variable running over the simulations in x, y, and z direction successively. Periodic boundary condition is applied in the j direction while no-slip boundary condition is applied on the lateral sides. The bounce-back rule (Zou & He, 1997) is applied at the solid-fluid boundary to ensure the no–slip boundary condition.

5.3.3.2 Two-phase flow

The two-phase Darcy's law is

$$\overline{U}_i = k_i(S_w)\frac{K.(-\nabla p + \rho_i g)}{\mu_i} \quad (5.3)$$

where the subscript *i* stands for the non-wetting gas (nw) or the wetting water (w) phase, *k* is the relative permeability and S_W is the saturation, which is the fraction of the wetting phase in the pore space. The average fluid velocity for the gas is computed as

$$\overline{U}_{nw} = \frac{1}{V}\sum U\,\frac{1-\varphi}{2} \quad (5.4)$$

$$\overline{U}_w = \frac{1}{V}\sum U\,\frac{1+\varphi}{2} \quad (5.5)$$

where summation is carried out over entire volume *V* of the simulation domain, and φ is the local phase-field variable, which identifies gas and water phases. The phase-field variable takes values -1 and 1 in the bulk non-wetting gas phase and wetting water phase, respectively. Similar to the single-phase case, U and φ result from the numerical solution of fluid dynamical equations via the lattice Boltzmann method. The wetting (water) phase saturation is related to the phase-field variable as

$$S_w = \frac{1}{V}\sum \frac{1+\varphi}{2} \quad (5.6)$$

Capillary number Ca and viscosity ratio $M = \frac{\mu_w}{\mu_{nw}}$ are dimensionless numbers, which characterize the two-phase flow of the non-wetting fluid gas with the wetting fluid water on the pore-scale. The capillary number is defined as $Ca = \frac{\mu_{nw}U}{\sigma}$, where μ_{nw} is the viscosity of the non-wetting fluid gas, U is the characteristic fluid velocity and σ is the surface tension. The capillary number provides a relative dominance of viscous forces compared to the surface tension ones. In this work, the capillary number is approximately 10^{-4} indicating an interplay of viscous and capillary forces. The viscosity ratio M is chosen as 10 corresponding to the typical petroleum reservoirs. In addition, the wetting contact angle Θ is chosen as Θ =164°.

5.4 Results

5.4.1 Laboratory results

The studied sample has a porosity of 18 % and a Klinkenberg-corrected permeability of 1040 mD (1.026 *10-9 m²) (Tab. 5.1). For the purpose of comparability with µCT data, petrographic results derived from point-counting (27 classes) have been simplified to five classes (Tab. 5.1). The sum of detrital and authigenic quartz, also including quartzite and mostly silicic rock fragments, is the most abundant constituent (89 %). The second most abundant constituent is the optical porosity (5.3 %), indicated by blue color in the thin-sections (Fig. 5.3), which comprises of intergranular and intragranular porosity. Feldspars (3.3 %), including K-feldspars and plagioclases, are the third most abundant class. The remaining components were grouped into clays (2.3 %), including mica as well as authigenic clay minerals, and iron oxides. Iron oxides occur in traces in the form of dust rims, and detrital grains and were not encountered during point-counting.

Table 5.1. Experimental petrophysical and petrographic results with statistical error ranges.

Petrophysical results	
Permeability	1040±30 mD (k_x)
Porosity	18.0±0.3 %
Petrographic results	
Quartz	89.0±2.8 %
Feldspar	3.3±1.7 %)
Optical porosity	5.3±2.3 %
Iron oxides	0.0±0.4 %
Clay	2.3±1.3 %

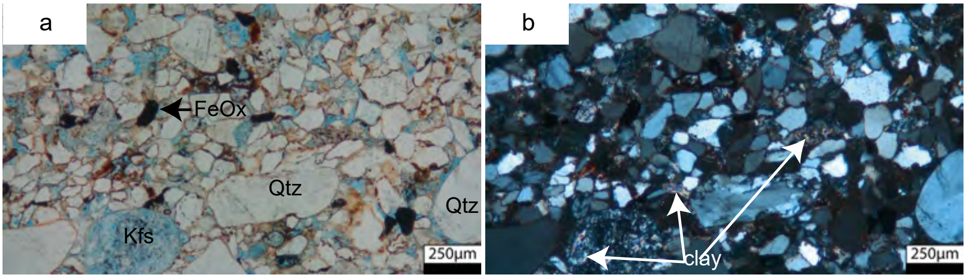

Figure 5.3. Figure caption on the next page.

Figure 5.3. Petrographic thin-section of an exemplary reservoir rock analog from the plug cap of the studied sample. Porosity is colored with blue epoxy. a) The studied sample is dominated by detrital quartz and overgrown cements, which can be distinguished from the detrital quartz due to the brown-reddish hematite coats. Feldspar dissolution (Kfs lower left) reflects the formation of secondary porosity during burial and uplift (further details about the diagenesis see (Busch et al., 2017)). Pictures in plane-polarized light. b) Arrows indicate small patches of clay minerals, mostly illite and mica, which occur as feldspar replacements or squeezed between the rigid grains. Picture in cross-polarized light. Qtz: quartz, Kfs: Potassium feldspar, FeOx: iron oxides.

5.4.2 Digital rock results

Digital petrography and porosity

Mineral composition is derived from µCT images by enhancing contrast and comparing to the most abundant minerals in petrographic thin-section analysis (Fig. 5.4 a). The black color represents phases with the smallest density (porosity), while the highest densities are present as bright white areas. The major constituent (quartz) is dark gray (Fig. 5.4 a). The selected cube primarily consists of quartz (81.6 %), and epoxy resin (porosity, 13.4 %) (Tab. 5.2, Fig. 5.4 b). Minor constituents are clay minerals (2.1 %), feldspars (1.6 %) and iron oxides (1.3 %) (Tab. 5.2, Fig. 5.4 b). The quantitative petrographic assessment by point-counting (Tab. 5.1) is used as a benchmark to threshold the µCT results (Tab. 5.2).

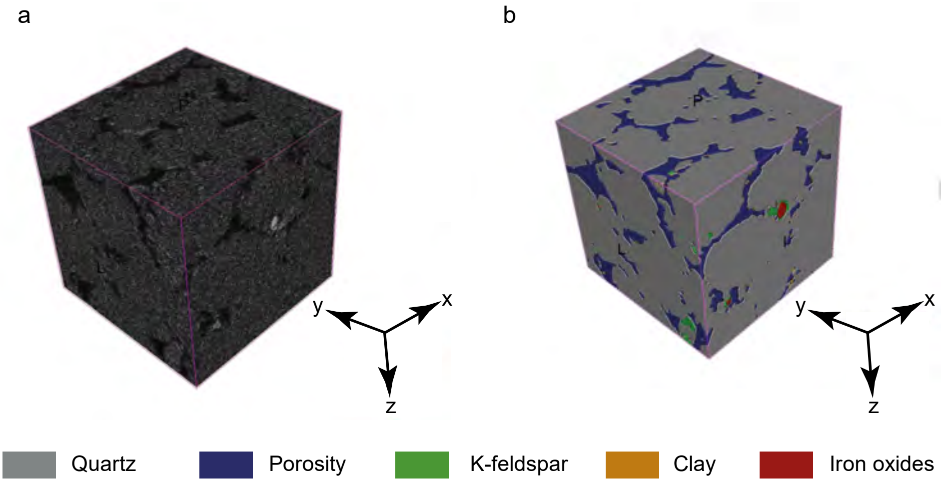

Figure 5.4. a) Stacked µCT data after contrast enhancement and cropping into a cube with the dimensions of 400*400*400 px. Porosity in black, quartz, feldspar, and clay in different shades of gray, and iron oxides as bright spots. b) Segmented µCT cube based on densities, coloring the distinguished classes porosity, quartz, feldspar, clay, and iron oxides.

Table 5.2. Results derived from µCT data for petrophysical simulation and petrographic data. Permeability was determined for all three principal directions.

Numerical results	
Permeability	1193 mD (k_x), 1585 mD (k_y), 827 mD (k_z)
Porosity	13.4 %
Digital petrography results	
Quartz	81.6 %
Feldspar	1.6 %
Iron oxides	1.3 %
Clay	2.1 %

Single phase fluid flow

The µCT image sequence intended for binary image segmentation was divided into solid matter and minerals based on the porosity of 18 % determined by helium pycnometry. Based on this porosity benchmark, a porous structure was generated in a 400*400*400 px cube. Under the influence of the applied gravity, the viscous forces continue to balance the effective pressure drop induced by the gravity until a steady state is reached. The permeability of the porous medium is then computed via Eqn. 5.1, where the average fluid velocity and the gravity induced pressure drop are known at the steady state. This process is repeated for other principal directions to quantify the anisotropic nature of the permeability tensor. These principal components in the x, y and z directions turn out to be 1193 mD, 1585 mD and 827 mD, respectively (Tab. 5.2). Simulated permeabilities are slightly higher following bedding direction, and lowest in z direction. Zones of flow can be visualized as color-coded flow lines based on fluid velocity, highlighting the interconnected porosity of the sample (Fig. 5.5). Flowlines are calculated per direction (x, y, z) based on a pressure gradient. Therefore, it is only possible to display flowlines along one axis per figure.

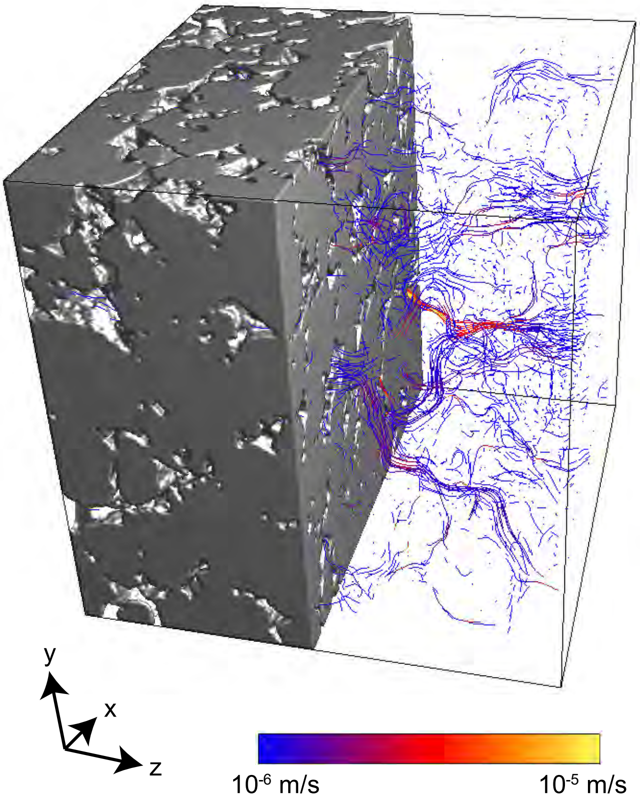

Figure 5.5. Flow streamlines of the local fluid velocity U, based on single-phase permeability simulation, here in z-direction. The color-coding represents the flow velocity and visualizes the interconnected flow-zones.

Two phase flow

Initially, the mixture of two fluids, with a given fraction of the wetting fluid S_W, is distributed randomly inside the simulation domain. Similar to the single-phase case, gravity is used to drive the fluid flow in different principle directions (Zhao et al., 2017; Zhao et al., 2018) with a no-slip boundary condition on the lateral directions. Due to the surface tension between the gas and water phases, the mixture slowly evolves to form distinguishable phases. Figure 5.6 shows the steady-state of the gas-water system at different water saturations when gravity is applied in the x direction. From these averaged fluid velocities and the known pressure drop created by the gravity, the relative permeabilities are evaluated and are shown in Figure 5.7.

Relative permeability of one phase (e.g., gas) decreases, as the relative amount of another phase (e.g., water) increases. More gas (k_{nw}) will be produced until the water saturation in the rock reaches ~0.45 (x-direction), ~0.55 (y-direction), or 0.50 (z-direction). At higher water saturations, the permeability of water (k_w) is larger than of that of gas (k_{nw}) and predominantly water will be produced (Fig. 5.7).

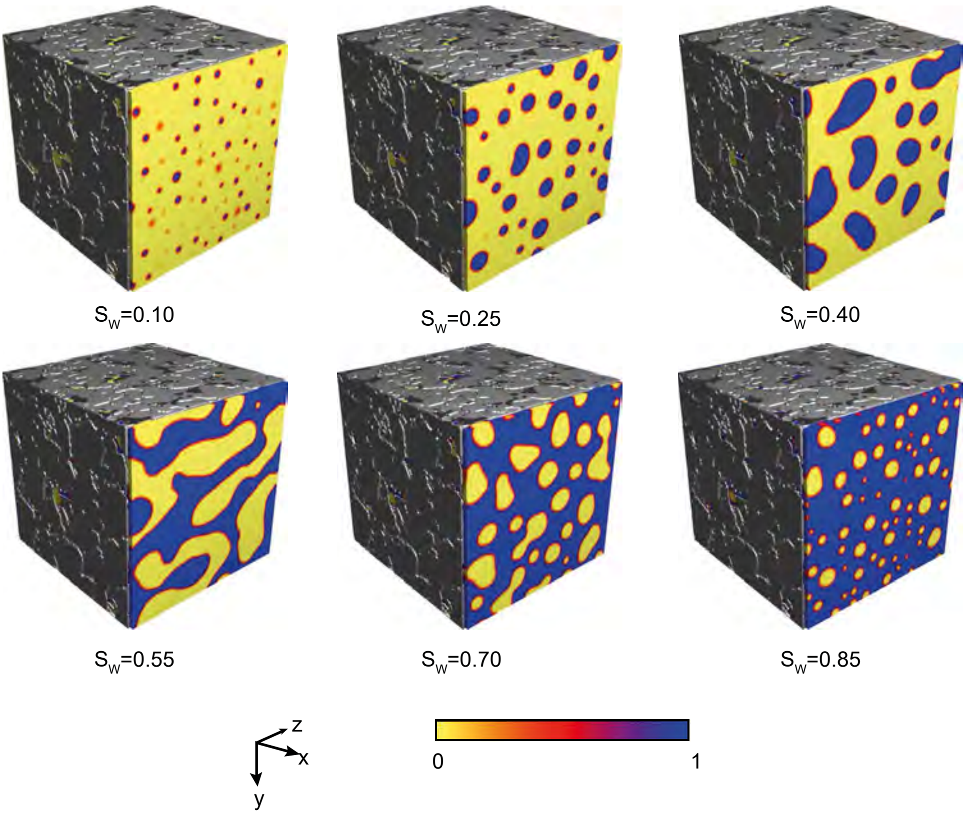

Figure 5.6. Two-phase flow simulations at variable wetting-phase saturations. The blue color represents the wetting-phase (water), and the yellow color represents the non-wetting phase (gas). Steady-state configuration of gas-water flow under the action of gravity for different wetting saturation S_w.

The relative permeability curves are determined for this sample from two-phase gas-water simulations (Fig. 5.7). For the evaluation of macroscopic properties (such as permeability) of generated digital structures, it is important to ensure that a sufficiently large domain is used. To choose such a volume, first, a series of single-phase permeability tests are carried out at increasingly large simulation domains. Once the permeability values obtained at two successive simulation domains are close to each other, this volume is chosen as the representative volume of the given sample. This representative volume is then further utilized in the two-phase simulations (Fig. 5.6). Two-phase simulations need to reach equilibrium in order to represent steady-state Darcy flow. The relative permeability under steady-state conditions is directly dependent on the saturation of the wetting phase (Fig. 5.6, 5.7).

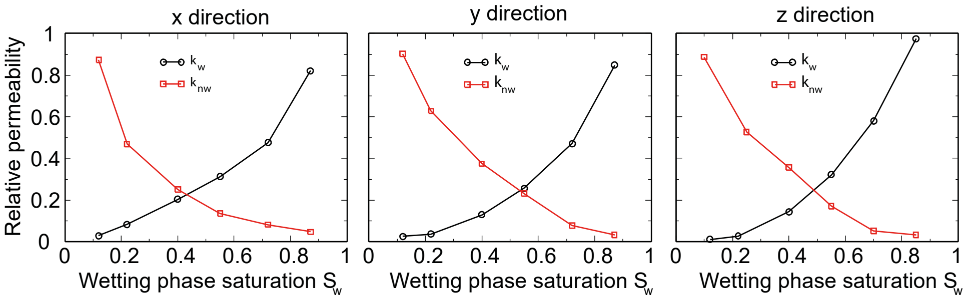

Figure 5.7. Relative permeability curves in relation to dependence of water saturation in the principal directions x, y, and z. The water and gas are the wetting and non-wetting phases. The relative permeability is computed at certain intervals of water saturation to optimize computational time.

5.5 Discussion

5.5.1 Rock composition

The conversion from 2D (thin-section) to 3D space (µCT digital rock) results causes a difference for the largest absolute mismatch of 7.4 % in quartz content (laboratory: 89.0±2.8 %, digital: 81.6 %). Clay content (laboratory: 2.3±1.3 %, digital: 2.1 %) was confidently identified within the confidence levels, and is commonly reported as straight forward to identify (Cnudde et al., 2011). Feldspars (laboratory: 3.3±1.7 %, digital: 1.6 %) match within their 95 % confidence level error margins. Quartz and feldspar are minerals of very similar attenuation, leading to challenging segmentation (Cnudde et al., 2011). This is interpreted as one reason for the match of digital and lab data for feldspars being barely within the confidence levels given by point-counting statistics. Another reason for the slight mismatch between digital and lab data is attributed to the partial dissolution of feldspars (Fig. 5.3 a), which results in segmentation of porosity instead of feldspar.

The quality of the µCT segmentation for different rock minerals is also influenced by large attenuation contrasts of individual minerals like iron oxides. Compared to the predominant constituents like quartz, these result in large color contrasts (Fig. 5.4 a). The heaviest minerals (here: hematite/iron oxides) generate bright spots in the µCT images, which lead to uncertainty in the image segmentation (or binarization of image into porous space and solid structure) due to over-illumination of adjacent minerals. Due to the abundance obtained from point-counting (0±0.4 %) compared with the abundance in the digital rock model (1.3 %), an overestimation factor of three was assumed for high attenuation minerals.

5.5.2 Porosity

The optical porosity of 5.3 % does not match with the petrophysical porosity of 18.0 %. This general mismatch is well established and attributed to micro-porosity, sample heterogeneity and the fractal effects, leading to a general underestimation of porosity (Markussen et al., 2019). Porosity differences between laboratory results (18.0 %) and digital rock results (13.4 %) were observed. Considering the content of clay minerals, which are predominantly illite (Busch et al., 2017), microporosity in clays is able to partly explain the mismatch due to 63±10 % microporosity in illite (Hurst & Nadeau, 1995). Due to 2.1 % of clays in the digital rock model, this would amount to an additional 1.3±0.2 %, resulting in a digital porosity of 14.7±0.2 %. Over-illumination effects due to large attenuation differences of iron oxides compared to quartz or porosity could also porosity lead to porosity being falsely segmented as iron oxides. However, it is not possible to exactly quantify the amount of porosity lost to that effect. At the very most, this may amount to 1 %, which corresponds to the difference between digital and laboratory iron oxide abundance (Tab. 5.1, 5.2).

The µCT resolution of 3.3 µm introduces an additional uncertainty in segmentation, especially on grain boundaries, where very narrow open pore throats could either be segmented as porosity or as solid mineral. Further effects on digital porosity, which are hard to quantify, are microporosities in feldspars, which can reach up to 5 % (Walker et al., 1995). Assuming these microporosities in conjunction with 1.6 % in digital feldspar abundance would result in the minor contribution <0.1 % and thus not be a significant factor.

Considering all these effects, the digital porosity would be increased to roughly 15–16 %. This is a closer representation of the petrophysical porosity. However, it needs to be considered that helium pycnometry can easily resolve porosity on a nanometer scale, while digital porosity is limited by resolution (here: 3.3 µm). Similar offsets of 30–40 % between helium porosity and digital porosity without considering microporosity were also reported in other sandstone studies (Peng et al., 2012), confirming quality and validity of the results in this study.

5.5.3 Permeability

The simulated permeability in the x-direction of the sample corresponds well with the experimental measurements also performed along the x-direction of the sample. Although the porosity segmentation did mismatch by over 30%, permeability matches within in an acceptable range of ±10%. This is due to permeability being almost exclusively controlled by the large pores, which µCT is able to display easily. The bottleneck of microporosity in porosity segmentation is interpreted to not contribute to permeability. Therefore, µCT segmentation can be considered as effective porosity, explaining the good fit of digital permeability with laboratory permeability.

The spatial anisotropy of the studied sandstone, especially in relation to bedding, grain size, and rock composition, plays an important role in controlling the fluid behavior at the pore-scale and beyond. For instance, permeability values measured in simulations and experimental results are in agreement within 15 % (k_x) (Tab. 5.1 & 5.2).

Close to water saturation (S_w=0.5), the relative permeability of the water phase is slightly higher than the gas phase in the x and z directions (Fig. 5.7). Given the higher wetting affinity of the water phase towards the solid porous medium, in fact, the opposite should be true. Thus, the simulations indicate that, in some cases, the initial random distribution of the gas-water phases may give rise to fluid patterns such that the gas phase is in contact with a larger surface area of the solid porous medium. According to the simulation, if water saturation exceeds 50 % in two-phase flow normal to bedding, production of water starts.

An advantage of µCT simulations is the applicability in reservoir rocks consisting of water-sensitive minerals or water-sensitive cement phases like anhydrite, evaporites and carbonate cements. Two-phase flow simulations could be used in these samples without altering the intrinsic permeability by dissolution of water-sensitive phases.

5.6 Conclusions

Our workflow links petrophysical rock and numerical digital rock permeability derived from µCT scans. Rock composition by µCT images and rock samples fall with in analysis bias.

The mismatch of higher petrophysical rock porosity is due to restricted resolution of µCT to segment for microporosity. This was observed to be less relevant for permeability simulations, as permeability is primarily controlled by large, connected pores, which can easily be detected. Large attenuation contrasts result in over-illuminated bright spots, which lead to a systematic overestimation of the volume of very dense minerals (e.g. hematite) by a factor of three. Furthermore, highly porous fibrous clay minerals might easily be segmented as porosity, leading to an overestimation in both porosity and subsequent permeability simulations.

Fluid simulations present an opportunity to analyze and quantify the anisotropic nature of the permeability tensor, in both single and two-phase flow. Differences between measured and simulated one-phase permeabilities are about 15 % (experimental 1040 mD vs. simulated 1190 mD). Results also highlight that the water production differs by almost 20 % in the x-y-z direction of the simulated cube and shows unexpected relative permeabilities. This suggests that water production starts at saturation levels where usually gas production is expected.

Overall, the tradeoff between resolution, representative volume and computational demands requires a case-by-case decision on how to process samples for µCT scans. Different shades of gray caused by molecular weight differences require pre-processing, mainly contrast enhancements, before mineral assessment based on grayscale intensity thresholds.

µCT-based mineralogy assessments can generally provide information about the major constituents, and µCT models can be used for fluid flow simulations easily highlighting permeability anisotropies for single and two-phase flow. However, it still requires the petrographic analysis since coats on mineral surfaces affecting wetting angles are not resolved by µCT.

6 Summary

6.1 Heterogeneity in reservoir quality

Four study areas have been investigated regarding their petrography and reservoir quality: Upper Rotliegend reservoir sandstones (burial depth: 4-5 km) from the Northern German Basin (well A & B), upper Rotliegend analog sandstones from the Flechtingen High (Sachsen-Anhalt, Germany), uppermost Rotliegend Cornberg Sandstones from the northern Hesse Basin (Hesse, Germany), and lower Rotliegend Penrith Sandstones from the Vale of Eden (Cumbria, UK).

Permeability and thus reservoir quality in the studied Rotliegend sandstones shows a wide range from 0.001 to 10000 mD (Fig. 6.1 a). Penrith Sandstones show the best reservoir quality (permeability: 100 to 10000 mD), while Cornberg Sandstones show the worst reservoir quality (permeability: 0.001 to 1 mD). Flechtingen Sandstones show intermediate reservoir quality (permeability: 0.1 to 100 mD), while reservoir sandstones show a wide range of reservoir quality from good to poor (permeability: 0.01 to 1000 mD) (Fig. 6.1 a).

The detrital composition of Penrith Sandstones (blue polygon) and Cornberg Sandstones is very mature and similar (Fig. 6.1 b); however, they represent best and poorest reservoir quality (Fig. 6.1 a). Flechtingen Sandstones and reservoir sandstones (well A & B) show a less mature detrital composition (Fig. 6.1 b), and intermediate reservoir quality (Fig. 6.1 a). Detrital composition is controlled by the distance and geologic setting of the source area, leading to variations in maturity. As a result, detrital composition is interpreted not to be the primary control on reservoir quality (Fig. 6.1 a, b). Dune sandstones show best and poorest reservoir quality, therefore the depositional environment is likely not the main control on reservoir quality (Fig. 6.1 c).

The main control on reservoir quality in the studied data set are authigenic quartz, clay mineral and carbonate cements (Fig. 6.1 d). Samples with highest quartz cement volumes and lowest clay mineral cement and carbonate cement volumes show best reservoir quality, while samples with highest clay mineral cement and carbonate cement volumes show poorest reservoir quality (Fig. 6.1 d).

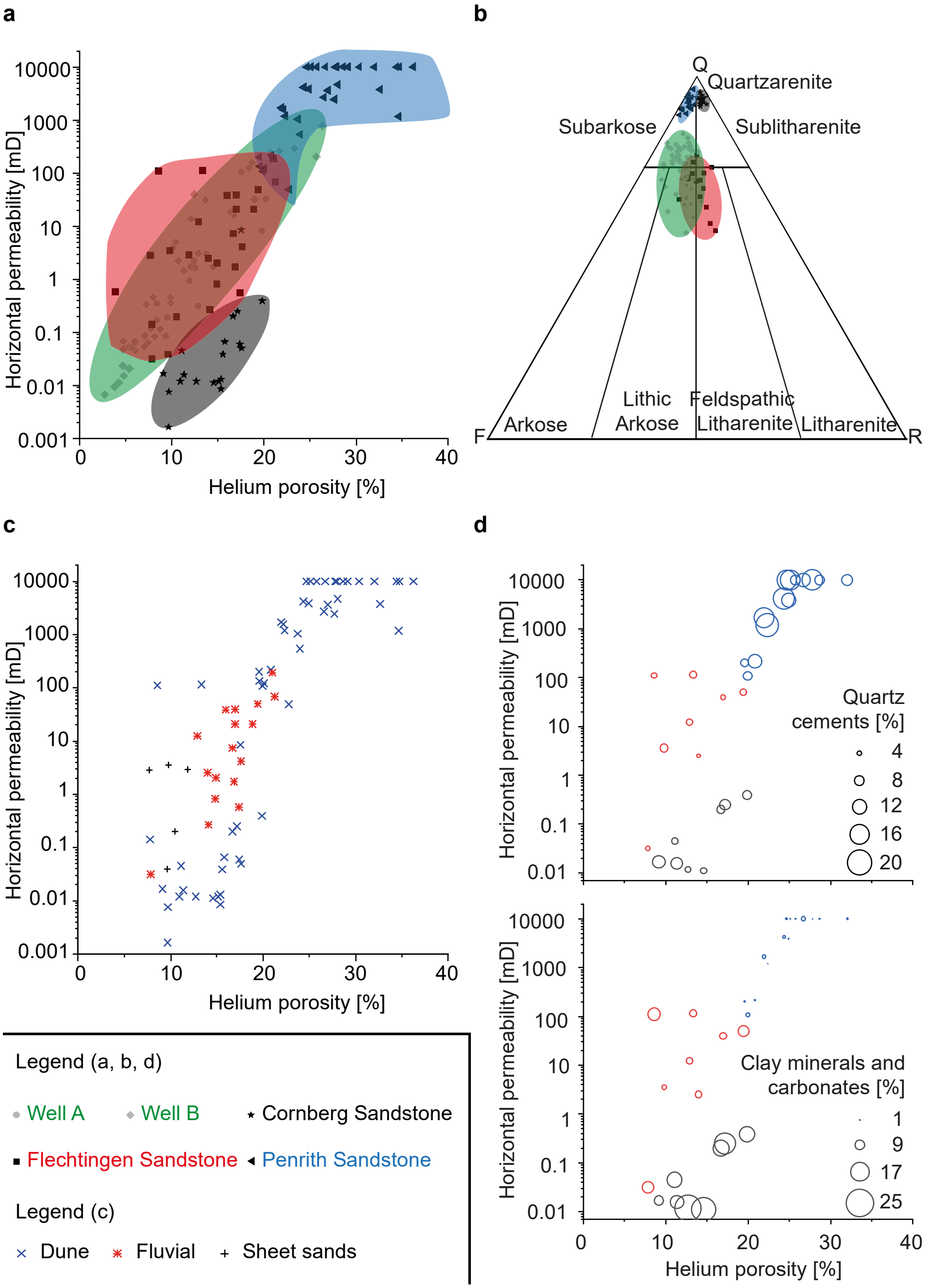

Figure 6.1. Reservoir quality control factors in investigated Rotliegend sandstones. a: porosity and permeability by study area, b: QFR diagram, c: porosity and permeability by depositional system, d: impact of cementation.

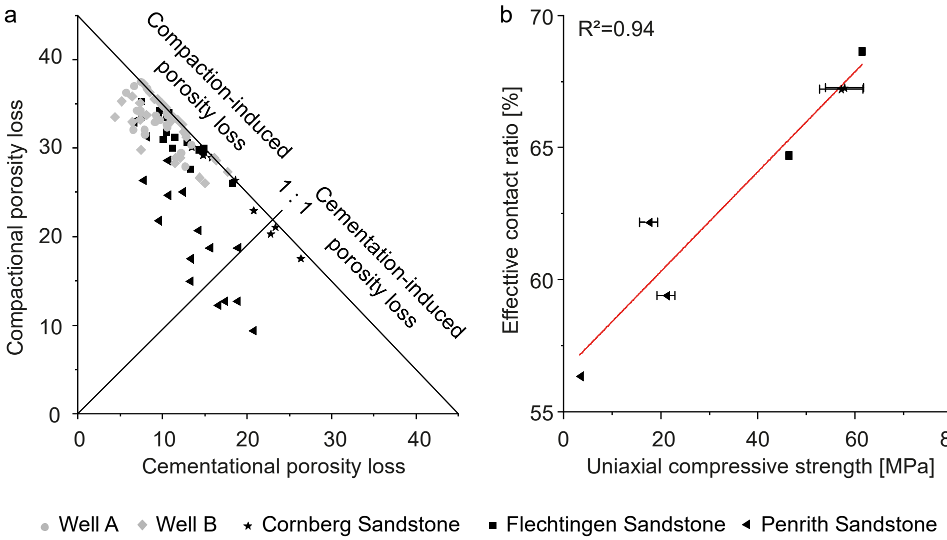

Figure 6.2. a: Compactional and cementational control on porosity loss after Lundegard (1992). b: Petrographic parameter effective contact ratio as proxy for uniaxial compressive strength (see Fig. 4.6 g1).

Reservoir quality is also related to the porosity reduction-process, which is compaction-induced and cementation-induced (Fig. 6.2 a). Flechtingen Sandstones and reservoir sandstones (well A & B) experienced a predominately compaction-induced porosity loss (Fig. 6.2 a), while Cornberg Sandstones and Penrith Sandstones show an approximately equal portion of cementation-induced and compaction induced porosity loss (Fig. 6.2 a). This is related to the detrital maturity (Fig. 6.1 b). Due to larger abundances of immature ductile detrital grains, Flechtingen Sandstones and reservoir sandstones have experienced a more intense mechanical compaction compared to cementation than mature Penrith Sandstones and Cornberg Sandstones (Fig. 6.2 a).

The effective contact ratio has been identified as a new petrographic proxy of uniaxial compressive strength (Fig. 6.2 b). The effective contact ratio is the contact length measured horizontal to bedding between the physical contact of minerals, normalized to the diameter of the smaller grain. The effective contact ratio enables a first-order estimate for rock strength in orientated sandstone samples, if geotechnical data is not available or sufficiently large samples are not obtainable.

Reservoir quality and mechanical parameters have been demonstrated to be controlled by the diagenetic parameters of cementation and compaction (Fig. 6.1, 6.2). The paragenetic sequences of all four study areas highlight the differences in authigenic composition and timing of the cements (Fig. 6.3). Low illitic clay mineral grain-coating coverages in Penrith

Sandstones in conjunction with a mature detrital composition enabled quartz cementation, which stabilized the framework against intense mechanical compaction (Fig. 6.3). Cornberg Sandstones have been cemented by carbonate cementation and authigenic clay minerals, which were sourced from replaced feldspars (Fig. 6.3). The highest amount of illitic clay mineral grain-coatings occurs in Flechtingen Sandstones and reservoir sandstones (well A & B), which also show the highest chemical compaction (Fig. 6.3).

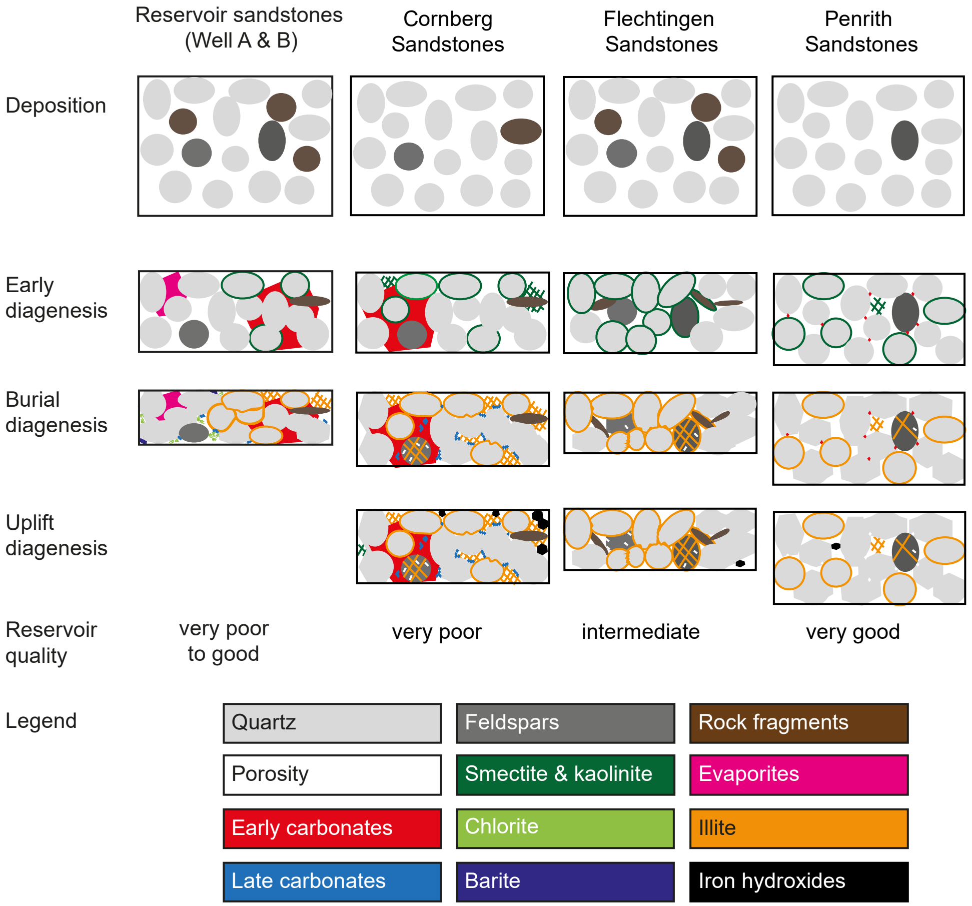

Figure 6.3. Compilation of the paragenetic control on porosity reduction during diagenesis, and its subsequent impact on reservoir quality. Reservoir quality in reservoir sandstones varies due to large heterogeneity of illitic clay mineral coatings and their impact on cementation and compaction. The height of the rectangles is linearly proportional to their intergranular volume after Paxton et al. (2002).

Best reservoir quality was encountered in Penrith Sandstones, which is characterized by its mature detrital and authigenic composition (Fig. 6.1 b, 6.3). Detrital maturity alone is no guarantor for good reservoir quality, as demonstrated by the poor reservoir quality of Cornberg Sandstones due to intense carbonate and clay mineral cementation (Fig. 6.1 d, 6.3). Furthermore, less mature sandstones may also result in fair reservoir quality dependent on the intensity of early cementation, clay-mineral grain coatings inhibiting quartz cementation, and illitic clay mineral grain-coatings enhancing chemical compaction (Fig. 6.3).

Reservoir quality encountered from exposed outcrops such as the mature Penrith Sandstones would need to be adjusted for additional quartz cementation in a subsurface scenario, as quartz cement growth is primarily dependent on time, temperature, silica availability and grain size (Busch et al., 2018). Therefore, quartz cement volumes of subsurface Penrith Sandstones would be higher, and the overall reservoir quality would be poorer in a mature subsurface reservoir sandstone with comparable boundary conditions.

7 Conclusions & Outlook

7.1 Conclusions

Reservoir quality in Rotliegend reservoir sandstones is mainly controlled by an interplay between compactional porosity-loss of intergranular volume (IGV) by mechanical compaction, authigenic quartz overgrowth cements, and chemical compaction. Although depositional parameters and detrital composition exhibit no control on reservoir quality between the different study areas, variation in permeability on vertical distances as little as 1 m can range from 100 to 0.01 mD. Tangential clay mineral coatings are exclusively illitic and are divided into coatings on grains in contact with the intergranular volume (grain-to-IGV (GTI) coatings), as well as into coatings on detrital grains in contact with other detrital grains (grain-to-grain (GTG) coatings). This distinction is necessary due to the ambivalent effect of illite on reservoir quality, preventing syntaxial quartz precipitation but enhancing chemical compaction. The differences in reservoir quality are related to an integrated control of compaction, quartz cementation, GTI and GTG coatings on porosity, permeability, and pressure sensitivity of permeability, resulting in three rock types typical for the range of observed reservoir qualities.

Type A shows best reservoir quality (avg. permeability: 126 mD) and is characterized by mostly continuous GTI coatings inhibiting quartz cementation and discontinuous GTG coatings preserving the IGV. Type B shows intermediate reservoir quality (avg. permeability: 1.2 mD) controlled by intense pore-filling authigenic cements due to the least continuous illite GTI coatings, but no major chemical compaction due to the lack of intense GTG coatings. Reservoir quality in type C is poorest (avg. permeability: 0.04 mD) due to extensive GTI and GTG coatings inhibiting quartz cementation but causing intense chemical compaction.

Rotliegend outcrop analog studies demonstrate similar reservoir quality controls as in subsurface reservoir sandstones, as well as additional controls not encountered in reservoir samples. Cornberg Sandstones are cemented, showing intense early diagenetic cementation by dolomite and kaolinite stabilizing the grain framework against mechanical compaction, subsequently retaining large intergranular volumes up to 30 %. Reservoir quality is poor (avg. permeability: 0.96 mD) due to aforementioned intense cementation with barely any optical porosity. Flechtingen Sandstones show intense GTI and GTG coatings in combination with no significant preserved early diagenetic cement phase. This results in intermediate reservoir quality (avg. permeability: 34.9 mD) due to moderate cementation but intense compaction. Best reservoir quality in Rotliegend analogs is encountered in Penrith Sandstones (avg. permeability: 5906 mD), showing almost no illite GTI or GTG coatings, leading to quartz overgrowth cementation which stabilized the framework, but also preserved large amounts of optical porosity. Overall, processes related to inversion and subsequent uplift diagenesis show an inconsistent effect on reservoir quality development: Reservoir quality in Flechtingen and Penrith Sandstones was slightly improved by feldspar and carbonate dissolution, however intense uplift-related kaolinite precipitation in conjunction in with iron hydroxide formation in Cornberg Sandstones deteriorated reservoir quality. The necessity for detailed diagenetic studies in reservoir quality assessment is demonstrated by the impact of framework stabilization and grain-coating processes on porosity preservation. In summary, reservoir quality constraints by depositional parameters are interpreted to be superimposed by diagenetic alteration due to significant burial depth, temperature, and fluid exposure on fluvio-eolian Rotliegend sandstones during diagenesis.

Outliers from the log-linear porosity-permeability correlation are attributed to an interplay between isolated secondary pores, contributing to porosity but only negligibly to permeability, and to microporosity in clay minerals, which does not contribute to permeability. The effective porosity derived from Helium porosity integrated with clay microporosity delivers a much better porosity-permeability fit compared to reservoir quality assessment purely based on petrophysical measurements.

Permeability measurements conducted on Rotliegend analogs parallel and normal to bedding highlight limitations in a standard industry approach of assuming permeability normal to bedding to be 10 % of permeability parallel to bedding. While being a reasonable estimation for low permeability samples (<10 mD) in this data set, highly permeable samples (>1000 mD) only show a negligible difference between measurements conducted parallel and normal to bedding.

The control of individual authigenic mineral phases on the mechanical properties uniaxial compressive strength (UCS), Young's modulus (E), strain at failure, and density is ambiguous in Rotliegend analogs. Optical porosity and clay mineral abundance are the only petrographic parameters showing a consistently good correlation ($R^2>0.8$) with UCS, E and density. While optical porosity shows the expected anti-correlation with these parameters, rock strengths are higher in specimen with higher clay mineral abundance. This apparent contradiction is caused by varying intensities of compaction leading to a reduction of the intergranular volume, which shows a consistent but relatively weak correlation ($R^2<0.7$) with UCS, E and density. More intensely compacted Flechtingen Sandstones have less IGV and higher UCS, while less compacted Penrith Sandstones show increased IGV and smaller UCS. This is related to framework-stabilizing early diagenetic cementation, and chemical compaction driven by illite GTG coatings. GTG coatings seem also to positively correlate with strain at failure, however meaningful conclusions are not possible due to outliers and the small data-set size.

Mechanical parameters are related to the grain-framework by the length of horizontal grain contacts between two rigid grains. These effective contact lengths were normalized to the individual grain size to exclude a grain-size bias. The resulting effective contact ratios positively correlate with UCS (R^2=0.97), Young's modulus (R^2=0.94) and density (R^2=0.85). The rock strength index S_R derived from optical porosity and effective contact ratios is proposed as an estimation of mechanical properties UCS and E purely based on petrographic data.

Petrographic and petrophysical parameters can also be determined from micro-computed x-ray tomography models. The presented workflow relates measured permeability to numerically derived digital rock permeability, while considering analysis bias in petrographic analysis for the assessment of mineralogy in digital rocks. Variable shades of gray caused by attenuation contrasts require pre-processing before mineral assessment can be conducted. Mismatches between experimental data and digital rock data are caused by segmentation, microporosity, and attenuation contrasts. Segmentation and microporosity mismatches mostly affect porosity, as permeability is controlled by easily segmentable large pores. Meanwhile, fibrous clays are prone to being segmented as porosity. Large attenuation contrasts result in over-illuminated bright spots, causing a systematic overestimation of the volume of very dense minerals by a factor of three. The anisotropic nature of the permeability tensor in single and two-phase flow can be analyzed by fluid flow simulations, delivering simulated one-phase permeabilities within 15 % of measured results.

7.2 Outlook

One of the defining pillars of this work is the differentiation of illitic clay mineral coatings into grain-to-IGV and grain-to-grain coatings. Their impact on cementation and compaction and subsequent control on reservoir quality has been extensively described in the Chapters 2 & 3. As illitic grain coating coverages were determined manually, they are therefore affected by analysis and observer bias. Due to very distinctive interference colors of illite under cross-polarized light, illite coatings could be detectable by automated image analysis. Existing pattern recognition algorithms using machine learning (e.g. Hensel et al. (2019)) could be trained on thin-section images. A well calibrated machine learning process would have to be able to consider the variability of interference colors caused by sample rotation in order to deliver standardized results without observer bias. This would result in a fraction of the time required for manual analysis, potentially even finding application in industry core analysis.

Grain coatings were studied in similar fluvio-eolian depositional environments due to the scope and goal of the project limited to terrestrial sandstones. Nevertheless, this might result in a population bias for the effect of illitic grain coatings on cementational and compactional behavior, which should be addressed by a follow-up study incorporating a wider range of depositional environments, including, but not limited to, fluvial, dune, sandflat, deltaic, estuarine, and tidal sandstones. Furthermore, the range of samples investigated herein is limited to sandstones of Lower Permian age, resulting in significant diagenetic overprint, leading to the conclusion that reservoir quality is not controlled by depositional environment due to diagenetic overprint. Meanwhile, studies on recent sediments (Woolridge et al., 2017) report a strong depositional control. Therefore, a follow-up study on sandstones from several depositional environments representing different stages of burial, e.g., 1 km, 3 km, and 5 km, might yield insight at which state of diagenesis reservoir quality controls exhibited by the depositional environment becomes a less important than the diagenetic overprint. These results could be integrated in reservoir prediction workflows, giving emphasis on facies modeling in shallow reservoirs, while focusing on diagenetic modeling at larger burial depths.

Samples in sufficient size for geotechnical standard tests are not always obtainable, therefore petrography-based models able to determine mechanical parameters via proxy are useful tool to predict mechanical properties of small, orientated samples. The rock strength index (S_R) proposed in Chapter 4 has shown promise to fulfill this role, however the small data set requires a detailed follow-up study on several sandstone types in sufficient quantity in order to better constrain uncertainties and variability regarding the validity of S_R. A semi-automated workflow using machine-learning to identify grain contacts on thin-section images of a known scale could be able to reduce analysis time.

Digital Rock models based on µCT deliver good results in regard to the major petrographic constituents and permeability simulations (Chapter 5). As they still require calibration by petrographic data, their use to mineralogy assessment remains limited. However, they are able to address 3D heterogeneity contrary to thin-sections, which are a determining factor for fluid flow properties. The tradeoff between resolution and representative volume will likely still limit simulations of very low permeability samples, as the required resolution to segment very small pores will either result in volumes becoming too small to be representative, or result in increasing computational demands, making it unfeasible for an industry application.

References

Aagaard, P., Egeberg, P. K., Saigal, G., Morad, S., & Bjørlykke, K. (1990). Diagenetic albitization of detrital K-feldspars in Jurassic, Lower Cretaceous and Tertiary clastic reservoir rocks from offshore Norway; II, Formation water chemistry and kinetic considerations. *Journal of Sedimentary Research, 60*, 575-581. doi:10.1306/212F91EC-2B24-11D7-8648000102C1865D

Aagaard, P., Jahren, J. S., Harstad, A. O., & Nilsen, O. (2000). Formation of grain-coating chlorite in sandstones. Laboratory synthesized vs. natural occurrences. *Clay Minerals, 35*, 261-269.

Aehnelt, M., & Katzung, G. (2007). Das Rotliegende im Richelsdorfer Gebirge-Stratigraphie, Lithologie und Paläogeographie. *Geol. Jb. Hessen, 134*, 5-36.

Ajdukiewicz, J. M., & Larese, R. E. (2012). How clay grain coats inhibit quartz cement and preserve porosity in deeply buried sandstones: Observations and experiments. *AAPG Bulletin, 96*, 2091-2119. doi:doi.org/10.1306/02211211075

Ajdukiewicz, J. M., Nicholson, P. H., & Esch, W. L. (2010). Prediction of deep reservoir quality using early diagenetic process models in the Jurassic Norphlet Formation, Gulf of Mexico. *AAPG Bulletin, 94*, 1189-1227. doi:10.1306/04211009152

Albrecht, D. (2015). *Untersuchungen zum Spannungseinfluss auf die Fluiddurchlässigkeiten von Rotliegend Tight Gas Sandsteinen.* (PhD thesis). Clausthal University of Technology, Clausthal-Zellerfeld.

Amann-Hildenbrand, A., Dietrichs, J. P., & Krooss, B. M. (2015). Effective gas permeability of Tight Gas Sandstones as a function of capillary pressure – a non-steady-state approach. *Geofluids, 16*(3), 367-383. doi:10.1111/gfl.12155

Ambrose, W. A., Lakshminarasimhan, S., Holtz, M. H., Núñez-López, V., Hovorka, S. D., & Duncan, I. (2008). Geologic factors controlling CO2 storage capacity and permanence: case studies based on experience with heterogeneity in oil and gas reservoirs applied to CO2 storage. *Environmental Geology, 54*, 1619-1633. doi:10.1007/s00254-007-0940-2

Andrä, H., Combaret, N., Dvorkin, J., Glatt, E., Han, J., Kabel, M., Keehm, Y., Krzikalla, F., Lee, M., Madonna, C., Marsh, M., Mukerji, T., Saenger, E. H., Sain, R.-., Saxena, N., Ricker, S., Wiegmann, A., & Zhan, X. (2013a). Digital rock physics benchmarks—Part I: Imaging and segmentation. *Computers & Geosciences, 50*, 25-32. doi:10.1016/j.cageo.2012.09.005

Andrä, H., Combaret, N., Dvorkin, J., Glatt, E., Han, J., Kabel, M., Keehm, Y., Krzikalla, F., Lee, M., Madonna, C., Marsh, M., Mukerji, T., Saenger, E. H., Sain, R.-., Saxena, N., Ricker, S., Wiegmann, A., & Zhan, X. (2013b). Digital rock physics benchmarks—part II: Computing effective properties. *Computers & Geosciences, 50*, 33-43. doi:10.1016/j.cageo.2012.09.008

Arthurton, R. S., & Wadge, A. J. (1981). *Geology of the country around Penrith* (Vol. 24): Institute of Geological Sciences, Natural Environment Research Council.

Atapour, H., & Mortazavi, A. (2018). The influence of mean grain size on unconfined compressive strength of weakly consolidated reservoir sandstones. *Journal of Petroleum Science and Engineering, 171*, 63-70. doi:10.1016/j.petrol.2018.07.029

Bachmann, G. H., Geluk, M. C., Warrington, G., Becker-Roman, A., Beutler, G., Hagdorn, H., Hounslow, M. W., Nitsch, E., Röhling, H.-G., Simon, T., & Szulc, A. (2010). Triassic. In J. C. Doornenbal & A. G. Stevenson (Eds.), Petroleum Geological Atlas of the Southern Permian Basin Area (pp. 149-173). Houten, NL: EAGE Publications.

Bachu, S. (2000). Sequestration of CO2 in geological media: Criteria and approach for site selection in response to climate change. *Energy Conversion and Management, 41*, 953-970. doi:10.1016/S0196-8904(99)00149-1

Bahlis, A. B., & De Ros, L. F. (2013). Origin and impact of authigenic chlorite in the Upper Cretaceous sandstone reservoirs of the Santos Basin, eastern Brazil. *Petroleum Geoscience, 19*, 185-199. doi:10.1144/petgeo2011-007

Barnard, P. L., Rubin, D. M., Harney, J., & Mustain, N. (2007). Field test comparison of an autocorrelation technique for determining grain size using a digital 'beachball' camera versus traditional methods. *Sedimentary Geology, 201*, 180-195. doi:10.1016/j.sedgeo.2007.05.016

Barnes, D. A., Bacon, D. H., & Kelley, S. R. (2009). Geological sequestration of carbon dioxide in the Cambrian Mount Simon Sandstone: Regional storage capacity, site characterization, and large-scale injection feasibility, Michigan Basin *Environmental Geosciences, 16*, 163-183. doi:10.1306/eg.05080909009

Baud, P., Wong, T. E., & Zhu, W. (2014). Effects of porosity and crack density on the compressive strength of rocks. *International Journal of Rock Mechanics & Mining Sciences, 67*, 202-211. doi:10.1016/j.ijrmms.2013.08.031

Becker, I., Busch, B., Koehrer, B., Adelmann, D., & Hilgers, C. (2019). Reservoir quality evolution of Upper Carboniferous (Westphalian) tight gas sandstones, Lower Saxony Basin, NW Germany. *Journal of Petroleum Geology, 42*, 371-392. doi:10.1111/jpg.12742

Becker, I., Wüstefeld, P., Koehrer, B., Felder, M., & Hilgers, C. (2017). Porosity and permeability variations in a tight gas sandstone reservoir analogue, Westphalian D, Lower Saxony Basin, NW Germany: influence of depositional setting and diagenesis. *Journal of Petroleum Geology, 40*(4), 363-390. doi:10.1111/jpg.12685

Bell, F. G. (1978). The physical and mechanical properties of the Fell Sandstones, Northumberland, England. *Eng. Geol., 12*, 1-29. doi:10.1016/0013-7952(78)90002-9

Benson, S. M., & Cole, D. R. (2008). CO2 sequestration in deep sedimentary formations *Elements, 4*, 325-331. doi:10.2113/gselements.4.5.325

Berger, G., Lacharpagne, J.-C., Velde, B., Beaufort, D., & Lanson, B. (1997). Kinetic constraints on illitization reactions and the effects of organic diagenesis in sandstone/shale sequences. *Applied Geochemistry, 12*, 23-35. doi:10.1016/S0883-2927(96)00051-0

Berner, R. A. (1969). Goethite stability and the origin of red beds. *Geochimica et Cosmochimica Acta, 33*, 267-273. doi:10.1016/0016-7037(69)90143-4

BGS. (2020). The BGS Lexicon of Named Rock Units. Retrieved from https://www.bgs.ac.uk/lexicon/

Binot, F., Gerling, P., Hiltmann, W., Kockel, F., & Wehner, H. (1993). The Petroleum System in the Lower Saxony Basin. In A. M. Spencer (Ed.), Generation, accumulation and production of Europe's hydrocarbons (Vol. 3, pp. 121-139): EAGE Special Publication.

Bjørlykke, K. (2006). Effects of compaction processes on stresses, faults, and fluid flow in sedimentary basins: examples from the Norwegian margin. *Geological Society, London, Special Publications, 253*, 359-379. doi:10.1144/GSL.SP.2006.253.01.19

Bjørlykke, K., & Høeg, K. (1997). Effects of burial diagenesis on stresses, compaction and fluid flow in sedimentary basins. *Marine and Petroleum Geology, 14*, 267-276. doi:10.1016/S0264-8172(96)00051-7

Bjørlykke, K., & Jahren, J. S. (2010). Sandstones and Sandstone Reservoirs. In K. Bjørlykke (Ed.), Petroleum Geoscience (pp. 113-140). Berlin, Heidelberg: Springerg.

Blakey, R. C., & Wong, T. E. (2003). Carboniferous – Permian paleogeography of the assembly of Pangaea. *Proceedings of the XVth International Congress on Carboniferous and Permian Stratigraphy*.

Busch, B. (2020). Pilot study on provenance and depositional controls on clay mineral coatings in active fluvio-eolian systems, western USA. *Sedimentary Geology, 406*, 105721. doi:10.1016/j.sedgeo.2020.105721

Busch, B., Becker, I., Koehrer, K., Adelmann, D., & Hilgers, C. (2019). Porosity evolution of two Upper Carboniferous tight-gas-fluvial sandstone reservoirs: Impact of fractures and total cement volumes on reservoir quality. *Marine and Petroleum Geology, 100*, 376-390. doi:10.1016/j.marpetgeo.2018.10.051

Busch, B., Hilgers, C., & Adelmann, D. (2020). Reservoir quality controls on Rotliegend fluvio-aeolian wells in Germany and the Netherlands, Southern Permian Basin – Impact of grain coatings and cements. *Marine and Petroleum Geology, 112*, 104075. doi:10.1016/j.marpetgeo.2019.104075

Busch, B., Hilgers, C., Gronen, L., & Adelmann, D. (2017). Cementation and structural diagenesis of fluvio-aeolian Rotliegend sandstones, northern England. *Journal of the Geological Society, 174*, 855-868. doi:10.1144/jgs2016-122

Busch, B., Hilgers, C., Lander, R. H., Bonnell, L. M., & Adelmann, D. (2018). Reservoir quality and burial model evaluation by kinetic quartz and illite cementation modeling: Case study of Rotliegendes, north Germany. *AAPG Bulletin, 102*(2), 293-307. doi:10.1306/0503171605217075

Busch, B., Winkler, R., Osivandi, K., Nover, G., Amann-Hildenbrand, A., & Hilgers, C. (2015). Evolution of small-scale flow barriers in German Rotliegend siliciclastics. *Geol. Soc. Spec. Pub., 435*, 141-160. doi:10.1144/SP435.3

Cannon, S. (2018). *Reservoir Modelling: A Practical Guide*: Wiley Blackwell.

Caulk, R. A., & Tomac, I. (2017). Reuse of abandoned oil and gas wells for geothermal energy production. *Renewable Energy, 112*, 388-397. doi:10.1016/j.renene.2017.05.042

Chan, M. A., Parry, W. T., & Bowman, J. R. (2000). Diagenetic hematite and manganese oxides and fault-related fluid flow in Jurassic sandstones, southeastern Utah *AAPG Bulletin, 84*, 1281–1310. doi:10.1306/A9673E82-1738-11D7-8645000102C1865D

Chandler, M. A., Kocurek, G., Goggin, D. J., & Lake, L. W. (1989). Effects of stratigraphic heterogeneity on permeability in eolian sandstone sequence, Page Sandstone, northern Arizona. *AAPG Bulletin, 73*(5), 658-668.

Chang, C., Zoback, M. D., & Khaskar, A. (2006). Empirical relations between rock strength and physical properties in sedimentary rocks. *Journal of Petroleum Science and Engineering, 51*, 223-237. doi:10.1016/j.petrol.2006.01.003

Chen, H., & Hu, Z.-Y. (2003). Some factors affecting the uniaxial strength of weak sandstones. *Bulletin of Engineering Geology and the Environment, 62*, 323-332. doi:10.1007/s10064-003-0207-4

Clauer, N., Liewig, N., & Zwingmann, H. (2012). Time-constrained illitization in gas-bearing Rotliegende (Permian) sandstones from northern Germany by illite potassium-argon dating. *AAPG Bulletin, 96*(3), 519-543. doi:doi.org/10.1306/07131111003

Cnudde, V., Boone, M., Dewanckele, J., Dierick, M., Van Hoorebeke, L., & Jacobs, P. (2011). 3D characterization of sandstone by means of X-ray computed tomography. *Geosphere, 7*, 54-61. doi:10.1130/GES00563.1

Cohen, K. M., Finney, S. C., Gibbard, P. L., & Fan, J.-X. (2013). The ICS international chronostratigraphic chart. *Episodes, 36*, 199-204. doi:10.18814/epiiugs/2013/v36i3/002

Curry, T. S., Dowdey, J. E., & Murry, R. C. (1990). *Christensen's physics of diagnostic radiology*. London: Lippincott Williams & Wilkins.

David, C., Menéndez, B., & Bernabé, Y. (1998). The mechanical behaviour of synthetic sandstone with varying brittle cement content. *Int. J. Rock Mech. Min. Sci., 35*, 759-770. doi:10.1016/S0148-9062(98)00003-5

David, C., Wong, T.-F., Zhu, W., & Zhang, J. (1994). Laboratory measurement of compaction-induced permeability change in porous rocks: Implications for the generation and maintenance of pore pressure excess in the crust. *Pure and Applied Geophysics, 143*, 425-456. doi:10.1007/BF00874337

Desbois, G., Urai, J. L., Hemes, S., Schröppel, B., Schwarz, J.-O., Mac, M., & Weiel, D. (2016). Multi-scale analysis of porosity in diagenetically altered reservoir sandstone from the Permian Rotliegend (Germany). *Journal of Petroleum Science and Engineering, 140*, 128-148. doi:10.1016/j.petrol.2016.01.019

DIN18136 (2003). Investigation and testing - Unconfined compression test, DIN German Institute for Standardization.

Dobereiner, L. (1986). Geotechnical properties of weak sandstones *Géotechnique, 36*, 79-94. doi:10.1680/geot.1986.36.1.79

dos Anjos, S. M. C., De Ros, L. F., de Souza, R. S., de Assis Silva, C. M., & Sombra, C. L. (2000). Depositional and diagenetic controls on the reservoir quality of Lower Cretaceous Pendencia sandstones, Potiguar rift basin, Brazil. *AAPG Bulletin, 84*, 1719-1742. doi:10.1306/8626C375-173B-11D7-8645000102C1865D

Dyke, C. G., & Dobereiner, L. (1991). Evaluating the strength and deformability of sandstones. *Quarterly Journal of Engineering Geology and Hydrogeology, 24*, 123-134. doi:10.1144/GSL.QJEG.1991.024.01.13

Ehrenberg, S. N. (1990). Relationship between diagenesis and reservoir quality in sandstones of the Garn Formation, Haltenbanken, Mid-Norwegian continental shelf. *AAPG Bulletin, 74*, 1538-1558. doi:10.1306/0C9B2515-1710-11D7-8645000102C1865D

Ehrenberg, S. N., & Nadeau, P. H. (1989). Formation of diagenetic illite in sandstones of the Garn Formation, Haltenbanken area, Mid-Norwegian continental shelf. *Clay Minerals, 24*, 233-253. doi:10.1180/claymin.1989.024.2.09

Esch, W. L., Ajdukiewicz, J. M., & Reynolds, A. C. (2008). Early grain-coat formation in Chaco dune field , New Mexico: insight into formation mechanisms, distribution, and implications for predictive modeling to assist in deep play identification. *AAPG Annual Convention.*

Fahy, M. P., & Guccione, M. J. (1979). Estimating strength of sandstone using petrographic thin-section data. *Environmental and Engineering Geoscience, 16*, 467-485. doi:10.2113/gseegeosci.xvi.4.467

Farrell, N. J. C., & Healy, D. (2017). Anisotropic pore fabrics in faulted porous sandstones. *Journal of Structural Geology, 104*, 125-141. doi:10.1016/j.jsg.2017.09.010

Farrell, N. J. C., Healy, D., & Taylor, C. W. (2014). Anisotropy of permeability in faulted porous sandstones. *Journal of Structural Geology, 63*, 50-67. doi:10.1016/j.jsg.2014.02.008

Fischer, C., Dunkl, I., von Eynatten, H., Wijbrans, J. R., & Gaupp, R. (2012). Products and timing of diagenetic processes in Upper Rotliegend sandstones from Bebertal (North German Basin, Parchim Formation, Flechtingen High, Germany). *Geol. Mag., 149*, 827-840. doi:10.1017/S0016756811001087

Folk, R. L. (1980). *Petrology of the sedimentary rocks*. Austin, Texas: Hemphill Publishing Company.

Folk, R. L., & Pittman, J. S. (1971). Length-slow chalcedony; a new testament for vanished evaporites. *Journal of Sedimentary Research, 41*, 1045–1058. doi:10.1306/74D723F1-2B21-11D7-8648000102C1865D

Fossen, H., Schultz, R. A., & Torabi, A. (2011). Conditions and implications for compaction band formation in the Navajo Sandstone, Utah. *Journal of Structural Geology, 33*, 1477-1490. doi:10.1016/j.jsg.2011.08.001

Fryberger, S. G., Knight, R., Hern, C., Moscariello, A., & Kabel, S. (2011). Rotliegend facies, sedimentary provinces, and stratigraphy, Southern Permian Basin UK and the Netherlands: A review with new observations. *The Permian Rotliegend of The Netherlands, 98*. doi:10.2110/pec.11.98.0051

Gaitzsch, B., Ellenberg, J., Lützner, H., & Benek, R. (1995). Stratigraphie des Rotliegend in Oberflächenaufschlüssen - Flechtinger Scholle. In E. Plein (Ed.), Stratigraphie von Deutschland I: Norddeutsches Rotliegendbeckken (Vol. 183, pp. 84-96): Courier Forschungsinstitut Senckenberg.

Gaitzsch, B., Geißler, M., Göthel, M., Kopp, J., & Legler, B. (2004). Karbon und Rotliegend der Flechtingen-Roßlau-Scholle. In C.-H. Friedel & H.-G. Röhling (Eds.), GeoLeipzig 2004 - Geowissenschaften sichern Zukunft (Vol. 35, pp. 150-164). Hannover: Deutsche Geologische Gesellschaft.

Gast, R., & Gundlach, T. (2006). Permian strike slip and extensional tectonics in Lower Saxony , Germany. *Z. dt. Ges. Geowiss.,, 157*, 41-56. doi:10.1127/1860-1804/2006/0157-0041

Gast, R. E. (1993). Sequenzanalyse von äolischen Abfolgen im Rotliegenden und deren Verzahnung mit Küstensedimenten. *Geologisches Jahrbuch, 131*, 117-139.

Gast, R. E. (1994). Cornberg outcrops revisited (Hessen, Germany): The depositional environment of its saurian tracks and Weissliegend Sandstones. *Meyniana, 46*, 59-75.

Gast, R. E., Dusar, M., Breitkreuz, C., Gaupp, R., Schneider, J. W., Stemmerik, L., Geluk, M. C., Geißler, M., Kiersnowski, H., Glennie, K. W., Kabel, S., & Jones, N. S. (2010). Rotliegend. In H. Doornenbaal & A. Stevenson (Eds.), Petroleum Geological Atlas of the Southern Permian Basin Area (pp. 101-121). Houten: EAGE.

Gaupp, R., Matter, A., Platt, J., Ramseyer, K., & Walzebuck, J. (1993). Diagenesis and fluid evolution of deeply buried Permian (Rotliegende) gas reservoirs, northwest Germany. *AAPG Bulletin, 77*. doi:10.1306/BDFF8E0C-1718-11D7-8645000102C1865D

Gaupp, R., & Okkerman, J. A. (2011). Diagenesis and reservoir quality of Rotliegend sandstones in the northern Netherlands, a review. *SEPM Special Publication, 98*, 193-226. doi:doi.org/10.2110/pec.11.98.0193

Geluk, M. C. (1999). Late Permian (Zechstein) rifting in the Netherlands: models and implications for petroleum geology. *Petroleum Geoscience, 5*, 189-199. doi:10.1144/petgeo.5.2.189

Geluk, M. C. (2005). Stratigraphy and tectonics of Permo-Triassic basins in the Netherlands.

Ghassemi, A. (2012). A review of some rock mechanics issues in geothermal reservoir development. *Geotech Geol Eng, 30*, 647-664. doi:10.1007/s10706-012-9508-3

Gibbons, K., Halvorsen, C., & Siring, E. (1993). Vertical and horizontal permeability variation within a sandstone reservoir based on minipermeameter measurements. *Marine and Petroleum Geology, 10*, 325-334. doi:10.1016/0264-8172(93)90077-6

Glennie, K. W. (2007). The Permo-Carboniferous Rotliegend of NW Europe. In T. E. Wong (Ed.), Proceedings of the XVth International Congress on Carboniferous and Permian Stratigraphy. (pp. 10-16). Amsterdam: Netherlands Academy of Arts and Sciences.

Glennie, K. W., & Buller, A. T. (1983). The Permian Weissliegend of NW Europe: the partial deformation of aeolian dune sands caused by the Zechstein transgression. *Sedimentary Geology, 35*, 43-81. doi:10.1016/0037-0738(83)90069-6

Golab, A. N., Knackstedt, M. A., Averdunk, H., Senden, T., Butcher, A. R., & Jaime, P. (2010). 3D porosity and mineralogy characterization in tight gas sandstones. *The Leading Edge, 29*, 1476-1483. doi:10.1190/1.3525363

Greene, G. W., Kristiansen, K., Meyer, E. E., Boles, J. R., & Israelachvili, J. N. (2009). Role of electrochemical reactions in pressure solution. *Geochimica et Cosmochimica Acta, 73*, 2862-2874. doi:10.1016/j.gca.2009.02.012

Griffiths, J., Worden, R. H., Woolridge, L. J., Utley, J. E. P., & Duller, R. A. (2019). Compositional variation in modern estuarine sands: Predicting major controls on sandstone reservoir quality. *AAPG Bulletin, 103*, 797-833. doi:10.1306/09181818025

Hancock, J. M., & Kauffman, E. G. (1979). The great trangsressions of the Late Cretaceous. *Journal of the Geological Society, 136*, 175-186. doi:10.1144/gsjgs.136.2.0175

Haubold, H., Lockley, M. G., Hunt, A. P., & Lucas, S. G. (1995). Lacertoid footprints from Permian dune sandstones, Cornberg and DeChelly sandstones. *Early Permian foot- prints and facies. New Mexico Museum of Natural History and Science Bulletin, 6*, 235-244.

Heald, M. T., & Larese, R. E. (1974). Influence of coatings on quartz cementation. *Journal of Sedimentary Petrology, 44*(4), 1269-1274. doi:10.1306/212F6C94-2B24-11D7-8648000102C1865D

Heap, M. J. (2019). The influence of sample geometry on the permeability of a porous sandstone. *Geoscientific Instrumentation, Methods and Data Systems, 8*, 55-61. doi:10.5194/gi-8-55-2019

Heap, M. J., Kushnir, A. R. L., Gilg, H. A., Wadsworth, F. B., Reuschlé, T., & Baud, P. (2017). Microstructural and petrophysical properties of the Permo-Triassic sandstones (Buntsandstein) from the Soultz-sous-Forêts geothermal site (France). *Geothermal Energy, 5*, 26. doi:10.1186/s40517-017-0085-9

Heidsiek, M., Butscher, C., Blum, P., & Fischer, C. (2020). Small-scale diagenetic facies heterogeneity controls porosity and permeability pattern in reservoir sandstones. *Environmental Earth Sciences, 79*, 425. doi:10.1007/s12665-020-09168-z

Heinemann, N., Wilkinson, M., Pickup, G. E., Haszeldine, R. S., & Cutler, N. A. (2012). CO2 storage in the offshore UK Bunter Sandstone Formation. *International Journal of Greenhouse Gas Contro, 6*, 210-219. doi:10.1016/j.ijggc.2011.11.002

Henkel, S., Pudlo, D., Gaupp, R., & H2STORE-Team. (2013). Research sites of the H2STORE project and the relevance of lithological variations for hydrogen storage at depths. *Energy Procedia, 40*, 25-33. doi:10.1016/j.egypro.2013.08.004

Hensel, S., Goebbels, S., & Kada, M. (2019). Facade reconstruction for testured LOD2 CITYGML models based on deep learning and mixed integer linear programming. *ISPRS Annals of the Photogrammetry, Remote Sensing and Spatial Information Sciences, 4*, 37-44. doi:10.5194/isprs-annals-IV-2-W5-37-2019

Hettema, M. H. H., Schutjens, P. M. T. M., Verboom, B. J. M., & Gussionklo, H. J. (2000). Production-induced compaction of a sandstone reservoir: The strong influence of stress path *SPE Reservoir Evaluation & Engineering, 3*, 342-347. doi:10.2118/65410-PA

Hoth, K., Huebscher, H. D., Korich, D., Gabriel, W., & Enderlein, F. (1993). Die Lithostratigraphie der permokarbonischen Effusiva im Zentralabschnitt der mitteleuropäischen Senke. *Geol. Jb., A 131*, 179-196.

Houseknecht, D. W. (1987). Assessing the relative importance of compaction processes and cementation to reduction of porosity in sandstones. *AAPG Bulletin, 71*, 633-642. doi:10.1306/9488787F-1704-11D7-8645000102C1865D

Howarth, R. J. (1998). Improved estimators of uncertainty in proportions, point-counting, and pass-fail test results. *American Journal of Science, 298*, 594-607. doi:10.2475/ajs.298.7.594

Hsieh, Y.-M., Li, H.-H., Huang, T.-H., & Jeng, F.-S. (2008). Interpretations on how the macroscopic mechanical behavior of sandstone affected by microscopic properties—Revealed by bonded-particle model. *Eng. Geol., 99*, 1-10. doi:10.1016/j.enggeo.2008.01.017

Huang, W.-L., Longo, J. M., & Pevear, D. R. (1993). An experimentally derived kinetic model for smectite-to-illite conversion and its use as a geothermometer. *Clays and Clay Minerals, 41*, 162-177. doi:10.1346/CCMN.1993.0410205

Hurst, A., & Nadeau, P. H. (1995). Clay microporosity in reservoir sandstones: An application of quantitative electron microscopy in petrophysical evaluation. *AAPG Bulletin, 79*, 563-573. doi:10.1306/8D2B1598-171E-11D7-8645000102C1865D

Iheanacho, P. C., Tiab, D., & Igbokoyi, A. O. (2012). *Vertical-horizontal permeability relationships for sandstone reservoirs* Paper presented at the SPE Nigeria Annual International Conference and Exhibition, Lagos, Nigeria.

Jackson, D. I., Johnson, H., & Smith, N. J. P. (1997). Stratigraphical relationships and a revised lithostratigraphical nomenclature for the Carboniferous, Permian and Triassic rocks of the offshore East Irish Sea Basin. *Geological Society, London, Special Publications, 124*, 11-32. doi:10.1144/GSL.SP.1997.124.01.02

Katzung, G. (1988). Tectonics and sedimentation of Variscan molasses in Central-Europe. *Zeitschrift für geologische Wissenschaften, 16*, 823-843.

Ketzer, J. M., Morad, S., & Amorosi, A. (2003). Predictive diagenetic clay-mineral distribution in siliciclastic rocks within a sequence stratigraphic framework. *Int. Assoc. Sedimentol. Spec. Publ., 34*, 43-61. doi:10.1002/9781444304336.ch2

Kiersnowski, H. (2013). Depositional development of the Polish Upper Rotliegend Basin and evolution of its sediment source areas. *Geological Quarterly, 41*, 433-455.

Kiersnowski, H., Paul, J., Peryt, T. M., & Smith, D. B. (1995). Facies, paleogeography, and sedimentary history of the Southern Permian Basin in Europe. In The Permian of Northern Pangea (pp. 199-136). Berlin: Springer.

Kley, J., & Voigt, T. (2008). Late Cretaceous intraplate thrusting in central Europe: Effect of Africa-Iberia-Europe convergence, not Alpine collision. *Geology, 36*, 839-842. doi:10.1130/G24930A.1

Klinkenberg, L. J. (1941). The permeability of porous media to liquids and gases. In Drilling and production practice: American Petroleum Institute.

Knauss, K. G., & Wolery, T. J. (1988). The dissolution kinetics of quartz as a function of pH and time at 70°C. *Geochimica et Cosmochimica Acta, 52*, 43-53. doi:10.1016/0016-7037(88)90055-5

Knox, R. W. O. B., Bosch, J. H. A., Rasmussen, E. S., Heilmann-Clausen, C., Hiss, M., De Lugt, I. R., Kasińksi, J., King, C., Köthe, A., Słodkowska, B., Standke, G., & Vandenberghe, N. (2010). Cenozoic. In J. C. Doornenbal & A. G. Stevenson (Eds.), Petroleum Geological Atlas of the Southern Permian Basin Area (pp. 211-223). Houten: EAGE Publication b.v.

Kocurek, G., Robinson, N. I., & Sharp Jr., J. M. (2001). The response of the water table in coastal aeolian systems tochanges in sea level. *Sedimentary Geology, 139*, 1-13. doi:10.1016/S0037-0738(00)00137-8

Kohlhepp, B. (2012). *Untersuchungen zu Fazies, Diagenese und Poren-/Mineralgrenzflächen an Rotliegend-Sandsteinen im Rahmen einer Analogstudie zur Wirkung von CO2 auf Gasspeichersysteme.* (PhD). Friedrich-Schiller-Universität Jena, Jena.

Kowalczyk, G., Herbst, A., & Heggemann, H. (2012). Rotliegend in den Hessischen Becken. In H. Lützner & G. Kowalczyk (Eds.), Stratigraphie von Deutschland X. Rotliegend. Teil I: Innervariscische Becken. (Vol. 61, pp. 378-417). Hannover: Deutsche Gesellschaft für Geowissenschaften.

Kristiansen, K., Valtiner, M., Greene, G. W., Boles, J. R., & Israelachvili, J. N. (2011). Pressure solution – The importance of the electrochemical surface potentials. *Geochimica et Cosmochimica Acta, 75*, 6882-6892. doi:10.1016/j.gca.2011.09.019

Kuila, U., McCarthy, D. K., Derkowski, A., Fisher, T. B., & Prasad, M. (2014). Total porosity measurement in gas shales by the water immersion porosimetry (WIP) method. *Fuel, 117*(B), 1115-1129. doi:10.1016/j.fuel.2013.09.073

Kulick, J., Leifeld, D., & Meisl, S. (1984). *Petrofazielle und chemische Erkundung des Kupferschiefers-der Hessischen Senke und des Harz-Westrandes.* (Vol. D 68). Hannover: Schweizerbart.

Kunkel, C., Aehnelt, M., Pudlo, D., Kukowski, N., Totsche, K. U., & Gaupp, R. (2018). Subsurface aquifer heterogeneities of Lower Triassic clastic sediments in central Germany. *Marine and Petroleum Geology, 97*, 209-222. doi:10.1016/j.marpetgeo.2018.06.022

Kushnir, A. R. L., Heap, M. J., & Baud, P. (2018). Assessing the role of fractures on the permeability of the Permo-Triassic sandstones at the Soultz-sous-Forêts (France) geothermal site. *Geothermics, 74*, 181-189. doi:10.1016/j.geothermics.2018.03.009

Lander, R. H., & Bonnell, L. M. (2010). A model for fibrous illite nucleation and growth in sandstones. *AAPG Bulletin, 94*, 1161-1187. doi:10.1306/04211009121

Lander, R. H., Larese, R. E., & Bonnell, L. M. (2008). Toward more accurate quartz cement models: The importance of euhedral versus noneuhedral growth rates. *AAPG Bulletin, 92*, 1537-1563. doi:10.1306/07160808037

Lanson, B., Beaufort, D., Berger, G., Bauer, A., Cassagnabère, A., & Meunier, A. (2002). Authigenic kaolin and illitic minerals during burial diagenesis of sandstones: a review. *Clay Minerals, 37*, 1-22. doi:10.1180/0009855023710014

Legarth, B., Huenges, E., & Zimmermann, G. (2005). Hydraulic fracturing in a sedimentary geothermal reservoir: Results and implications. *International Journal of Rock Mechanics and Mining Sciences, 42*, 1028-1041. doi:10.1016/j.ijrmms.2005.05.014

Legler, B., & Schneider, J. W. (2008). Marine ingressions into the Middle/Late Permian saline lake of the Southern Permian Basin (Rotliegend, Northern Germany) possibly linked to sea-level highstands in the Arctic rift system. *Palaeogeography, Palaeoclimatology, Palaeoecology, 267*, 102-114. doi:10.1016/j.palaeo.2008.06.009

Liewig, N., & Clauer, N. (2000). K-Ar dating of varied microtextural illite in Permian gas reservoirs, northern Germany. *Clay Minerals, 35*, 271-281. doi:10.1180/000985500546648

Line, H. L., Jahren, J., & Hellevang, H. (2018). Mechanical compaction in chlorite-coated sandstone reservoirs – Examples from Middle – Late Triassic channels in the southwestern Barents Sea. *Marine and Petroleum Geology, 96*, 348-370.

Lohr, T., Kramczyk, C. M., Tanner, D. C., Samiee, R., Endres, H., Oncken, O., Trappe, H., & Kukla, P. A. (2007). Strain partitioning due to salt: insights from interpretation of a 3D seismic data set in the NW German Basin. *Basin Research, 19*, 579-597. doi:10.1111/j.1365-2117.2007.00338.x

Lott, G. K., Wong, T. E., Dusar, M., Andsbjerg, J., Mönnig, E., Feldman-Olszewska, A., & Verreussel, R. M. C. H. (2010). Jurassic. In J. C. Doornenbal & A. G. Stevenson (Eds.), Petroleum Geological Atlas of the Southern Permian Basin Area (pp. 175-193). Houten, NL: EAGE Publications.

Lundegard, P. D. (1992). Sandstone porosity loss; a" big picture" view of the importance of compaction. *Journal of Sedimentary Petrology, 62*, 250-260. doi:10.1306/D42678D4-2B26-11D7-8648000102C1865D

Macchi, L. C. (1981). *Sedimentology of the Penrith sandstone and Brockrams (Permo-Triassic) of Cumbria, north-west England.* (PhD). University of Hull,

Mader, D., & Yardley, M. J. (1985). Migration, modification and merging in aeolian systems and the significance of the depositional mechanisms in Permian and Triassic dune sands of Europe and North America. *Sedimentary Geology, 43*, 85-218. doi:10.1016/0037-0738(85)90056-9

Mahmic, O., Dypvik, H., & Hammer, E. (2018). Diagenetic influence on reservoir quality evolution, examples from Triassic conglomerates/arenites in the Edvard Grieg field, Norwegian North Sea. *Marine and Petroleum Geology, 93*, 247-271. doi:10.1016/j.marpetgeo.2018.03.006

Markussen, Ø., Dypvik, H., Hammer, E., Long, H., & Hammer, Ø. (2019). 3D characterization of porosity and authigenic cementation in Triassic conglomerates/arenites in the Edvard Grieg field using 3D micro-CT imaging. *Marine and Petroleum Geology, 99*, 265-281. doi:10.1016/j.marpetgeo.2018.10.015

Matlack, K. S., Houseknecht, D. W., & Applin, K. R. (1989). Emplacement of clay into sand by infiltration. *Journal of Sedimentary Research, 59*, 77-87. doi:10.1306/212F8F21-2B24-11D7-8648000102C1865D

McCann, T. (1998). Sandstone composition and provenance of the Rotliegend of the NE German Basin. *Sedimentary Geology, 116*, 177-198. doi:10.1016/S0037-0738(97)00106-1

McCune, L. K., & Wilhelm, R. H. (1949). Mass and momentum transfer in a solid-liquid system. *Industrial & Engineering Chemistry, 41*, 1124-1134.

McKinley, J. M., Atkinson, P. M., Lloyd, C. D., Ruffell, A. H., & Worden, R. H. (2011). How porosity and permeability vary spatially with grain size, sorting, cement volume, and mineral dissolution in fluvial Triassic sandstones: The value of geostatistics and local regression. *Journal of Sedimentary Research, 81*, 844-858. doi:10.2110/jsr.2011.71

McKinley, J. M., Worden, R. H., & Ruffell, A. H. (1999). Smectite in sandstones: A review of the controls on occurrence and behaviour during diagenesis. *Int. Assoc. Sedimentol. Spec. Publ., 34*, 109-128. doi:10.1002/9781444304336.ch5

Menning, M. (1995). A numerical time scale for the Permian and Triassic periods: an integrated time analysis. In P. A. Scholle, T. M. Peryt, & D. S. Ulmer-Scholle (Eds.), The Permian of Northern Pangea (Vol. Volume 1: Paleogeography, Paleoclimates, Stratigraphy). Berlin, Heidelberg: Springer.

Menning, M., Schröder, B., Plein, E., Simon, T., Lepper, J., Röhling, H.-G., Heunisch, C., Stapf, K., Lützner, H., Käding, K.-C., Paul, J., Horn, M., Hagdorn, H., Beutler, G., & Nitsch, E. (2011). Beschlüsse der Deutschen Stratigraphischen Kommission 1991–2010 zu Perm und Trias von Mitteleuropa. *Zeitschrift der Deutschen Gesellschaft für Geowissenschaften, 162*, 1-18. doi:10.1127/1860-1804/2011/0162-0001

Meyer, R. (2002). Anisotropy of sandstone permeability. *CREWES Research Report, 14*, 1-12.

Milliken, K. L. (1992). Chemical behavior of detrital feldspars in mudrocks versus sandstones, Frio Formation (Oligocene), South Texas. *Journal of Sedimentary Research, 65*, 790-801. doi:10.1306/D42679DD-2B26-11D7-8648000102C1865D

Millionshchikov, M. D. (1941). On the theory of homogeneous isotropic turbulence. *Dokl. Akad. Nauk SSSR, 32*, 611-614.

Moeck, I., Schandelmeier, H., & Holl, H. G. (2009). The stress regime in a Rotliegend reservoir of the Northeast German Basin. *International Journal of Earth Sciences, 98*, 1643-1654. doi:10.1007/s00531-008-0316-1

Molenaar, N., & Felder, M. (2018). Clay cutans and the origin of illite rim cement: An example from the siliciclastic Rotliegend sandstone in the Dutch Southern Permian Basin. *Journal of Sedimentary Research, 88*, 641-658. doi:10.2110/jsr.2018.33

Monsees, A. C., Busch, B., Schöner, N., & Hilgers, C. (2020a). Rock typing of diagenetically induced heterogeneities – a case study from a deeply-buried clastic Rotliegend reservoir of the Northern German Basin *Marine and Petroleum Geology, 113*, 104163. doi:10.1016/j.marpetgeo.2019.104163

Monsees, A. C., Subhedar, A., Busch, B., Nestler, B., & Hilgers, C. (2020b). Calibrating micro-computed tomography data to permeability experiments and petrography – insights from Digital Rocks. *OIL GAS European Magazine, 70*(3), 28-33. doi:10.19225/200908

Morad, S. (1998). Carbonate cementation in sandstones: distribution patterns and geochemical evolution. *Spec. Publ. int. Ass. Sediment., 26*, 1-26. doi:10.1002/9781444304893

Morad, S., Al-Ramadan, K., Ketzer, J. M., & De Ros, L. F. (2010). The impact of diagenesis on the heterogeneity of sandstone reservoirs: A review of the role of depositional facies and sequence stratigraphy. *AAPG Bulletin, 94*, 1267-1309. doi:10.1306/04211009178

Motzka-Nöring, R., Anderle, H.-J., Blum, R., Diederich, G., Gundlach, H., Hentschel, G., Herrmann, A., Horn, M., Kulick, J., Lindstedt, H.-J., Malzahn, E., Prinz, H., Reichmann, H., Schade, H., Stoppel, D., & Theuerjahr, A.-K. (1987). Erläuterungen zur Geologischen Karte von Hessen 1:25000 Blatt Nr. 4925 Sontra, Hessisches Landesamt für Bodenforschung.

Mumm, A. S., & Wolfgramm, M. (2002). Diagenesis and fluid mobilisation during the evolution of the North German Basin—evidence from fluid inclusion and sulphur isotope analysis. *Marine and Petroleum Geology, 19*, 229-246. doi:10.1016/S0264-8172(02)00015-6

Mutschler, T. (2004). Neufassung der Empfehlung Nr. 1 des Arbeitskreises "Versuchstechnik Fels" der Deutschen Gesellschaft für Geotechnik e. V.: Einaxiale Druckversuche an zylindrischen Gesteinsprüfkörpern. *Bautechnik, 81*, 825-834. doi:10.1002/bate.200490194

Nadoll, P., Sosnicka, M., Kraemer, D., & Duschl, F. (2019). Post-Variscan structurally-controlled hydrothermal Zn-Fe-Pb sulfide and F-Ba mineralization in deep-seated Paleozoic units of the North German Basin: A review. *Ore Geology Reviews, 106*, 273-299. doi:10.1016/j.oregeorev.2019.01.022

Otto, V. (2003). Inversion-related features along the southeastern margin of the North German Basin (Elbe Fault System). *Tectonophysics, 373*, 107-123. doi:10.1016/S0040-1951(03)00287-7

Paul, J. (2012). Weißliegend, Grauliegend und das Zechstein-Konglomerat: die Rotliegend/Zechstein-Grenze. In H. Lützner & G. Kowalczyk (Eds.), Stratigraphie von Deutschland X. Rotliegend. Teil I: Innervariscische Becken (Vol. 61, pp. 707-714). Hannover: Deutsche Gesellschaft für Geowissenschaften.

Paxton, S. T., Szabo, J. O., Ajdukiewicz, J. M., & Klimentidis, R. E. (2002). Construction of an intergranular volume compaction curve for evaluating and predicting compaction and porosity loss in rigid-grain sandstone reservoirs. *AAPG Bulletin, 86*, 2047-2067. doi:10.1306/61EEDDFA-173E-11D7-8645000102C1865D

Peng, S., Hu, Q., Dultz, S., & Zhang, M. (2012). Using X-ray computed tomography in pore structure characterization for a Berea sandstone: Resolution effect. *Journal of Hydrology, 472-473*, 254-261. doi:10.1016/j.jhydrol.2012.09.034

Pfeiffer, W. T., Beyer, C., & Bauer, S. (2017). Hydrogen storage in a heterogeneous sandstone formation: dimensioning and induced hydraulic effects *Petroleum Geoscience, 23*, 315-326. doi:10.1144/petgeo2016-050

Pijnenburg, R. P. J., Verberne, B. A., Hangx, S. J. T., & Spiers, C. J. (2019a). Inelastic deformation of the Slochteren sandstone: Stress-strain relations and implications. *JGR: Solid Earth, 124*, 5254–5282. doi:10.1029/2019JB017366

Pijnenburg, R. P. J., Verberne, B. A., Hangx, S. J. T., & Spiers, C. J. (2019b). Intergranular clay films control inelastic deformation in the Groningen gas reservoir: Evidence from split-cylinder deformation tests. *JGR: Solid Earth, 124*, 12679-12702. doi:10.1029/2019JB018702

Pittman, E. D., Larese, R. E., & Heald, M. T. (1992). Clay coats: occurrence and relevance to preservation of porosity in sandstones. *SEPM Special Publication, 47*, 241-255. doi:10.2110/pec.92.47.0241

Plein, E., & van Adrichem Boogaert, A. (1995). *Stratigraphie von Deutschland. Band 1. Norddeutsches Rotliegendbecken. Teil 2. Rotliegend-Monographie*: Senckenbergische Naturforschende Gesellschaft.

Prajapati, N., Abad Gonzalez, A., Selzer, M., Nestler, B., Busch, B., & Hilgers, C. (2020). Quartz cementation in polycrystalline sandstone: Insights from phase-field simulations. *JGR Solid Earth, 125*(2). doi:10.1029/2019JB019137

Prajapati, N., Selzer, M., Nestler, B., Busch, B., Hilgers, C., & Ankit, K. (2018). Three-dimensional phase-field investigation of pore space cementation and permeability in quartz sandstone. *JGR Solid Earth, 123*, 6378-6396. doi:10.1029/2018JB015618

Pryor, A. W. (1971). Petrology of the Weißliegendes sandstones in the Harz and Werra-Fulda area. *Geol. Rundsch., 80*, 524-552. doi:10.1007/BF02000468

Pudlo, D., Reitenbach, V., Albrecht, D., Ganzer, L., Gernert, U., Wienand, J., Kohlhepp, B., & Gaupp, R. (2012). The impact of diagenetic fluid–rock reactions on Rotliegend sandstone composition and petrophysical properties (Altmark area, central Germany). *Environ Earth Sci, 67*, 369-384. doi:10.1007/s12665-012-1723-y

Rassenfoss, S. (2011). Digital rocks out to become a core technology *Journal of Petroleum Technology, 63*, 36-41. doi:10.2118/0511-0036-JPT

Regenspurg, S., Feldbusch, E., Byrne, J., Deon, F., Driba, D. L., Henninges, J., Kappler, A., Naumann, R., Reinsch, T., & Schubert, C. (2015). Mineral precipitation during production of geothermal fluid from a Permian Rotliegend reservoir. *Geothermics, 54*, 122-135. doi:10.1016/j.geothermics.2015.01.003

Renard, F., Ortoleva, P., & Gratier, J. P. (1997). Pressure solution in sandstones: influence of clays and dependence on temperature and stress. *Tectonophysics, 280*, 257-266. doi:10.1016/S0040-1951(97)00039-5

Rieke, H. (2001). *Sedimentologie, Faziesarchitektur und Faziesentwicklung des kontinentalen Rotliegenden im Norddeutschen Becken (NEDB).* (PhD thesis). University of Potsdam, Potsdam.

Salem, A. M., Morad, S., Mato, L. F., & Al-Aasm, I. S. (2000). Diagenesis and reservoir-quality evolution of fluvial sandstones during progressive burial and uplift: Evidence from the Upper Jurassic Boipeba Member, Reconcavo basin, northeastern Brazil. *AAPG Bulletin, 84*, 1015-1040. doi:10.1306/A9673B9E-1738-11D7-8645000102C1865D

Saxena, N., Hofmann, R., Alpak, F. O., Berg, S., Dietderich, J., Agarwal, U., Tandon, K., Hunter, S., Freeman, J., & Wilson, O. B. (2017). References and benchmarks for pore-scale flow simulated using micro-CT images of porous media and digital rocks. *Advances in Water Resources, 109*, 211-235. doi:10.1016/j.advwatres.2017.09.007

Sayers, C. M., & Schutjens, P. M. T. M. (2007). An introduction to reservoir geomechanics. *The Leading Edge, 26*. doi:10.1190/1.2737100

Scheck, M., Bayer, U., Otto, V., Lamarche, J., Banka, D., & Pharaoh, T. (2002). The Elbe Fault System in North Central Europe—a basement controlled zone of crustal weakness. *Tectonophysics, 360*, 281-299. doi:10.1016/S0040-1951(02)00357-8

Schmid, S., Worden, R. H., & Fisher, Q. J. (2004). Diagenesis and reservoir quality of the Sherwood Sandstone (Triassic), Corrib Field, Slyne Basin, west of Ireland. *Marine and Petroleum Geology, 21*, 299-315. doi:10.1016/j.marpetgeo.2003.11.015

Schmidt, C., Busch, B., & Hilgers, C. (2018). *Coupling Diagenesis and Petrophysics in Red Bed Siliciclastics to Infer Fluid Flow Anisotropies – Analog Studies From SW Germany*. Paper presented at the EAGE Annual, Copenhagen.

Schmidt, C., Busch, B., & Hilgers, C. (2020a). Compaction and cementation control on bleaching in Triassic fluvial red beds, S-Germany. *Zeitschrift der Deutschen Gesellschaft für Geowissenschaften*. doi:10.1127/zdgg/2020/0233

Schmidt, C., Busch, B., & Hilgers, C. (2020b). Lateral variations of detrital, authigenic and petrophysical properties in an outcrop analog of the fluvial Plattensandstein, Lower Triassic, Central S-Germany. *Z. Dt. Ges. Geowiss., 171*. doi:10.1127/zdgg/2020/0234

Schneider, J., & Gebhardt, U. (1993). Litho- und Biofaziesmuster in intra- und extramontanen Senken des Rotliegend (Perm, Nord- und Ostdeutschland). *Geologisches Jahrbuch Reihe A, 131*, 57–98.

Schöner, R. (2006). *Comparison of Rotliegend sandstone diagenesis from the northern and southern margin of the North German Basin, and implications for the importance of organic maturation and migration.* (PhD thesis). University of Jena, Jena.

Schröder, L., Plein, E., Bachmann, G.-H., Gast, R. E., Gebhardt, U., Graf, R., Helmuth, H.-J., Pasternak, M., Porth, H., & Süssmuth, S. (1995). Stratigraphische Neugliederung des Rotliegend im Norddeutschen Becken. *Geologisches Jahrbuch Reihe A, 148*, 3-21.

Schumacher, C. (1985). *Die Kupfervererzungen des basalen Zechsteins im Rahmen der sedimentären Entwicklung des Werra-Fulda-Beckens.* (PhD). FU Berlin, Berlin.

Schwarzer, D., & Littke, R. (2007). Petroleum generation and migration in the `Tight Gas' area of the German Rotliegend natural gas play: a basin modelling study. *Petroleum Geoscience, 13*, 37-62. doi:10.1144/1354-079306-703

Scotese, C. R., & Langford, R. P. (1995). *Pangea and the paleogeography of the Permian*. Berlin: Springer.

Selley, R. C. (1998). *Elements of petroleum geology*: Gulf Professional Publishing.

Shakoor, A., & Bonelli, R. E. (1991). Relationship between petrographic characteristics, engineering index properties, and mechanical properties of selected sandstones. *Environmental and Engineering Geoscience, 28*, 55-71. doi:10.2113/gseegeosci.xxviii.1.55

Shepherd, R. G. (1989). Correlations of permeability and grain size. *Groundwater, 27*, 633-638. doi:10.1111/j.1745-6584.1989.tb00476.x

Smith, D. B. (1979). Rapid marine transgressions and regressions of the Upper Permian Zechstein Sea. *Journal of the Geological Society, 136*, 155-156. doi:10.1144/gsjgs.136.2.0155

Stollhofen, H., Bachmann, G. H., Barnasch, J., Bayer, U., Beutler, G., Franz, M., Kästner, M., Legler, B., Mutterlose, J., & Radies, D. (2008). Upper Rotliegend to Early Cretaceous basin development. In R. Littke, U. Bayer, S. Gajewski, & S. Nelskamp (Eds.), Dynamics of complex intracontinental basins. The Central European Basin System (pp. 181-210). Berlin, Heidelberg: Springer.

Storvoll, V., Bjørlykke, K., Karlsen, D., & Saigal, G. (2002). Porosity preservation in reservoir sandstones due to grain-coating illite: A study of the Jurassic Garn Formation from the Kristin and Lavrans fields, offshore Mid-Norway. *Marine and Petroleum Geology, 19*, 767-781. doi:10.1016/S0264-8172(02)00035-1

Sullivan, M. D., Haszeldine, R. S., & Fallick, A. E. (1990). Linear coupling of carbon and strontium isotopes in Rotliegend Sandstone, North Sea: Evidence for cross-formational fluid flow. *Geology, 18*, 1215-1218. doi:10.1130/0091-7613(1990)018%3C1215:LCOCAS%3E2.3.CO;2

Sweet, M. L. (1999). Interaction between aeolian, fluvial and playa environments in the Permian Upper Rotliegend Group. *Sedimentology, 46*, 171-187. doi:10.1046/j.1365-3091.1999.00211.x

Tada, R., & Siever, R. (1989). Pressure solution during diagenesis. *Annual Review of Earth and Planetary Sciences, 17*, 89-118. doi:annurev.ea.17.050189.000513

Talwani, P., & Acree, S. (1985). Pore pressure diffusion and the mechanism of reservoir-induced seismicity. In K. Shimazaki & W. Stuart (Eds.), Earthquake Prediction. Basel, Switzerland: Birkhäuser

Taylor, J. M. (1950). Pore-Space Reduction in Sandstones. *AAPG Bulletin, 34*, 701-716. doi:10.1306/3D933F47-16B1-11D7-8645000102C1865D

Taylor, T. R., Giles, M. R., Hathon, L. A., Diggs, T. N., Braunsdorf, N. R., Birbiglia, G. V., Kittridge, M. G., MacAulay, C. I., & Espejo, I. S. (2010). Sandstone diagenesis and reservoir quality prediction: Models, myths, and reality. *AAPG Bulletin, 94*, 1093-1132. doi:10.1306/04211009123

Taylor, T. R., Kittridge, M. G., Winefield, P., Bryndzia, L. T., & Bonnell, L. M. (2015). Reservoir quality and rock properties modeling - Triassic and Jurassic sandstones, greater Shearwater area, UK Central North Sea. *Marine and Petroleum Geology, 65*, 1-21. doi:10.1016/j.marpetgeo.2015.03.020

Trask, P. D. (1930). Mechanical analyses of sediments by centrifuge. *Economic Geology, 25*, 581-599. doi:10.2113/gsecongeo.25.6.581

Turner, P., Burley, S. D., Rey, D., & Prosser, J. (1995). Burial history of the Penrith Sandstone (Lower Permian) deduced from the combined study of fluid inclusion and palaeomagnetic data. In P. Turner & A. Turner (Eds.), Palaeomagnetic Applications in Hydrocarbon Exploration and Production (Vol. 98, pp. 43-78): Geol. Soc. Spec. Pub.

Ulusay, R., Türeli, K., & Ider, M. H. (1994). Prediction of engineering properties of a selected litharenite sandstone from its petrographic characteristics using correlation and multivariate statistical techniques. *Engineering Geology, 38*, 135-157. doi:10.1016/0013-7952(94)90029-9

Underhill, J. R., Gayer, R. A., Woodcock, N. H., Donnely, R., Jolley, E. J., & Stimpson, I. G. (1988). The Dent Fault System, northern England-reinterpreted as a major oblique-slip fault zone. *Journal of the Geological Society, London, 145*, 303-316. doi:10.1144/gsjgs.145.2.0303

Van Geet, M., Swennen, R., & Wevers, M. (2001). Towards 3-D petrography: application of microfocus computer tomography in geological science. *Computers & Geosciences, 27*, 1091-1099. doi:10.1016/S0098-3004(00)00154-0

van Houten, F. B. (1973). Origin of Red Beds - A Review - 1961-1972. *Annual Review of Earth and Planetary Sciences, 1*, 39-61. doi:10.1146/annurev.ea.01.050173.000351

Vejbæk, O. V., Andersen, C., Dusar, M., Herngreen, G. F. W., Krabbe, H., Leszczyński, K., Lott, G. K., Mutterlose, J., & Van der Molen, A. S. (2010). Cretaceous. In J. C. Doornenbal & A. G. Stevenson (Eds.), Petroleum Geological Atlas of the Southern Permian Basin Area (pp. 195-209). Houten: EAGE Publications b.v.

Vincent, B., Waters, J., Witkowski, F., Daniau, G., Oxtoby, N. H., Crowley, S., & Ellam, R. (2018). Diagenesis of Rotliegend sandstone reservoirs (offshore Netherlands): The origin and impact of dolomite cements. *Sedimentary Geology, 373*, 272-291. doi:10.1016/j.sedgeo.2018.06.012

Wadsworth, F. B., Vasseur, J., Scheu, B., Kendrick, J. E., Lavallée, Y., & Dingwell, D. B. (2016). Universal scaling of fluid permeability during volcanic welding and sediment diagenesis. *Geology, 44*, 219-222. doi:10.1130/G37559.1

Walderhaug, O. (1990). A fluid inclusion study of quartz-cemented sandstones from offshore mid-Norway; possible evidence for continued quartz cementation during oil emplacement. *Journal of Sedimentary Research, 60*, 203-210. doi:10.1306/212F9151-2B24-11D7-8648000102C1865D

Walderhaug, O. (1994). Temperatures of quartz cementation in Jurassic sandstones from the Norwegian continental shelf - Evidence from fluid inclusions. *Journal of Sedimentary Research, 64*, 311-323. doi:10.1306/D4267D89-2B26-11D7-8648000102C1865D

Walderhaug, O., & Bjørkum, P. A. (2003). The effect of stylolite spacing on quartz cementation in the Lower Jurassic Stø Formation, southern Barents Sea. *Journal of Sedimentary Research, 73*(2), 146-156. doi:10.1306/090502730146

Walderhaug, O., Lander, R. H., Bjørkum, P. A., Oelkers, E. H., Bjørlykke, K., & Nadeau, P. H. (2000). Modelling quartz cementation and porosity in reservoir sandstones: Examples from the Norwegian continental shelf. *Int. Assoc. Sedimentol. Spec. Publ., 29*, 39-50. doi:10.1002/9781444304237.ch3

Walker, F. D. L., Lee, M. R., & Parsons, I. (1995). Micropores and micropermeable texture in alkali feldspars: geochemical and geophysical implications. *Mineralogical Magazine, 59*, 505-534. doi:10.1180/minmag.1995.059.396.12

Walker, T. R., & Honea, R. M. (1969). Iron content of modern deposits in the Sonoran Desert: A contribution to the origin of red beds *GSA Bulletin, 80*, 535-544. doi:10.1130/0016-7606(1969)80[535:ICOMDI]2.0.CO;2

Waugh, B. (1970a). Formation of quartz overgrowths in the Penrith Sandstone (Lower Permian) of Northwest England as revealed by scanning electron microscopy. *Sedimentology, 14*, 309-320. doi:10.1111/j.1365-3091.1970.tb00197.x

Waugh, B. (1970b). Petrology, provenance and silica diagenesis of the Penrith Sandstone (Lower Permian) of Northwest England. *Journal of Sedimentary Petrology, 40*, 1226-1240. doi:10.1306/74D72171-2B21-11D7-8648000102C1865D

Weng, M. C., Jeng, F. S., Huang, T. H., & Lin, M. L. (2005). Characterizing the deformation behavior of Tertiary sandstones. *International Journal of Rock Mechanics & Mining Sciences, 42*, 388-401. doi:10.1016/j.ijrmms.2004.12.004

Whitaker, S. (1996). The Forchheimer equation: A theoretical development. *Transport in Porous Media, 25*, 27-61. doi:10.1007/BF00141261

Woodcock, N. H., Sayers, N. J., & Dickson, J. A. (2008). Fluid flow history from damage zone cements near the Dent and Rawthey faults, NW England. *Journal of the Geological Society, London, 165*, 829-837. doi:10.1144/0016-76492007-133

Woolridge, L. J., Worden, R. H., Griffiths, J., & Utley, J. E. P. (2017). Clay-coated sand grains in petroleum reservoirs: Understanding their distribution via a modern analogue. *Journal of Sedimentary Research, 87*, 338-352. doi:10.2110/jsr.2017.20

Worden, R. H., Armitage, P. J., Butcher, A., Churchill, J., Csoma, A., Hollis, C., Lander, R., & Omma, J. (2018). Petroleum reservoir quality prediction : overview and contrasting approaches from sandstone and carbonate communities. *Geological Society, London, Special Publications, 435*, 1-31. doi:10.1144/SP435.21

Worden, R. H., & Burkley, S. D. (2003). Sandstone diagenesis: the evolution of sand to stone. In S. D. Burley & R. H. Worden (Eds.), Sandstone Diagenesis: Recent and Ancient (pp. 2-44): Wiley Blackwell.

Worden, R. H., & Morad, S. (2000). Quartz cementation in oil field sandstones: a review of the key controversies. *Int. Assoc. Sedimentol. Spec. Publ., 29*, 1-20. doi:10.1002/9781444304237.ch1

Worden, R. H., & Morad, S. (2003). Clay minerals in sandstones: Controls on formation, distribution and evolution. *Int. Assoc. Sedimentol. Spec. Publ., 34*, 3-41. doi:10.1002/9781444304336.ch1

Wüstefeld, P., Hilse, U., Koehrer, B., Adelmann, D., & Hilgers, C. (2017a). Critical evaluation of an Upper Carboniferous tight gas sandstone reservoir analog: Diagenesis and petrophysical aspects. *Marine and Petroleum Geology, 86*, 689-710. doi:10.1016/j.marpetgeo.2017.05.034

Wüstefeld, P., Hilse, U., Lüders, V., Wemmer, K., Koehrer, B., & Hilgers, C. (2017b). Kilometer-scale fault-related thermal anomalies in tight gas sandstones. *Marine and Petroleum Geology, 86*, 288-303. doi:10.1016/j.marpetgeo.2017.05.015

Yale, D. P. (1984). *Network modelling of flow, storage and deformation in porous rocks.* (PhD thesis). Stanford University, Stanford.

Yuan, G., Cao, Y., Gluyas, J., Li, X., Xi, K., Wang, Y., Jia, Z., Sun, P., & Oxtoby, N. H. (2015). Feldspar dissolution, authigenic clays, and quartz cements in open and closed sandstone geochemical systems during diagenesis: Typical examples from two sags in Bohai Bay Basin, East China. *AAPG Bulletin, 99*, 2121-2154. doi:10.1306/07101514004

Zhao, H., Ning, Z., Kang, Q., Chen, L., & Zhao, T. (2017). Relative permeability of two immiscible fluids flowing through porous media determined by lattice Boltzmann method. *International Communications in Heat and Mass Transfer, 85*, 53-61. doi:10.1016/j.icheatmasstransfer.2017.04.020

Zhao, J., Kang, Q., Yao, J., Viswanathan, H., Pawar, R., Zhang, L., & Sun, H. (2018). The effect of wettability heterogeneity on relative permeability of two-phase flow in porous media: A lattice Boltzmann study. *Water Resources Research, 54*, 1295-1311. doi:10.1002/2017WR021443

Ziegler, K. (2006). Clay minerals of the Permian Rotliegend Group in the North Sea and adjacent areas. *Clay Minerals, 41*, 355-393. doi:10.1180/0009855064110200

Ziegler, P. A. (1990). *Geological atlas of western and central Europe*. The Hague: Shell Internationale Petroleum Maatschappij B.V.

Zoback, M. D., & Zinke, J. C. (2002). Production-induced normal faulting in the Valhall and Ekofisk oil fields. In C. I. Trifu (Ed.), The Mechanism of Induced Seismicity (pp. 403-420). Basel, Switzerland: Birkhäuser.

Zorlu, K., Gokceoglu, C., Ocakoglu, F., Nefeslioglu, H. A., & Acikalin, S. (2008). Prediction of uniaxial compressive strength of sandstones using petrography-based models. *Engineering Geology, 96*, 141-158. doi:10.1016/j.enggeo.2007.10.009

Zou, Q., & He, X. (1997). On pressure and velocity boundary conditions for the lattice Boltzmann BGK model. *Physics of Fluids, 9*, 1591-1598. doi:10.1063/1.869307

Zwingmann, H., Clauer, N., & Gaupp, R. (1998). Timing of fluid flow in a sandstone reservoir of the north German Rotliegend (Permian) by K-Ar dating of related hydrothermal illite. *Geological Society, London, Special Publications, 144*, 91-106. doi:10.1144/GSL.SP.1998.144.01.07

Zwingmann, H., Clauer, N., & Gaupp, R. (1999). Structure-related geochemical (REE) and isotopic (K-Ar, Rb-Sr, d18O) characteristics of clay minerals from Rotliegend sandstone reservoirs (Permian, northern Germany). *Geochimica et Cosmochimica Acta, 63*, 2805-2823. doi:10.1016/S0016-7037(99)00198-2

Appendix

Alphabetical list of methods

Cathodoluminescence was studied with an optical cathodoluminescence system by Cambridge Image Technology Ltd mounted on a Leitz Dialux microscope. The microscope is equipped with a Jenoptik Gryphax camera, which captures long exposure images to increase the color gain (t=2 s, at gain =1). The system was operated with a voltage of 15±1 kV for carbonate cements and accessories and 20±1 kV for quartz. Applied currents ranged from 325-350 μA.

Clay mineral grain coatings were determined on at least 50 grains per sample using digital image analysis. It was distinguished between clay mineral coatings on grain-to-IGV (GTI) interfaces (Busch et al., 2017) and clay mineral coatings on grain-to-grain (GTG) interfaces (Monsees et al., 2020a).

The **effective contact length** is used to quantify the length of physical quartz-quartz, quartz-feldspar, and feldspar-feldspar particle contacts (grain plus syntaxial cement) orientated subparallel (max. ±20°) to the bedding axis at n=50 randomly selected grain contacts using digital image analysis.

Decane porosity was measured on cylindrical samples (3.00 cm diameter) using the Archimedes or flotation/liquid resaturation method with decane as flotation medium. The rock samples were dried at 120° C, weighed, and put in a desiccator. The desiccator was evacuated and afterwards the samples were saturated with decane. Samples were then put in a pressure chamber filled with decane at 9 MPa for one day. Decane saturated samples were weighed in decane and outside decane under normal air pressure. The relative decane porosity was calculated from the determined differences in weight (Kuila et al., 2014).

Grain size was measured along the long-axis of 100 grains per thin-section with digital image analysis (Becker et al., 2017). Median grain sizes determined by digital image analysis have been demonstrated to reach accuracies >96% compared to conventional methods like sieving (Barnard et al., 2007).

Helium pycnometry was conducted on cylindrical samples (2.54 cm diameter) dried in a vacuum oven at 40° C and 0.1 bar for at least 72 hours prior to the measurement. The absolute helium porosity (φ) was measured with an AccuPyc II 1340 pycnometer (Becker et al., 2017). The porosity values given here are the average of ten measurement cycles per sample.

The **intergranular volume (IGV)** was classified after Paxton et al. (2002) and includes intergranular porosity, authigenic cements and detrital clay mineral matrix.

Micro-computed tomography (µCT) scans were performed by MITOS GmbH with an image resolution of 2048*2048 px. This results in a horizontal µCT resolution of 3.3 µm/px for samples with a diameter of 6.2 mm. Petrography and porosity measurements serve as calibration for the segmentation of pore-space in the µCT image batch. Images from µCT were stacked and segmented with ImageJ, using helium porosity from rock plugs as a control factor on the segmented porosity. The grayscale intensity is related to differences in parameter-specific x-ray **attenuation** of the respective mineral (Curry et al., 1990). The software Slicer was used to render a high-resolution 3D petrographic model. **Fluid flow velocities** through the µCT models were computed using the **Lattice Boltzmann method** (Andrä et al., 2013b), and converted to permeability using Darcy's Law.

Permeability was measured at a constant confining pressures of 1.2 MPa with an air permeameter manufactured by Westphal Mechanik using dry, oil-free lab air (80% N_2, 20% O_2) as permeant, automatically checking for turbulent flow-conditions (Forchheimer regime) and automatically correcting for slip flow using the **Klinkenberg correction** (Klinkenberg, 1941). **Reynolds numbers** were determined using the methods proposed by McCune and Wilhelm (1949) and Millionshchikov (1941) on samples with permeability higher than 1000 mD. Reynolds numbers <<1.0 suggest that a laminar flow regime is present and no Forchheimer correction is required. Permeability was also measured under decreasing confining pressures (50, 30, 10, 5, 2 MPa) at room temperature (22±1° C) on n=46 samples using helium as a permeant ($\eta = 1.97 * 10^{-5} Pa * s$ at 22° C). All samples were loaded up to 50 MPa confining pressure and permeabilities are measured during the unloading cycle in a DBHS-50-150 pressure cell from GL Test Systems GmbH. The cell is fitted with a hydraulic pump to adjust confining pressures. Apparent permeabilities are measured at varying p_{mean} and corrected for slip flow (Amann-Hildenbrand et al., 2015), using the Klinkenberg correction (Klinkenberg, 1941). The **pressure sensitivity coefficient of permeability (γ)** was determined graphically after David et al. (1994) using Eqn. A.1 with the reference permeability (K_0) at reference confining pressure (p_0) and the measured permeability (K) at the effective pressure P_{eff}.

$$K = K_0 * e^{-\gamma * (P_{eff} - P_0)} \tag{A.1}$$

Point-counting was conducted with 300 counts per thin-section on a grid adjusted to the maximum grain size (determined by image analysis) with a semi-automated Pelcon Point

Counter installed on a Leitz Aristomet microscope. Point-counting was conducted in accordance with Touchstone point-counting categories.

Sandstone composition was classified as a ternary plot after Folk (1980). The quartz-pole includes all quartz and metaquartzite, but not chert. The feldspar-pole includes all feldspar grains, plus granite and gneiss fragments (plutonic and coarse grained, deep-crustal rocks). The rock fragment pole includes all other fine-grained rock fragments (supracrustal), incl. chert, slate, schist, volcanics, sandstone, shale, etc.

Sandstone porosity loss was divided into compactional porosity loss (COPL, Eqn. A.2) and cementational porosity loss (CEPL, Eqn. A.3), and corresponding compactional indices (ICOMPACT, Eqn. A.4) were calculated after Lundegard (1992). The required input parameters are the initial porosity (P_i) assumed to be 45 % (Lundegard, 1992), and the minus-cement porosity (P_{mc}), which is defined as the sum of the optical porosity and the cement volume (C) determined by point-counting.

$$COPL = \frac{(100-P_i)*P_{mc}}{100-P_{mc}} \tag{A.2}$$

$$CEPL = \frac{P_i-COPL}{C/P_{mc}} \tag{A.3}$$

$$ICOMPACT = \frac{COPL}{(COPL+CEPL)} \tag{A.4}$$

Uniaxial compression tests were conducted according to DIN18136 (2003) and Mutschler (2004) to determine the uniaxial compressive strength as well as Young's modulus and strain at failure.

Supplementary material I

Table A.1. Table on pages 152-158. Supplementary point-counting, petrographic and petrophysical data table for chapter 2. Abbreviations in order of appearance. RL- HS: Rotliegend - Havel Subgroup, DN: Dune, DSF: Dry sandflat, RF: rock fragment, PRF: Plutonic rock fragment, VRF: Volcanic rock fragment, rp: replaces, GTG: grain-to-grain, GTI: grain-to-IGV, IGV: intergranular volume, ws: well sorted, vws: very well sorted, mws: moderately well sorted, ms: moderately sorted, ews: extremely well sorted, COPL: Compactional porosity loss, CEPL: Cementational porosity loss.

Sample ID	A_01	A_02	A_03	A_04	A_05	A_06	A_07	A_08
Stratigraphy	RL- HS	R - HS	RL- HS	RL- HS	RL- HS	RL- HS	RL- HS	RL- HS
Depositional Environment	DN	DN	DN	DN	DN	DN	DN	DN
Detrital components (%)								
Quartz	59.7	61.7	53.3	58.7	55.3	58.7	57.0	59.7
K-feldspars	4.7	6.0	7.7	8.0	3.7	5.7	8.0	7.3
Plagioclases	0.0	0.0	0.0	0.3	0.3	0.3	0.3	0.0
Chert	0.3	0.0	0.3	0.0	0.3	0.0	0.7	0.0
Shale RF	0.0	0.3	0.0	0.3	0.3	0.0	0.3	0.0
Sandstone RF	0.0	0.3	0.7	0.0	1.0	0.3	0.7	0.3
Siltstone RF	1.3	0.3	0.3	0.7	0.7	0.0	0.3	0.3
Silicic VRF	4.3	3.3	4.7	4.3	3.7	4.7	4.0	3.3
Feldspathic VRF	0.0	2.3	1.0	1.3	2.3	2.3	0.7	1.7
Basaltic VRF	0.0	0.0	0.7	0.7	0.3	0.3	0.0	0.3
Volcanic glass	0.3	0.0	0.3	0.0	0.0	0.0	0.0	0.3
Felsic PRF	2.3	2.3	4.7	2.7	8.3	5.0	3.7	2.3
Granitic PRF	0.7	0.7	0.0	0.3	0.7	0.3	0.3	0.7
Quartzite	3.3	1.7	0.7	1.7	1.7	1.7	1.3	2.0
Schist	0.0	0.0	0.0	0.0	0.0	0.3	0.0	0.0
Phyllite	0.0	1.0	0.0	0.3	0.3	0.7	0.3	0.7
Undifferentiated Metamorphic RF	1.7	1.3	0.3	1.0	0.0	0.3	1.0	0.3
Muscovite	0.0	0.0	0.0	0.0	0.0	0.7	0.0	0.0
Zircon	0.0	0.0	0.3	0.0	0.0	0.0	0.3	0.0
Rutile	0.0	0.3	0.0	0.7	0.0	0.3	0.0	0.0
Hornblende	0.0	0.0	0.0	0.0	0.0	0.0	0.0	0.0
Clay Matrix	0.0	1.0	0.0	0.7	0.7	0.0	0.3	0.0
Authigenic components (%)								
Quartz	5.3	3.0	7.3	3.0	2.3	1.3	3.3	3.0
Calcite	2.0	7.0	0.3	2.0	4.0	0.0	0.0	0.0
Anhydrite	0.0	0.0	0.3	0.3	3.0	0.3	1.3	0.0
Gypsum	0.0	0.0	0.0	0.0	0.3	0.0	0.0	0.0
Illite (pore-filling)	0.0	0.0	0.0	0.0	0.0	0.3	0.7	0.3
Illite (pore-lining)	2.7	2.0	3.0	2.7	2.7	4.3	3.7	3.0
Chlorite (pore-filling)	0.7	3.7	1.7	3.3	1.0	4.0	2.7	3.3
Kaolinite	0.0	0.0	0.0	0.0	0.0	0.0	0.0	0.0
Barite	0.7	0.0	5.0	0.0	0.3	0.0	0.0	0.0
Halite	0.0	0.0	0.0	0.3	0.0	0.0	0.3	0.0
Feldspar	0.0	0.0	0.0	0.0	0.0	0.3	0.0	0.0
Iron Oxides (pore-lining)	0.3	0.3	0.0	0.0	0.0	0.0	0.0	0.0
Chlorite rp VRF	0.0	0.0	0.3	0.0	0.3	0.0	0.0	0.0
Illite rp K-feldspar	0.7	0.0	0.3	0.7	0.7	1.3	0.3	0.7
Kaolinite rp K-feldspar	0.0	0.0	0.0	0.0	0.0	0.0	0.0	0.0
Calcite rp K-feldspar	0.0	0.0	0.0	0.0	0.3	0.0	0.3	0.0
Optical porosity (%)								
Intergranular porosity	8.0	1.0	6.0	5.3	4.3	5.7	7.3	9.3
Secondary porosity - Feldspars	0.7	0.0	0.0	0.7	0.3	0.0	0.3	0.3
Secondary porosity - Rock Fragments	0.3	0.3	0.7	0.0	0.7	0.7	0.3	0.7
Additional sample information								
Intergranular volume (%)	19.7	17.0	23.7	16.7	18.0	16.3	19.0	19.0
Plug porosity (%)	-	3.6	-	7.7	6.8	-	-	-
Plug permeability (mD)	-	2.257	-	105.518	16.344	-	-	-
Pressure sensitivity of permeability [10^-2MPa^-1]	-	4.100	-	5.000	1.100	-	-	-
GTG coating coverage (%)	20.1	19.8	6.3	11.5	18.2	12.6	18.6	18.4
GTI coating coverage (%)	81.1	70.9	76.8	74.7	80.6	76.3	81.1	81.1
Total pore-filling cement (%)	7.7	13.7	9.3	8.0	10.3	6.0	8.3	6.3
Mean grain size (mm)	0.336	0.419	0.371	0.204	0.445	0.359	0.342	0.319
Sorting	ws	vws	mws	mws	ws	ws	vws	ws
COPL (%)	31.5	33.7	27.9	34.0	32.9	34.3	32.1	32.1
CEPL (%)	8.0	10.6	12.7	7.5	9.2	7.0	7.9	6.6

Sample ID	A_09	A_10	A_11	A_12	A_13	A_14	A_15	A_16
Stratigraphy	RL - HS	RL - HS	RL - HS	RL - HS	RL - HS	RL - HS	RL - HS	RL - HS
Depositional Environment	DN	DN	DN	DN	DN	DN	DN	DN
Detrital components (%)								
Quartz	59.0	53.7	57.7	50.7	61.3	63.7	61.7	72.0
K-feldspar	7.3	7.3	7.0	8.7	6.7	6.0	9.7	7.7
Plagioclases	0.0	0.0	0.0	0.0	0.0	0.0	0.0	0.0
Chert	0.0	0.3	0.7	0.7	0.0	0.0	0.0	0.0
Shale RF	0.0	0.0	0.0	0.0	0.0	0.0	0.3	0.0
Sandstone RF	0.7	0.3	1.0	0.3	1.0	1.0	0.0	0.0
Siltstone RF	0.3	0.0	0.3	0.3	0.0	0.0	0.0	0.0
Silicic VRF	7.3	8.3	5.3	8.0	5.3	4.3	3.3	2.7
Feldspathic VRF	1.0	3.7	0.7	2.7	1.0	1.7	0.7	1.0
Basaltic VRF	0.3	0.0	0.0	0.3	0.0	0.0	0.0	0.0
Volcanic glass	0.3	0.0	0.3	0.7	0.0	0.0	0.0	0.0
Felsic PRF	7.0	9.3	5.7	6.0	4.7	2.3	2.3	1.3
Granitic PRF	0.7	1.0	0.3	0.7	0.3	0.7	0.3	0.0
Quartzite	1.0	2.0	1.7	2.0	1.3	0.3	1.7	1.3
Schist	0.0	0.0	0.3	0.0	0.0	0.0	0.0	0.0
Phyllite	0.7	0.0	0.3	0.0	0.3	0.3	0.7	0.3
Undifferentiated Metamorphic RF	0.0	0.0	0.7	0.0	0.3	0.0	0.3	0.7
Muscovite	0.0	0.0	0.0	0.0	0.0	0.0	0.0	0.0
Zircon	0.0	0.0	0.0	0.0	0.0	0.0	0.0	0.0
Rutile	0.3	0.0	0.0	0.0	0.3	0.0	0.0	0.3
Hornblende	0.0	0.0	0.0	0.0	0.0	0.0	0.0	0.0
Clay Matrix	0.0	0.0	0.0	0.0	0.0	0.0	0.0	0.0
Authigenic components (%)								
Quartz	3.7	3.0	3.7	5.7	4.0	2.3	6.3	8.3
Calcite	1.0	0.3	3.3	1.0	1.7	1.7	2.3	0.0
Anhydrite	0.3	0.0	0.3	0.0	0.3	0.3	1.3	0.0
Gypsum	0.0	0.0	0.0	0.0	0.0	0.0	0.3	0.0
Illite (pore-filling)	1.0	0.7	0.0	0.7	0.3	0.0	0.0	0.0
Illite (pore-lining)	2.7	5.0	4.3	6.3	2.7	7.3	3.0	2.0
Chlorite (pore-filling)	0.3	1.0	2.3	0.7	2.3	4.0	2.3	1.7
Kaolinite	0.0	0.0	0.0	0.3	0.0	0.3	0.3	0.0
Barite	0.0	0.0	0.0	0.0	0.0	0.0	0.0	0.0
Halite	0.0	0.0	0.0	0.0	0.0	0.0	0.3	0.3
Feldspar	0.0	0.7	0.0	0.0	0.0	0.0	0.0	0.0
Iron Oxides (pore-lining)	0.0	0.0	0.0	0.0	0.0	0.0	0.0	0.0
Chlorite rp VRF	0.0	0.0	0.0	0.0	0.0	0.0	0.0	0.0
Illite rp K-feldspar	0.0	0.3	0.3	0.3	0.7	0.7	0.7	0.0
Kaolinite rp K-feldspar	0.0	0.0	0.0	0.0	0.0	0.0	0.3	0.0
Calcite rp K-feldspar	0.0	0.0	0.0	0.0	0.0	0.0	0.0	0.0
Optical porosity (%)								
Intergranular porosity	4.7	2.0	3.0	3.0	5.0	3.0	0.7	0.0
Secondary porosity - Feldspars	0.0	0.0	0.3	0.3	0.0	0.0	0.0	0.0
Secondary porosity - Rock Fragments	0.3	1.0	0.3	0.7	0.3	0.3	1.0	0.3
Additional sample information								
Intergranular volume (%)	13.7	12.7	17.0	17.7	16.3	18.7	16.7	12.0
Plug porosity (%)	9.3	6	7.1	6.9	8	6	-	2.6
Plug permeability (mD)	32.927	1.747	3.024	1.753	8.242	1.686	-	0.359
Pressure sensitivity of permeability [10^-2 MPa^-1]	1.300	6.700	3.900	5.700	3.200	3.700	-	7.100
GTG coating coverage (%)	19.8	40.8	20.8	10.1	15.2	20.0	24.1	31.3
GTI coating coverage (%)	74.6	85.2	71.9	76.0	62.2	58.5	41.5	51.4
Total pore-filling cement (%)	6.3	5.7	9.3	7.7	7.3	6.7	10.3	9.3
Mean grain size (mm)	0.410	0.420	0.371	0.438	0.364	0.284	0.230	0.331
Sorting	vws	vws	ws	ws	ws	mws	vws	vws
COPL (%)	36.3	37.0	33.7	33.2	34.3	32.4	34.0	37.5
CEPL (%)	5.7	6.7	9.3	9.8	7.5	10.6	10.6	7.5

Sample ID	A_17	A_18	A_19	A_20	B_01	B_02	B_03	B_04
Stratigraphy	RL- HS	RL- HS	RL- HS	RL- HS	RL- HS	RL- HS	RL- HS	RL- HS
Depositional Environment	DN	DN	DN	DN	DSF	DSF	DSF	DSF
Detrital components (%)								
Quartz	49.3	61.3	58.7	56.0	64.0	61.7	62.7	56.3
K-feldspar	4.7	9.0	8.3	7.3	5.7	9.7	10.0	10.3
Plagioclases	0.0	0.0	0.0	0.0	0.0	0.0	0.0	0.0
Chert	0.7	0.0	0.0	0.0	0.3	1.3	0.3	0.3
Shale RF	0.0	0.0	0.0	0.0	0.7	0.3	0.0	0.3
Sandstone RF	1.0	0.7	1.3	0.0	1.3	1.3	0.7	0.0
Siltstone RF	0.0	0.3	0.0	0.0	0.3	0.0	0.0	0.7
Silicic VRF	11.0	2.3	4.7	4.7	3.3	1.3	1.0	4.3
Feldspathic VRF	1.3	0.0	1.7	1.0	0.3	0.3	0.3	0.0
Basaltic VRF	0.3	0.0	0.0	0.3	0.0	0.0	0.3	0.0
Volcanic glass	0.7	0.0	0.0	0.0	0.0	0.0	0.0	0.3
Felsic PRF	12.0	1.3	3.7	3.7	2.3	3.7	3.0	0.3
Granitic PRF	0.7	0.0	0.3	0.3	0.3	0.7	0.7	0.0
Quartzite	2.7	1.3	1.0	0.7	1.0	1.0	1.0	1.0
Schist	0.3	0.0	0.3	0.3	0.3	0.0	0.3	0.7
Phyllite	0.3	0.0	0.0	0.0	2.0	0.0	1.0	1.7
Undifferentiated Metamorphic RF	0.0	0.7	0.0	0.0	0.0	0.3	0.0	0.0
Muscovite	0.0	0.0	0.3	0.0	0.0	0.0	0.0	0.0
Zircon	0.0	0.0	0.0	0.0	0.0	0.0	0.0	0.0
Rutile	0.0	0.0	0.3	0.3	0.0	0.0	0.0	0.0
Hornblende	0.0	0.0	0.0	0.0	0.0	0.0	0.0	0.0
Clay Matrix	0.7	0.0	1.0	3.7	2.3	0.0	0.0	2.0
Authigenic components (%)								
Quartz	1.0	8.7	4.3	7.0	1.0	4.3	5.3	7.3
Calcite	4.3	0.7	4.0	2.3	8.3	4.7	6.0	2.7
Anhydrite	1.7	0.0	0.0	0.3	0.0	0.0	0.0	0.0
Gypsum	0.0	0.0	0.0	0.0	0.3	0.0	0.3	0.0
Illite (pore-filling)	0.0	0.0	0.0	0.0	0.0	0.0	0.0	0.0
Illite (pore-lining)	4.7	4.7	4.3	5.0	3.0	1.3	2.0	3.7
Chlorite (pore-filling)	1.3	3.3	3.0	4.7	0.3	2.0	0.3	7.0
Kaolinite	0.0	0.0	0.0	0.0	0.0	0.0	0.0	0.0
Barite	0.0	0.0	0.0	0.0	0.0	0.0	0.0	0.0
Halite	0.0	0.0	0.0	0.0	1.0	0.0	0.0	0.0
Feldspar	0.0	0.0	0.0	0.0	0.0	0.0	0.0	0.0
Iron Oxides (pore-lining)	0.0	0.0	0.0	0.0	0.0	0.0	0.0	0.0
Chlorite rp VRF	0.3	0.0	0.0	0.0	0.0	0.3	0.3	0.3
Illite rp K-feldspar	0.3	0.7	0.0	0.3	0.7	0.0	0.3	0.7
Kaolinite rp K-feldspar	0.0	0.0	0.0	0.0	0.0	0.0	0.0	0.0
Calcite rp K-feldspar	0.3	0.0	0.0	0.3	0.0	0.3	0.0	0.0
Optical porosity (%)								
Intergranular porosity	0.0	4.7	2.7	1.7	1.0	4.7	3.7	0.0
Secondary porosity - Feldspars	0.0	0.3	0.0	0.0	0.0	0.3	0.0	0.0
Secondary porosity - Rock Fragments	0.3	0.0	0.0	0.0	0.0	0.3	0.3	0.0
Additional sample information								
Intergranular Volume (%)	13.0	22.0	18.3	21.0	17.0	17.0	17.7	22.7
Plug porosity (%)	3.3	6.1	5.1	3.4	2.0	6.3	6.2	2.1
Plug permeability (mD)	0.172	0.963	0.315	0.193	1.461	3.128	2.234	0.069
Pressure sensitivity of permeability [10^-2 MPa^-1]	6.600	4.100	4.900	6.200	2.700	2.900	3.600	10.900
GTG coating coverage (%)	26.2	25.0	32.8	18.9	30.1	25.7	18.1	30.2
GTI coating coverage (%)	56.2	53.1	67.0	57.4	73.1	57.0	53.5	62.4
Total pore-filling cement (%)	8.3	11.0	10.0	12.7	10.7	11.0	12.0	15.7
Mean grain size (mm)	0.297	0.227	0.274	0.225	0.316	0.298	0.285	0.206
Sorting	ms	vws	mws	ws	mws	ws	ws	ws
COPL (%)	36.8	29.5	32.7	30.4	33.7	33.7	33.2	28.9
CEPL (%)	8.2	12.2	10.6	13.5	10.6	8.2	9.4	16.1

Sample ID	B_05	B_06	B_07	B_08	B_09	B_10	B_11	B_12
Stratigraphy	RL- HS	RL- HS	R - HS	RL- HS	RL- HS	RL- HS	RL- HS	RL- HS
Depositional Environment	DSF	DSF	DSF	DSF	DSF	DSF	DSF	DSF
Detrital components (%)								
Quartz	53.7	62.3	61.0	63.7	61.0	67.0	58.0	64.0
K-feldspar	7.3	8.3	9.3	12.3	12.7	9.0	8.0	8.3
Plagioclases	0.0	0.0	0.0	0.0	0.0	0.0	0.0	0.0
Chert	0.7	0.3	0.0	0.3	0.0	0.7	0.0	0.3
Shale RF	0.0	0.3	0.3	0.7	0.0	0.0	0.3	1.0
Sandstone RF	1.0	0.3	0.3	0.3	1.3	0.3	0.7	0.3
Siltstone RF	0.3	0.0	0.0	0.0	0.0	0.3	0.0	0.0
Silicic VRF	5.0	3.3	3.3	2.0	2.0	3.0	2.7	4.0
Feldspathic VRF	3.3	0.3	0.3	2.3	1.0	0.0	1.3	1.0
Basaltic VRF	0.0	0.0	0.0	0.0	0.0	0.0	0.0	0.0
Volcanic glass	0.3	0.0	0.0	0.0	0.0	0.0	0.0	0.0
Felsic PRF	8.0	3.3	2.0	1.0	1.7	1.3	3.0	0.7
Granitic PRF	0.3	0.7	0.0	0.0	0.3	0.3	1.3	0.3
Quartzite	0.7	1.3	0.7	1.0	1.3	1.3	1.0	0.3
Schist	0.0	0.0	0.0	0.3	0.0	0.3	0.0	0.0
Phyllite	1.0	0.7	0.0	0.3	0.7	1.0	0.7	0.3
Undifferentiated Metamorphic RF	0.0	0.0	0.3	0.0	0.0	0.0	0.0	0.0
Muscovite	0.0	0.0	0.0	0.3	0.0	0.0	0.0	0.0
Zircon	0.0	0.0	0.0	0.0	0.0	0.0	0.0	0.0
Rutile	0.3	0.3	0.0	0.0	0.0	0.0	0.0	0.0
Hornblende	0.0	0.0	0.0	0.0	0.0	0.0	0.0	0.0
Clay Matrix	1.3	0.0	1.7	0.3	1.0	0.0	0.0	0.7
Authigenic components (%)								
Quartz	3.3	2.7	4.7	3.3	5.0	3.3	4.0	1.0
Calcite	0.3	0.3	0.3	1.0	1.3	1.7	5.7	0.3
Anhydrite	0.7	0.0	0.0	0.0	0.0	0.0	0.0	0.0
Gypsum	0.0	0.0	0.0	0.0	0.0	0.0	0.0	0.0
Illite (pore-filling)	0.3	0.3	0.0	0.0	0.3	0.7	1.0	0.0
Illite (pore-lining)	3.0	2.7	1.7	2.3	2.3	3.0	4.7	4.7
Chlorite (pore-filling)	3.7	0.7	2.3	1.0	1.0	1.0	1.7	3.0
Kaolinite	0.0	0.0	0.0	0.0	0.0	0.0	0.0	0.0
Barite	0.0	0.0	0.0	0.0	0.0	0.0	0.0	0.0
Halite	0.0	0.0	0.0	0.0	0.0	0.0	0.0	0.0
Feldspar	0.0	0.0	0.0	0.0	0.0	0.0	0.0	0.0
Iron Oxides (pore-lining)	0.0	0.0	0.0	0.0	0.0	0.0	0.0	0.0
Chlorite rp VRF	0.3	0.3	0.0	0.0	0.0	0.0	0.0	0.0
Illite rp K-feldspar	0.3	0.3	0.3	0.0	0.0	0.3	0.0	0.0
Kaolinite rp K-feldspar	0.0	0.0	0.0	0.0	0.0	0.0	0.0	0.0
Calcite rp K-feldspar	0.0	0.0	0.0	0.0	0.0	0.3	0.0	0.0
Optical porosity (%)								
Intergranular porosity	4.7	10.7	11.0	7.0	6.7	4.3	5.7	8.3
Secondary porosity - Feldspars	0.0	0.0	0.0	0.3	0.3	0.3	0.0	0.7
Secondary porosity - Rock Fragments	0.0	0.3	0.3	0.0	0.0	0.3	0.3	0.7
Additional sample information								
Intergranular volume (%)	17.0	17.3	21.7	15.0	17.7	14.3	22.7	18.0
Plug porosity (%)	12.2	7.2	13.0	14.5	11.3	11.1	10.6	11.8
Plug permeability (mD)	262.884	13.602	247.521	780.817	202.426	123.196	125.679	174.231
Pressure sensitivity of permeability [10^-2 MPa^-1]	-	1.200	-	-	1.400	1.000	0.700	0.800
GTG coating coverage (%)	39.0	25.0	22.0	37.4	31.6	35.9	15.0	22.1
GTI coating coverage (%)	76.1	70.9	73.6	79.3	70.1	70.9	72.4	71.5
Total pore-filling cement (%)	6.7	4.0	6.7	4.7	7.3	6.3	11.3	3.7
Mean grain size (mm)	0.389	0.354	0.299	0.317	0.283	0.283	0.323	0.295
Sorting	ws	ws	vws	vws	ws	vws	ws	ws
COPL (%)	33.7	33.5	29.8	35.3	33.2	35.8	28.9	32.9
CEPL (%)	8.2	4.4	7.5	5.2	7.3	6.4	12.1	6.5

Sample ID	B_13	B_14	B_15	B_16	B_17	B_18	B_19	B_20
Stratigraphy	RL- HS	RL- HS	RL- HS	RL- HS	RL- HS	RL- HS	RL- HS	RL- HS
Depositional Environment	DSF	DSF	DSF	DSF	DSF	DSF	DSF	DSF
Detrital components (%)								
Quartz	57.7	63.7	56.3	51.7	61.0	58.0	55.0	43.7
K-feldspar	9.0	10.0	8.0	5.7	9.0	11.7	11.0	7.7
Plagioclases	0.0	0.0	0.0	0.7	0.0	0.0	0.0	0.0
Chert	0.7	0.7	0.0	0.7	0.0	0.0	0.0	0.0
Shale RF	0.0	0.0	0.0	0.0	0.0	0.0	0.0	0.0
Sandstone RF	0.0	0.7	0.0	0.0	1.0	0.3	0.3	0.0
Siltstone RF	0.7	0.0	0.3	0.0	0.0	0.0	0.0	0.0
Silicic VRF	1.3	2.7	2.3	2.7	2.3	2.3	2.3	10.0
Feldspathic VRF	0.7	1.0	1.0	0.3	1.0	1.0	0.7	2.3
Basaltic VRF	0.0	0.7	0.0	0.0	0.0	0.0	0.0	0.3
Volcanic glass	0.0	0.0	0.3	0.0	0.3	0.0	0.0	1.3
Felsic PRF	1.0	3.0	10.3	10.0	1.0	0.7	4.0	10.3
Granitic PRF	0.3	0.0	0.0	0.7	0.7	0.0	0.0	0.7
Quartzite	1.3	0.3	1.7	0.3	-	1.3	0.7	0.3
Schist	0.0	0.0	0.0	0.3	0.0	0.0	0.0	0.3
Phyllite	0.7	0.3	0.7	1.7	0.0	1.0	0.0	0.3
Undifferentiated Metamorphic RF	0.0	0.0	0.0	0.0	0.0	0.0	0.0	0.0
Muscovite	0.0	0.3	0.0	0.0	0.0	0.0	0.0	0.0
Zircon	0.0	0.0	0.0	0.0	0.0	0.0	0.0	0.0
Rutile	0.0	0.7	0.0	0.0	0.0	0.0	0.3	0.0
Hornblende	0.0	0.0	0.0	0.0	0.0	0.0	0.0	0.0
Clay Matrix	0.0	0.3	6.3	10.0	0.0	0.0	1.0	0.0
Authigenic components (%)								
Quartz	8.3	2.3	2.3	2.7	12.0	12.3	9.7	2.3
Calcite	5.0	3.7	2.3	0.0	0.0	0.0	4.0	4.3
Anhydrite	0.0	0.0	0.3	0.7	0.0	0.0	0.0	1.7
Gypsum	0.0	0.0	0.0	0.0	0.0	0.0	0.0	0.0
Illite (pore-filling)	0.7	0.3	0.0	0.0	0.3	0.7	0.3	0.0
Illite (pore-lining)	3.3	3.3	3.3	4.0	2.7	2.3	2.7	4.7
Chlorite (pore-filling)	3.0	1.3	3.7	7.0	1.0	1.0	1.3	5.3
Kaolinite	0.0	0.0	0.0	0.0	0.0	0.0	0.3	0.0
Barite	0.0	0.0	0.0	0.0	0.0	0.0	0.0	0.0
Halite	0.0	0.0	0.0	0.0	0.0	0.0	0.0	0.0
Feldspar	0.0	0.0	0.0	0.0	0.0	0.0	0.3	0.0
Iron Oxides (pore-lining)	0.0	0.0	0.0	0.0	0.0	0.0	0.0	0.0
Chlorite rp VRF	0.0	0.3	0.0	0.3	0.0	0.0	0.0	0.0
Illite rp K-feldspar	0.0	0.0	0.7	0.7	0.0	0.0	0.0	1.0
Kaolinite rp K-feldspar	0.0	0.0	0.0	0.0	0.0	0.0	0.0	0.0
Calcite rp K-feldspar	0.0	0.0	0.0	0.0	0.0	0.0	0.3	1.3
Optical porosity (%)								
Intergranular porosity	5.3	4.0	0.0	0.0	7.3	6.3	5.3	1.0
Secondary porosity - Feldspars	0.0	0.0	0.0	0.0	0.0	0.0	0.0	0.3
Secondary porosity - Rock Fragments	1.0	0.3	0.0	0.0	0.3	1.0	0.3	0.7
Additional sample information								
Intergranular volume (%)	25.7	15.3	18.3	24.3	23.3	22.7	25.0	19.3
Plug porosity (%)	8.9	8.7	1.5	0.6	11.9	12.2	7.8	3.5
Plug permeability (mD)	32.435	18.676	0.048	0.009	293.922	157.393	31.264	0.084
Pressure sensitivity of permeability [10^-2 MPa^-1]	1.000	1.000	12.500	22.200	0.800	0.500	0.900	8.400
GTG coating coverage (%)	13.9	24.9	39.6	67.4	16.2	17.8	22.2	15.1
GTI coating coverage (%)	71.0	64.7	81.6	81.6	45.2	43.9	55.5	72.3
Total pore-filling cement (%)	15.7	7.0	8.3	10.0	13.0	14.0	15.0	11.3
Mean grain size (mm)	0.271	0.289	0.426	0.363	0.335	0.307	0.310	0.365
Sorting	ws	ws	ws	mws	vws	vws	ews	mws
COPL (%)	26.0	35.0	32.7	27.3	28.3	28.9	26.7	31.8
CEPL (%)	15.0	7.4	12.3	17.7	11.5	11.6	14.4	12.5

Sample ID	B_21	B_22	B_23	B_24	B_25	B_26	B_27	B_28
Stratigraphy	RL- HS	RL- HS	RL- HS	RL- HS	RL- HS	RL- HS	RL- HS	RL- HS
Depositional Environment	DSF	DSF	DSF	DSF	DSF	DSF	DSF	DSF
Detrital components (%)								
Quartz	67.3	64.0	59.0	69.0	53.7	69.7	68.0	60.3
K-feldspar	7.3	10.3	8.3	7.3	7.0	5.3	12.7	15.7
Plagioclases	0.0	0.0	0.0	0.0	0.0	0.3	0.0	0.0
Chert	0.0	0.0	0.0	0.0	0.0	0.0	0.0	0.0
Shale RF	0.3	0.0	0.3	0.7	0.0	0.0	0.0	0.0
Sandstone RF	0.0	0.0	0.3	0.7	0.3	0.3	0.3	2.0
Siltstone RF	0.0	0.3	0.3	0.0	0.7	0.0	0.0	0.0
Silicic VRF	4.7	2.3	4.3	3.3	4.7	3.3	1.3	1.0
Feldspathic VRF	0.3	0.3	3.3	1.0	2.3	0.7	0.0	0.0
Basaltic VRF	0.0	0.0	0.0	0.0	0.0	0.0	0.0	0.0
Volcanic glass	0.0	0.0	0.0	0.0	0.0	0.3	0.0	0.0
Felsic PRF	1.3	2.3	5.7	1.3	8.7	2.0	0.7	0.3
Granitic PRF	0.7	0.3	0.7	0.7	0.0	0.3	0.0	0.0
Quartzite	0.3	1.0	0.3	-	0.7	1.0	0.7	-
Schist	0.3	0.0	0.0	0.0	0.0	0.0	0.0	0.0
Phyllite	1.0	0.0	0.0	0.3	1.0	0.7	0.0	0.3
Undifferentiated Metamorphic RF	0.0	0.0	0.0	0.0	1.3	1.0	0.3	0.0
Muscovite	0.0	0.0	0.0	0.3	0.0	0.3	0.0	0.0
Zircon	0.0	0.3	0.0	0.0	0.0	0.0	0.0	0.0
Rutile	0.0	0.0	1.0	0.0	0.3	0.0	0.0	0.0
Hornblende	0.3	0.0	0.0	0.0	0.0	0.0	0.0	0.0
Clay Matrix	1.3	1.3	0.3	0.7	0.3	2.3	0.0	0.0
Authigenic components (%)								
Quartz	1.7	5.7	2.0	5.0	3.0	3.3	11.7	15.0
Calcite	1.3	1.0	3.7	2.0	5.0	0.0	0.3	1.0
Anhydrite	3.0	0.3	3.3	0.0	2.7	0.0	0.3	0.3
Gypsum	0.0	0.0	0.0	0.0	0.3	0.0	0.0	0.0
Illite (pore-filling)	0.0	0.0	0.0	0.0	0.0	0.0	0.0	0.3
Illite (pore-lining)	4.7	7.7	4.3	4.0	5.7	7.3	1.7	2.0
Chlorite (pore-filling)	4.0	1.7	1.3	1.7	0.0	1.7	1.0	0.0
Kaolinite	0.0	0.0	0.0	0.0	0.0	0.0	0.0	0.0
Barite	0.0	0.0	0.0	0.0	0.3	0.0	0.0	0.0
Halite	0.0	0.0	0.0	0.0	0.7	0.0	0.3	0.0
Feldspar	0.0	0.0	0.0	0.0	0.0	0.0	0.0	0.0
Iron Oxides (pore-lining)	0.0	0.0	0.0	0.0	0.0	0.0	0.0	0.0
Chlorite rp VRF	0.0	0.3	0.0	0.0	0.0	0.0	0.0	0.0
Illite rp K-feldspar	0.0	0.3	0.7	0.0	0.3	0.0	0.3	0.3
Kaolinite rp K-feldspar	0.0	0.0	0.0	0.0	0.0	0.0	0.0	0.0
Calcite rp K-feldspar	0.0	0.0	0.0	1.7	0.3	0.0	0.3	0.0
Porosity (%)								
Intergranular porosity	0.0	0.0	0.3	0.3	0.0	0.0	0.0	1.3
Secondary porosity - Feldspars	0.0	0.0	0.0	0.0	0.7	0.0	0.0	0.0
Secondary porosity - Rock Fragments	0.0	0.3	0.3	0.0	0.0	0.0	0.0	0.0
Additional sample information								
Intergranular volume (%)	16.0	17.7	15.3	13.7	18.3	14.7	15.3	20.0
Plug porosity (%)	1.8	3.9	4.7	3.4	2.9	1.7	3.0	4.1
Plug permeability (mD)	0.053	0.116	0.115	0.052	0.063	0.021	0.088	0.462
Pressure sensitivity of permeability [10^-2 MPa^-1]	12.200	9.200	9.800	7.700	12.700	9.000	7.200	7.400
GTG coating coverage (%)	26.1	33.9	39.8	44.1	24.7	45.1	33.2	21.9
GTI coating coverage (%)	74.1	59.2	76.7	61.3	76.3	79.1	46.7	40.7
Total pore-filling cement (%)	8.7	7.3	9.7	8.0	12.0	5.0	13.7	16.7
Mean grain size (mm)	0.175	0.200	0.177	0.197	0.257	0.276	0.270	0.317
Sorting	ms	mws	mws	mws	mws	mws	vws	vws
COPL (%)	34.5	33.2	35.0	36.3	32.7	35.5	35.0	31.3
CEPL (%)	10.5	11.8	9.7	8.5	12.3	9.5	10.0	12.8

Sample ID	B_29	B_30	B_31	B_32	B_33	B_34	B_35
Stratigraphy	RL- HS	RL- HS	RL- HS	RL- HS	RL- HS	RL- HS	RL- HS
Depositional Environment	DSF	DN	DN	DN	DN	DN	DN
Detrital components (%)							
Quartz	65.0	59.7	52.0	61.7	53.0	62.0	54.0
K-feldspar	13.0	7.0	3.3	6.0	4.7	8.3	8.0
Plagioclases	0.0	0.0	0.0	0.0	0.0	0.0	0.3
Chert	0.0	0.0	0.0	0.0	0.0	0.0	0.3
Shale RF	0.0	0.0	0.0	0.3	0.3	0.7	0.7
Sandstone RF	0.7	0.0	0.0	0.0	0.0	1.7	0.7
Siltstone RF	0.0	0.0	0.0	0.0	0.3	0.3	0.0
Silicic VRF	1.0	8.7	6.3	5.3	6.3	2.3	10.7
Feldspathic VRF	0.3	3.3	2.3	1.7	1.7	1.3	1.3
Basaltic VRF	0.0	0.0	0.0	0.0	0.0	0.0	0.0
Volcanic glass	0.0	0.0	0.0	0.0	0.0	0.3	0.0
Felsic PRF	0.0	7.3	16.7	4.3	4.3	1.3	4.3
Granitic PRF	0.0	0.0	0.3	0.3	0.7	0.3	0.3
Quartzite	0.0	0.7	0.3	0.3	1.0	0.3	1.3
Schist	0.0	0.0	0.0	0.0	0.0	0.0	0.0
Phyllite	0.3	0.3	1.0	0.7	1.3	1.0	1.7
Undifferentiated Metamorphic RF	0.3	0.3	1.0	1.7	1.7	0.0	0.7
Muscovite	0.0	0.0	0.0	0.0	0.3	0.0	0.0
Zircon	0.0	0.0	0.0	0.0	0.3	0.0	0.0
Rutile	0.0	0.0	0.3	0.0	0.7	0.0	0.3
Hornblende	0.0	0.0	0.3	0.0	0.0	0.0	0.0
Clay Matrix	0.0	1.7	1.3	1.0	5.7	0.3	0.3
Authigenic components (%)							
Quartz	9.3	1.3	3.3	3.0	3.3	11.3	2.3
Calcite	1.0	0.0	1.7	4.7	0.3	0.7	7.3
Anhydrite	0.3	0.3	0.7	0.3	0.0	0.3	1.0
Gypsum	0.0	0.0	0.0	0.0	0.0	0.0	0.0
Illite (pore-filling)	0.3	0.7	0.0	0.0	0.0	0.3	0.3
Illite (pore-lining)	5.3	8.0	7.3	8.0	13.0	5.7	1.7
Chlorite (pore-filling)	0.0	0.3	1.0	0.0	1.0	0.0	1.0
Kaolinite	0.0	0.0	0.0	0.0	0.0	0.0	0.0
Barite	0.0	0.0	0.0	0.0	0.0	0.0	0.0
Halite	0.0	0.0	0.0	0.0	0.0	0.0	0.0
Feldspar	0.0	0.0	0.0	0.0	0.0	0.0	0.0
Iron Oxides (pore-lining)	0.0	0.0	0.0	0.0	0.0	0.0	0.0
Chlorite rp VRF	0.3	0.3	0.3	0.0	0.0	0.0	0.3
Illite rp K-feldspar	0.0	0.0	0.0	0.3	0.0	0.3	0.0
Kaolinite rp K-feldspar	0.0	0.0	0.0	0.0	0.0	0.0	0.0
Calcite rp K-feldspar	0.0	0.0	0.0	0.0	0.0	0.0	0.3
Optical Porosity (%)							
Intergranular porosity	1.7	0.0	0.3	0.3	0.0	1.0	0.7
Secondary porosity - Feldspars	1.0	0.0	0.0	0.0	0.0	0.0	0.0
Secondary porosity - Rock Fragments	0.0	0.0	0.0	0.0	0.0	0.0	0.0
Additional sample information							
Intergranular volume (%)	18.0	12.3	15.7	17.3	23.0	19.7	14.7
Plug porosity (%)	4.5	2.5	3.5	3.6	1.2	2.6	4.0
Plug permeability (mD)	0.439	0.068	0.064	0.086	0.023	0.054	0.353
Pressure sensitivity of permeability [10^-2 MPa^-1]	9.600	10.100	11.600	12.600	15.600	9.400	7.7
GTG coating coverage (%)	29.3	41.1	28.8	28.7	43.7	30.0	29.0
GTI coating coverage (%)	54.9	80.0	73.3	67.3	70.9	48.3	74.8
Total pore-filling cement (%)	11.0	2.7	6.7	8.0	4.7	12.7	11.0
Mean grain size (mm)	0.279	0.312	0.427	0.242	0.262	0.281	0.377
Sorting	vws	mws	ms	mws	ms	vws	vws
COPL (%)	32.9	37.3	34.8	33.5	28.6	31.5	35.5
CEPL (%)	11.0	7.7	10.0	11.3	16.4	12.8	9.0

Supplementary material II

Table A.2. Table on pages 160-166. Supplementary point-counting, petrographic and petrophysical data and statistics tables for chapter 3. Quarry A: Cornberg Sandstone, Quarry B & C: Flechtingen Sandstone, Quarry D to F: Penrith Sandstone. Abbreviations in order of appearance. RL: Rotliegend, AB: Appleby Group, RF: rock fragment, VRF: volcanic rock fragment, PRF: plutonic rock fragment, MRF: metamorphic rock fragment, undiff.: undifferentiated, Ill,: illite, Kln: kaolinite, pf: pore-filling, cmt: cement, pl: pore-lining, Cal: calcite, rp: replaces, Kfs: potassium feldspar, Sec. poro: secondary porosity, IGV: intergranular volume, COPL: Compactional porosity loss, CEPL: Cementational porosity loss, GTG: grain-to-grain, GTI: grain-to-IGV, K_H: horizontal permeability, K_V: vertical permeability.

Sample	*Depositional parameters*	Facies	Depositional Environment	Stratigraphy	Median grain size [mm]	Sorting coefficient	Sorting (Trask, 1930)	Q [%] (Folk, 1980)	F [%] (Folk, 1980)	R [%] (Folk, 1980)	Accessory minerals [%]
A_01		Eolian	Dune	RL – Weißliegend	0.288	1.283	vws	94.8	1.4	3.8	1.3
A_02		Eolian	Dune	RL – Weißliegend	0.304	1.342	vws	92.9	2.0	5.1	1.7
A_03		Eolian	Dune	RL – Weißliegend	0.357	1.684	mws	91.8	3.3	4.9	1.0
A_04		Eolian	Dune	RL – Weißliegend	0.316	1.250	vws	95.8	1.4	2.8	0.7
A_05		Eolian	Dune	RL – Weißliegend	0.336	1.331	vws	94.0	2.8	3.2	0.7
A_06		Eolian	Dune	RL – Weißliegend	0.476	1.308	vws	93.6	2.3	4.1	0.7
A_07		Eolian	Dune	RL – Weißliegend	0.310	1.316	vws	93.8	1.5	4.6	1.0
A_08		Eolian	Dune	RL – Weißliegend	0.252	1.385	vws	92.5	3.0	4.5	1.3
A_09		Eolian	Dune	RL – Weißliegend	0.237	1.474	ws	92.4	1.4	6.2	1.3
A_10		Eolian	Dune	RL – Weißliegend							
A_11		Eolian	Dune	RL – Weißliegend							
B_01		Fluvio-eolian	Dune	RL - Parchim	0.204	1.272	vws	64.2	15.6	20.2	0.7
B_02		Fluvio-eolian	Dune	RL - Parchim	0.183	1.333	vws	73.2	14.6	12.2	0.7
B_03		Fluvio-eolian	Dune	RL - Parchim	0.386	1.658	mws	67.0	15.9	17.2	0.3
B_04		Fluvio-eolian	Dune	RL - Parchim	0.310	1.288	vws	75.1	9.0	15.9	0.3
B_05		Fluvio-eolian	Sheet sand	RL - Parchim	0.169	1.492	ws	73.5	11.7	14.8	2.3
B_06		Fluvio-eolian	Dune	RL - Parchim	0.238	1.343	vws	76.5	12.6	10.9	0.0
B_07		Fluvio-eolian	Dune	RL - Parchim	0.243	1.346	vws	78.3	10.8	10.8	0.0
B_08		Fluvio-eolian	Dune	RL - Parchim	0.226	1.453	ws	71.1	14.7	14.2	0.0
C_01		Fluvio-eolian	Fluvial	RL -Mirow	0.306	1.323	vws	70.8	13.4	14.8	0.0
C_02		Fluvio-eolian	Fluvial	RL -Mirow							
C_03		Fluvio-eolian	Fluvial	RL -Mirow	0.295	1.530	ws	57.7	16.7	25.6	0.0
C_04		Fluvio-eolian	Fluvial	RL -Mirow							
C_05		Fluvio-eolian	Fluvial	RL -Mirow							
C_06		Fluvio-eolian	Fluvial	RL -Mirow							
C_07		Fluvio-eolian	Fluvial	RL -Mirow	0.318	1.250	vws	72.2	16.3	11.5	1.3
C_08		Fluvio-eolian	Fluvial	RL -Mirow							
C_09		Fluvio-eolian	Fluvial	RL -Mirow	0.430	1.395	vws	59.6	17.0	23.4	0.7
C_10		Fluvio-eolian	Fluvial	RL -Mirow	0.303	1.427	ws	66.2	21.2	12.6	0.3
C_11		Fluvio-eolian	Sheet sand	RL -Mirow	0.347	1.535	ws	69.1	14.0	16.9	0.0
C_12		Fluvio-eolian	Sheet sand	RL -Mirow	0.334	1.325	vws	71.9	16.0	12.1	0.3
C_13		Fluvio-eolian	Sheet sand	RL -Mirow							
C_14		Fluvio-eolian	Sheet sand	RL -Mirow							
D_01		Eolian	Dune	AB - Penrith	0.364	1.327	vws	94.4	4.1	1.5	0.0
D_02		Eolian	Dune	AB - Penrith	0.302	1.591	ws	91.6	5.9	2.5	0.3
D_03		Eolian	Dune	AB - Penrith	0.304	1.449	ws	91.6	6.0	2.3	0.0
D_04		Eolian	Dune	AB - Penrith	0.275	1.310	vws	92.3	4.4	3.3	0.3
D_05		Eolian	Dune	AB - Penrith	0.354	1.224	vws	91.2	8.3	0.6	0.0
D_06		Eolian	Dune	AB - Penrith	0.476	1.319	vws	92.8	5.7	1.4	0.3
D_07		Eolian	Dune	AB - Penrith	0.471	1.189	ews	93.6	5.0	1.5	0.0
D_08		Eolian	Dune	AB - Penrith	0.489	1.206	vws	94.1	4.9	1.0	0.3
D_09		Eolian	Dune	AB - Penrith	0.551	1.197	ews	95.0	4.4	0.6	0.0
D_10		Eolian	Dune	AB - Penrith	0.521	1.206	vws	89.8	7.6	2.5	0.0
D_11		Eolian	Dune	AB - Penrith	0.536	1.380	vws	93.5	5.1	1.4	0.0
D_12		Eolian	Dune	AB - Penrith	0.353	1.219	vws	91.0	7.9	1.1	0.3
D_13		Eolian	Dune	AB - Penrith	0.359	1.173	ews	89.5	9.5	1.1	0.0
D_14		Eolian	Dune	AB - Penrith							
E_01		Eolian	Dune	AB - Penrith	0.428	1.198	ews	93.5	5.1	1.4	0.0
E_02		Eolian	Dune	AB - Penrith							
E_03		Eolian	Dune	AB - Penrith							
E_04		Eolian	Dune	AB - Penrith							
E_05		Eolian	Dune	AB - Penrith	0.492	1.179	ews	91.1	5.8	3.2	0.0
F_01		Eolian	Dune	AB - Penrith	0.342	1.650	mws	92.0	5.8	2.2	0.3
F_02		Eolian	Dune	AB - Penrith	0.544	1.725	mws	96.6	2.6	0.9	0.0

Sample	Detrital component [%]	Quartz	K-feldspar	Plagioclase	Chert	Shale RF	Sandstone RF	siltstone RF	Silicic VRF	Feldspathic VRF	Felsic PRF	Granitic PRF	Quartzite	Phyllite	MRF undiff	RF undiff	Mica	Zircon	Hornblende
A_01		65.3	1.0	0.0	0.0	0.7	0.0	0.3	0.0	0.0	0.0	0.0	0.0	0.0	0.7	1.0	0.0	1.3	0.0
A_02		59.3	1.3	0.0	0.0	0.3	0.0	0.7	0.0	0.0	0.0	0.0	0.3	0.3	0.7	1.3	0.3	1.3	0.0
A_03		54.0	1.7	0.0	0.0	0.0	0.0	0.0	0.0	0.0	0.0	0.0	0.3	0.0	1.7	1.3	0.0	1.0	0.0
A_04		67.0	0.3	0.0	0.0	0.3	0.3	0.0	0.0	0.0	0.0	0.0	0.3	0.0	0.7	0.7	0.0	0.7	0.0
A_05		66.3	1.3	0.0	0.0	0.7	0.0	0.3	0.0	0.0	0.0	0.0	1.0	0.0	0.0	1.3	0.0	0.7	0.0
A_06		66.7	1.7	0.0	0.0	0.0	0.0	0.3	0.0	0.0	0.0	0.0	1.0	0.3	0.3	2.0	0.0	0.7	0.0
A_07		60.3	1.0	0.0	0.0	1.0	0.0	0.0	0.0	0.0	0.0	0.0	0.7	0.0	0.0	2.0	0.0	1.0	0.0
A_08		61.7	2.0	0.0	0.0	1.0	0.0	0.0	0.0	0.0	0.0	0.0	2.0	0.0	0.7	1.3	0.0	1.3	0.0
A_09		64.7	1.0	0.0	0.0	0.0	0.3	0.0	0.0	0.0	0.0	0.0	0.7	0.3	0.7	3.0	0.3	1.0	0.0
A_10																			
A_11																			
B_01		54.3	8.0	0.0	0.7	1.3	0.3	0.0	7.3	2.0	0.3	3.0	1.7	1.0	1.0	0.0	0.7	0.0	0.0
B_02		54.7	10.7	0.3	0.3	0.3	0.7	0.7	4.0	1.7	0.7	0.7	0.7	0.0	1.7	0.0	0.7	0.0	0.0
B_03		51.7	7.3	1.3	1.0	1.0	1.0	0.0	5.3	4.0	0.7	3.0	0.3	0.7	0.3	0.0	0.3	0.0	0.0
B_04		57.7	5.3	0.0	1.3	2.0	0.0	0.3	5.7	1.3	0.0	1.7	0.7	0.7	1.0	0.0	0.3	0.0	0.0
B_05		52.7	4.0	2.7	0.0	1.3	0.0	0.3	3.7	2.0	0.0	2.0	2.0	1.3	2.3	0.0	2.0	0.3	0.0
B_06		58.0	5.7	1.3	0.0	0.7	0.0	0.7	3.3	0.7	0.3	2.3	0.7	1.7	1.3	0.0	0.0	0.0	0.0
B_07		60.7	5.7	2.0	1.3	1.0	0.0	0.3	3.0	1.3	0.0	1.0	2.0	0.7	1.0	0.0	0.0	0.0	0.0
B_08		54.3	7.7	1.0	0.7	0.7	0.0	0.3	5.3	2.0	0.7	2.0	0.7	1.3	0.7	0.0	0.0	0.0	0.0
C_01		48.7	7.7	0.0	0.7	0.7	0.3	0.0	4.7	4.0	2.0	0.0	2.3	0.3	0.0	0.0	0.0	0.0	0.0
C_02																			
C_03		42.0	10.3	0.0	1.3	2.3	1.7	0.0	9.0	5.3	0.0	2.7	3.0	0.0	0.3	0.0	0.0	0.0	0.0
C_04																			
C_05																			
C_06																			
C_07		48.0	10.0	0.0	0.3	0.7	0.3	0.0	1.3	1.3	0.0	1.3	2.3	0.3	0.3	2.0	1.3	0.0	0.0
C_08																			
C_09		45.3	10.0	0.3	0.3	1.0	0.0	0.0	6.7	6.0	1.3	1.7	1.3	0.7	0.3	2.7	0.3	0.3	0.0
C_10		47.3	13.7	0.0	0.7	0.7	0.3	0.3	1.7	2.0	0.3	1.7	1.7	1.0	0.0	2.3	0.3	0.0	0.0
C_11		50.7	9.7	0.0	1.7	1.7	1.0	0.0	7.7	3.7	0.3	2.7	1.3	0.3	0.3	0.0	0.0	0.0	0.0
C_12		49.0	5.0	1.3	0.7	1.0	0.0	0.7	3.7	1.7	1.3	2.7	3.0	0.0	1.0	0.0	0.3	0.0	0.0
C_13																			
C_14																			
D_01		60.7	2.0	0.7	0.3	0.0	0.0	0.0	0.3	0.3	0.0	0.0	0.7	0.0	0.0	0.0	0.0	0.0	0.0
D_02		70.7	4.0	0.0	0.0	0.3	0.0	0.7	0.7	0.0	0.3	0.3	1.7	0.0	0.0	0.3	0.3	0.0	0.0
D_03		65.0	4.0	0.0	0.0	0.0	0.3	0.3	0.0	0.7	0.0	0.3	0.7	0.3	0.0	0.0	0.0	0.0	0.0
D_04		55.3	2.7	0.0	1.0	0.0	0.3	0.0	0.3	0.3	0.0	0.0	0.3	0.0	0.0	0.0	0.3	0.0	0.0
D_05		55.0	4.7	0.0	0.0	0.0	0.0	0.0	0.3	0.0	0.3	0.0	0.0	0.0	0.0	0.0	0.0	0.0	0.0
D_06		64.7	3.3	0.0	0.3	0.0	0.3	0.0	0.3	0.0	0.0	0.7	0.0	0.0	0.0	0.0	0.0	0.3	0.0
D_07		63.0	3.3	0.0	0.0	0.0	0.3	0.7	0.0	0.0	0.0	0.0	0.0	0.0	0.0	0.0	0.0	0.0	0.0
D_08		63.7	2.7	0.0	0.0	0.0	0.0	0.7	0.0	0.0	0.0	0.7	0.0	0.0	0.0	0.0	0.0	0.0	0.3
D_09		57.0	2.3	0.0	0.0	0.0	0.0	0.0	0.3	0.0	0.0	0.3	0.3	0.0	0.0	0.0	0.0	0.0	0.0
D_10		58.7	5.0	0.0	0.0	0.0	1.0	0.0	0.7	0.0	0.0	0.0	0.3	0.0	0.0	0.0	0.0	0.0	0.0
D_11		66.7	3.3	0.0	0.0	0.0	0.3	0.3	0.3	0.0	0.0	0.3	0.7	0.0	0.0	0.0	0.0	0.0	0.0
D_12		53.0	4.7	0.0	0.0	0.0	0.3	0.3	0.0	0.0	0.0	0.0	0.7	0.0	0.0	0.0	0.3	0.0	0.0
D_13		55.7	5.7	0.0	0.7	0.0	0.0	0.0	0.0	0.0	0.0	0.3	1.0	0.0	0.0	0.0	0.0	0.0	0.0
D_14																			
E_01		66.7	3.3	0.0	0.0	0.0	0.3	0.3	0.3	0.0	0.0	0.3	0.7	0.0	0.0	0.0	0.0	0.0	0.0
E_02																			
E_03																			
E_04																			
E_05		56.7	3.7	0.0	0.0	0.3	0.0	0.7	0.3	0.0	0.0	0.0	1.0	0.0	0.0	0.7	0.0	0.0	0.0
F_01		66.7	4.0	0.0	0.0	0.0	0.7	0.3	0.7	0.0	0.0	0.3	2.0	0.0	0.0	0.0	0.3	0.0	0.0
F_02		74.3	0.3	0.0	0.0	0.0	0.0	0.0	0.7	0.0	0.7	1.0	0.7	0.0	0.0	0.0	0.0	0.0	0.0

Sample	*Authigenic minerals [%]*	Quartz	Calcite	Dolomite	Siderite	Feldspar	Barite	Rutile pf	Ill cmt, pf	Ill cmt, pl	Kln cmt, pf	FeOx pl	FeOH	*Replacements [%]*	Cal rp Kfs	Ill rp Kfs	Kln rp Kfs	Ill rp Kln
A_01		8.3	0.0	2.0	1.3	0.0	0.0	3.3	9.0	0.7	1.7	0.0	0.7		0.3	0.0	0.0	0.3
A_02		9.7	0.0	1.3	1.0	0.0	0.0	2.0	12.3	0.3	4.3	0.0	1.0		0.0	0.3	0.0	0.3
A_03		6.0	0.0	9.7	5.3	0.0	0.0	1.3	2.3	0.0	1.0	0.7	2.3		1.3	3.3	3.3	0.0
A_04		10.3	0.0	2.3	1.0	0.0	0.0	1.0	4.3	0.7	0.7	0.3	0.7		2.0	3.3	1.0	0.0
A_05		6.3	0.0	4.0	2.3	0.0	0.0	0.7	2.3	0.3	1.3	1.3	2.3		1.0	3.0	1.3	0.0
A_06		11.3	0.0	0.3	0.3	0.0	0.0	0.7	4.0	0.3	1.0	0.7	0.7		2.0	3.3	0.3	0.0
A_07		6.0	0.0	4.3	3.7	0.0	0.3	1.7	8.7	1.3	1.0	0.0	2.7		0.0	3.3	0.3	0.0
A_08		7.0	0.0	4.0	4.7	0.0	0.0	0.3	4.0	1.7	0.7	0.0	3.0		1.3	2.7	0.7	0.0
A_09		7.7	0.0	2.7	2.0	0.0	0.0	0.7	4.0	1.3	1.3	0.0	2.7		0.7	3.7	0.7	0.0
A_10																		
A_11																		
B_01		5.3	0.0	0.0	0.0	1.3	0.0	0.3	0.3	6.3	0.0	2.0	0.7		0.0	1.0	0.0	0.0
B_02		7.7	1.0	0.0	0.0	1.7	0.0	0.0	0.0	5.0	0.0	0.7	0.7		0.3	1.0	0.0	0.0
B_03		6.0	0.3	0.0	0.0	1.0	0.0	0.0	0.0	2.7	0.0	1.0	0.3		0.0	1.7	0.0	0.0
B_04		7.3	5.3	0.0	0.0	1.0	0.3	0.0	0.0	5.0	0.0	0.3	1.0		0.0	0.3	0.0	0.0
B_05		6.0	0.0	0.0	0.0	1.3	0.0	0.0	0.0	11.3	0.0	0.7	2.0		0.0	2.0	0.0	0.0
B_06		7.0	0.0	0.0	0.0	0.7	0.3	0.0	0.3	6.3	0.0	0.3	0.3		0.0	1.0	0.0	0.0
B_07		5.7	1.7	0.0	0.0	2.0	0.3	0.0	0.3	4.3	0.0	0.7	0.7		0.7	2.0	0.0	0.0
B_08		5.7	3.0	0.0	0.0	0.7	0.0	0.0	1.0	6.7	0.0	0.0	1.7		0.3	1.7	0.0	0.0
C_01		4.7	5.3	0.0	0.0	0.0	0.0	0.0	0.3	3.3	1.0	1.3	2.3		0.3	0.0	1.0	0.0
C_02																		
C_03		4.0	0.0	0.0	0.0	1.0	0.0	0.0	1.0	4.0	0.0	1.0	0.7		0.0	1.7	0.7	0.0
C_04																		
C_05																		
C_06																		
C_07		6.3	0.0	0.0	0.0	1.3	0.0	0.0	2.0	4.7	0.0	1.0	0.7		0.0	4.0	0.3	0.0
C_08																		
C_09		6.0	0.0	0.0	0.0	1.0	0.0	0.0	0.3	5.7	0.0	0.7	0.7		0.0	1.3	0.0	0.0
C_10		5.0	0.0	0.0	0.0	2.3	0.0	0.0	0.3	5.0	0.0	1.3	0.7		0.0	2.0	0.0	0.0
C_11		7.0	0.0	0.0	0.0	1.7	0.0	0.0	0.3	4.3	0.0	1.0	0.3		0.0	1.0	0.0	0.0
C_12		15.7	2.0	0.0	0.0	3.3	0.3	0.3	0.0	2.0	0.0	0.0	1.0		1.3	1.3	0.0	0.0
C_13																		
C_14																		
D_01		12.7	0.0	0.0	0.0	0.0	0.0	0.7	0.0	2.0	0.0	0.7	0.3		0.0	0.0	0.0	0.0
D_02		7.3	0.0	0.0	0.0	0.0	0.0	0.0	0.0	1.3	0.0	0.3	1.0		0.0	1.3	0.0	0.0
D_03		12.0	0.0	0.0	0.0	0.0	0.0	0.3	0.0	2.3	0.0	1.0	1.0		0.0	0.0	0.0	0.0
D_04		12.3	0.0	0.0	0.0	0.3	0.0	1.3	0.7	3.3	0.0	0.7	1.3		0.0	0.7	0.0	0.0
D_05		18.3	0.0	0.0	0.0	0.0	0.0	0.0	0.3	1.7	0.0	0.7	0.7		0.0	1.7	0.0	0.0
D_06		13.0	0.0	0.0	0.0	0.0	0.0	0.0	0.0	1.0	0.0	0.3	0.0		0.0	0.3	0.3	0.0
D_07		17.0	0.0	0.0	0.0	0.0	0.0	0.0	0.0	0.7	0.0	0.3	0.0		0.0	0.0	0.3	0.0
D_08		10.0	0.0	0.0	0.0	0.0	0.0	0.0	0.3	1.3	0.3	0.3	0.0		0.0	0.3	0.3	0.0
D_09		16.7	0.0	0.0	0.0	0.0	0.0	0.0	0.0	1.0	0.7	0.7	0.0		0.0	0.3	0.7	0.0
D_10		17.7	0.0	0.0	0.0	0.0	0.0	0.0	0.0	1.0	0.0	0.3	0.3		0.0	0.3	0.0	0.0
D_11		9.0	0.0	0.0	0.0	0.0	0.0	0.0	0.0	1.0	0.0	0.7	0.0		0.0	0.7	0.7	0.0
D_12		19.3	0.0	0.0	0.0	0.0	0.0	0.3	0.3	0.7	0.0	1.7	0.7		0.0	0.3	0.0	0.0
D_13		16.7	0.0	0.0	0.0	0.0	0.0	0.7	0.0	3.0	0.0	2.0	1.0		0.0	1.0	0.3	0.3
D_14																		
E_01		9.0	0.0	0.0	0.0	0.0	0.0	0.0	0.0	1.0	0.0	0.7	0.0		0.0	0.7	0.7	0.0
E_02																		
E_03																		
E_04																		
E_05		13.7	0.0	0.0	0.0	0.0	0.0	0.0	0.3	0.7	0.0	0.7	0.3		0.0	0.3	0.3	0.3
F_01		8.0	0.0	0.0	0.0	0.3	0.0	1.3	0.7	3.7	0.0	1.0	0.0		0.0	0.3	0.0	0.0
F_02		5.0	0.0	0.0	0.0	0.0	0.0	0.0	2.7	3.3	1.0	0.0	0.0		0.0	0.7	0.0	0.3

Sample	*Diagenetic parameter [%]*	IGV	Cement volume	Optical porosity	COPL	CEPL	Compact. index	GTI coverage	GTG coverage	Quartz cements	Carbonate cements	Clay minerals	Carbonates + clays	Microporosity
A_01		28.7	27.0	2.0	22.9	20.8	0.5	20.3	20.0	8.3	3.3	12.3	15.7	7.8
A_02		33.3	32.0	1.3	17.5	26.4	0.4	23.1	21.0	9.7	2.3	18.0	20.3	11.3
A_03		31.0	28.7	3.3	20.3	22.9	0.5	30.4	22.3	6.0	15.0	10.0	25.0	6.3
A_04		22.0	21.3	2.0	29.5	15.0	0.7	15.7	24.9	10.3	3.3	10.3	13.7	6.5
A_05		22.3	21.0	2.0	29.2	14.9	0.7	17.1	26.0	6.3	6.3	9.0	15.3	5.7
A_06		21.3	19.3	2.0	30.1	13.5	0.7	11.8	28.5	11.3	0.7	9.0	9.7	5.7
A_07		30.3	29.7	0.7	21.1	23.4	0.5	33.5	20.9	6.0	8.0	15.7	23.7	9.9
A_08		25.3	25.3	0.0	26.3	18.7	0.6	35.7	24.8	7.0	8.7	10.7	19.3	6.7
A_09		22.7	22.3	0.7	28.9	15.9	0.6	28.3	26.6	7.7	4.7	11.0	15.7	6.9
A_10														
A_11														
B_01		16.7	16.3	1.0	34.0	10.8	0.8	32.4	24.0	7.0	0.0	9.0	9.0	5.7
B_02		20.0	16.7	4.3	31.3	11.5	0.7	20.0	30.8	15.7	1.0	6.3	7.3	4.0
B_03		17.3	11.3	9.0	33.5	7.5	0.8	46.4	18.6	6.0	0.3	5.3	5.7	3.4
B_04		21.7	20.3	1.3	29.8	14.3	0.7	41.0	38.0	7.3	5.3	7.3	12.7	4.6
B_05		21.3	21.3	0.0	30.1	14.9	0.7	66.3	52.4	6.0	0.0	14.7	14.7	9.2
B_06		19.3	15.3	7.0	31.8	10.5	0.8	58.0	45.4	7.0	0.0	8.3	8.3	5.3
B_07		17.3	15.7	1.7	33.5	10.4	0.8	56.0	43.6	5.7	1.7	7.7	9.3	4.8
B_08		20.7	18.7	2.0	30.7	12.9	0.7	63.6	42.3	5.7	3.0	10.0	13.0	6.3
C_01		24.0	18.3	8.3	27.6	13.3	0.7	64.3	25.9	4.7	5.3	7.0	12.3	4.4
C_02														
C_03		15.0	11.7	8.0	35.3	7.5	0.8	74.5	39.4	4.0	0.0	7.3	7.3	4.6
C_04														
C_05														
C_06														
C_07		21.3	16.0	10.0	30.1	11.2	0.7	50.2	27.7	6.3	0.0	11.0	11.0	6.9
C_08														
C_09		17.0	14.3	6.0	33.7	9.5	0.8	54.6	34.5	6.0	0.0	7.3	7.3	4.6
C_10		20.3	14.7	9.3	31.0	10.1	0.8	58.0	30.6	5.0	0.0	7.3	7.3	4.6
C_11		16.3	14.7	3.0	34.3	9.6	0.8	61.6	48.6	5.3	0.0	6.0	6.0	3.8
C_12		25.7	24.7	1.3	26.0	18.3	0.6	67.2	36.2	7.7	2.0	3.3	5.3	2.1
C_13														
C_14														
D_01		33.3	16.3	18.7	17.5	13.5	0.6	28.8	21.8	12.7	0.0	2.0	2.0	1.3
D_02		18.0	10.0	9.3	32.9	6.7	0.8	32.4	24.2	7.3	0.0	2.7	2.7	1.7
D_03		26.7	16.7	11.7	25.0	12.5	0.7	31.4	13.4	12.0	0.0	2.3	2.3	1.5
D_04		37.0	20.0	18.3	12.7	17.5	0.4	32.4	10.9	12.3	0.0	5.0	5.0	3.2
D_05		37.0	21.7	16.3	12.7	18.9	0.4	22.4	13.2	18.3	0.0	3.7	3.7	2.3
D_06		27.0	14.3	15.0	24.7	10.8	0.7	24.0	14.0	13.0	0.0	1.7	1.7	1.1
D_07		30.7	18.0	14.3	20.7	14.3	0.6	17.8	9.2	17.0	0.0	1.0	1.0	0.6
D_08		29.7	12.3	19.0	21.8	9.6	0.7	25.4	12.2	10.0	0.0	2.7	2.7	1.7
D_09		37.3	19.0	19.7	12.2	16.7	0.4	15.0	8.2	16.7	0.0	2.7	2.7	1.7
D_10		32.3	19.3	14.7	18.7	15.7	0.5	11.4	5.6	17.7	0.0	1.3	1.3	0.8
D_11		25.3	10.7	16.0	26.3	7.9	0.8	45.0	19.4	9.0	0.0	2.3	2.3	1.5
D_12		39.3	23.0	17.3	9.3	20.9	0.3	11.8	7.4	19.3	0.0	1.3	1.3	0.8
D_13		32.3	23.3	11.7	18.7	19.0	0.5	18.3	14.5	16.7	0.0	4.7	4.7	2.9
D_14														
E_01		25.3	10.7	16.0	26.3	7.9	0.8	32.0	29.5	9.0	0.0	2.3	2.3	1.5
E_02														
E_03														
E_04														
E_05		35.3	15.7	20.0	14.9	13.3	0.5	19.1	10.9	13.7	0.0	2.0	2.0	1.3
F_01		23.0	15.0	9.7	28.6	10.7	0.7	58.0	24.6	8.0	0.0	4.7	4.7	2.9
F_02		20.0	12.0	9.3	31.3	8.3	0.8	56.0	24.5	5.0	0.0	8.0	8.0	5.0

Sample	*Petrographic porosity [%]*	Intergr. porosity	Sec. poro Kfs + RF	Sec. poro. dolomite	*Petrophysical data*	Helium ϕ [%]	K_H [mD]	K_V [mD]	Effective He ϕ [%]
A_01		1.7	0.3	0.0		19.9	0.390	0.050	12.1
A_02		1.3	0.0	0.0		17.2	0.249	0.039	5.8
A_03		2.3	1.0	0.0		12.7	0.012		6.4
A_04		0.7	1.3	0.0		11.4	0.016	0.012	4.8
A_05		1.3	0.7	0.0		11.1	0.045	0.002	5.4
A_06		2.0	0.0	0.0		9.1	0.017	0.008	3.5
A_07		0.7	0.0	0.0		14.6	0.011	0.013	4.7
A_08		0.0	0.0	0.0					
A_09		0.3	0.3	0.0		16.7	0.200	0.060	9.8
A_10						17.5	8.602	0.009	
A_11						15.8	0.066	0.012	
B_01		0.3	0.7	0.0					
B_02		3.3	1.0	0.0					
B_03		6.0	3.0	0.0		7.8		0.143	4.4
B_04		1.3	0.0	0.0					
B_05		0.0	0.0	0.0					
B_06		4.0	3.0	0.0		13.4	115.235		8.1
B_07		1.7	0.0	0.0					
B_08		2.0	0.0	0.0		8.6	110.610		2.3
C_01		5.0	3.3	0.0		7.8	0.032		3.4
C_02						16.7	7.454	4.187	
C_03		3.3	4.7	0.0		14.0	2.528	0.577	9.4
C_04						16.0	38.272	0.824	
C_05						21.3	68.847	191.221	
C_06						14.9		2.032	
C_07		5.3	4.7	0.0		19.4	50.089	20.804	12.5
C_08						16.9		1.743	
C_09		2.7	3.3	0.0		12.9	12.358	0.271	8.3
C_10		5.7	3.7	0.0		17.0	39.667	20.884	12.4
C_11		1.3	1.7	0.0					
C_12		1.0	0.3	0.0		9.8	3.589		7.7
C_13						11.9	2.896	0.199	
C_14						7.7	2.835	0.040	
D_01		17.0	1.7	0.0		24.9	3875.441	2694.981	23.6
D_02		8.0	1.3	0.0		19.6	201.137	122.254	17.9
D_03		10.0	1.3	0.3		20.8	215.920	135.308	19.4
D_04		16.7	1.3	0.3		26.7	10000.000	10000.000	23.5
D_05		15.3	1.0	0.0		24.3	4199.971	4709.060	22.0
D_06		12.7	2.3	0.0		22.2		1583.241	21.1
D_07		12.7	1.3	0.3		25.1	10000.000		24.5
D_08		17.3	1.7	0.0		32.0	10000.000	10000.000	30.4
D_09		18.3	1.0	0.3		24.7	10000.000	3650.147	23.0
D_10		13.0	1.7	0.0		27.8	10000.000		27.0
D_11		14.7	1.3	0.0		28.6	10000.000		27.2
D_12		16.3	0.7	0.3		22.3	1196.470		21.5
D_13		9.0	2.7	0.0		21.9	1695.573		19.0
D_14						23.7	1045.874	536.198	
E_01		14.7	1.3	0.0		25.7	10000.000	10000.000	24.3
E_02						34.8	10000.000	10000.000	
E_03						34.4	10000.000		
E_04						32.7	3770.940	1164.679	
E_05		19.7	0.3	0.0					
F_01		8.0	1.7	0.0		20.0	108.461	48.505	17.0
F_02		8.0	1.0	0.3					

	Average			Standard Deviation			Error			Minimum			Maximum		
	Cornberg	Flechtingen	Penrith	Cornberg	Flechtingen	Penrith	Cornberg	Flechtingen	Penrith	Cornberg	Flechtingen	Penrith	Cornberg	Flechtingen	Penrith
Depositional parameters															
Grain size	0.32	0.29	0.42	0.07	0.07	0.09	0.02	0.02	0.02	0.24	0.20	0.28	0.48	0.43	0.55
Sorting	1.38	1.40	1.33	0.13	0.11	0.17	0.04	0.03	0.04	1.25	1.25	1.17	1.68	1.66	1.73
Q [%] (Folk, 1980)	93.5	69.8	92.6	1.2	5.7	1.8	0.4	1.5	0.4	91.8	57.7	89.5	95.8	2.3	0.3
F [%] (Folk, 1980)	2.1	14.6	5.8	0.7	2.8	1.7	0.2	0.7	0.4	1.4	9.0	2.6	3.3	74.5	58.0
R [%] (Folk, 1980)	4.4	15.5	1.7	1.0	4.4	0.8	0.3	1.1	0.2	2.8	10.8	0.6	6.2	52.4	29.5
Accessories [%]	1.1	0.5	0.1	0.3	0.6	0.2	0.1	0.2	0.0	0.7	0.0	0.0	1.7	5.3	0.0
Detrital components [%]															
Quartz	62.8	51.7	62.0	4.1	4.9	5.9	1.4	1.3	1.4	54.0	42.0	53.0	67.0	60.7	74.3
K-feldspar	1.3	8.0	3.5	0.5	2.6	1.2	0.2	0.7	0.3	0.3	4.0	0.3	2.0	13.7	5.7
Plagioclase	0.0	0.7	0.0	0.0	0.8	0.2	0.0	0.2	0.0	0.0	0.0	0.0	0.0	2.7	0.7
Chert	0.0	0.7	0.1	0.0	0.5	0.3	0.0	0.1	0.1	0.0	0.0	0.0	0.0	1.7	1.0
Shale RF	0.4	1.1	0.0	0.4	0.5	0.1	0.1	0.1	0.0	0.0	0.3	0.0	1.0	2.3	0.3
Sandstone RF	0.1	0.4	0.2	0.1	0.5	0.3	0.0	0.1	0.1	0.0	0.0	0.0	0.3	1.7	1.0
Siltstone RF	0.2	0.2	0.3	0.2	0.3	0.3	0.1	0.1	0.1	0.0	0.0	0.0	0.7	0.7	0.7
Silicic VRF	0.0	4.8	0.3	0.0	2.1	0.2	0.0	0.5	0.1	0.0	1.3	0.0	0.0	9.0	0.7
Feldspathic VRF	0.0	2.6	0.1	0.0	1.5	0.2	0.0	0.4	0.0	0.0	0.7	0.0	0.0	6.0	0.7
Felsic PRF	0.0	0.5	0.1	0.0	0.6	0.2	0.0	0.2	0.0	0.0	0.0	0.0	0.0	2.0	0.7
Granitic PRF	0.0	1.9	0.3	0.0	0.8	0.3	0.0	0.2	0.1	0.0	0.0	0.0	0.0	3.0	1.0
Quartzite	0.7	1.6	0.6	0.6	0.8	0.5	0.2	0.2	0.1	0.0	0.3	0.0	2.0	3.0	2.0
Phyllite	0.1	0.7	0.0	0.2	0.5	0.1	0.1	0.1	0.0	0.0	0.0	0.0	0.3	1.7	0.3
MRF undiff	0.6	0.8	0.0	0.5	0.6	0.0	0.2	0.2	0.0	0.0	0.0	0.0	1.7	2.3	0.0
RF undiff	1.6	0.5	0.1	0.6	0.9	0.2	0.2	0.2	0.0	0.7	0.0	0.0	3.0	2.7	0.7
Mica	0.1	0.4	0.1	0.1	0.6	0.1	0.0	0.1	0.0	0.0	0.0	0.0	0.3	2.0	0.3
Zircon	1.0	0.0	0.0	0.3	0.1	0.1	0.1	0.0	0.0	0.7	0.0	0.0	1.3	0.3	0.3
Hornblende	0.0	0.0	0.0	0.0	0.0	0.1	0.0	0.0	0.0	0.0	0.0	0.0	0.0	0.0	0.3
Matrix undiff	0.0	0.1	0.0	0.0	0.2	0.1	0.0	0.0	0.0	0.0	0.0	0.0	0.0	0.7	0.3
Authigenic Minerals [%]															
Quartz	8.1	6.6	12.8	1.9	2.6	4.2	0.6	0.7	1.0	6.0	4.0	5.0	11.3	15.7	19.3
Calcite	0.0	1.2	0.0	0.0	1.8	0.0	0.0	0.5	0.0	0.0	0.0	0.0	0.0	5.3	0.0
Dolomite	3.4	0.0	0.0	2.5	0.0	0.0	0.8	0.0	0.0	0.3	0.0	0.0	9.7	0.0	0.0
Siderite	2.4	0.0	0.0	1.7	0.0	0.0	0.6	0.0	0.0	0.3	0.0	0.0	5.3	0.0	0.0
Feldspar	0.0	1.4	0.0	0.0	0.8	0.1	0.0	0.2	0.0	0.0	0.0	0.0	0.0	3.3	0.3
Barite	0.0	0.1	0.0	0.1	0.1	0.0	0.0	0.0	0.0	0.0	0.0	0.0	0.3	0.3	0.0
Rutile pf	1.3	0.0	0.3	0.9	0.1	0.4	0.3	0.0	0.1	0.3	0.0	0.0	3.3	0.3	1.3
Illite cmt, pf	5.7	0.4	0.3	3.3	0.5	0.6	1.1	0.1	0.2	2.3	0.0	0.0	12.3	2.0	2.7
Illite cmt, pl	0.7	5.0	1.7	0.5	2.1	1.0	0.2	0.5	0.2	0.0	2.0	0.7	1.7	11.3	3.7
Kaolinite cmt, pf	1.4	0.1	0.1	1.1	0.2	0.3	0.4	0.1	0.1	0.7	0.0	0.0	4.3	1.0	1.0
FeOx pl	0.3	0.8	0.7	0.4	0.5	0.5	0.1	0.1	0.1	0.0	0.0	0.0	1.3	2.0	2.0
FeOH	1.8	0.9	0.4	0.9	0.6	0.4	0.3	0.2	0.1	0.7	0.3	0.0	3.0	2.3	1.3
Replacements & petrographic porosity [%]															
Calcite rp Kfs	1.0	0.2	0.0	0.7	0.4	0.0	0.2	0.1	0.0	0.0	0.0	0.0	2.0	1.3	0.0
Illite rp Kfs	2.6	1.5	0.5	1.3	0.9	0.4	0.4	0.2	0.1	0.0	0.0	0.0	3.7	4.0	1.7
Kaolinite rp Kfs	0.9	0.1	0.2	1.0	0.3	0.3	0.3	0.1	0.1	0.0	0.0	0.0	3.3	1.0	0.7
Illite rp Kaolinite	0.1	0.0	0.1	0.1	0.0	0.1	0.0	0.0	0.0	0.0	0.0	0.0	0.3	0.0	0.3
Intergr. Porosity	1.1	2.9	13.6	0.7	1.9	3.7	0.2	0.5	0.9	0.0	0.0	8.0	2.3	6.0	19.7
Sec. Poro. Kfs + RF	0.4	2.0	1.4	0.5	1.7	0.5	0.2	0.4	0.1	0.0	0.0	0.3	1.3	4.7	2.7
Sec. Poro. dolomite	0.0	0.0	0.1	0.0	0.0	0.2	0.0	0.0	0.0	0.0	0.0	0.0	0.0	0.0	0.3

	Average			Standard Deviation			Error			Minimum			Maximum		
	Cornberg	Flechtingen	Penrith	Cornberg	Flechtingen	Penrith	Cornberg	Flechtingen	Penrith	Cornberg	Flechtingen	Penrith	Cornberg	Flechtingen	Penrith
Diagenetic parameters															
Intergranular volume [%]	26.3	19.6	30.0	4.3	2.9	4.4	1.4	0.7	1.1	21.3	15.0	18.0	33.3	25.7	39.3
Cement volume [%]	25.2	16.7	16.4	4.2	3.4	4.2	1.4	0.9	1.0	19.3	11.3	10.0	32.0	24.7	23.3
Optical porosity [%]	1.6	4.8	15.1	0.9	3.4	3.5	0.3	0.9	0.9	0.0	0.0	9.3	3.3	10.0	20.0
Compactional porosity loss	25.1	31.5	20.8	4.5	2.5	6.9	1.5	0.6	1.7	17.5	26.0	9.3	30.1	35.3	32.9
Cementational porosity loss	19.1	11.5	13.2	4.3	2.8	4.3	1.4	0.7	1.0	13.5	7.5	6.7	26.4	18.3	20.9
Compactional index	0.6	0.7	0.6	0.1	0.1	0.2	0.03	0.02	0.04	0.4	0.6	0.3	0.7	0.8	0.8
GTI coverage [%]	24.0	54.3	28.3	7.9	13.9	13.5	2.6	3.6	3.3	11.8	20.0	11.4	35.7	81.0	79.0
GTG coverage [%]	23.9	35.9	15.5	2.8	9.3	6.9	0.9	2.4	1.7	20.0	18.6	5.6	28.5	78.3	96.6
Quartz cements [%]	8.1	6.6	12.8	1.9	2.6	4.2	0.6	0.7	1.0	6.0	4.0	5.0	11.3	15.7	19.3
Carbonate cements [%]	5.8	1.2	0.0	4.1	1.8	0.0	1.4	0.5	0.0	0.7	0.0	0.0	15.0	21.2	9.5
Clay Minerals [%]	11.8	7.9	3.0	2.9	2.5	1.7	1.0	0.7	0.4	9.0	3.3	1.0	18.0	14.7	8.0
Carbonates + Clays [%]	17.6	9.1	3.0	4.6	2.8	1.7	1.5	0.7	0.4	9.7	5.3	1.0	25.0	14.7	8.0
Microporosity [%]	7.4	5.0	1.9	1.8	1.6	1.1	0.6	0.4	0.3	5.7	2.1	0.6	11.3	9.2	5.0
Petrophysical measurements															
Helium porosity [%]	14.6	13.5	25.9	3.2	4.2	4.6	1.0	1.2	1.1	9.1	7.7	19.6	19.9	21.3	34.8
Horizontal permeability [mD]	0.96	35	5906	2.55	39	4245	0.81	10.9	1029	0.01	0.03	109	8.6	115	10^4
Vertical permeability [mD]	0.02	20	4203	0.02	52	4088	0.01	15.0	1092	0.002	0.04	49	0.06	191	10^4
Effective Helium porosity [%]	6.6	7.6	22.8	2.7	3.4	3.5	0.9	1.0	0.9	3.5	2.3	17.0	12.1	12.5	30.4

Reservoir quality of Rotliegend sandstones is mainly controlled by their permeability, and porosity, and their mechanical properties. As a result, diagenetic porosity-reducing processes need to be understood to evaluate reservoir quality and geotechnical properties in sandstones. The position and abundance of tangential grain-coating illite is identified as key control on syntaxial quartz cementation and chemical compaction. Best reservoir qualities are achieved in mature sandstones with large amounts of quartz cementation, but small quantities of clay minerals and carbonate cements and thus lower mechanical and chemical compaction. Moreover, the relative length of grain-contacts compared to the respective grain diameter is identified as proxy for rock strength.

ISBN 978-3-7315-1107-6

9 783731 511076 >

Gedruckt auf FSC-zertifiziertem Papier